Mathematical modelling of auxin dynamics in the model plant *Arabidopsis thaliana*

Heather Collis

A thesis presented for the degree of Doctor of Philosophy



School of Mathematical Sciences
University of Nottingham
8th August 2022

Abstract

The plant hormone auxin plays a crucial role in many aspects of plant development including growth, organ initiation, and tropic responses. In the root tip of *Arabidopsis thaliana*, auxin is transported via influx (AUX1/LAX) and efflux (PIN/ABCB) carriers, as well as diffusing through plasmodesmata. Existing mathematical models of auxin transport in the root-tip capture the auxin maxima seen experimentally around the quiescent centre region of the root tip, however, these models often rely on a simplified fixed auxin concentration boundary condition at the root-shoot boundary. By working towards the formulation of a hybrid seedling model that captures cell-scale auxin transport in the root-tip and long-distance auxin transport via the phloem, work in this thesis aims to understand how environmental conditions at the shoot can influence auxin patterning in the root tip of *Arabidopsis thaliana*. The initial development of a root-tip auxin transport model with a constant flux boundary condition at the root-shoot boundary, highlighted the important role of auxin biosynthesis in root tissues on root-tip auxin patterning. The incorporation of the constant flux boundary condition, in order to consider proportions of shoot-derived and root-derived auxin, emphasised the need to include a more biologically relevant auxin delivery mechanism to the root tip. We expanded upon phloem transport models in the literature to include the transport of a second small solute alongside sugar (in this thesis considered auxin). Model simulations revealed how environmental conditions that influence sugar dynamics can effect the amount of auxin delivered to the root tip in the case of passively loaded hormones. Finally, these models were coupled together with an additional shoot compartment to create a novel hybrid model of auxin dynamics in a "virtual" seedling. The hybrid model captures how environmental cues can effect auxin and sugar concentration in cotyledons and how this affects phloem transport velocity, auxin delivery to the root tip, and auxin patterning within the root tip. Results highlight the importance of considering the influence of environmental cues on both sugar and auxin parameters when investigating root-tip auxin patterning.

Acknowledgements

"You do not need anyone's permission to become a great mathematician"

(Dr. Nira Chamberlain)

This work was funded by the Leverhulme Trust and the University of Nottingham as part of the Modelling and Analytics for a Sustainable Society DTP. I would like to thank my supervisors Leah Band, Markus Owen, and Malcolm Bennett as well as Nathan Mellor for their support throughout this project. I would also like to thank my fellow members of the MASS DTP for providing useful discussions and encouragement throughout my studies. Special thanks must go to the biologists in the School of Plant Sciences and beyond who have always shown a keen interest in making maths and biology collaborations a core part of their work. I would also like to thank the community in the School of Mathematical Sciences who have enabled me to thrive in areas of interest outside of my PhD research including EDI work and science outreach. Finally, I would like to thank my family for always encouraging me.

Contents

1 Literature review **8**

1.1 Motivation 8

1.2 The plant hormone auxin 10

1.2.1 Auxin metabolism 10

1.2.2 Auxin transport 12

1.2.3 Auxin and the environment 12

1.2.4 Auxin sensors 14

1.3 Models of auxin dynamics in the root tip 14

1.3.1 Models of auxin transport in the *Arabidopsis* root tip 14

1.3.2 Models of auxin metabolism in the *Arabidopsis* root tip . . . 19

1.4 Local auxin biosynthesis in the Arabidopsis root tip 20

1.5 The phloem transport system 23

1.5.1 Phloem transport models 24

1.5.2 Hormones in the phloem 28

1.5.3 Environmental impacts on phloem transport 29

2 Modelling local auxin biosynthesis **31**

2.1 Introduction 31

2.2 Auxin transport model 32
2.2.1 Model structure 32
2.2.2 Model fluxes 34
2.2.3 Auxin production and degradation 35
2.2.4 Auxin concentration equations 36
2.2.5 Boundary and initial conditions 36
2.2.6 DII-VENUS model equations 36
2.3 Modelling local auxin synthesis 39
2.3.1 Reciprocal-grafting experiments 40
2.3.2 Initial modelling results 41
2.3.3 Modifying the shoot boundary condition 44
2.3.4 Model optimisation 45
2.4 Local auxin biosynthesis experiments 54
2.5 Conclusions 54

3 Modelling hormone transport in the phloem **55**

3.1 Introduction 55
3.2 Phloem transport model 57
3.2.1 Governing equations 57
3.2.2 Velocity of water at the membrane 59
3.2.3 Solute flux at the boundary 61
3.2.4 Non-dimensionalisation 62
3.2.5 Integrating with respect to R 65
3.2.6 Deriving the Münch flow equations 67

3.3 Modelling hormone transport in the phloem 68

3.3.1 Stokes-Einstein calculations for plant hormone diffusion coefficients 68

3.3.2 Hormone transport equations 69

3.4 Analytical solutions to transport equations 73

3.4.1 Model zonation 73

3.4.2 Solving in the limit Mü $\ll 1$ 75

3.4.3 Loading zone 76

3.4.4 Unloading zone 79

3.4.5 Translocation zone 80

3.4.6 Specific solution: $\bar{U}_1(X) = AX$ 82

3.5 Numerical solutions to transport equations 85

3.5.1 Shooting method 85

3.5.2 Upwind scheme for numerical simulations 86

3.5.3 Prescribing biologically motivated loading and unloading parameters 87

3.6 Results 89

3.6.1 The rate of delivery to the root tip does not depend on phloem transport velocity for actively loaded sugar and hormones . 89

3.6.2 Bulk flow unloading increases the phloem transport velocity 89

3.6.3 Bulk flow unloading can dominate over diffusive unloading when the ratio between root and shoot external sugar concentrations is increased 93

3.6.4 Increasing active sugar loading increases phloem transport velocity and increases the rate of delivery of passively loaded hormones 98

3.6.5 Increasing the ratio between root and shoot external sugar concentrations has little impact on the unloading of hormones 100

3.6.6 Varying plasmodesmata density modifies phloem transport velocity though the exact relationship remains unclear . . . 101

3.7 Conclusions . . . 105

4 Hybrid model of auxin dynamics in the *Arabidopsis* seedling 107

4.1 Introduction . . . 107

4.2 Hybrid model development . . . 107

4.2.1 Auxin root dynamics . . . 110

4.2.2 Incorporating a shoot compartment . . . 113

4.2.3 Sugar root dynamics . . . 116

4.2.4 Summary . . . 117

4.3 Numerical simulations . . . 118

4.4 Investigating the relationship between parameters J_{pla} and $\beta_{a,3}$ . . . 118

4.5 Investigating the impact of environmental conditions on root-tip auxin patterning . . . 121

4.5.1 Temperature variation . . . 122

4.5.2 Exogenous sucrose application . . . 128

4.5.3 Varying plasmodesmata density . . . 132

4.6 Conclusions . . . 141

5 Conclusions 143

5.1 Local auxin biosynthesis in the root tip is important for root tip auxin patterning . . . 144

5.2 Environmental conditions that modify phloem transport velocity affect hormone delivery to the root tip . . . 145

5.3 Varying environmental conditions influences root-tip auxin patterning via changes in both sugar and auxin parameters. 147

5.4 Future directions 148

5.4.1 Local auxin biosynthesis experiments 148

5.4.2 Modelling auxin transport in the model crop species *Oryza sativa* 149

5.4.3 Extending the phloem transport model to incorporate Taylor dispersion 150

5.4.4 Transport models for other small signalling molecules . . . 151

5.4.5 Whole plant modelling with a "virtual" seedling 152

A Supplementary Figures **154**

Chapter 1

Literature review

1.1 Motivation

The Food Security Information Network (2019) deem people to have food security if sufficient quantities of food are consistently available and households have the ability to obtain their required nutrition from it. Acute food insecurity is defined to be when, for any period of time, a specific region experiences a lack of food security so extreme that it threatens to cause death for the people experiencing it (Food Security Information Network, 2019). In recent years, evidence suggests world hunger is rising: it is estimated that, in 2017, nearly 821 million people lacked food security (Food and Agriculture Organization of the United Nations, 2018), and that more than 113 million people were living with acute food insecurity (Food Security Information Network, 2019).

The effects of living with food insecurity are varied. In low income countries, communities living with acute food insecurity are at a high risk of being malnourished through under-nutrition (Food Security Information Network, 2019). However, it is important to note that food insecurity also occurs in middle to high income countries where healthy and nutritious food is often expensive, and so communities experiencing food insecurity in these countries are often at a higher risk of being overweight or obese (Food and Agriculture Organization of the United Nations, 2018).

There are many causes that may trigger a household to experience a lack of food security. The most common causes include conflict, climate change, and economic turbulence (Food Security Information Network, 2019). Causes of food insecurity that are triggered by climate change can be addressed using science and mathemat-

ics. Key triggers associated with climate change that may lead to food insecurity include drought, extreme/nonseasonal temperatures, and disease/infestation. These environmental stresses can cause crop species to produce lower yields or fail entirely.

Environmental conditions, such as drought and extreme temperatures, that reduce the growth or yield of a plant below an optimum level are known as abiotic stresses (Andjelkovic, 2018, Cramer et al., 2011). These environmental conditions and their impacts are increasingly being exacerbated by climate change; with drought and extreme temperatures amongst the abiotic stresses expected to be most severely affected by climate change (Andjelkovic, 2018). It is therefore important that we are able to develop crop varieties that are resilient to these changes in the environment.

Lynch (2007) provides a detailed review of methods by which root architecture of crops can be manipulated or improved to increase nutrient acquisition for crops grown in poor soil conditions. In a call for a "Second Green Revolution", Lynch (2007) highlights the impact the global food crisis has on developing nations where agriculture is a core form of income but yields are often diminished by poor soil fertility or drought.

A potential method for adapting crops to improve their tolerance of certain abiotic stresses is to manipulate their root system architecture (RSA). RSA describes the shape and structure of the root system (de Dorlodot et al., 2007). One of the main benefits of manipulating RSA is the potential to increase the plant's ability to uptake water and nutrients. Improvements in RSA can produce plants with higher yield potentials as crops can be developed to have ideal RSAs for the environment they are grown in (Malekpoor Mansoorkhani et al., 2014).

The plant hormone auxin plays an important role in the regulation of root system architecture. Auxin distribution within the root apex has been shown to play a crucial role in primary root growth (Rahman et al., 2007) and lateral root initiation (Casimiro et al., 2001, Swarup et al., 2005). As such, it is important to have an understanding of how environmental changes caused by climate change effect auxin dynamics within the root tip. Most existing studies of auxin dynamics in the root tip focus on the model species *Arabidopsis thaliana* as this is a fast growing plant with roots that are easy to image. The aim of this thesis is to investigate factors that affect auxin transport and delivery to the root tip of *Arabidopsis thaliana*. In particular, our objectives include:

1. Determining the role of local auxin biosynthesis on root-tip auxin patterning. We aim to develop a multicellular model of auxin dynamics in the root tip

that can capture variations in the ratio between shoot-derived and root-derived auxin.

2. Determining the effect of environmental conditions on the long-distance transport of hormones to the root tip. We aim to develop a fluid dynamics model of hormone transport in the phloem that includes the transport of sugar, hormone, and water. This model will capture the affects of various loading and unloading mechanisms including bulk flow unloading.

3. We aim to develop a model of a virtual seedling by coupling together models in the phloem and root tip from previous chapters. We seek to understand how long-distance and short-distance transport of auxin combine to affect root-tip auxin patterning within the hybrid model.

Below follows a review of the literature relevant to this thesis. This begins by covering the biological literature relevant to auxin, our hormone of interest (Section 1.2). We introduce key methods by which auxin is regulated such as metabolism and transport before discussing its role in responses to environmental cues. We then discuss key developments in mathematical modelling of auxin dynamics in the root tip (Section 1.3) including models that incorporate transport and metabolism. In Section 1.4 and Section 1.5 we introduce key literature that closely aligns with the direct research topics of this thesis – auxin biosynthesis and transport via the phloem.

1.2 The plant hormone auxin

A plant's root system determines its ability to absorb water and nutrients from the soil (Taiz and Zeiger, 2010). As such, a knowledge of how a plant's root structure develops is a crucial element in understanding how environmental changes affect a plants ability to take up the nutrients it requires to grow. The plant hormone auxin (IAA) plays a crucial role in many aspects of plant development and the spatial distribution of auxin in the plant root tip helps to regulate growth, initiate lateral roots, and produce tropic responses (turning movements directed by external stimuli) (Grieneisen et al., 2007, Swarup et al., 2005, Band et al., 2012b).

1.2.1 Auxin metabolism

The main auxin biosynthesis pathway in Arabidopsis was shown to be via the IPyA pathway (see Figure 1.1) (Mashiguchi et al., 2011, Zhao, 2018). In the IPyA pathway,

IPyA is produced mainly by the conversion of tryptophan (Trp) by the *TAA* gene family. The second step of this pathway is the conversion of IPyA to IAA by the *YUC* gene family (Mashiguchi et al., 2011). In this pathway the conversion of IPyA to IAA is thought to be the rate-limiting step (Mashiguchi et al., 2011). Zhao (2018) provides a comprehensive review of auxin biosynthesis in Arabidopsis. Reduced auxin biosynthesis in Arabidopsis mutants *wei8 tar2* has been linked to the loss of auxin gradients in the root tip (Stepanova et al., 2008) and experiments have shown that auxin overproduction in shoots cannot rescue auxin deficiencies in the root (Chen et al., 2014). A more detailed discussion of auxin biosynthesis can be found in Section 1.4.

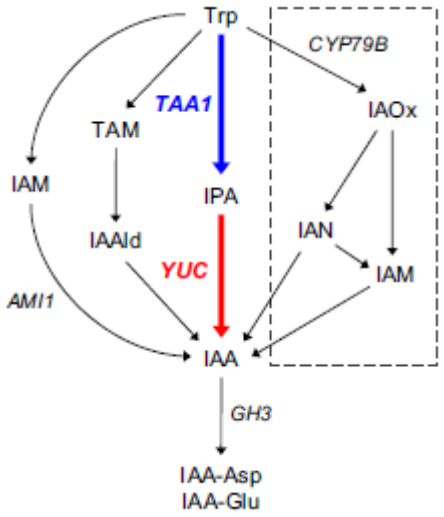


Figure 1.1: Auxin biosynthesis in *Arabidopsis* as proposed by (Mashiguchi et al., 2011).

Auxin degradation and inactivation occurs through multiple pathways in the root tip. Recent studies have highlighted the important role of the *AtDAO1/2* genes in the regulation of auxin oxidation (a major form of auxin catabolism) in the Arabidopsis root tip (Porco et al., 2016) and complementary studies have shown that the *GH3* gene family plays a crucial role in auxin conjugation in Arabidopsis (Mellor et al., 2016). The results of the studies performed by Porco et al. (2016) and Mellor et al. (2016) suggest that auxin catabolism (via the *DAO* pathway) and auxin conjugation (via the *GH3* gene family) regulate auxin homeostasis in a redundant manner. However, more recently the pathway has been refined by Hayashi et al. (2021). Hayashi et al. (2021) use knockout mutants of auxin inactivation genes to show that the *GH3* pathway plays a key role in auxin inactivation. Septuple knockout mutants of *GH3* genes, *gh3.1 2 3 4 5 6 17*, had significantly reduced root length and exhibited auxin overaccumulation phenotypes consistent with reduced auxin inactivation (Hayashi et al., 2021).

1.2.2 Auxin transport

Auxin transport plays an important role in plant development and polar auxin transport via auxin influx (AUX1/LAX proteins) and efflux (PIN/ABCB proteins) carriers is well characterised in Arabidopsis (see Spalding (2013)). In their work investigating the role of auxin signalling in root gravitropism, Bennett et al. (1996) found that the *AUX1* gene mediated the transport of amino acid-like molecules. Due to the similarities between IAA and the amino acid tryptophan, Bennett et al. (1996) suggested that the *AUX1* gene encodes an auxin influx carrier.

Blilou et al. (2005) show that the polar localisation of PIN efflux carriers enables the basipetal and lateral transport of auxin within the root tip. They suggest that the ability to redistribute auxin via the PIN efflux carriers in the root tip enables plants to regulate the size of the root meristem and highlight that the localisation of PIN proteins can be used as a map for auxin transport routes within the root tip (Blilou et al., 2005).

ABCB proteins have also been linked to the transport of auxin. In particular, the *abcb1 abcb19* double mutant has been shown to have a 70% reduction in polar auxin transport (more than the reduction in polar auxin transport seen in *pin1* mutants) (Blakeslee et al., 2007, Titapiwatanakun and Murphy, 2009). Both *abcb1 abcb19* and *pin1* mutants show reductions in root growth; however, *abcb1 abcb19* mutants do not exhibit defects in organogenesis seen in *pin1* mutants (Noh et al., 2001, Titapiwatanakun and Murphy, 2009). This suggests that transport via ABCB proteins is important in the long-distance transport of auxin, but is not involved in generating the directed fluxes (associated with PIN proteins) that are important for oragnogenesis (Titapiwatanakun and Murphy, 2009).

1.2.3 Auxin and the environment

Given auxin plays a major role in controlling plant phenotypes, it is important to understand how the biosynthesis, degradation, and transport of auxin are affected by environmental stresses, especially since environmental factors are rarely isolated; for example, plants responding to shade are also likely to be affected by stresses relating to light intensity (Mroue et al., 2018). These responses to environmental stresses give rise to altered auxin dynamics and hence altered plant phenotypes. A comprehensive overview of auxin responses to environmental conditions are summarised in Figure 1.2 (Mroue et al., 2018).

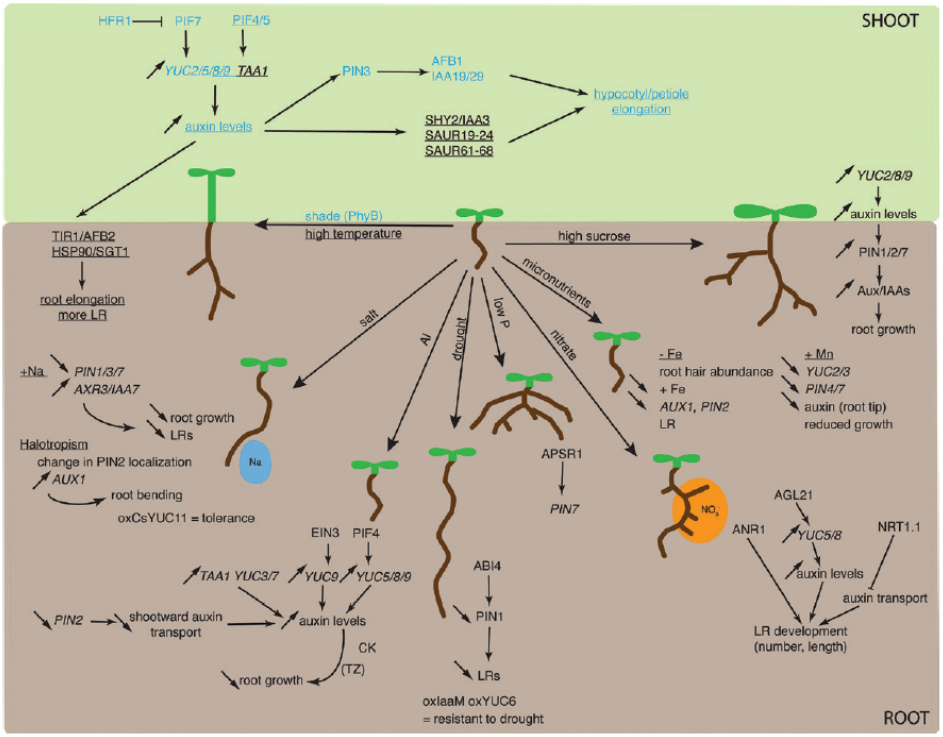


Figure 1.2: Overview of auxin responses to abiotic stress (Mroue et al., 2018).

Auxin biosynthesis has been shown to play an important role in a plant's response to abiotic stresses. In particular, the *YUC* auxin biosynthesis genes have been shown to be involved in increasing a plant's resistance to specific abiotic stresses (Mroue et al., 2018). Some studies have shown decreased auxin levels in osmotically stressed plants, with the *YUC* genes being down-regulated in rice (Du et al., 2013, Naser and Shani, 2016), however, other studies have shown that up-regulation of *YUC* genes in Arabidopsis plants experiencing dehydration can increase drought resistance (Lee et al., 2012, Naser and Shani, 2016). These studies surrounding auxin biosynthesis as a response mechanism to osmotic stresses are contradictory. The inconsistent role of auxin biosynthesis in response to osmotic stresses may be due to the effect auxin biosynthesis has on the growth of plants, which in turn may cause drought resistance or sensitivity (Naser and Shani, 2016). Auxin biosynthesis has also been shown to be involved in a plant's response to parasite/pathogen interactions. Local auxin biosynthesis, mediated by the *YUC* pathway, plays an important role in the development of haustorium (the projection that allows a parasitic plant to penetrate a host plant and absorb nutrients) (Zhao, 2018).

As well as auxin biosynthesis, auxin degradation and auxin transport also play important roles in a plant's response to the environment. The *GH3* auxin degradation gene family respond to abiotic stresses and, alongside the role of auxin biosynthesis in osmotic stress responses, this suggests that auxin homeostasis plays a crucial

role in a plant's response to osmotic stresses (Naser and Shani, 2016). Finally, PIN-mediated efflux plays an important role in hydropatterning (Bao et al., 2014)(the positioning of lateral roots to increase access to available water), and salt stresses can repress PIN expression (Liu et al., 2015, van den Berg et al., 2016, Naser and Shani, 2016). Salt stresses have also been shown to affect AUX1 expression (van den Berg et al., 2016). Overall, this indicates that auxin biosynthesis, degradation, and transport all form part of a plant's response mechanism to abiotic stresses.

1.2.4 Auxin sensors

High-resolution sensors of plant hormones are important for the analysis of hormone distributions and signalling events. Many studies have used the DR5 auxin reporter (Ulmasov et al., 1997) which provides a read out of the spatial distribution of the auxin response. More recently, Brunoud et al. (2012) developed the fluorescent auxin signalling sensor DII-VENUS which is an Aux/IAA based reporter. Auxin signalling is monitored through the degradation of the DII-VENUS signal, and hence, the spatial distribution of DII-VENUS is complementary to that of the existing auxin sensor *DR5::VENUS* (Brunoud et al., 2012). The DII-VENUS auxin reporter was shown to report auxin levels without interfering with the signalling pathway and was also shown to respond rapidly to changes in auxin level (Brunoud et al., 2012).

1.3 Models of auxin dynamics in the root tip

Mathematical models have been used to support investigations in many areas of the field of biology – including plant biology. Models have been used to capture key processes in plant development and growth. Here, we review the literature relating to mathematical models of the transport and metabolism of auxin.

1.3.1 Models of auxin transport in the *Arabidopsis* root tip

Swarup et al. (2005) show that the differential growth of epidermal cells during root gravitropism relies on an auxin gradient determined by the auxin influx carrier AUX1. As part of their investigation, they use a 3D idealised geometry model with prescribed auxin carrier expression and localisation patterns in the epidermis, cortex, and endodermis in Arabidopsis (Swarup et al., 2005). Model simulations of auxin transport within the epidermis of wild-type, *pin2*, and *aux1* roots indicated that *aux1*

plants were unable to transport the asymmetric auxin pulse caused by gravitropism through the elongation zone without the auxin gradient being diminished (whereas the wild-type and *pin2* plants were able to maintain the auxin gradient) (Swarup et al., 2005). The authors used these model simulations to guide experimental studies that confirmed that the differential growth of epidermal cells in the elongation zone during gravitropism relies on an auxin gradient that depends on the auxin influx carrier AUX1 (Swarup et al., 2005).

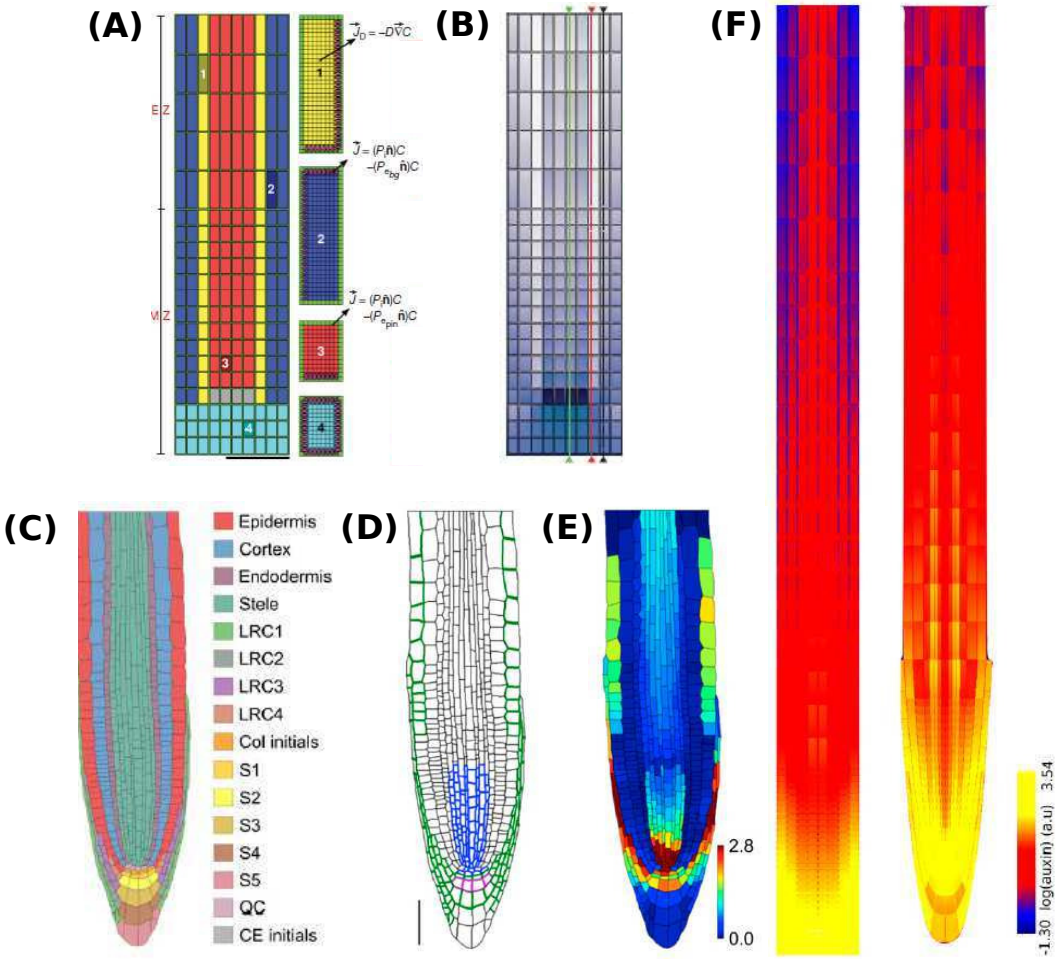


Figure 1.3: Examples of existing auxin transport models in Arabidopsis. **(A)** Grieneisen et al. (2007) model the root tip using a lattice-based structure with specified PIN localisation and uniform AUX1/LAX distribution; **(B)** Simulated auxin distribution from (Grieneisen et al., 2007); **(C)** Arabidopsis root tip structure and cell types (Band et al., 2014); **(D)** AUX/LAX distribution used by Band et al. (2014) in their auxin transport model; **(E)** Simulated auxin distribution from (Band et al., 2014); **(F)** van den Berg et al. (2016) use different forms of idealised root geometries in their auxin transport model. Simulated results for their baseline (specified PIN distribution, uniform AUX distribution) model are shown for two idealised geometries.

In their paper, *"Auxin transport is sufficient to generate a maximum and gradient guiding root growth"*, Grieneisen et al. (2007) investigate the role of auxin transport, via the auxin efflux carriers (PINs), in controlling root growth (Grieneisen et al.,

2007). They develop a spatial model for polar auxin transport using a lattice based structure to describe the geometry of the root tip. The lattice structure is a simplified geometry of the Arabidopsis root tip that captures the essential features of the root, including the cell walls (Grieneisen et al., 2007). The authors assign PIN localisation for specific cell types based on experimental results (Figure 1.3A), where vascular tissues have PINs localised to the base of the cell, epidermal tissues have PINs localised to the top of the cell, border cells have PINs localised to the base and sides of the cell, and cells in the root cap region have PINs localised to all sides of the cell (Grieneisen et al., 2007). Simulations with this model assume a uniform distribution of auxin influx carriers (AUX1/LAX), and excludes auxin decay and auxin synthesis, revealing that the PINs were necessary and sufficient to create the reverse fountain auxin fluxes and reflux loop that maintain the auxin maximum in the root (Figure 1.3B) (Grieneisen et al., 2007). Further work by Grieneisen and coworkers has extended this model to incorporate the regulation of auxin transporters via the plant hormones auxin and cytokinin (el Showk et al., 2015). The results of this model reveal the auxin distribution required for vascular patterning does not depend on their being an informative cytokinin gradient in the root tip (el Showk et al., 2015). Di Mambro et al. (2017) further show that cytokinin regulation of PIN activity and auxin degradation plays an important role in positioning the transition zone in the Arabidopsis root tip (see Section 1.3.2 for a detailed review).

More recent mathematical studies of the auxin distribution in the root tip have shown that auxin transport via auxin influx carriers is essential for the development of the auxin distribution in the root tip. Band et al. (2014) develop a realistic model for the distribution of auxin in the Arabidopsis root tip by utilising real cell geometries. They extract cell geometries from confocal microscopy images of root tips stained with propidium iodide via two software packages: SurfaceProject (developed by Band et al. (2014)) and CellSeT (developed by Pound et al. (2012)). Initially, they modelled the auxin dynamics in the root tip by assigning only PIN efflux carriers and modelling the movement of auxin between cells and apoplast compartments (Band et al., 2014). Utilising a model that describes auxin's relationship to the DII-VENUS reporter (Band et al., 2012b), Band et al. (2014) compare the results of their model to confocal microscopy images of DII-VENUS distrbution in the root tip (obtained using SurfaceProject and CellSeT). The results of their model, where only PIN efflux carriers are assigned, do not corroborate the experimental data. The authors conclude that PIN efflux carriers alone are insufficient to obtain the auxin distribution in the root tip (Band et al., 2014).

Band et al. (2014) extend their model to incorporate the distribution of the auxin influx carriers AUX1/LAX (Figure 1.3b). The AUX1/LAX influx carriers are as-

signed to cells based on localisation data available in the literature, as well as in elongating cortical cells (a novel location for AUX1 localisation discovered by the authors) (Band et al., 2014). The results of simulating the auxin dynamics in the root tip using the updated model resulted in a much better match between the predicted DII-VENUS distributions and the experimental DII-VENUS data (Figure 1.3E). By performing simulations of *aux1* mutants, Band et al. (2014) were able to show that the AUX1/LAX influx carriers are essential for determining the auxin distribution in the root tip and the PIN efflux carriers are required to control the direction of auxin transport within the root tip. More recently, this model has been extended to incorporate the affects of plasmodesmata on auxin dynamics in the root tip (Mellor et al., 2020). This extended model reveals that inclusion of auxin fluxes through plasmodesmata improves the models ability to replicate the auxin distribution seen in the root tip experimentally. The inclusion of plasmodesmata also enables the model to capture the auxin reflux loop (first proposed by (Grieneisen et al., 2007) but that the model in (Band et al., 2014) was unable to capture) (Mellor et al., 2020).

Continuing to expand upon the auxin transport models of Band et al. (2014) and Mellor et al. (2020), Mellor et al. (2022) focus on including auxin transport via ABCBs, a feature which had not been looked at in detail in previous mathematical models. Results in the experimental literature do not indicate a clear relationship between the transport of auxin via ABCBs and its transport via the PIN efflux carriers (often the experimental results are conflicting (Mellor et al., 2022)). Mellor et al. (2022) test their model with five different ABCB-PIN relationship scenarios (proposed in Spalding (2013) and Geisler et al. (2017)). Their results show that auxin transport via ABCBs occurs independently of PINs, however, auxin transport via PINs occurs predominantly via a co-dependent efflux when PINs are co-localised with ABCB transporters (Mellor et al., 2022).

Another computational modelling framework for simulating auxin dynamics has been developed by the Ten Tusscher group. In their work investigating the role of auxin in halotropic responses, van den Berg et al. (2016) report that during halotropism (changes in the direction of growth due to salt exposure) there is a decrease in PIN2 in epidermal cells on the side of the root exposed to the halotropic signal (van den Berg et al., 2016). They develop a computational model for auxin transport in the Arabidopsis root tip that initially utilises a rectangular idealised root geometry similar to the one proposed by Grieneisen et al. (2007). They find that the proposed reduction in PIN2 fails to capture the expected redistribution of auxin in the root tip. Their extended model, which is based on an idealised root geometry with a wedge shaped tip (Figure 1.3F), however, does partially capture the auxin asymmetry in the root tip expected from the decrease in PIN2 due to salt exposure (van den Berg et al.,

2016). This work shows the importance of using realistic root geometries when mathematically modelling auxin dynamics in the root tip. They refine their model by investigating the effect of auxin feedback on auxin transporters, in particular the AUX1 auxin influx carriers. This work shows that the upregulation of AUX1/LAX transporters by auxin significantly enhances the auxin asymmetry in the root tip (van den Berg et al., 2016). The authors were able to verify their model predictions using experimental data. Overall, the authors conclude that PIN2 is important for generating the auxin asymmetry seen in the Arabidopsis root tip after exposure to a halotropic stimulus, however, the upregulation of the AUX1/LAX auxin influx carriers is required for a sufficiently large asymmetry to be generated (van den Berg et al., 2016). More recently, the modelling framework of the Ten Tusscher group has been extended to include growth, leading to novel insights into lateral root initiation (van den Berg et al., 2021).

Alternative approaches to modelling auxin distribution in the Arabidopsis root tip have been made. In their paper, *"Multiscale modelling of auxin transport in the plant-root elongation zone"*, Band and King (2012) apply asymptotic methods to cell-based models to derive a continuum description of auxin distribution in the root tip (Band and King, 2012). They use a cell-based model with a simplified cell geometry consisting of only the three outer layers of the root elongation zone as the foundation for their asymptotic analysis and are able to simplify the system so it can be described by a system of partial differential equations (Band and King, 2012). Their analysis reveals that the overall behaviour of the continuum system is dependent on cell length with the tissue-scale dynamics being different for short cells located near the root tip compared to longer cells located further through the elongation zone (Band and King, 2012). The authors observe that the analytical approach they take could be extended to more complex models such as that describe by Grieneisen et al. (2007); however, there is no simple way to apply this technique to simplify cell-based models that incorporate the real cell geometries and connectivities at the root apex, such as the one described by Band et al. (2014).

Computational cell-based models have also been used to investigate cross-talk between auxin and other hormones. Moore et al. (2015) developed a mathematical model for hormonal cross-talk in the Arabidopsis root tip. Their model incorporates interactions between the plant hormones auxin, ethylene, and cytokinin, as well as the POLARIS protein and the AUX1 and PIN auxin transporters. The model is constructed using the idealised root geometries of Grieneisen et al. (2007) with cell lengths being increased towards the elongation zone to more accurately reflect Arabidopsis root geometry (Moore et al., 2015). The model indicates that AUX1 and PIN permeabilities must be limited to certain ranges for correct auxin patterning

to be seen in the root tip. The authors concluded that the coordinated activity of AUX1 and PIN proteins is important for the development of root auxin patterning (Moore et al., 2015). The model also has the ability to generate predicted hormone concentrations for ethylene and cytokinin. The model predictions for average hormone concentrations are in agreement with experimental data, however, the model has limitations in its cytokinin modelling as patterning of cytokinin in the root tip does not reflect experimental data (Moore et al., 2015).

1.3.2 Models of auxin metabolism in the *Arabidopsis* root tip

As described above, recent studies have provided us with an in-depth knowledge of auxin transport in the root tip. However, less is known about the effects of auxin biosynthesis, catabolism, and conjugation on the auxin distribution in the root tip.

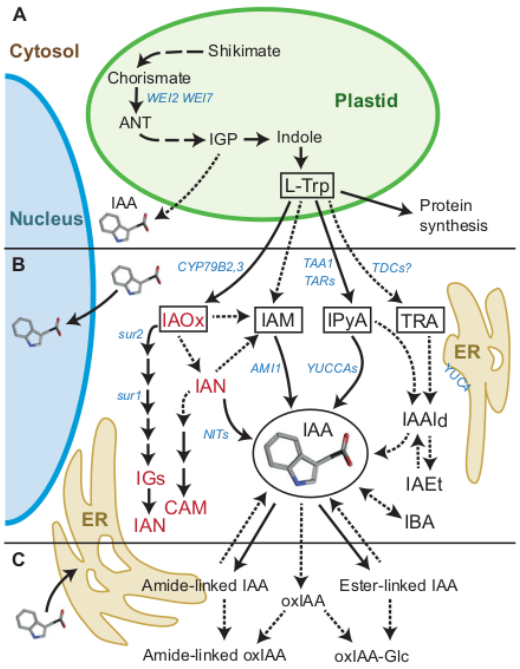


Figure 1.4: IAA metabolism in higher plants (Ljung, 2013)

Porco et al. (2016) use the *pDAO1:GUS* promoter to visualise the expression pattern of *DAO1* in the Arabidopsis root tip. They show that *DAO1* is expressed widely across the root tip, as well as in the vascular tissues (Porco et al., 2016). In their paper, Mellor et al. (2016) describe an ODE model for auxin metabolism (biosynthesis, catabolism, and conjugation). They incorporate auxin catabolism via the *DAO1/2* pathway, prescribing uniform rates to degradation via *DAO1* and *DAO2* across all cells (Mellor et al., 2016). The model also describes the effects of irreversible conjugation via the *GH3* gene family. This is modelled via constant rates for

conjugation to IAA-Asp and IAA-Glu (Mellor et al., 2016). Auxin biosynthesis is modelled as a constant rate of production. Mellor et al. (2016) extend their model to include the dynamic, auxin-inducible regulation of *AtDAO1* and *GH3*.

Mellor et al. (2016) coupled their model for auxin metabolism with the existing multicellular model, described by Band et al. (2014), to develop a model for auxin homeostasis in the Arabidopsis root tip (Mellor et al., 2016). Simulations from the auxin homeostasis model predicted an increase in IAA concentration in *dao1* mutants which is consistent with experimental findings (Mellor et al., 2016). The resulting simulated auxin distribution in the root tip suggests that the auxin increase in the *dao1* mutant is not spatially homogenous, with there being larger predicted increases in the outer layers of the root tip. This finding is consistent with experimental results that show that *dao1* mutants have elongated root phenotypes (Mellor et al., 2016).

Recent studies have highlighted further the role of the *GH3* gene family in auxin degradation. In particular, Di Mambro et al. (2017) show that auxin degradation triggered by the *GH3.17* gene plays a crucial role in the positioning of the auxin minimum that determines the location of the transition zone. They verify their results with a mathematical model that incorporates the effects of polar auxin transport via the PINs, auxin synthesis, and auxin degradation (Di Mambro et al., 2017). The expression pattern of the *GH3.17* gene was established using a GFP translational fusion of the *GH3.17* gene. This showed that *GH3.17* is localised the outermost file of the collumella and lateral root cap (Di Mambro et al., 2017). Di Mambro et al. (2017) used the expression location of *GH3.17* as location of auxin degradation in their model.

1.4 Local auxin biosynthesis in the Arabidopsis root tip

Determining the mechanisms that regulate auxin dynamics is a vital step in understanding auxin's role in plant development. Several mathematical models have captured the effects of influx and efflux carriers on root tip auxin dynamics, based on a primary source of auxin originating in the shoot and delivered to the root via the phloem (Grieneisen et al., 2007, Band et al., 2014, van den Berg et al., 2016). Less clear from the models, however, is the role that local auxin synthesis may play in patterning the root tip.

Understanding how auxin in the root tip gets there is an important step in determining

what governs auxin patterning in the root tip. Ljung et al. (2005) investigate the sites of auxin biosynthesis in Arabidopsis roots. Their results suggest that the whole root is capable of auxin biosynthesis (Ljung et al., 2005) with high rates of auxin biosynthesis in the most apical 2mm of the root tip (for both intact and excised seedlings). They conclude that there is an auxin source in the meristematic region of the root tip (Ljung et al., 2005). Ljung et al. (2005) also investigate the role of auxin synthesised in aerial plant tissues. The results show that excised plant roots have a lower auxin concentration level but that their auxin biosynthesis rate is not significantly reduced. The authors suggest the decreased concentration level is caused by the lack of transport of auxin from aerial tissues (Ljung et al., 2005). However, the authors show, through the inhibition of polar auxin transport in the root tip for intact and excised roots, that the synthesis of new auxin is only reduced in excised roots in the early stages of development (4DAG) (Ljung et al., 2005), this could indicate that the role of auxin synthesised in aerial tissues is only important in the early stages of development.

The auxin biosynthesis genes, *WEI8/TAR*, are expressed at and near the quiescent centre (Figure 2.7) and catalyse the conversion of Tryptophan to the IAA precursor IPyA (Stepanova et al., 2008). The *WEI8* gene family is also commonly referred to as the *TAA1* gene family. In their paper, Stepanova et al. (2008) use different mutants of the *WEI8/TAR* gene families to develop an understanding of their role in auxin biosynthesis. The results of knock-out mutants show that the *wei8* single mutant and the *wei8-1 tar2-1* double mutant both have an inability to reorientate themselves after a gravitropic stimulus, with the defect being more extreme in the double mutant (Stepanova et al., 2008). As the auxin gradient in the Arabidopsis root tip has been shown to regulate gravitropic responses (Band et al., 2012b), a lack of response to gravitropic stimuli in the *WEI8/TAR* mutants could be an indication that auxin biosynthesis plays a key role in the formation or maintenance of the root tip auxin gradient.

Although auxin biosynthesis is essential for plant root growth and development, it is currently unclear whether growth is primarily controlled by auxin biosynthesis in the shoot (a systemic signal) or whether local auxin biosynthesis in the root is a key regulator (for a detailed review see (Zhao, 2018)). In previous studies, the *wei8 tar2* auxin biosynthesis double mutant was shown to have reduced auxin synthesis via the IPyA pathway which led to the loss of auxin gradients in the root tip of Arabidopsis (Stepanova et al., 2008). Recent experimental studies of the *YUCCA* and *WEI8/TAR* genes show that local auxin synthesis may play a crucial role in root tip auxin patterning (Chen et al., 2014, Brumos et al., 2018).

Chen et al. (2014) identify five *YUC* genes that are expressed in the root tip of Arabidopsis seedlings (*YUC3, YUC5, YUC7, YUC8,* and *YUC9*). *YUC* genes are associated with the rate-limiting step of the dominant auxin biosynthesis pathway in Arabidopsis (Mashiguchi et al., 2011). The Arabidopsis quintuple knockout mutant *yucQ* shows auxin deficiency phenotypes with short primary roots and abnormal gravitropic responses (Chen et al., 2014). Application of exogenous auxin in the growth medium or inducing expression of *YUC* genes in the root of *yucQ* mutants rescued root defects. However, overexpression of *YUC* genes in the shoot did not rescue *yucQ* root defects and instead produced auxin overexpression phenotypes in the shoot (Chen et al., 2014). As such, Chen et al. (2014) suggest that local auxin synthesis in the root plays an important role in normal root development.

Brumos et al. (2018) performed reciprocal grafting experiments of WT and *wei8 tar2* roots and shoots which had been introgressed with the DR5:GFP auxin reporter. Experiments where a WT shoot was grafted onto a *wei8 tar2* root showed a loss of DR5:GFP signal in the root tip and did not prevent the root meristem from degenerating (Brumos et al., 2018). On the other hand, experiments where a *wei8 tar2* shoot was grafted onto a WT root showed no loss in DR5:GFP signalling in the root tip and the root meristem was maintained (Brumos et al., 2018). This suggests that auxin biosynthesis in the root tip plays a key role in maintaining a local auxin maxima in the root tip. The authors further investigate the role of shoot and root derived auxin in the maintenance of the root meristem by performing heat shock experiments and by exposing mutant shoots to exogenous auxin (Brumos et al., 2018). The results of these experiments corroborate that auxin biosynthesis in the root is required to maintain a healthy root meristem and that shoot-derived auxin is unable to maintain the root stem cell niche (Brumos et al., 2018). They propose that the assumption that the primary source of auxin in the root tip comes from the shoot via the phloem may not be crucial to the development and maintenance of a local auxin maxima in the root tip.

Brumos et al. (2018) discuss existing mathematical models of auxin transport, including (Grieneisen et al., 2007) and (Band et al., 2014) (discussed in Section 1.3.1). They suggest the results from Grieneisen et al. (2007), that auxin transport alone can generate root tip auxin gradients, are consistent with experiments that suggest local auxin biosynthesis is not required for root-tip auxin patterning (such as experiments from Stepanova et al. (2011) that show IAA supplied in the growth medium is enough to suppress root defects in auxin biosynthesis mutants). Band et al. (2014) account for local auxin biosynthesis in their model by increasing auxin biosynthesis rates in the quiescent center and cortex/endodermal initials in correspondence with expression patterns of the *TAA1* gene family (Stepanova et al., 2008). Brumos et al.

(2018) highlight the fact that changes in the rate of local auxin biosynthesis in these cells do not qualitatively change the root-tip auxin gradient produce by the model (see Supplementary Figure 19 of (Band et al., 2014)). They suggest the failure of the (Band et al., 2014) model to capture changes in the root-tip auxin gradient is due to the inclusion of a low rate of auxin biosynthesis in all cells, something the authors feel contradicts the expression patterns of the auxin biosynthesis genes *TAA1/TAR* (Brumos et al., 2018).

1.5 The phloem transport system

Existing auxin transport models in the root tip assume there is a fixed auxin concentration at the boundary between the modelled root-tip tissue and the region of long-distance transport (Grieneisen et al., 2007, Band et al., 2012b, van den Berg et al., 2016, Mellor et al., 2020). The processes that regulate the auxin dynamics at this boundary have not been studied directly. Long-distance transport in plants occurs via the phloem, and as such, it is important to understand the mechanisms that regulate phloem transport in order to understand how best to incorporate hormone delivery from the shoot to the root tip into mathematical models of auxin transport.

The phloem forms part of a plant's vascular system (alongside the xylem) and is responsible for long distance transport of sugars, proteins, and signalling molecules. This long distance transport occurs through phloem sieve elements (Taiz and Zeiger, 2010). Phloem cells have no nucleus yet remain functional – in a living-dead sort of way. Sieve elements are often found in complexes with companion cells. These companion cells help to sustain sieve elements throughout their lifetime (Taiz and Zeiger, 2010).

Sieve element companion cell complexes, SE-CC, play an important role in loading, unloading, and transportation within the phloem (Oparka and Turgeon, 1999). There are two methods that allow sugar to be loaded into the phloem. Active (or apoplastic) loading refers to loading into SE-CC across cell walls mediated by membrane transporters. Passive (or symplastic) loading refers to loading into SE-CC via plasmodesmata (Taiz and Zeiger, 2010, Oparka and Turgeon, 1999, Thompson and Holbrook, 2003). Passive loading commonly occurs into the CC of a SE-CC as most plasmodesmata connect into the CC. As such, the CC plays an important role in passive loading and SE connectivity to a CC can commonly be used as a tentative measure of whether plant loads actively or passively (Oparka and Turgeon, 1999). Phloem unloading can also occur actively or passively. Passive unloading is thought

to be more common as active unloading would require membrane transport that is highly selective for the wide range of molecules (including proteins, sugars, RNAs, and signalling molecules) that may be transported within the phloem (Oparka and Turgeon, 1999).

Knoblauch et al. (2015) identify a range of fluorescent probes that can aid in visualisation of translocation within the phloem. They showed that esculin and fraxin were both loaded into the phloem of Arabidopsis by the sucrose transporter AtSUC2 (Knoblauch et al., 2015). The loading of esculin by the AtSUC2 transporter makes it a useful proxy for sucrose in phloem transport studies (Knox and Oparka, 2018). In particular, esculin can be used to study phloem transport rates.

1.5.1 Phloem transport models

Understanding how the phloem transports vital sugars throughout a plant has been a topic of interest in biology (and mathematics!) since Ernst Münch released his paper on the transport of matter in plants in 1926 (Münch, 1926). Minchin et al. (1993) developed a simple model for sugar transport in the phloem based on convective bulk flow driven by an osmotically generated pressure gradient in the phloem (originally hypothesised by Münch (1926)). The model incorporated a single source connected to two sinks, as well as phloem unloading via Michaelis-Menten kinetics. This model was intended to be the simplest mechanistic model that would provide insight into observations made in experiments about phloem transport (Minchin et al., 1993). As such, this model has made assumptions that are not biologically relevant such as the phloem tube between the source and sink region being impermeable to both water and sugar. Despite model simplifications, the model was able to capture the behaviour of sinks operating close to saturation – the removal of a sink did not result in the remaining sinks being able to use the increased amount of photosynthate available to them (Minchin et al., 1993).

Bidel et al. (2000) expanded upon the model of Minchin et al. (1993) to produce a model that has one source connected to a series of compartments representing phloem segments and sinks. Their model uses the convective bulk flow hypothesised by Münch (1926) (and described in Minchin et al. (1993)) and also incorporated growth and branching. Each root meristem in the model produced a new segment each day, with the length of the segment produced depending on consumption of photoassimilates (Bidel et al., 2000). The model was able to replicate the growth of taproots (the main root from which lateral roots can develop (Taiz and Zeiger, 2010)) and generate hierarchical photoassimilate uptake where decreasing source

activity saw an increased proportion of photoassimilates available being consumed by the taproot (Bidel et al., 2000). Experimentally measured parameters for this model came from *Prunus persica* L. Batsch (peach) (Bidel et al., 2000).

The phloem model developed by Thompson and Holbrook (2003) provides a more detailed description of phloem transport. They incorporated non-linear viscosity, wall elasticity, and sieve pore resistance to provide one of the most complete descriptions of phloem transport (Thompson and Holbrook, 2003). They use their model to investigate limitations of osmotically driven flow over long distances. They show that transport times increase proportionally to the square of the sieve tube length indicating that plants with longer distances over which to transport sugars and hormones would need shorter sieve elements linked in series to maintain transport timescales physiologically relevant to the plant (Thompson and Holbrook, 2003).

As plants vary dramatically in size across the plant kingdom, this leads to questions over the suitability of Münch flow as the method of transport across this wide range of sizes. Jensen et al. (2011) used a mathematical model of convective bulk flow to investigate how well Münch mechanisms describe the translocation of sugars in different plant species. In particular, they investigate the optimality of translocation speed given the phloem's role in the transport of signalling molecules and the plant's need to respond to these rapidly. The model results in the identification of a scaling between the phloem radius and characteristic lengths of a plant (Jensen et al., 2011). The authors investigated whether real plants follow their model scaling by taking experimental measurements of a wide range of plants, as well as making comparisons to experimental data available in the literature. Overall, their results provide quantitative evidence to support the use of Münch flow across a wide range of plant sizes (Jensen et al., 2011).

Similarly to Thompson and Holbrook (2003), Jensen et al. (2012) split the phloem tube into three distinct zones (loading, translocation, and unloading) and use the equations for Münch flow to describe the velocity of the phloem sap and sugar concentration within the phloem. They make the assumption that loading and unloading rates are linear functions of concentration, proportional to the difference between the internal concentration and a target external concentration, in order to be able to solve the equations for Münch flow analytically in the limit of very large or very small Münch number (Mü) (Jensen et al., 2012). They find a very good agreement between analytical and numerical solutions for a wide range of parameter values (finding that the analytical solution for Mü$\ll 1$ is very similar to numerical results for Mü$= 1$) and suggest that future modelling studies may benefit from using the simplest mathematical description of phloem loading or unloading (Jensen et al.,

2012).

In the majority of phloem models, due to the large Péclet number of phloem sap, diffusion of sugar is neglected. Payvandi et al. (2014) investigate the appropriateness of neglecting diffusion in high Münch number scenarios through matched asymptotics to determine the importance of diffusion in phloem transport models. Their model incorporates active loading into a loading zone, which is coupled to the translocation zone, which is then coupled to an unloading zone (where the authors consider both passive and active unloading). The results of their asymptotic analysis indicates the validity of neglecting diffusion depends on the loading/unloading of the phloem (Payvandi et al., 2014). They observe that the system behaved differently for active and passive unloading, and that the validity for neglecting diffusion for passive unloading was determined by the magnitude of loading at the shoot. The authors conclude that until the methods of phloem loading/unloading are more accurately characterised, it is important to consider the role of diffusion in phloem transport models (even in the case of high Péclet number) as diffusion terms can dominate in the boundary layer close to the end of the phloem tube (Payvandi et al., 2014).

A detailed review of the transport of sugar through the xylem and phloem is given by Jensen et al. (2016). They derive equations for the radially averaged concentration and flow in the phloem from the Navier-Stokes equations whilst providing full details of the fluid mechanics behind osmotically driven flow (Jensen et al., 2016). They describe solutions for the time-dependent and stationary equations, obtaining detailed equations describing the velocity and concentration profiles. However, it is important to note (and was highlighted by the authors), that these detailed descriptions of velocity and concentration cannot currently be easily compared to experimental results (Jensen et al., 2016).

More recently, Ross-Elliott et al. (2017) have developed a novel mathematical model for phloem unloading that considers the water and sugar fluxes through individual plasmodesmata in the Arabidopsis root tip. The model sought to capture the affects of diffusion and bulk flow as methods of phloem unloading and the authors conclude that, due to the unusual funnel shape of the plasmodesmata in this region, bulk flow is likely to be the dominant form of unloading of sugars in Arabidopsis (Ross-Elliott et al., 2017). As part of their investigation, they sought to precisely define the location and dimensions of the phloem-unloading zone. Through the use of the fluorescent phloem-probe esculin, they were able to accurately determine the specific zones that phloem cells were organised in (Ross-Elliott et al., 2017) (Figure 1.5). Of the five zones identified, there is one zone that is rootward of the phloem-unloading zone; the protophloem development zone, which plays no part in phloem unloading

(Ross-Elliott et al., 2017). As such, for mathematical models of auxin transport to accurately capture the effects of phloem unloading, they must represent a deposition of shoot auxin into the root tip, within the rootward half of the elongation zone, but not directly at the root apex.

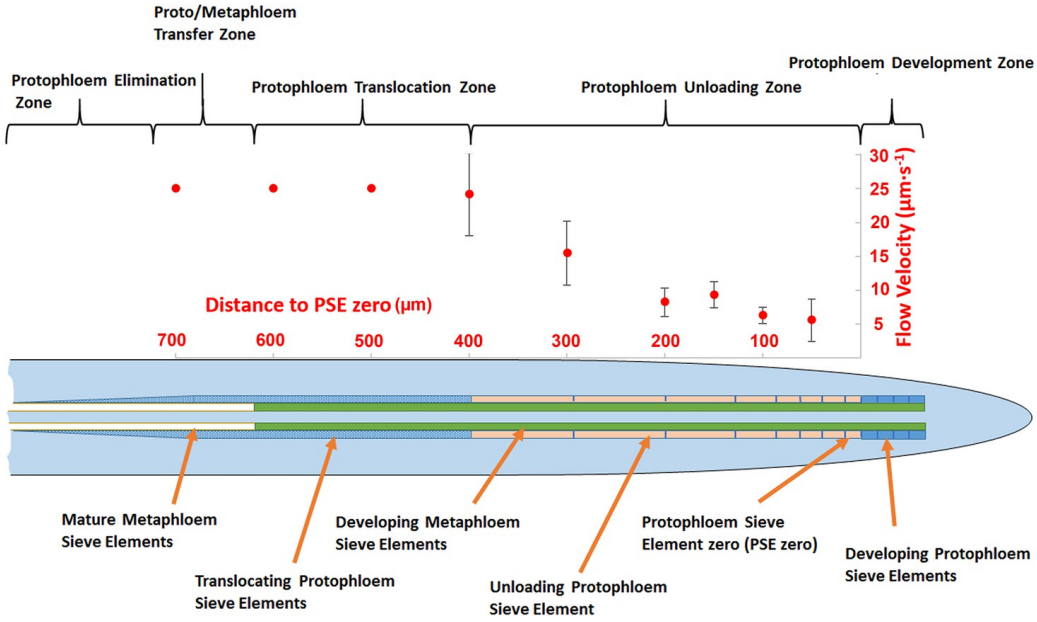


Figure 1.5: *"Schematic diagram illustrating the organization of phloem cells in specific zones in the root tip of Arabidopsis"* (Ross-Elliott et al., 2017). In Arabidopsis, phloem unloading occurs exclusively in protophloem sieve elements (protophloem cells are short-lived and functional in the root elongation zone) (Ross-Elliott et al., 2017).

Mathematical models of phloem transport velocity have primarily been focused on large plant species such as trees (Thompson and Holbrook, 2003, Payvandi et al., 2014, Jensen et al., 2016). van den Herik et al. (2021) develop a mechanistic model for phloem transport fully parameterised for potato plants. Their phloem model follows the work of (Thompson and Holbrook, 2003) closely, extending it to include sucrose export from the phloem via SWEET transporters and sucrose retrieval from the apoplast via the SUT transporters (van den Herik et al., 2021). The model also moves away from considering the xylem as an external reservoir of water and explicitly describes water flow in the xylem described by cohesion-tension theory (van den Herik et al., 2021). This model represents a key step forward in the development of phloem transport models of agriculturally relevant crop species such as potato.

The mathematical models discussed above all neglect to include the effects of Taylor dispersion. Taylor (1953) showed that, when radially averaging, the interactions between concentration and velocity within a impermeable pipe lead to an adjustment term that increases the effect of diffusion. It is likely that existing models do not

seek to include Taylor dispersion as they assume the effects of diffusion negligible due to the high value of the Péclet number. However, Nakad et al. (2021) sought to include the effects of Taylor dispersion in phloem transport. Phloem flow is osmotically driven and as well as recovering the adjusted diffusion coefficient seen in impermeable tubes, Nakad et al. (2021) also recover an adjustment term for radially averaged advection. This highlights that the effects of Taylor dispersion are not just limited to diffusion for osmotically driven flows and is hence an important inclusion for phloem transport models.

1.5.2 Hormones in the phloem

Analysis of phloem (and xylem) sap has been used to demonstrate the presence of plant hormones, including auxin, in the vascular transport system. Alongside the polar, cell-to-cell transport system for auxin, it has been shown that auxin is transported through the vascular system, in particular the phloem (Baker, 2000a). Baker (2000a) suggests the distinct lack of auxin in xylem sap indicates that auxin transported by the phloem is synthesised by mature leaves and exported into the phloem.

Swarup et al. (2001) investigated the role of the AUX1 influx carrier in long-distance transport of auxin in the model plant Arabidopsis. Their work suggests that AUX1 contributes to the delivery of shoot-derived auxin to the root tip through the asymmetric distribution of AUX1 in protophloem cells (Kleine-Vehn et al., 2006) which promotes the acropetal movement of auxin to the root apex (Swarup et al., 2001). A further study of the role of AUX1 in the long-distance transport of auxin was conducted by Marchant et al. (2002). Their study revealed that AUX1 promotes the export of auxin from leaves of the model plant Arabidopsis suggesting that AUX1 plays an important role in the loading of auxin into the phloem. Overall, these studies highlight that the AUX1 influx carrier plays an important role in the long-distance transport of auxin by facilitating phloem loading and increased acropetal transport of auxin to the root tip in protophloem cells (Marchant et al., 2002, Swarup et al., 2001).

Paterlini (2020) discusses the importance of auxin transport via advection in the phloem and its potential interaction with the active transport pathway for auxin. In their review, they observe that whilst inhibitors of active auxin transport did not affect the translocation of auxin in the phloem, it did impact the uptake of auxin in the leaves. They highlight that the potential feedback from blocked symplastic transport of auxin in the phloem on active auxin transport has not been investigated

in detail (Paterlini, 2020), though PIN7 has been shown to have a small reduction in its expression domain when symplastic transport is blocked (Bishopp et al., 2011).

As well as auxin, other plant hormones are transported in the plant vascular system. Recently, Regnault et al. (2015) showed that the gibberellin (GA) precursor GA_{12} moves through the vasculature system of Arabidopsis. They showed, through reciprocal grafting experiments, that GA_{12} is transported by both the xylem and the phloem, which suggests that long-range transport of GA_{12} may play an important role in the control of a plant's response to developmental or environmental cues (Regnault et al., 2015).

1.5.3 Environmental impacts on phloem transport

Abiotic stresses triggered by environmental changes (such as drought and high temperature) have the potential to impact signalling pathways in the shoot and root of plants. As such, it is important to understand how changes in root or shoot environments impact the long-distance transport via the phloem.

The sucrose transporter AtSUC2 (for Arabidopsis) plays an important role in the loading of sucrose into the phloem (Gong et al., 2015). High sucrose concentration in the loading zone of the phloem establishes an osmotic gradient that attracts water, in turn increasing the hydrostatic pressure gradient that drives phloem transport (Knox et al., 2018). As such, understanding how environmental conditions influence AtSUC2 behaviour is a key step in understanding how environmental conditions can influence phloem transport in general.

Gong et al. (2015) establish that AtSUC2 (along with AtSUC4) plays an important role in the abiotic stress tolerance of Arabidopsis. They show that exposure to abiotic stresses (such as salt, drought, osmotic, and low temperature stresses) leads to an up-regulation in AtSUC2 expression in the shoot and roots of Arabidopsis. Alongside this, they also show that *atsuc2* mutants have perturbed sugar balances between shoot and root (higher sucrose concentrations in the shoot and lower sucrose concentration in the root compared to WT) with these perturbations being more pronounced under stressed conditions (Gong et al., 2015). The perturbation to sugar balance in *atsuc2* mutants and the up-regulation of AtSUC2 in WT plants in response to abiotic stresses suggests that AtSUC2 is important for the timely delivery of sucrose to meet demand in the root tip. The importance of the up-regulation of AtSUC2 expression in roots remains unclear as AtSUC2 has not been linked to a role in phloem unloading (Gong et al., 2015). Gong et al. (2015) suggest AtSUC2 expression in the root may be

important for the retrieval of escaped sucrose back into the phloem under stressed conditions.

Xu et al. (2018) investigated the impact environmental changes have on phloem loading and sucrose transporters in a variety of species (including Arabidopsis and crop species such as maize and rice). They show that changes in CO_2 concentration and light levels has minimal impact on sucrose transporter expression (Xu et al., 2018) (this result for varying light levels contrasts with results from Knox et al. (2018) – see paragraph below). However, Xu et al. (2018) show that sucrose transporter expression did change significantly under drought, salt, and heat stresses. Drought and salt stresses resulted in an up-regulation of the Arabidopsis sucrose transporter AtSUC2 (consistent with results from Gong et al. (2015)) and heat stresses resulted in a down regulation of AtSUC2. Knox et al. (2018) see a reduction in relative expression of AtSUC2 at high temperatures, but also see an increased relative expression level for standard experimental temperatures compared to low temperatures. This suggests the relationship between temperature and AtSUC2 expression levels is non-linear.

Using the fluorescent coumarin glucoside, esculin, as a proxy for sucrose, Knox et al. (2018) investigated how phloem transport velocity responds to environmental changes. They found that environmental cues such as changes in light intensity and temperature, and the application of exogenous sucrose to the root tip resulted in modifications to phloem transport velocity (Knox et al., 2018). They also found the same conditions resulted in modifications to AtSUC2 relative expression levels and that differing environmental conditions would lead to sucrose accumulation in shoots (consistent with the findings of Gong et al. (2015)). Combining this evidence, the authors conclude that the variation of phloem transport velocity in response to environmental conditions that impact photosynthesis rates (such as light intensity and temperature) indicates that phloem transport velocity may be regulated by the amount of sucrose available for transport (Knox et al., 2018). Further, with phloem transport velocity and AtSUC2 relative expression both varying under environmental conditions (and often in consistent patterns), Knox et al. (2018) suggest that phloem transport velocity may also be linked to the regulation of the AtSUC2 transporter.

Chapter 2

Modelling local auxin biosynthesis

2.1 Introduction

Auxin plays an important role in many aspects of plant development. As such, auxin dynamics and patterning in the root tip have been popular areas of study for many years. Many studies focusing on auxin patterning in the root tip use mathematical modelling to enhance their understanding of auxin patterning (Grieneisen et al., 2007, Band and King, 2012, Band et al., 2014, van den Berg et al., 2016, Mellor et al., 2020, 2022). These models predominantly focus on the transport of auxin within the root tip. Key modelling results include: the important role of PINs in determining auxin fluxes within the root tip (Grieneisen et al., 2007); that transport via AUX1 influx carriers is essential for the development of auxin patterning in the root tip (Band et al., 2014); that the use of realistic cell geometries is important to model results (Band et al., 2012b, van den Berg et al., 2016); and that auxin flux via plasmodesmata is needed to capture the auxin reflux loop within the root tip (Mellor et al., 2020).

Whilst most existing mathematical models focus on the importance of auxin transport in root-tip patterning, few models have looked at the role of auxin metabolism (Mellor et al., 2016, Di Mambro et al., 2017). These models capture many aspects of auxin metabolism, but, the primary focus of these studies has been auxin degradation. As far as we are aware, auxin synthesis has not been the focus of an auxin mathematical modelling study in the root tip.

Experimental evidence such as the existence of an auxin source in the meristematic region of the root tip (Ljung et al., 2005), the localisation of auxin biosynthesis genes to the quiescent centre (Stepanova et al., 2008), and results from grafting experiments

(Brumos et al., 2018), suggest that the role of auxin biosynthesis in the root tip may be more important than previously thought.

In this chapter, we further develop the multicellular auxin-transport model of the Arabidopsis root tip (described in Section 1.3.1 (Band et al., 2014)) to investigate how the location and rate of auxin biosynthesis affects the root-tip auxin distribution. We test the model's ability to capture the results of reciprocal-grafting experiments of WT and *wei8 tar2* roots (Brumos et al., 2018). We find that only decreasing the contribution of auxin from the shoot relative to the rate of local auxin synthesis in the root tip produces simulated auxin reporter distributions consistent with the experimental data. We conclude that local auxin biosynthesis across the root tip is a critical component in auxin patterning within the root tip.

2.2 Auxin transport model

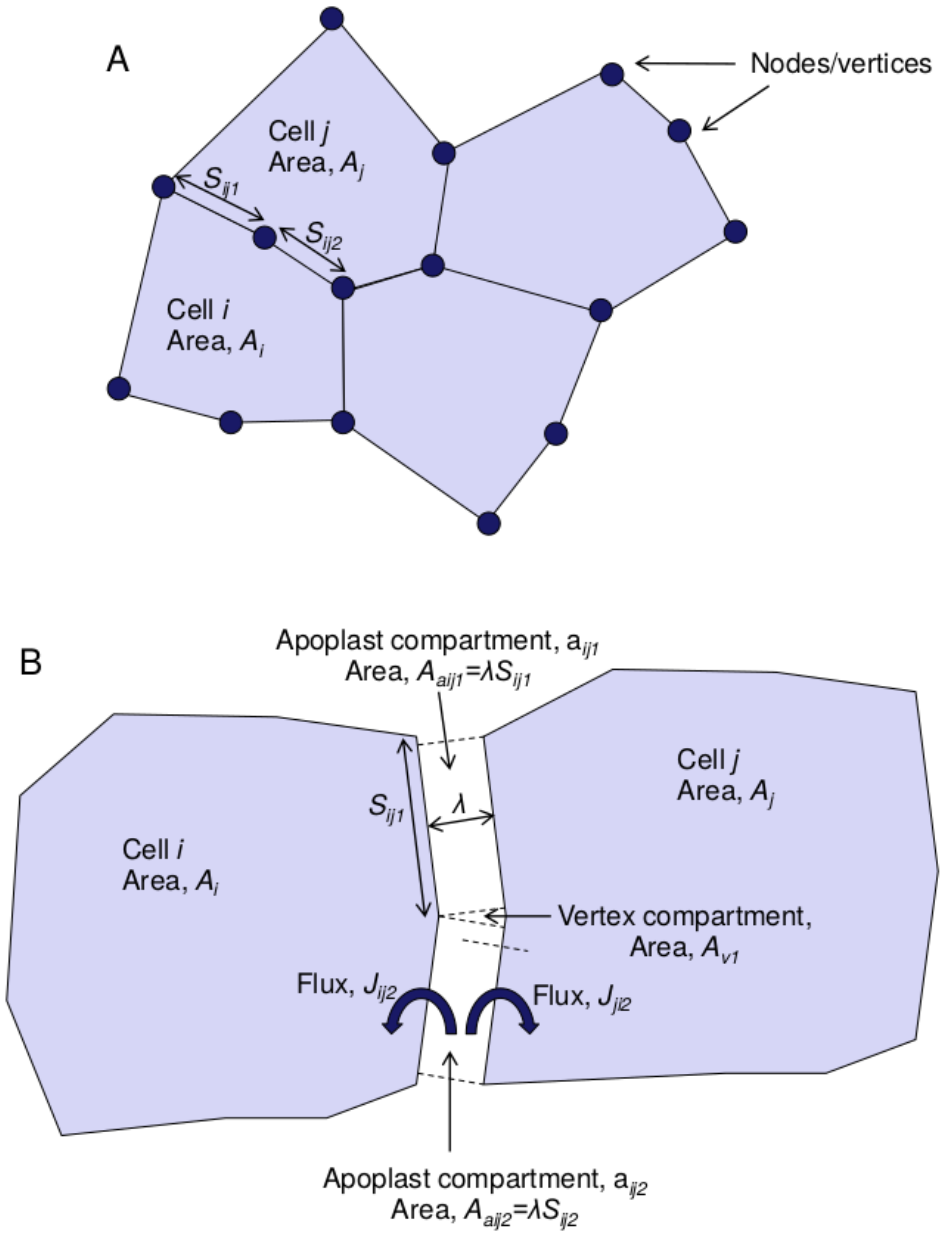
In this section, we describe a mathematical model for auxin distribution in the root tip. We consider the effect of auxin transport via auxin influx carriers, AUX1/LAX, and auxin efflux carriers, PIN. We also incorporate the auxin fluxes through plasmodesmata. The model description closely follows that found in Band et al. (2012b, 2014) and Mellor et al. (2020).

2.2.1 Model structure

The cell geometries used for modelling the root tip are extracted from confocal microscope images of the Arabidopsis root tip that are stained with propidium iodide in order to visualise the cell walls. These root tips have also been crossed with the DII-VENUS fluorescent reporter which is found in the nucleus and enables the visualisation of DII-VENUS levels within each cell (Band et al., 2012b). The software package SurfaceProject, developed by Band et al. (2014), is then used to extract a 2D cross-section of the root tip with the nuclei in focus. Once this cross-section is obtained, the package CellSet (Pound et al., 2012) is used to obtain the position of cells and their cell walls, assign cell types, and quantify DII-VENUS fluorescence levels for every cell (Mellor et al., 2020).

The Python-based framework Openalea (Pradal et al., 2008) is used to set-up the model tissue. The tissue is defined as a vertex based model with a set of points in space that represent the vertices of the cells (Band et al., 2014). Figure 2.1 shows

a schematic of the vertex model set-up. Between two neighbouring cells, i and j, there is one or more apoplast compartments, a_{ijk}, which correspond to the cell wall segments defined by CellSet. The area of each apoplast compartment is given by $A_{a_{ijk}} = \lambda S_{ijk}$, where λ is the cell wall thickness (which we assume to be constant) and S_{ijk} is the distance between the two vertices defining the cell wall segment. Between adjacent apoplast compartments, we have vertex compartments with area A_{vl}. We consider A_i to be the area of cell i.



Supplemental Figure 23. Schematics illustrating the vertex-based interpretation of the multicellular plant tissues.

Figure 2.1: Schematic of the vertex based model as described by Band et al. (2014).

2.2.2 Model fluxes

Auxin can move between cells using a range of transport methods. Auxin may be transported via passive diffusion in the cell cytoplasm and apoplast, or it can be actively transported between the cell cytoplasm and apoplast via auxin influx and efflux carriers. Within a cell, auxin exists in two main forms. Auxin can exist as *IAAH*, which is its protonated form, and as IAA^{-}, which is its anionic form. Protonated auxin can permeate cell walls via passive diffusion, whereas, anionic auxin requires influx and efflux carriers to actively transport it across cell membranes.

The mathematical equations used to describe auxin dynamics in the root tip are based on the ordinary differential equations defined by Band et al. (2014). To represent the movement of auxin from the cell wall compartments to adjacent cells (and vice versa), via influx and efflux carriers and passive diffusion, we define the flux from apoplast compartment a_{ijk} into cell i by,

$$\begin{aligned} J_{ijk} = {} & P_{IAHH}(B_1[\text{Auxin}]_{a_{ijk}} - C_1[\text{Auxin}]_i) \\ & + P_{AUX1}[\text{AUX1}]_{ijk}(B_2[\text{Auxin}]_{a_{ijk}} - C_2[\text{Auxin}]_i) \\ & + P_{LAX}[\text{LAX}]_{ijk}(B_2[\text{Auxin}]_{a_{ijk}} - C_2[\text{Auxin}]_i) \\ & + P_{PIN}[\text{PIN}]_{ijk}(B_3[\text{Auxin}]_{a_{ijk}} - C_3[\mathit{Auxin}]_i) \\ & + P_{back}(B_3[\text{Auxin}]_{a_{ijk}} - C_3[\text{Auxin}]_i), \end{aligned} \tag{2.1}$$

where $[\text{Auxin}]_i$ is the concentration of auxin in cell i, $[\text{Auxin}]_{a_{ijk}}$ is the concentration of auxin in apoplast compartment a_{ijk}, B_1, B_2, B_3, and, C_1, C_2, C_3 are constants (given in Table 2.1) defined in Band and King (2012) (where B_1 and C_1 represent the proportion of protonated auxin within the apoplast and cytoplasm respectively), and P_{IAAH}, P_{AUX1}, P_{LAX}, P_{PIN}, and P_{back} are the permeabilities associated with passive flux, AUX1 dependent, LAX dependent, PIN dependent and background carrier mediated flux respectively (also given in Table 2.1) (Band et al., 2014).

To model the flux within the cell wall, we define the flux representing the movement of auxin from apoplast compartment a_{ijk} to the vertex compartment l as,

$$J_{ijkl} = \frac{2D}{S_{ijk}}([\text{Auxin}_{vl} - [\text{Auxin}]_{a_{ijk}}), \tag{2.2}$$

where $[\text{Auxin}]_{vl}$ is the concentration of auxin in vertex compartment l, D is the auxin diffusion coefficient in the apoplast, and S_{ijk} is the length of the cell wall compartment a_{ijk} (Band et al., 2014).

Finally, we model the flux through the plasmodesmata. Plasmodesmata link the cytoplasm's of two cells, hence, we can define the movement of auxin between cells without the need for it to pass through the cell wall. Hence, the flux through plasmodesmata, from cell j to cell i, is given by,

$$J_{ij}^{p} = P_{plas} d_{ij} ([\text{Auxin}]_j - [\text{Auxin}]_i), \tag{2.3}$$

where P_{plas} is the permeability per plasmodesmata (given in Table 2.1) and d_{ij} is the plasmodesmatal density between cells i and j (Mellor et al., 2020).

Parameter	Value
B_1	0.24
B_2	3.57
B_3	0.034
C_1	0.004
C_2	0.045
C_3	4.68
P_{IAAH}	5.6×10^{-7} ms^{-1}
P_{AUX1}	5.6×10^{-7} ms^{-1}
P_{LAX}	5.6×10^{-7} ms^{-1}
P_{PIN}	5.6×10^{-7} ms^{-1}
P_{back}	1.68×10^{-7} ms^{-1}
P_{plas}	8.06×10^{-7} m^{3}s^{-1}

Table 2.1: Parameter values for auxin transport modelling (Band et al., 2014, Mellor et al., 2020)

2.2.3 Auxin production and degradation

Alongside the movement of auxin between cells and cell wall compartments, we include in the model the production and degradation of auxin within each cell. We define the auxin production rate in cell i to be α_i, whose value depends on the cell type, and the auxin degradation rate to be μ, which is a uniform, linear degradation rate.

In the published model, the auxin degradation rate is uniform across all cell types. The auxin production rate is uniform across all cells, except in the quiescent centre

(QC) and cortex/endodermal initials where the production rate is 10 fold higher (Band et al., 2014) due to the expression pattern of the *TAA1/TAR* genes being localised to this area (Stepanova et al., 2008).

2.2.4 Auxin concentration equations

Combining the flux equations with the auxin production and degradation terms, we obtain the following system of equations to describe auxin concentration within the system,

$$\frac{d[\text{Auxin}]_i}{dt} = \alpha_i - \mu[\text{Auxin}]_i + \frac{1}{A_i}\sum_{j\in C_i}\sum_{k=1}^{N_{ij}} S_{ijk}(J_{ijk} + J^p_{ij}), \tag{2.4a}$$

$$\frac{d[\text{Auxin}]_{a_{ijk}}}{dt} = -\frac{1}{\lambda}(J_{ijk} + J_{jik}) + \frac{1}{S_{ijk}}\sum_{m\in V_{ijk}} J_{ijkm}, \tag{2.4b}$$

$$\frac{d[\text{Auxin}]_{vl}}{dt} = -\frac{1}{\lambda}\sum_{ijk\in W_l} J_{ijkl}, \tag{2.4c}$$

where C_i represents the set of cells adjacent to cell i, N_{ij} is the number of apoplast compartments between cells i and j, V_{ijk} denotes the pair of vertex compartments associated with either end of apoplast compartment a_{ijk}, and W_l is the number of apoplast compartments adjacent to vertex l (Band et al., 2014).

2.2.5 Boundary and initial conditions

Following the model described by Band et al. (2014), we define a fixed boundary condition in stele cells such that $[\text{Auxin}]_b = 1$. The fixed boundary condition represents a constant supply of auxin to the root from the shoot. In the remaining boundary cells, we define a constant gradient boundary condition. This means, at steady-state, for a given boundary cell, p, and its neighbouring cell, in a rootward direction in the same cell layer , q, we have, $[\text{Auxin}]_p - [\text{Auxin}]_q = 0$.

2.2.6 DII-VENUS model equations

Following closely the work of Band et al. (2012b), we can define a system of ordinary differential equations that describe DII-VENUS dynamics within the system. The system of ODEs describe the evolution of the concentration of auxin, $[\text{Auxin}]_i$,

DII-VENUS, $[\text{VENUS}]_i$, TIR1/AFB receptors, $[\text{TIR1}]_i$, auxin-TIR1/AFB complexes, $[\text{Auxin}\cdot\text{TIR1}]_i$, and auxin-TIR1/AFB-DII-VENUS complexes, $[\text{Auxin}\cdot\text{TIR1}\cdot\text{VENUS}]_i$. The system of ODEs describing DII-VENUS dynamics is,

$$\begin{aligned}
\frac{d[\text{Auxin}]_i}{dt} &= k_d[\text{Auxin}\cdot\text{TIR1}]_i - k_a[\text{Auxin}]_i[\text{TIR1}]_i \\
&\quad + \frac{1}{A_i}\sum_{j\in C_i}\sum_{k=1}^{N_{ij}} S_{ijk}(J_{ijk}+J_{ij}^p) \\
&\quad + \alpha_i - \mu[\text{Auxin}]_i, && \text{(2.5a)} \\
\frac{d[\text{TIR1}]_i}{dt} &= -k_a[\text{Auxin}]_i[\text{TIR1}]_i \\
&\quad + k_d[\text{Auxin}\cdot\text{TIR1}]_i, && \text{(2.5b)} \\
\frac{d[\text{Auxin}\cdot\text{TIR1}]_i}{dt} &= k_a[\text{Auxin}]_i[\text{TIR1}]_i - k_d[\text{Auxin}\cdot\text{TIR1}]_i \\
&\quad + (l_d+l_m)[\text{Auxin}\cdot\text{TIR1}\cdot\text{VENUS}]_i \\
&\quad - l_a[\text{Auxin}\cdot\text{TIR1}]_i[\text{VENUS}]_i, && \text{(2.5c)} \\
\frac{d[\text{Auxin}\cdot\text{TIR1}\cdot\text{VENUS}]_i}{dt} &= l_a[\text{Auxin}\cdot\text{TIR1}]_i[\text{VENUS}]_i \\
&\quad - (l_d+l_m)[\text{Auxin}\cdot\text{TIR1}\cdot\text{VENUS}]_i, && \text{(2.5d)} \\
\frac{d[\text{VENUS}]_i}{dt} &= \delta - l_a[\text{Auxin}\cdot\text{TIR1}]_i[\text{VENUS}]_i \\
&\quad + l_d[\text{Auxin}\cdot\text{TIR1}\cdot\text{VENUS}]_i, && \text{(2.5e)}
\end{aligned}$$

where k_a is the rate of association between auxin and TIR1/AFB receptors, k_d is the rate of dissociation of the auxin-TIR1/AFB complex, l_a is the rate of association of DII-VENUS and auxin-TIR1/AFB, l_d is the rate of dissociation of the auxin-TIR1/AFB-DII-VENUS complex into DII-VENUS and auxin-TIR1/AFB, l_m is the rate of dissociation of the auxin-TIR1/AFB-DII-VENUS complex into ubiquitinated DII-VENUS and auxin-TIR1/AFB, and δ is the rate of DII-VENUS production.

We nondimensionalise the system using the following substitutions,

$$t = \frac{[\text{VENUS}_b]}{\delta} t^*, \qquad [\text{Auxin}]_i = [\text{Auxin}]_b [\text{Auxin}]_i^*,$$

$$[\text{VENUS}]_i = [\text{VENUS}]_b [\text{VENUS}]_i^*, \qquad [\text{TIR1}]_i = [\text{TIR1}]_b [\text{TIR1}]_i^*,$$

$$[\text{Auxin}\cdot\text{TIR1}]_i = [\text{Auxin}\cdot\text{TIR1}]_b [\text{Auxin}\cdot\text{TIR1}]_i^*,$$

$$[\text{Auxin}\cdot\text{TIR1}\cdot\text{VENUS}]_i = [\text{Auxin}\cdot\text{TIR1}\cdot\text{VENUS}]_b [\text{Auxin}\cdot\text{TIR1}\cdot\text{VENUS}]_i^*,$$

$$(l_d^*, l_m^*, k_d^*, \mu^*) = \frac{[\text{VENUS}]_b}{\delta}(l_d, l_m, k_d, \mu), \qquad k_a^* = \frac{k_a [\text{TIR1}]_b [,VENUS]_b}{\delta},$$

$$l_a^* = \frac{l_a [\text{VENUS}]_b^2}{\delta}, \qquad \eta_{AT}^* = \frac{\alpha}{[\text{TIR1}]_b \mu}, \qquad \alpha^* = \frac{\alpha [\text{VENUS}]_b}{\delta [\text{Auxin}]_b}, \tag{2.6}$$

where a subscript b denotes a reference concentration. We can now substitute equation (2.6) into the system of equations (2.5a) – (2.5e) to obtain the dimensionless system,

$$\begin{aligned}
\frac{d[\text{Auxin}]_i^*}{dt^*} &= k_a^*([\text{Auxin}\cdot\text{TIR1}]_i - [\text{Auxin}]_i[\text{TIR1}]_i) \\
&\quad + \frac{[\text{VENUS}]_b}{\delta}\frac{1}{A_i}\sum_{j\in C_i}\sum_{k=1}^{N_{ij}} S_{ijk}(J_{ijk}^* + J_{ij}^{p^*}) \\
&\quad + \alpha_i^* - \mu^* [\text{Auxin}]_i^*, && \text{(2.7a)} \\
\frac{d[\text{TIR1}]_i^*}{dt^*} &= k_a^* \eta_{AT}^* (-[\text{Auxin}]_i^*[\text{TIR1}]_i^* \\
&\quad + [\text{Auxin}\cdot\text{TIR1}]_i^*), && \text{(2.7b)} \\
\frac{d[\text{Auxin}\cdot\text{TIR1}]_i^*}{dt^*} &= k_d^*([\text{Auxin}]_i^*[\text{TIR1}]_i^* - [\text{Auxin}\cdot\text{TIR1}]_i^* \\
&\quad + l_a^*([\text{Auxin}\cdot\text{TIR1}\cdot\text{VENUS}]_i^* \\
&\quad - [\text{Auxin}\cdot\text{TIR1}]_i^*[\text{VENUS}]_i^*), && \text{(2.7c)} \\
\frac{d[\text{Auxin}\cdot\text{TIR1}\cdot\text{VENUS}]_i^*}{dt^*} &= (l_d^* + l_m^*)([\text{Auxin}\cdot\text{TIR1}]_i^*[\text{VENUS}]_i^* \\
&\quad - [\text{Auxin}\cdot\text{TIR1}\cdot\text{VENUS}]_i^*), && \text{(2.7d)} \\
\frac{d[\text{VENUS}]_i^*}{dt^*} &= 1 - \frac{(l_d^* + l_m^*)}{l_m^*}[\text{Auxin}\cdot\text{TIR1}]_i^*[\text{VENUS}]_i^* \\
&\quad + \frac{l_d^*}{l_m^*}[\text{Auxin}\cdot\text{TIR1}\cdot\text{VENUS}]_i^*. && \text{(2.7e)}
\end{aligned}$$

Here, $(J_{i,j,k}^*, J_{ij}^{p^*}) = \frac{1}{[\text{Auxin}]_b}(J_{ijk}, J_{ij}^p)$ gives the flux relative to the auxin boundary concentration. Now, making the assumption that complex formation and dissociation happen rapidly (i.e. by setting equations (2.7b) to (2.7d) equal to zero), we can reduce the system of equations to obtain a single equation that describes the DII-

VENUS dynamics in the system (we return to dimensional time in the process),

$$\frac{d[\text{VENUS}]_i^*}{dt} = p_2\Big(1 - \frac{[\text{Auxin}]_i^*[\text{VENUS}]_i^*}{p_3 + p_4[\text{Auxin}]_i^* + p_1[\text{Auxin}]_i^*[\text{VENUS}]_i^*}\Big), \tag{2.8}$$

where the coefficients p_1, p_2, p_3, and p_4 (Band et al., 2012b) are given by,

$$p_1 = \frac{[\text{Auxin}\cdot\text{TIR1}\cdot\text{VENUS}]_b}{[\text{TIR1}]_T}, \qquad p_2 = \frac{\delta}{[\text{VENUS}]_b},$$
$$p_3 = \frac{[\text{TIR1}]_b}{[\text{TIR1}]_T}, \qquad p_4 = \frac{[\text{Auxin}\cdot\text{TIR1}]_b}{[\text{TIR1}]_T}. \tag{2.9}$$

For our model, we are interested in the auxin distribution at steady-state. As such, we can set equation (2.8) equal to zero to find a direct relationship between auxin concentration and DII-VENUS concentration, given by,

$$[\text{VENUS}]_i^* = \frac{\frac{p_3}{[\text{Auxin}]_i^*} + p_4}{1 - p_1}. \tag{2.10}$$

The parameter values used in the reduced DII-VENUS model are estimated in Band et al. (2012b) and are given in Table 2.2.

Parameter	**Value**
p_1	0.06
p_3	0.91
p_4	0.03
α_i^*	0.001s^{-1}
α_{QC}^*	0.01s^{-1}
μ^*	0.001s^{-1}

Table 2.2: Parameter values for reduced DII-VENUS model. Parameters p_1, p_3, p_4 are estimated in (Band et al., 2012b) and are dimensionless. α_i^* and μ^* are the production and degradation rate in all cells, apart from the QC region which has an increased production rate given by α_{QC}.

2.3 Modelling local auxin synthesis

The plant hormone auxin (IAA) plays a crucial role in many aspects of plant development. The spatial distribution of auxin in the plant root tip helps to regulate growth, initiate lateral roots, and produce tropic responses (Grieneisen et al., 2007, Swarup

et al., 2005, Band et al., 2012b). Determining the mechanisms that regulate auxin dynamics is a vital step in understanding auxin's role in plant development. In this section, we extend our mathematical model (Section 2.2) to investigate the effect of local auxin synthesis on auxin dynamics in the Arabidopsis root tip by mimicking the reciprocal grafting experiments performed by Brumos et al. (2018).

2.3.1 Reciprocal-grafting experiments

The auxin biosynthesis genes, *WEI8/TAR*, are expressed at and near the quiescent centre (QC) and catalyse the conversion of Tryptophan to the IAA precursor IPyA (Figure 1.4) (Ljung, 2013). Recent experimental studies, performed by Brumos et al. (2018), involving these genes show that local auxin synthesis may play a crucial role in root auxin patterning. Brumos et al. (2018) performed reciprocal grafting experiments of WT and *wei8 tar2* (auxin biosynthesis deficient mutant) shoots and roots and the results of their experiments are shown in Figure 2.2A. The intensity of

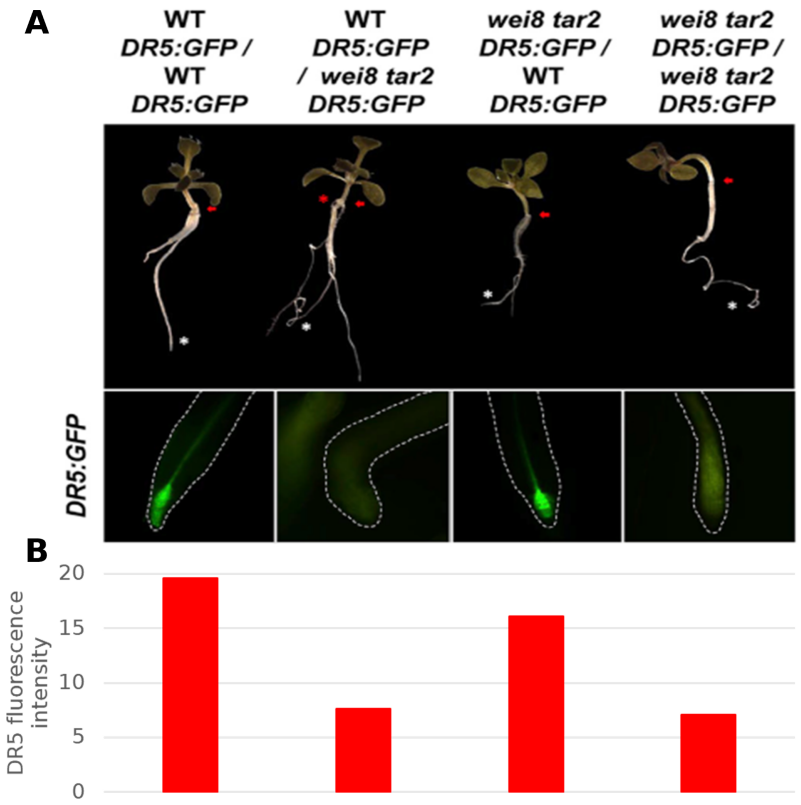


Figure 2.2: Reciprocal grafting experiments suggest an important role for local auxin synthesis in the auxin patterning of Arabidopsis root tip. **(A)** Grafting of auxin-deficient *wei8 tar2* and WT seedlings harboring the DR5:GFP auxin responsive reporter (Brumos et al., 2018); **(B)** Auxin signal intensity plot.

the auxin signal is shown in Figure 2.2B (calculated using Fiji ImageJ). We see a 2.6 fold decrease in auxin signal intensity between the *WT-WT* graft and the *WT-wei8 tar2* graft, and a 1.2 fold decrease between the *WT-WT* graft and the *wei8 tar2-WT* graft. Visually, these changes are clear in the high-low-high pattern seen across these three grafts.

Several mathematical models have captured the effects of influx and efflux carriers on auxin dynamics, based on a primary source of auxin originating in the shoot and delivered to the root via the phloem. These root-tip models assume there is a fixed auxin concentration at the boundary between the modelled root-tip tissue and the region of long-distance transport (Grieneisen et al., 2007, Band et al., 2014, van den Berg et al., 2016). Less clear from the models is the role that local auxin synthesis may play in patterning the root tip. Grieneisen et al. (2007) do not account for local auxin biosynthesis in their model work, Band et al. (2014) have a background level of auxin biosynthesis in all cells which is increased in the quiescent center and cortex/endodermal initials (QC region), and van den Berg et al. (2016) also have an auxin production term for all cells in their model, however, they do not vary the production rate based on cell-type and the auxin production rate is 50% lower than the background auxin biosynthesis rate used by Band et al. (2014).

To investigate the role of local auxin synthesis in the patterning of the Arabidopsis root tip, we adapt the existing multicellular model of auxin dynamics in the Arabidopsis root tip (Section 2.2, (Band et al., 2014, Mellor et al., 2020)) and test the model's ability to explain the grafting experiments presented by Brumos et al. (2018). It is important to note that the auxin reporter, DR5:GFP, used in the reciprocal grafting experiments is not a label for auxin, and as such, the relationship between reporter levels and auxin levels may be non-linear.

2.3.2 Initial modelling results

Initially, we leave all model parameters as described in Section 2.2 (Tables 2.1 and 2.2) and design a method for defining *wei8 tar2* mutant conditions in relation to our initial model parameters. In the model, there are three key parameters that are related to the biosynthesis of auxin, these are α_b, α_{qc}, and $[\text{Auxin}]_b$. Here, α_b is the rate of auxin biosynthesis in the majority of root cells, α_{qc} is the rate of auxin biosynthesis in the QC region (quiescent center and cortical/endodermal initial cells), and $[\text{Auxin}]_b$ is the concentration in boundary cells. Figure 2.3 indicates the cells where each of these parameters are specified. We define auxin synthesis mutant conditions to be 10% of their corresponding WT condition. Table 2.3 shows parameter values for

each of the reciprocal grafting experiments.

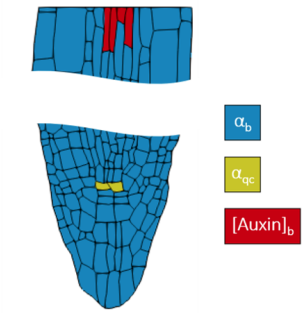


Figure 2.3: Location of auxin biosynthesis parameters within the root tip geometry.

Modelling reciprocal grafting experiments, using the parameters given in Table 2.3, we obtain the results shown in Figure 2.4.

Shoot	**Root**	**Background synthesis,** α_b	**QC region synthesis,** α_{qc}	**Shoot auxin supply,** $[\text{Auxin}]_b$
WT	*WT*	0.001s^{-1}	0.01s^{-1}	1.0
WT	*wei8 tar2*	0.0001s^{-1}	0.001s^{-1}	1.0
wei8 tar2	*WT*	0.001s^{-1}	0.01s^{-1}	0.1
wei8 tar2	*wei8 tar2*	0.0001s^{-1}	0.001s^{-1}	0.1

Table 2.3: Auxin synthesis and boundary conditions for reciprocal grafting modelling. Parameters are given in Tables 2.1 and 2.2.

Quantifying the fold-change between the *WT-WT* simulation and simulations for *WT-wei8 tar2* and *wei8 tar2-WT* simulations, we obtain fold decreases of 1.5 and 2.4 respectively (Figure 2.3B). This is inconsistent with the fold decrease seen in experimental results, where the fold decrease between *WT-WT* and *wei8 tar2* grafts is larger than the one between *wei8 tar2* and *WT-WT* grafts. Hence, it is clear the current model set-up is not able to replicate the results seen in grafting experiments.

In their paper, Brumos et al. (2018) discuss the modelling work of Band et al. (2014). They suggest that the inclusion of a small auxin synthesis term in all cells may be masking the impacts of local auxin synthesis in the QC region. We decided to investigate these suggestions further by removing background synthesis from all cells.

Leaving the remaining parameters as before, we removed background auxin synthesis

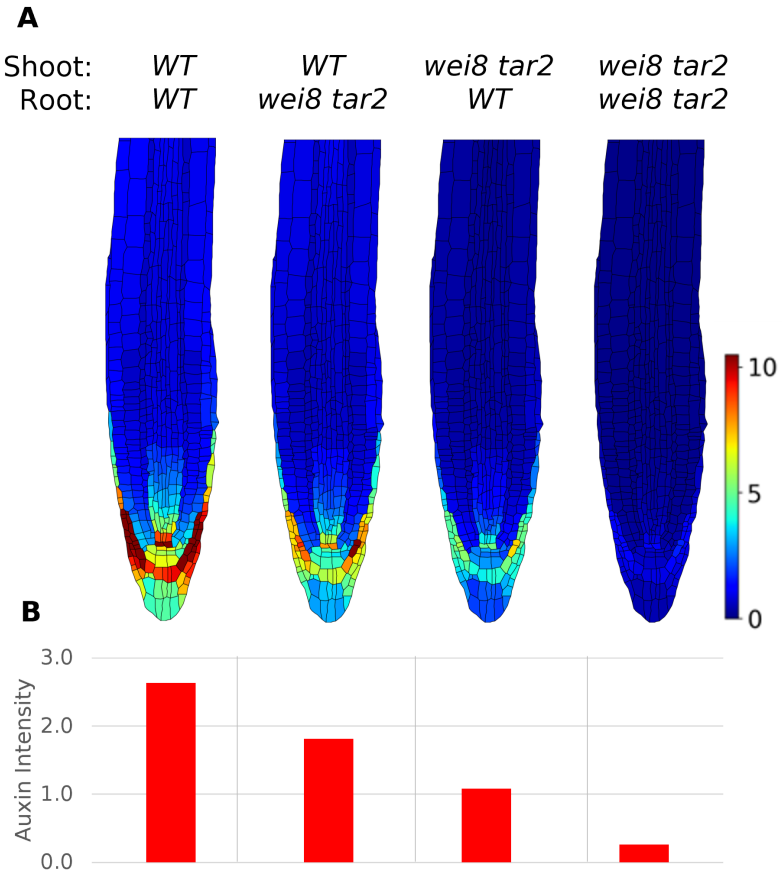


Figure 2.4: Initial simulations of grafting experiments are unable to replicate the fold-change behaviour seen in experimental results. **(A)** Model results for simulations of grafting experiments using parameters listed in Table 2.3 (Band et al., 2014); **(B)** Auxin intensity plot.

from the model by setting $\alpha_b = 0$. The remaining parameters do not change from our initial simulations (full parameters given in Table 2.4).

Shoot	**Root**	**Background synthesis, α_b**	**QC region synthesis, α_{qc}**	**Shoot auxin supply, $[\text{Auxin}]_b$**
WT	*WT*	0.0s^{-1}	0.01s^{-1}	1.0
WT	*wei8 tar2*	0.0s^{-1}	0.001s^{-1}	1.0
wei8 tar2	*WT*	0.0s^{-1}	0.01s^{-1}	0.1
wei8 tar2	*wei8 tar2*	0.0s^{-1}	0.001s^{-1}	0.1

Table 2.4: Auxin synthesis and boundary conditions for reciprocal grafting modelling with background synthesis removed ($\alpha_b = 0$). Parameters are given in Tables 2.1 and 2.2.

The results of this modelling are still unable to replicate the auxin patterns shown

by reciprocal grafting experiments (Figure 2.5). As such, we chose to maintain the original model set-up of having a background synthesis rate in all cells, with increased synthesis in the QC region. We choose to maintain background auxin synthesis rates as there is evidence to suggest that all root cells have auxin biosynthesis capabilities (Ljung et al., 2005, Petersson et al., 2009).

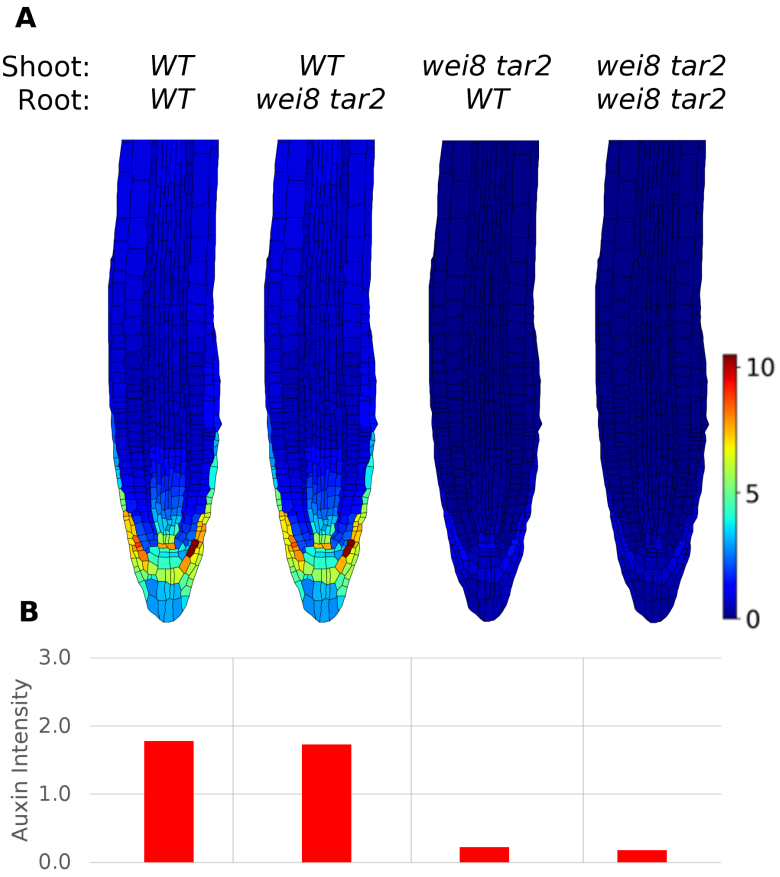


Figure 2.5: Removing background synthesis in simulations of grafting experiments does not enable the model to replicate the fold-change behaviour seen in experimental results. **(A)** Model results for simulations of grafting experiments using parameters listed in Table 2.4 (Band et al., 2014); **(B)** Auxin intensity plot.

2.3.3 Modifying the shoot boundary condition

In the previous section, we showed that our existing auxin transport model is unable to replicate reciprocal grafting experimental results. Initial modifications of removing background synthesis in all cells did not resolve the issue. As such, in this section, we modified the boundary condition described in Section 2.2.5 to enable us to make more direct comparisons between auxin produced in the shoot and auxin produced

in the root of the model.

We maintained the zero-gradient condition described in the outer shoot-boundary cells and instead of fixing auxin concentration in the inner shoot-boundary cells, we prescribe a higher production rate in the stele cells at the shootward boundary to mimic a constant rate of auxin delivery to the root tip from the shoot.

We define the auxin biosynthesis mutants using the same method described in Section 2.3.2, where auxin biosynthesis mutant conditions are set to be 10% of the original WT condition. The parameters for reciprocal grafting experiments with the new boundary condition are shown in Table 2.5. Here the shoot auxin supply WT value of 0.195s^{-1} is set to be equivalent to the fixed auxin boundary condition of 1.0.

Shoot	**Root**	**Background synthesis, α_b**	**QC region synthesis, α_{qc}**	**Shoot auxin supply, α_s**
WT	*WT*	0.001s^{-1}	0.01s^{-1}	0.195s^{-1}
WT	*wei8 tar2*	0.0001s^{-1}	0.001s^{-1}	0.195s^{-1}
wei8 tar2	*WT*	0.001s^{-1}	0.01s^{-1}	0.0195s^{-1}
wei8 tar2	*wei8 tar2*	0.0001s^{-1}	0.001s^{-1}	0.0195s^{-1}

Table 2.5: Auxin synthesis and boundary conditions for reciprocal grafting modelling with new flux boundary condition. Parameters are given in Tables 2.1 and 2.2.

We modelled the grafting experiments with the new boundary condition and the results can be seen in Figure 2.6. Fold change analysis reveals that there is a 1.8 fold decrease between *WT-WT* simulations and both *WT-wei8 tar2* and *wei8 tar2-WT* simulations. These results are different from the results of the fixed boundary condition model but are still unable to replicate experimental results (as expected as the current boundary condition is designed to be equivalent to the fixed boundary condition used in Section 2.3.2).

2.3.4 Model optimisation

2.3.4.1 Manipulating auxin biosynthesis in the QC region

We investigated the role of auxin biosynthesis in the QC region of the Arabidopsis root tip to try to understand the impact of local auxin biosynthesis on root tip auxin patterning. We chose to investigate the role of local auxin synthesis in the QC region

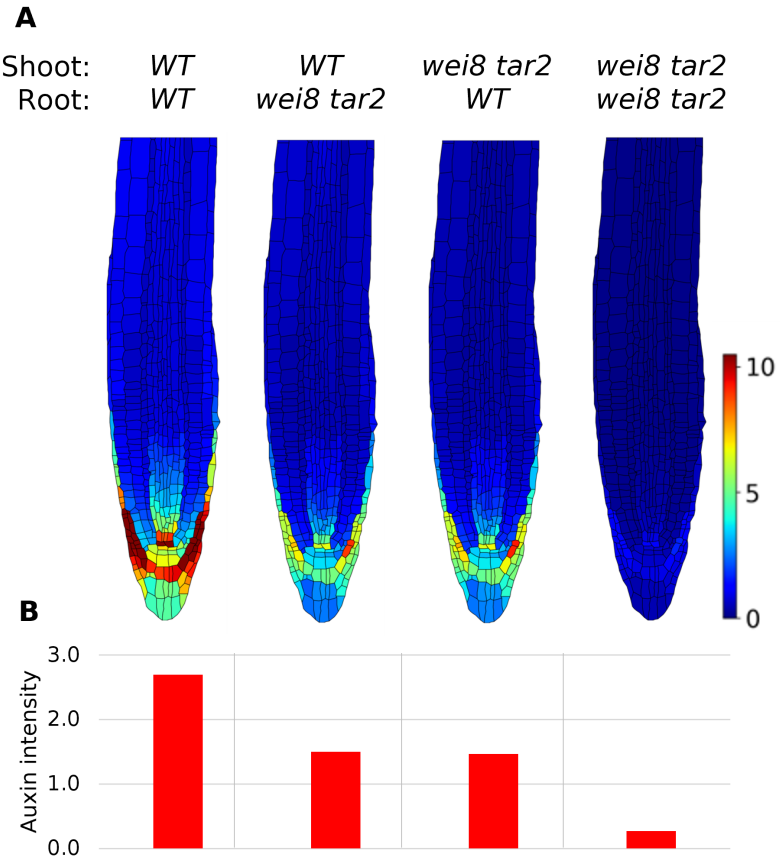


Figure 2.6: Simulations of grafting experiments with a boundary condition prescribing increased production in shoot boundary cells reproduce results of simulations with fixed boundary condition. **(A)** Model results for simulations of grafting experiments using parameters listed in Table 2.5 (Band et al., 2014); **(B)** Auxin intensity plot. **WT influx rate: 0.195s^{-1}.**

as there is strong evidence to suggest the auxin biosynthesis gene *TAA1* (also known as *WEI8*) is localised to this region of the root tip (Stepanova et al., 2008) (see Figure 2.7).

To investigate the role auxin synthesis in the QC region plays in root tip auxin patterning, we needed a method to compare our modelling results to the experimental data. In order to quantify the difference between the experimental images and model results, we calculated the mean GFP fluorescence intensity in each experimental case. Next, we defined a measure to quantify the fit of the model to the experimental intensities. We took the ratio of the *WT-wei8 tar2* and *wei8 tar2-WT* fluorescence intensities against the *WT-WT* fluorescence intensity. We then defined the measure of "fit" as,

$$f = \frac{(R-r)^2}{r} + \frac{(S-s)^2}{s} \tag{2.11}$$

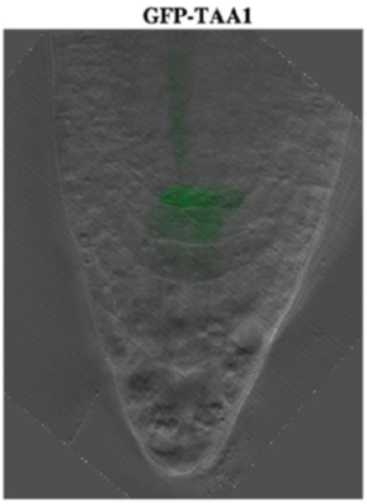


Figure 2.7: Location of the auxin biosynthesis gene *TAA1* in the Arabidopsis root tip (Stepanova et al., 2008).

where R is the ratio of the *WT-wei8 tar2* model average auxin intensity against *WT-WT* model average auxin intensity, S is the ratio of the *wei8 tar2-WT* model average auxin intensity against *WT-WT* model average auxin intensity, and r and s are the corresponding ratios calculated from the image analysis of the experimental images.

The total level of auxin in our system is determined by the total amount of production and degradation within the system, and the patterning is driven by the auxin transporters and plasmodesmata. We seek to find an optimal fit for our model against parameters that have biological relevance. As such, there may exist other mathematically optimal fits to our system of equations that yield similar total auxin levels that rely on biologically infeasible parameters.

To evaluate the role of local auxin synthesis in the QC region of the root tip, we plotted the measure of fit, equation (2.11), as a function of QC region synthesis to background synthesis ratio. The results are shown in Figure 2.8. A greater than 100-fold increase in auxin biosynthesis in the QC region compared to background auxin biosynthesis is required to obtain a qualitative match to experimental data, with a 285-fold change (square in Figure 2.8) required to obtain an optimal fit to the experimental data. The fold change required to produce optimal results is unrealistic as we expect synthesis in the QC to be only 10-fold larger than background synthesis (Ljung et al., 2005).

Due to the unrealistic increase in auxin synthesis in the QC region required to replicate reciprocal grafting experiments, we conclude that auxin biosynthesis in the QC region alone cannot be responsible for root-tip auxin patterning in Arabidopsis.

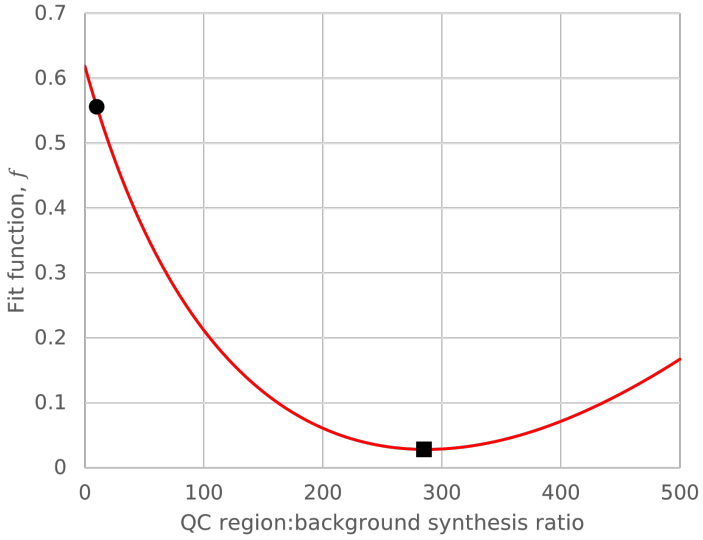


Figure 2.8: Measure of fit (Equation (2.11)) plotted as a function of QC region synthesis to background synthesis ratio. Black circle marks a QC ratio of 10 (the value consistent with literature (Ljung et al., 2005)). Black square marks the optimal QC region:background synthesis ratio of 285.

In order to replicate reciprocal grafting experiments, we shifted our focus away from localised auxin synthesis in the QC region and investigated the role of auxin biosynthesis across the wider set of root-tip tissues.

2.3.4.2 Shoot vs root auxin biosynthesis

Using the measure of fit, equation (2.11), we investigated the importance of root auxin synthesis vs shoot produced auxin. We vary the model parameter α_s to capture changes in the amount of auxin produced by the shoot. We plotted the measure as a function of the ratio of shoot-derived auxin to root-derived auxin. The results are shown in Figure 2.9. We find that only shifting the shoot:root ratio away from shoot-dominance towards synthesis in the root produces a good qualitative comparison to the experimental data. The optimal fit occurs at a shoot:root ratio of 0.6 (corresponding to a flux boundary condition of 0.08; square in Figure 2.9). Optimal parameter values for all reciprocal grafting experiments are shown in Table 2.6.

Fold change analysis of Figure 2.10B, reveals that there is a 2.7 fold decrease from *WT-WT* simulations and *WT-wei8 tar2* simulations and a 1.4 fold decrease from *WT-WT* simulations and *wei8 tar2-WT* simulations. These results are consistent with fold-change behaviour seen in experiments. Hence, we conclude that local auxin biosynthesis across the whole root tip plays an important role in root-tip auxin

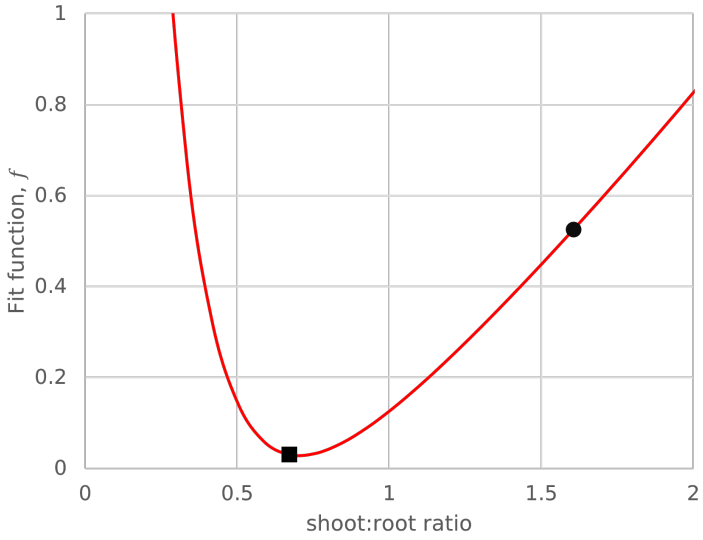


Figure 2.9: Measure of fit (Equation (2.11)) plotted as a function of shoot synthesis to root synthesis ratio. Black circle marks the original ratio for flux boundary condition consistent with fixed boundary condition model. Black square marks the optimal shoot:root ratio.

Shoot	**Root**	**Background synthesis, α_b**	**QC region synthesis, α_{qc}**	**Shoot auxin supply, α_s**
WT	*WT*	0.001s^{-1}	0.01s^{-1}	0.08s^{-1}
WT	*wei8 tar2*	0.0001s^{-1}	0.001s^{-1}	0.08s^{-1}
wei8 tar2	*WT*	0.001s^{-1}	0.01s^{-1}	0.008s^{-1}
wei8 tar2	*wei8 tar2*	0.0001s^{-1}	0.001s^{-1}	0.008s^{-1}

Table 2.6: Auxin synthesis and boundary conditions for reciprocal grafting modelling with optimised flux boundary condition parameters. Parameters are given in Tables 2.1 and 2.2.

patterning.

2.3.4.3 Data comparison and visualisation

Having obtained a model set-up that allows us to mimic the fold change behaviour seen in the grafting experiments conducted by Brumos et al. (2018), we wish to define a method that will allow us to compare the model simulations with cell-based experimental data. For this we require data using the DII-VENUS fluorescent reporter. Further experiments are required to obtain this data for grafting experiments, however, we are able to compare the *WT-WT* simulations to data we have for WT Arabidopsis seedlings.

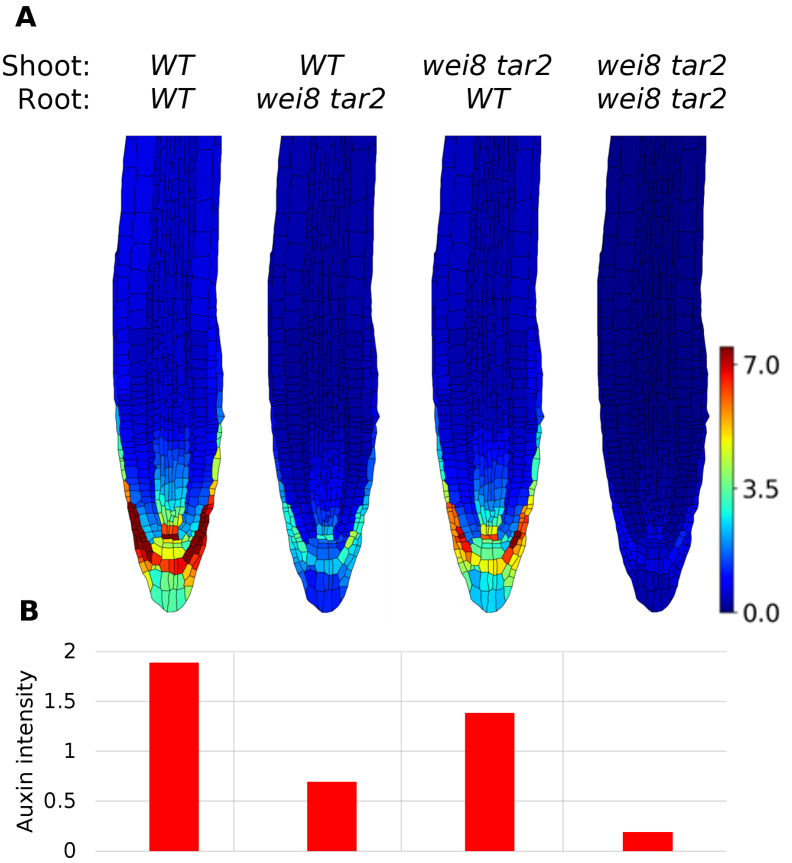


Figure 2.10: Simulations of grafting experiments with an optimal boundary condition where increased production is prescribed in shoot boundary cells reproduce fold change behaviour seen in experiments. **(A)** Model results for simulations of grafting experiments using parameters listed in Table 2.6 (Band et al., 2014); **(B)** Auxin intensity plot. **WT influx rate: 0.08s^{-1}.**

We follow the model evaluation techniques described in (Mellor et al., 2020). Each cell in the model and experimental datasets are normalised with the minimum value for each dataset, i.e.,

$$m_i^* = \frac{m_i}{\min(M)}, \tag{2.12}$$

where m_i is the value for cell i, M is the set of all values, and m_i^* is the normalised value for cell i. We then plot the difference between the two normalised datasets to compare the model with the experimental data. Figure 2.11A shows the original WT-WT model (fixed concentration boundary condition) compared with existing DII-VENUS fluorescent data and Figure 2.11E shows the optimal flux boundary condition model compared with existing DII-VENUS data. These figures show that, when normalised, the newly adapted model captures the DII-VENUS experimental data as well as the original model.

To quantify the difference between the models and the data, we take the mean absolute difference between the normalised model and normalised experimental data i.e.,

$$F = \frac{\sum_{i \in C} |m_i^* - d_i^*|}{|C|}, \tag{2.13}$$

where C is the set of all cells in the root geometry ($|C|$ is the number of cells), and m_i^* and d_i^* are the normalised model and experimental DII-VENUS values for cell i. Figure 2.11F shows the quantification of the difference between the original WT-WT model and the DII-VENUS experimental data compared to the quantification of the difference between the optimal flux boundary condition model and the DII-VENUS experimental data.

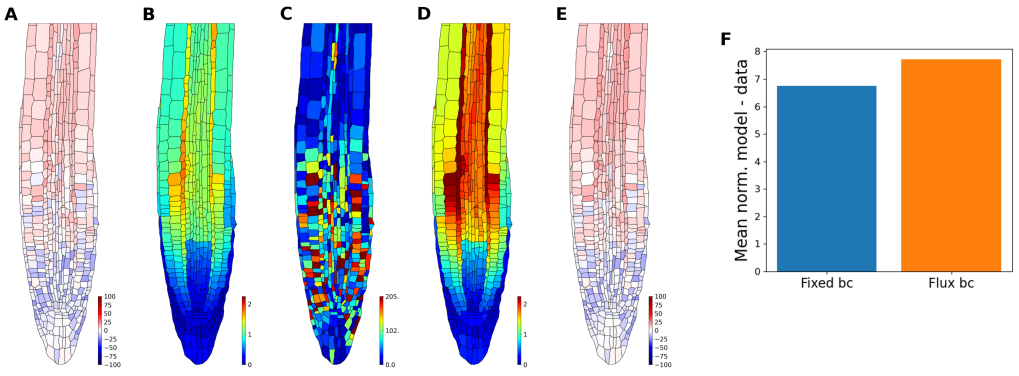


Figure 2.11: Examples of data comparison technique. **(A,E)** WT model results compared with DII-VENUS experimental data for the fixed boundary condition and optimal flux boundary condition respectively; **(B,D)** Model DII-VENUS outputs for the fixed boundary condition and optimal flux boundary condition models respectively; **(C)** DII-VENUS experimental data; **(F)** Quantified difference between model simulations and experimental data. Cosine similarity between fixed model simulations and flux model simulations is 0.9999.

As we can see from the results shown in Figure 2.11, changing the boundary condition to a flux boundary condition has not significantly impacted the fit of the WT model to experimental data. In particular, we can calculate the cosine similarity between model auxin for the fixed concentration boundary condition model and the optimal flux boundary condition,

$$\text{cosine similarity} = \frac{\bar{A} \cdot \bar{B}}{||\bar{A}|| \cdot ||\bar{B}||} = 0.9999 \tag{2.14}$$

where $\bar{A}$ and $\bar{B}$ are the simulation auxin vectors for the fixed concentration boundary condition and optimal flux boundary conditions respectively. This gives a value very close to 1, showing that the adjustments we have made to the boundary condition have not impacted the auxin pattern within the root tip. These data comparison techniques can also be used to quantify the difference between model simulations and results from grafting experiments that are conducted in plants expressing the DII-VENUS fluorescent reporter.

Finally, we ensure that modifications made to the model to capture grafting experiments does not affect the previously published results on *aux1* and *pin2* auxin patterns in the root tip (Band et al., 2014, Mellor et al., 2020). Figures 2.12 and 2.13 compare simulations of *aux1* and *pin2* mutants using the optimal flux boundary condition model to results from Mellor et al. (2020). These results, alongside cosine similarity measurements of 0.99997 and 0.999992 (for *aux1* and *pin2* respectively) indicate that adjustments to the model to capture grafting experiments do not affect previously published results from the model.

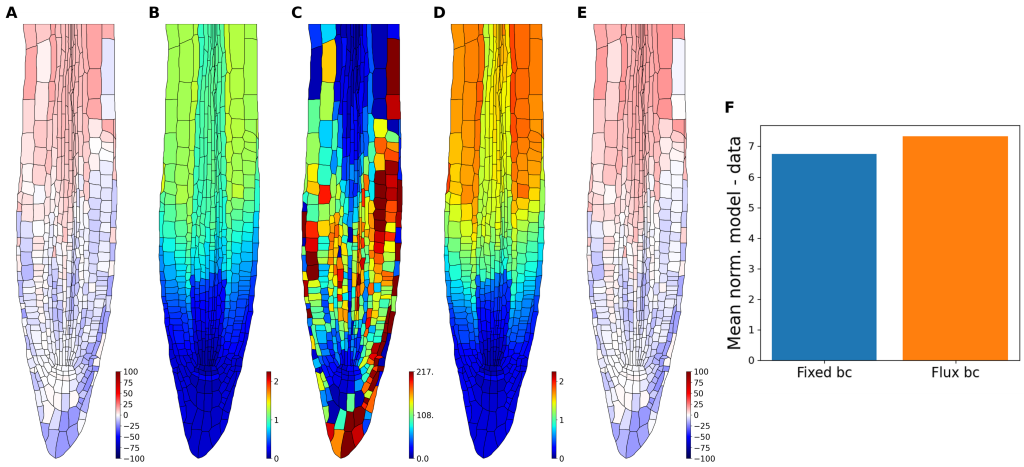


Figure 2.12: Data comparison for *aux1* mutant roots. **(A,E)** *aux1* model results compared with DII-VENUS experimental data for the fixed boundary condition and optimal flux boundary condition respectively; **(B,D)** Model DII-VENUS outputs for the fixed boundary condition and optimal flux boundary condition models respectively; **(C)** DII-VENUS experimental data; **(F)** Quantified difference between model simulations and experimental data. Cosine similarity between fixed model simulations and flux model simulations is 0.99997.

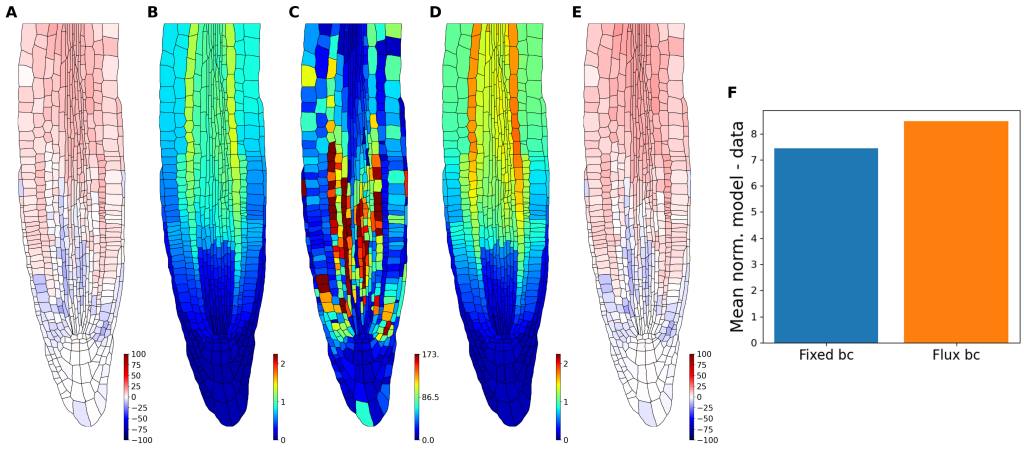


Figure 2.13: Data comparison for *pin2* mutant roots. **(A,E)** *pin2* model results compared with DII-VENUS experimental data for the fixed boundary condition and optimal flux boundary condition respectively; **(B,D)** Model DII-VENUS outputs for the fixed boundary condition and optimal flux boundary condition models respectively; **(C)** DII-VENUS experimental data; **(F)** Quantified difference between model simulations and experimental data. Cosine similarity between fixed model simulations and flux model simulations is 0.999992.

2.4 Local auxin biosynthesis experiments

COVID-19 impact on experimental data

The experiments discussed in Section 5.4.1 were scheduled to be performed during the COVID-19 pandemic. Due to time restraints on lab access and the far reaching impact of the pandemic on experimental colleagues, the decision was made to cancel these experiments. Figure 5.1 shows the proposed experimental design for these experiments. Section 5.4.1 is presented with details of what we had intended to study to add further verification to the model simulations.

2.5 Conclusions

We have used mathematical modelling to explore the role of auxin synthesis in the shoot and root tissues for controlling auxin levels in the primary root apex. Our results suggest that an unrealistically large increase in auxin biosynthesis in the QC and cortex/endodermal initials is needed to replicate experimental grafting results. As such, our modelling suggests a shift in the shoot:root ratio away from shoot dominance is required to capture the effect of reciprocal grafting experiments. We show that changing the boundary condition of the model to a flux boundary condition does not impact on the quantitative fit of the model to WT experimental DII-VENUS data and that changing this boundary condition allows us to capture the affects of reciprocal grafting experiments on auxin distribution in the Arabidopsis root tip. We conclude that local auxin synthesis in a wider set of root tip tissues than just the QC plays a critical role in determining auxin levels in the primary root apex.

Chapter 3

Modelling hormone transport in the phloem

3.1 Introduction

In Chapter 2, we developed a cell-based model of the auxin dynamics in the root tip of an Arabidopsis seedling that captured the effect of local auxin biosynthesis on auxin patterning in the root tip. In the development of this model, we introduced a constant flux boundary condition in order to be able to investigate the relative contributions of auxin transported into the root from the shoot to auxin synthesised in the root. In this chapter, we investigate in more detail the transport of hormones from shoot to root.

The phloem forms part of a plant's vascular system and is responsible for the long-distance transport of sugars, proteins, and hormones from the shoot to the root (Taiz and Zeiger, 2010). Many studies have shown that shoot-derived hormones are transported long distances within the phloem to regulate developmental processes in the root (Lacombe and Achard, 2016, Baker, 2000b). The transport of the gibberellin (GA) precursor GA_{12} through the Arabidopsis phloem acts as a long-distance signal mediating growth responses (Regnault et al., 2015). Translocation of cytokinins from shoot to root via the phloem is important for nitrogen acquisition (Kiba et al., 2011), the regulation of root nodulation (Sasaki et al., 2014), and maintenance of vascular patterning in the root (Bishopp et al., 2011). Lateral root development has been shown to depend on long-distance transport of both auxin (Bhalerao et al., 2002, Chhun et al., 2007) and ABA (Zhang et al., 2021).

Although it is well established that hormones are advected through the phloem (Lacombe and Achard, 2016), as far as we are aware, no previous mathematical models have considered this directly and investigated how parameters affect hormone delivery from the shoot to the root tip. Instead, existing plant-hormone models focus on hormone dynamics within a specific organ or tissue, for example, modelling auxin dynamics in the root tip. Previously published root-tip models assume there is a fixed auxin concentration at the boundary between the modelled root-tip tissue and the region of long-distance transport (Grieneisen et al., 2007, Band et al., 2012b, van den Berg et al., 2016, Mellor et al., 2020). However, the processes that regulate the auxin dynamics at this boundary have not been studied directly.

Existing mathematical models of phloem transport focus on the movement of sugars through the phloem via the pressure flow hypothesis (Minchin et al., 1993, Bidel et al., 2000, Thompson and Holbrook, 2003, Jensen et al., 2011, 2012, Payvandi et al., 2014, Jensen et al., 2016, Nakad et al., 2021) initially proposed by Münch (Münch, 1926); this describes how phloem sap movement is generated by osmotic pressure differences caused by a gradient in sugar concentration between source and sink tissues (Jensen et al., 2016). Sugar is loaded into the phloem at the shoot, reducing the phloem sap osmotic potential and causing an influx of water, whereas sugar unloading in the root increases the phloem osmotic potential causing water efflux. The resulting gradient in hydrostatic pressure drives phloem water flow that advects the sugar and other solutes (Payvandi et al., 2014). Key developments from previous models include non-steady-state dynamics (Thompson and Holbrook, 2003), the development of analytical solutions in high and low Münch number limits (Jensen et al., 2012), investigating the importance of diffusion in boundary layers at high Münch number (Payvandi et al., 2014), and the role of Taylor dispersion (Nakad et al., 2021). Many of these models have focused on larger plant species such as barley (Minchin et al., 1993), peach (Bidel et al., 2000), and black locust (Payvandi et al., 2014) which all have a Münch number greater than 1.

In this chapter, we expand upon the phloem transport models in the literature to include the transport of a generic hormone (though we note that the model presented is also applicable to the transport of any small passively advected molecules in the phloem). The model also includes adaptations that allow us to capture more realistic loading and unloading mechanisms. This formulation enables us to introduce parameters that represent specific physical processes such as passive diffusion through plasmodesmata and active transport via known membrane proteins. Motivated by experimental findings (Ross-Elliott et al., 2017, Bret-Harte and Silk, 1994), we also incorporate loading and unloading via bulk flow, by introducing the Staverman reflection coefficient (Staverman, 1951) which allows for solutes to leak across the

membrane in the direction of water flow. In the results section, we focus our attention to model scenarios with low Münch number to be representative of smaller model species, such as *Arabidopsis thaliana* for which bulk flow has been shown to be the dominant form of phloem unloading (Ross-Elliott et al., 2017).

3.2 Phloem transport model

In order to formulate the mathematical model, we consider the phloem as a long, thin, narrow pipe of through which water and solutes are transported. The phloem is split into three zones: the loading zone ($x \in [0, x_1]$); translocation zone ($x \in [x_1, x_2]$); and unloading zone ($x \in [x_2, x_3]$). The phloem tube has radius a and the length of the translocation zone is given by L (where $a \ll L$). Water can flow into / out of the phloem tube along the length of the pipe, however, solutes may only enter/leave the phloem in the loading/unloading zone respectively. Water is considered to be transferred to/from the xylem, whereas solutes are considered to be transferred to/from sink/source tissues. The phloem tube walls are comprised of membranes whose permeability properties are dependent on the distance along the phloem tube. A schematic of the modelling structure is given in Figure 3.1.

3.2.1 Governing equations

We develop a model that describes the velocity of the phloem sap (water with the solutes dissolved in it) and the concentration of the solutes along the length of the phloem. We model the phloem sap as an incompressible Newtonian fluid. The velocity in the $x-$ and $r-$directions is given by $v_x(r,x)$ and $v_r(r,x)$ respectively, and $p_p = p_p(r,x)$ denotes the in-tube hydrostatic pressure, where x denotes the distance along the length of the phloem tube and r the radial position within the phloem. Considering the dynamics at steady state, the flow of phloem sap is described by the following Navier-Stokes equations (3.1) and incompressibility condition (3.2),

$$\rho\left(v_r\frac{\partial v_x}{\partial r} + v_x\frac{\partial v_x}{\partial x}\right) = -\frac{\partial p_p}{\partial x} + \eta\left(\frac{1}{r}\frac{\partial}{\partial r}\left(r\frac{\partial v_x}{\partial r}\right) + \frac{\partial^2 v_x}{\partial x^2}\right) \tag{3.1a}$$

$$\rho\left(v_r\frac{\partial v_r}{\partial r} + v_x\frac{\partial v_r}{\partial x}\right) = -\frac{\partial p_p}{\partial r} + \eta\left(\frac{1}{r}\frac{\partial}{\partial r}\left(r\frac{\partial v_r}{\partial r}\right) + \frac{\partial^2 v_r}{\partial x^2} - \frac{v_r}{r^2}\right) \tag{3.1b}$$

$$\frac{1}{r}\frac{\partial}{\partial r}\left(rv_r\right) + \frac{\partial v_x}{\partial x} = 0 \tag{3.2}$$

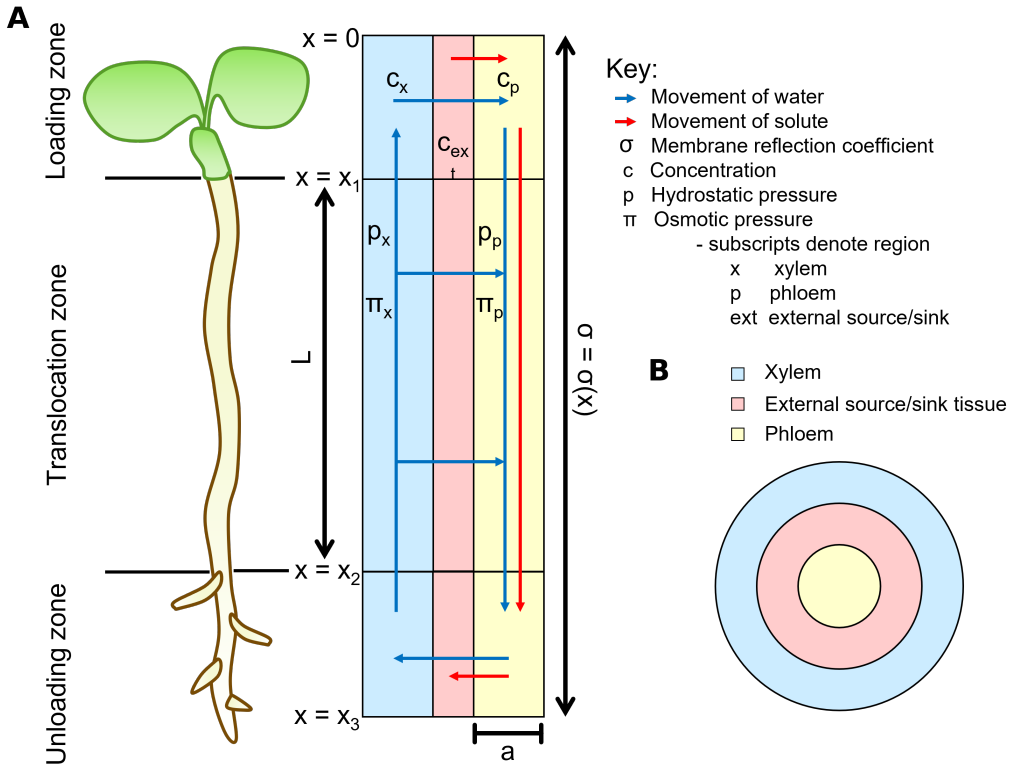


Figure 3.1: Schematic showing the modelling structure. The phloem is considered a long thin pipe split into three zones (loading, translocation, unloading). Water is considered to be transferred directly from xylem to phloem (and the xylem contains no solute), whereas the solute is transferred to/from and external tissue source/sink (which may have a solute concentration).

where η is the viscosity of the sap, ρ is the phloem sap density, and gravitational effects are assumed negligible (Jensen et al., 2016, Thompson and Holbrook, 2003).

We begin by considering only one solute, sugar, as this is the most common solute in phloem sap. The concentration of sugar in the phloem, $c_p(r,x)$, is given by the steady-state advection-diffusion equation,

$$\nabla \cdot (v c_p) = D\nabla^2 c_p, \tag{3.3}$$

where D is the diffusivity coefficient of sugar. Alongside this, we define the concentration of sugar outside the phloem tube in the xylem as c_x and the pressure outside the phloem tube in the xylem as p_x, where c_x and p_x are constants. We also note that the concentration of sugar external to the phloem in the source/sink tissues is denoted c_{ext}.

We assume the following boundary conditions on the phloem sap velocity,

$$v_r(0,x) = 0, \qquad \text{(symmetry about the centre-line)} \tag{3.4a}$$

$$\frac{\partial}{\partial r} v_x(0,x) = 0, \qquad \text{(symmetry about the centre-line)} \tag{3.4b}$$

$$v_x(a,x) = 0. \qquad \text{(no slip condition at } r = a\text{)} \tag{3.4c}$$

We model the end points of the phloem tube to be impermeable to water. This yields the following additional boundary conditions,

$$v_x(r,0) = 0, \qquad \text{no axial flow at left end point} \tag{3.5a}$$

$$v_x(r,x_3) = 0. \qquad \text{no axial flow at right end point} \tag{3.5b}$$

The radial velocity at $r = a$ will be equal to the velocity of water moving across the membrane (from the xylem into the phloem),

$$v_r(a,x) = -v_{mem}(x), \quad \text{(radial velocity at } r = a \text{ equal to velocity across membrane)} \tag{3.6}$$

where $v_{mem}(x)$ is the velocity of water at the membrane.

3.2.2 Velocity of water at the membrane

To finish specifying the velocity boundary conditions for phloem transport, we need to define the velocity of the water at the membrane, $v_{mem}(x)$. To do this, we consider the Starling forces acting on the phloem (Starling, 1896, Blaustein et al., 2011).

From Figure 3.2, we consider the forces acting on the phloem sap at the membrane of the phloem with the xylem. The xylem hydrostatic pressure, p_x, and phloem

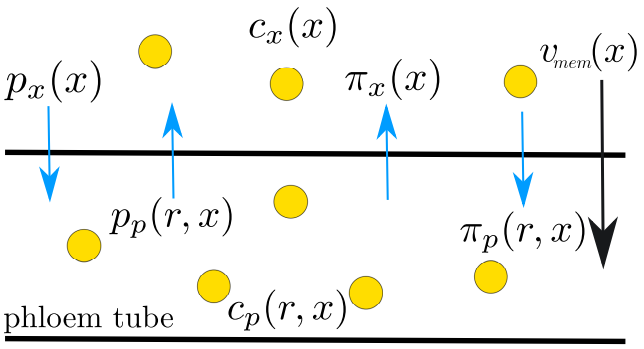


Figure 3.2: Figure showing the Starling forces acting along a phloem tube. Yellow circles represent solute particles and blue arrows indicate the direction of water movement across the membrane driven by the corresponding hydrostatic or osmotic pressure.

osmotic pressure, π_p, drive the movement of water into the phloem (from the xylem). The phloem hydrostatic pressure, p_p, and xylem osmotic pressure, π_x, drive the movement of water out of the phloem (into the xylem). The velocity of the water moving across the membrane from the xylem into the phloem, v_{mem}, is then given by:

$$v_{mem} = L_p\big((p_x - p_p) - \sigma(\pi_x - \pi_p)\big) \tag{3.7}$$

where L_p is the membrane water permeability and $\sigma = \sigma(x)$ is the Staverman reflection coefficient (Staverman, 1951, Truskey et al., 2004). The Staverman reflection coefficient varies between zero and one, where $\sigma = 1$ represents a perfectly semi-permeable membrane, permeable only to water, and $\sigma = 0$ represents a membrane that is permeable to both water and sugar equally. Values in between zero and one represent membranes that are semi-permeable but with some leakage of sugar along with the water (Truskey et al., 2004).

Phloem sap is comprised of solutes dissolved in water (Nobel, 2020). As such, we can apply the van't Hoff equation for dilute concentrations (Truskey et al., 2004) which enables us to relate osmotic potentials to sugar concentrations,

$$\pi_p = RTc_p(r,x), \qquad \pi_x = RTc_x, \tag{3.8}$$

where R is the ideal gas constant and T is the absolute temperature. Hence, the velocity of the water, v_{mem}, at the membrane is given by,

$$v_{mem}(x) = L_p\big((p_x - p_p) - \sigma RT(c_x - c_p)\big). \tag{3.9}$$

We can see that the water flow across the membrane depends on the local difference

in concentration and hydrostatic pressure across the membrane (Jensen et al., 2011). Equation (3.9) can be substituted into equation (3.6) to fully define the velocity boundary condition at the membrane.

3.2.3 Solute flux at the boundary

At the membrane, we require a final boundary condition that describes the flux of the solute at the membrane. For this we need to introduce the concentration of sugar in the external source/sink tissues, $c_{ext}(x)$. We define the flux of solute from the phloem to the surrounding tissues, J_s, by

$$J_s = J_v(1-\sigma)\bar{c} + \beta^*(c_p - c_{ext}) - \gamma^* c_p + \lambda^* c_{ext}, \tag{3.10}$$

where J_v is the fluid velocity across the membrane (in this case $J_v = -v_{mem}$), $\bar{c}$ is the average concentration inside the membrane (given by $\bar{c} = {}^{(c_{ext}+c_p)}/_2$, β^* is the rate of solute diffusion across the membrane (Truskey et al., 2004), γ^* is the rate of active loading, and λ^* is the rate of active unloading. The first term on the right-hand-side of equation (3.10) represents solute being dragged across the phloem membrane with the flow of water, whereas the second term represents passive diffusion through the phloem-tissue membrane. These two terms form the solute flux equation of Kedem and Katchalsky (1958). The final two terms in (3.10) represent active transport of solute into and out of the phloem. The equation for solute flux, (3.10), varies from previous phloem models as they assumed the membrane of the phloem was perfectly semi-permeable ($\sigma = 1$) (Jensen et al., 2012, Payvandi et al., 2014, Jensen et al., 2016). Furthermore, by formulating the solute flux, (3.10), in terms of passive and active components that depend on the external concentrations, the model parameters relate directly to biological processes that can be perturbed experimentally and can vary in response to environmental conditions.

To define the boundary condition, we equate the outward normal solute flux at the boundary of the phloem model to the flux of the solute across the membrane (Figure 3.3).

Thus, the solute flux boundary condition is given by,

$$c_p(a,x)v_r(a,x) - D\frac{\partial c_p}{\partial r}\bigg|_{(a,x)} = J_s$$

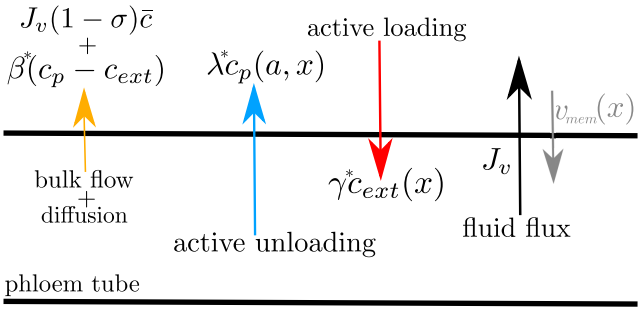


Figure 3.3: Diagram showing the components that affect the outward solute flux at the membrane boundary.

which yields, upon substitution of J_s, (3.10),

$$D\frac{\partial c_p}{\partial r}\bigg|_{(a,x)} = c_p(a,x)v_r(a,x) - (1-\sigma)\bar{c}v_r(a,x) + \beta^*(c_{ext}(x) - c_p(a,x)) + \gamma^* c_{ext}(x) - \lambda^* c_p(a,x). \tag{3.11}$$

We note that $\beta^*, \gamma^*, \lambda^* \geq 0$ and $0 \leq \sigma \leq 1$. This general boundary condition allows us to represent various forms of phloem loading, unloading, and membrane transport. For example, in the translocation zone of the phloem (where no loading or unloading occurs) we set $\beta^* = \gamma^* = \lambda^* = 0$ and $\sigma = 1$ to represent the case where the phloem tube walls are semi-permeable membranes (impermeable to sugar) and we have no flux of sugars at the membrane.

3.2.4 Non-dimensionalisation

We non-dimensionalise the system with the scales,

$$x = LX, \qquad r = aR, \qquad v_x = UV_x,$$
$$v_r = \varepsilon U V_r, \qquad p_p = \frac{\eta L U}{a^2} P_p, \qquad \varepsilon = \frac{a}{L},$$
$$c_p = C^* C_p, \qquad Re = \frac{\rho U L}{\eta}, \qquad Pe = \frac{UL}{D},$$

where U is a characteristic flow speed of the phloem sap in the x-direction (Jensen et al., 2016), C^* is the external concentration of sugar at $x = 0$, Re is the Reynolds' number, and Pe is the Péclet number. Substituting these scales into the governing equations, (3.1) – (3.3), we obtain,

$$\frac{1}{R}\frac{\partial}{\partial R}\left(RV_r\right) + \frac{\partial V_x}{\partial X} = 0, \tag{3.12}$$

$$\varepsilon^2 Re\left(V_r\frac{\partial V_x}{\partial R}+V_x\frac{\partial V_x}{\partial X}\right)=-\frac{\partial P_p}{\partial X}+\frac{1}{R}\frac{\partial}{\partial R}\left(R\frac{\partial V_x}{\partial R}\right)+\varepsilon^2\frac{\partial^2 V_x}{\partial X^2}, \tag{3.13a}$$

$$\varepsilon^4 Re\left(V_r\frac{\partial V_r}{\partial R}+V_x\frac{\partial V_r}{\partial X}\right)=-\frac{\partial P_p}{\partial R}+\varepsilon^2\left(\frac{1}{R}\frac{\partial}{\partial R}\left(R\frac{\partial V_r}{\partial R}\right)+\varepsilon^2\frac{\partial^2 V_r}{\partial X^2}-\frac{V_r}{R^2}\right), \tag{3.13b}$$

$$\varepsilon^2 Pe\left(V_r\frac{\partial C_p}{\partial R}+V_x\frac{\partial C_p}{\partial X}+\frac{C_p}{R}\frac{\partial}{\partial R}(RV_r)+C_p\frac{\partial V_x}{\partial X}\right)=\frac{1}{R}\frac{\partial}{\partial R}\left(R\frac{\partial C_p}{\partial R}\right)+\varepsilon^2\frac{\partial^2 C_p}{\partial X^2}. \tag{3.13c}$$

with the nondimensionalised boundary conditions, (3.4), (3.6), and (3.11),

$$V_r(0,X)=0, \tag{3.14a}$$

$$\left.\frac{\partial V_x}{\partial R}\right|_{(0,X)}=0, \tag{3.14b}$$

$$V_x(1,X)=0, \tag{3.14c}$$

$$V_x(R,0)=0, \tag{3.14d}$$

$$V_x(R,X_3)=0, \tag{3.14e}$$

$$V_r(1,X)=-\mathscr{V}(X), \tag{3.14f}$$

$$\left.\frac{\partial C_p}{\partial R}\right|_{(1,X)}=Pe\big[C_p(1,X)V_r(1,X)-(1-\sigma)\bar{C}V_r(1,X)+\beta(C_{ext}(X)-C_p(1,X)) +\gamma C_{ext}(X)-\lambda C_p(1,X)\big], \tag{3.14g}$$

where $X_3=x_3/L$, $\beta^*=\varepsilon U\beta$, $\gamma^*=\varepsilon U\gamma$, $\lambda^*=\varepsilon U\lambda$, $c_{ext}(x)=C^*C_{ext}(X)$, $\bar{c}=C^*\bar{C}$, and $v_{mem}(x)=\varepsilon U\mathscr{V}(X)$.

In the limit of a long narrow tube, with $a\ll L$, we have $\varepsilon\ll 1$. Hence, we can consider the expansions,

$$V_r(R,X)=V_{r,0}(R,X)+\varepsilon^2V_{r,1}(R,X)+\varepsilon^4V_{r,2}(R,X)+..., \tag{3.15a}$$

$$V_x(R,X)=V_{x,0}(R,X)+\varepsilon^2V_{x,1}(R,X)+\varepsilon^4V_{x,2}(R,X)+..., \tag{3.15b}$$

$$C_p(R,X)=C_0(R,X)+\varepsilon^2C_1(R,X)+\varepsilon^4C_2(R,X)+..., \tag{3.15c}$$

$$P_p(R,X)=P_0(R,X)+\varepsilon^2P_1(R,X)+\varepsilon^4P_2(R,X)+.... \tag{3.15d}$$

We also take $\varepsilon^2 Re\ll 1$ and $\varepsilon^2 Pe\ll 1$. Thus, we can substitute these expansions into

equations (3.13) to obtain the following leading-order equations,

$$\frac{1}{R}\frac{\partial}{\partial R}(RV_{r,0}) + \frac{\partial V_{x,0}}{\partial X} = 0 \tag{3.16a}$$

$$\frac{\partial P_0}{\partial X} = \frac{1}{R}\frac{\partial}{\partial R}\left(R\frac{\partial V_{x,0}}{\partial R}\right), \tag{3.16b}$$

$$\frac{\partial P_0}{\partial R} = 0, \tag{3.16c}$$

$$\frac{1}{R}\frac{\partial}{\partial R}\left(R\frac{\partial C_0}{\partial R}\right) = 0. \tag{3.16d}$$

Note that this form of Stoke's flow is called the lubrication equations. In order to understand the dynamics governing concentration, we require an additional equation for C. Hence, we consider the $O(\varepsilon^2)$ equation,

$$Pe\left(V_{r,0}\frac{\partial C_0}{\partial R} + V_{x,0}\frac{\partial C_0}{\partial X} + \frac{C_0}{R}\frac{\partial}{\partial R}(RV_{r,0}) + C_0\frac{\partial V_{x,0}}{\partial X}\right) = \frac{1}{R}\frac{\partial}{\partial R}\left(R\frac{\partial C_1}{\partial R}\right) + \frac{\partial^2 C_0}{\partial X^2}. \tag{3.17}$$

The leading-order boundary conditions are given by,

$$V_{r,0}(0,X) = 0, \tag{3.18a}$$

$$\left.\frac{\partial V_{x,0}}{\partial R}\right|_{(0,X)} = 0, \tag{3.18b}$$

$$V_{x,0}(1,X) = 0, \tag{3.18c}$$

$$V_{x,0}(R,0) = 0, \tag{3.18d}$$

$$V_{x,0}(R,X_3) = 0, \tag{3.18e}$$

$$V_{r,0}(1,X) = -\mathscr{V}(X), \tag{3.18f}$$

$$\begin{aligned}\left.\frac{\partial C_1}{\partial R}\right|_{(1,X)} &= Pe\big[C_0(X)V_{r,0}(1,X) - (1-\sigma)\bar{C}V_{r,0}(1,X) + \beta(C_{ext}(X) - C_0(X)) \\ &\quad + \gamma C_{ext}(X) - \lambda C_0(X)\big].\end{aligned} \tag{3.18g}$$

By substituting the nondimensional scales into (3.9), we obtain the nondimensional velocity across the membrane,

$$\mathscr{V}(X) = \frac{L_p}{\varepsilon U}\Big(\frac{\eta LU}{a^2}(P_x(X) - P_p(R,X)) - \sigma RTC^*(C_x(X) - C_p(R,X))\Big). \tag{3.19}$$

Using expansions (3.15c) and (3.15d), we obtain the membrane velocity at leading order as,

$$\mathscr{V}_0(X) = \frac{L_p}{\varepsilon U}\Big(\frac{\eta LU}{a^2}(P_x(X) - P_0(X)) - \sigma RTC^*(C_x(X) - C_0(X))\Big), \tag{3.20}$$

where $\mathscr{V}_0$ is the leading-order component of $\mathscr{V}$ as $\varepsilon \to 0$. This tells us that ${}^{L_p\sigma RTC^*}/_{U}$ and ${}^{\eta L_p L^2}/_{a^3} = O(\varepsilon)$. We note that the dimensionless scales can be related to each other via the following equations,

$$RTC^* = P^*, \qquad U = \frac{2L}{a} L_p P^*,$$

(Jensen et al., 2016), where L is the system length-scale, L_p is the membrane water permeability, C^* is the external sugar concentration at $X = 0$, and P^* is the scale parameter for osmotic pressure. This yields,

$$\mathscr{V}_0(X) = \frac{1}{2}\left(\frac{\text{Mü}}{8}(P_x(X) - P_0(X)) - \sigma(C_x(X) - C_0(X))\right), \tag{3.21}$$

where Mü$= {}^{16\eta L_p L^2}/_{a^3}$ is called the Münch number.

3.2.5 Integrating with respect to R

We can reduce the system complexity by integrating the governing equations (3.16) and (3.17) with respect to R. Equations (3.16c) and (3.16d) reveal that, at leading order, pressure and concentration are functions of X only (i.e. $C_0(R,X) = C_0(X)$ and $P_0(R,X) = P_0(X)$).

The LHS of equation (3.16b) is a function of X only, hence, upon integrating with respect to R, we obtain,

$$V_{x,0}(R,X) = \frac{R^2}{4}\frac{\partial P_0}{\partial X} + A\log(R) + B. \tag{3.22}$$

Since the solution must be bounded as $R \to 0$ we know that $A = 0$ (from boundary condition (3.18b)) Applying boundary condition (3.18c), we obtain $B = -\frac{1}{4}\frac{\partial P_0}{\partial X}$. This yields,

$$V_{x,0}(R,X) = \frac{(R^2-1)}{4}\frac{\partial P_0}{\partial X}. \tag{3.23}$$

Next, we integrate the incompressibility condition (3.16a) with respect to R to obtain,

$$V_{r,0}(R,X) + \frac{\partial^2 P_0}{\partial X^2}\frac{(R^3-2R)}{16} + \frac{A}{R} = 0. \tag{3.24}$$

Applying boundary condition (3.18a) tells us that A = 0 (as $V_{r,0}$ is bounded as $R \to 0$). Hence,

$$V_{r,0}(R,X) + \frac{\partial^2 P_0}{\partial X^2}\frac{(R^3-2R)}{16} = 0. \tag{3.25}$$

We can then apply the boundary condition $V_{r,0}(1,X) = -\mathscr{V}_0(X)$, which tells us that,

$$\frac{\partial^2 P_0}{\partial X^2} = 16\mathscr{V}_0(X). \tag{3.26}$$

We integrate the concentration equation (3.17) with respect to R, to obtain,

$$\begin{aligned}
Pe\Bigg[\frac{\partial C_0}{\partial X}\int RV_{x,0}dR + C_0\int\frac{\partial}{\partial R}(RV_{r,0})dR \\
+ C_0\frac{\partial}{\partial X}\int RV_{x,0}dR\Bigg] = R\frac{\partial C_1}{\partial R} + \frac{R^2}{2}\frac{\partial^2 C_0}{\partial X^2}, \\
Pe\Bigg[\frac{\partial C_0}{\partial X}\int\frac{\partial P_0}{\partial X}\frac{R^3-2R}{4}dR + C_0\int\frac{\partial}{\partial R}(RV_{r,0})dR \\
+ C_0\frac{\partial}{\partial X}\int\frac{\partial P_0}{\partial X}\frac{R^3-2R}{4}dR\Bigg] = R\frac{\partial C_1}{\partial R} + \frac{R^2}{2}\frac{\partial^2 C_0}{\partial X^2}, \\
Pe\Bigg[\Big(\frac{\partial C_0}{\partial X}\frac{\partial P_0}{\partial X} + C_0\frac{\partial^2 P_0}{\partial X^2}\Big)\Big(\int\frac{R^3-2R}{4}dR\Big) \\
+ RC_0V_{r,0}\Bigg] = R\frac{\partial C_1}{\partial R} + \frac{R^2}{2}\frac{\partial^2 C_0}{\partial X^2}, \\
Pe\Bigg[\Big(\frac{\partial C_0}{\partial X}\frac{\partial P_0}{\partial X} + C_0\frac{\partial^2 P_0}{\partial X^2}\Big)\Big(\frac{R^4-2R^2}{16}\Big) \\
+ RC_0V_{r,0}\Bigg] = R\frac{\partial C_1}{\partial R} + \frac{R^2}{2}\frac{\partial^2 C_0}{\partial X^2} + A,
\end{aligned} \tag{3.27}$$

where A is a constant. Evaluating at $R = 0$, we obtain that $A = 0$. Evaluating at $R = 1$ and applying boundary conditions (3.18f) and (3.18g) yields,

$$\begin{aligned}
-\frac{1}{16}\Big(\frac{\partial C_0}{\partial X}\frac{\partial P_0}{\partial X} + C_0\frac{\partial^2 P_0}{\partial X^2}\Big) = (1-\sigma)\bar{C}\mathscr{V}_0(X) + \beta(C_{ext}(X) - C_0(X)) \\
+ \gamma C_{ext}(X) - \lambda C_0(X) + \frac{1}{2}\frac{\partial^2 C_0}{\partial X^2}.
\end{aligned} \tag{3.28}$$

To reduce to a one-dimensional system, we write the governing equations in terms of the average axial flow speed, given by $\bar{U}(X) = Q(X)/\pi$ where $Q(X)$ is the volumetric flow rate:

$$\bar{U}(X) = \frac{Q(X)}{\pi} = \int_0^1 2RV_{x,0}(R,X)dR = -\frac{1}{8}\frac{\partial P_0}{\partial X}. \tag{3.29}$$

Substituting $\partial P_0/\partial X$, (3.29), and $\mathscr{V}_0$, (3.21) into equations (3.26) and (3.28) we obtain,

$$\frac{\partial \bar{U}}{\partial X} = \sigma(C_0(X) - C_x(X)) - \frac{\text{Mü}}{8}(P_0(X) - P_x(X)), \tag{3.30a}$$

$$\frac{\partial \bar{U}C_0}{\partial X} = \frac{1}{Pe}\frac{\partial^2 C_0}{\partial X^2} + (1-\sigma)\bar{C}\Big(\sigma\Big(C_0(X) - C_x(X)\Big) - \frac{\text{Mü}}{8}\Big(P_0(X) - P_x(X)\Big)\Big) + 2\beta(C_{ext}(X) - C_0(X)) + 2\gamma C_{ext}(X) - 2\lambda C_0(X) \tag{3.30b}$$

$$\frac{\partial P_0}{\partial X} = -8\bar{U}(X), \tag{3.30c}$$

Hence, we have reduced the governing equations to a 1-D system of equations. Alongside these equations we have two remaining boundary conditions for X. These boundary conditions are (3.18d) and (3.18e) which can be simplified to give boundary conditions for $\bar{U}$,

$$\bar{U}(0) = 0, \tag{3.31a}$$

$$\bar{U}(X_3) = 0. \tag{3.31b}$$

3.2.6 Deriving the Münch flow equations

In existing mathematical models for Münch pressure flow, the Staverman reflection coefficient is assumed to be equal to one everywhere. This assumption allows the governing equation for pressure to be uncoupled from the rest of the system. Whilst pressure cannot be uncoupled from the system of equations when the Staverman reflection coefficient doesn't equal one, we still differentiate equation (3.30a) with respect to X to obtain,

$$\frac{\partial^2 \bar{U}}{\partial X^2} = \sigma\left(\frac{\partial C_0}{\partial X} - \frac{\partial C_x}{\partial X}\right) + \frac{\partial \sigma}{\partial x}\left(C_0 - C_x\right) + \text{Mü}\left(\bar{U} + \frac{1}{8}\frac{\partial P_x}{\partial X}\right), \tag{3.32}$$

so that when the Staverman reflection coefficient does equal one everywhere, the pressure equation can easily be uncoupled.

Hence, we have derived the 1D Münch flow equations that describe phloem sap velocity and sugar concentration levels along the longest axis of the phloem. These

are given by,

$$\frac{\partial^2 \bar{U}}{\partial X^2} = \sigma\left(\frac{\partial C_0}{\partial X} - \frac{\partial C_x}{\partial X}\right) + \frac{\partial \sigma}{\partial x}\left(C_0 - C_x\right) + \text{Mü}\left(\bar{U} + \frac{1}{8}\frac{\partial P_x}{\partial X}\right), \tag{3.33a}$$

$$\frac{\partial \bar{U} C_0}{\partial X} = \frac{1}{Pe}\frac{\partial^2 C_0}{\partial X^2} + (1-\sigma)\bar{C}\Big(\sigma\Big(C_0(X) - C_x(X)\Big) - \frac{\text{Mü}}{8}\Big(P_0(X) - P_x(X)\Big)\Big) + 2\beta(C_{ext}(X) - C_0(X)) + 2\gamma C_{ext}(X) - 2\lambda C_0(X), \tag{3.33b}$$

$$\frac{\partial P_0}{\partial X} = -8\bar{U}(X), \tag{3.33c}$$

with boundary conditions,

$$\bar{U}(0) = 0, \tag{3.34a}$$

$$\bar{U}(X_3) = 0. \tag{3.34b}$$

3.3 Modelling hormone transport in the phloem

Equations (3.33) describe a single solute (sugar) being transported through the phloem. It has been shown that hormones are transported by the phloem (see Baker (2000b) for a review and references within) and we now extend the equations to incorporate a hormone (or other passively advected solute). Hormone molecules are tiny compared to sugar molecules, and so it is appropriate to assume that the hormone concentration does not contribute significantly to the osmotic pressure gradient.

3.3.1 Stokes-Einstein calculations for plant hormone diffusion coefficients

We now investigate the timescales for diffusion, advection, and growth, as well as the Péclet number, for a range of hormones and sugar. In order to do this we require a range of parameters including $D_s = 5.0 \times 10^{-10}\text{m}^2\text{s}^{-1}$ the diffusivity coefficient of sugar (Gosting and Morris, 1949), $U = 23\mu\text{ms}^{-1}$ the sap flow speed (Ross-Elliott et al., 2017), $RER = 3.6 \times 10^{-4}\text{mh}^{-1}$ the root elongation rate for Arabidopsis, $L = 30.6\text{mm}$ the primary root length of an Arabidopsis seedling 7DAG (Martin et al., 2002), and the diffusivity coefficients for a range of hormones.

The diffusivity coefficients for some hormones are not readily available in the literature. As such, we calculate their diffusivity coefficients using the Stokes-

Einsten equation (Truskey et al., 2004),

$$D_a = \frac{k_B T}{6\pi\mu}\left(\frac{4\pi N_A}{3\bar{v}M}\right)^{\frac{1}{3}}, \tag{3.35}$$

where D_a is the diffusion coefficient of the hormone to be determined, k_B is the Boltzmann constant, T is the absolute temperature, μ is viscosity of water, N_A is Avogadro's constant, $\bar{v}$ is the specific volume of the hormone (given by the inverse of its density), and M is the molecular weight of the hormone. Table 3.1 shows the diffusivity coefficient for the hormones we consider. Table 3.2 gives the values used in these calculations and their corresponding references.

Hormone	**Diffusion coefficient ($m^2 \cdot s^{-1}$)**
Auxin	6.7×10^{-10} (Kramer and Went, 1949)
Cytokinin	6.2×10^{-10}
Brassinosteriods	4.4×10^{-10}
Giberellin	5.4×10^{-10}

Table 3.1: Diffusivity coefficients for a range of plant hormones calculated using the Stokes-Einstein equation.

From Table 3.3, we see that the Péclet number is large for both hormones and sugar. Therefore, we assume, in line with models in the literature (Jensen et al., 2012, 2016), that diffusion is negligible. The timescale of growth is also much slower than transport timescales, this justifies our use of the steady-state equations.

3.3.2 Hormone transport equations

Due to the Péclet number for sugar and a range of plant hormones being large (see Table 3.3), we neglect diffusion terms and hence the equations governing the

Parameter	Value	Unit	Reference
k_B	1.38×10^{-23}	kg m^2 s^{-2} K^{-1}	Boltzmann constant
T	298.15	K	(Truskey et al., 2004)
N_A	6.02×10^{23}	mol^{-1}	Avogadro's constant
μ	0.89×10^{-3}	kg m^{-1} s^{-1}	(Korson et al., 1969)
$\bar{v}$ (Cytokinin)	0.714×10^{-3}	kg m^{-3}	(ChemSpider, Royal Society of Chemistry, 2021b)
$\bar{v}$ (Brassinosteriods)	0.909×10^{-3}	kg m^{-3}	(ChemSpider, Royal Society of Chemistry, 2021a)
$\bar{v}$ (Giberellin)	0.667×10^{-3}	kg m^{-3}	(ChemSpider, Royal Society of Chemistry, 2021c)
M (Cytokinin)	219.1×10^{-3}	kg mol^{-1}	(ChemSpider, Royal Society of Chemistry, 2021b)
M (Brassinosteriods)	480.3×10^{-3}	kg mol^{-1}	(ChemSpider, Royal Society of Chemistry, 2021a)
M (Giberellin)	346.1×10^{-3}	kg mol^{-1}	(ChemSpider, Royal Society of Chemistry, 2021c)

Table 3.2: Parameter values used in the calculation of plant hormone diffusivity coefficients using the Stokes-Einstein equation.

Timescale	Formula	Value
Diffusion of sugar	L^2/D_s	520 h
Diffusion of auxin	L^2/D_a	388 h
Diffusion of cytokinin	L^2/D_a	420 h
Diffusion of brassinosteriods	L^2/D_a	591 h
Diffusion of giberellin	L^2/D_a	482 h
Advection	$L/\bar{u}$	0.37 h
Growth	L/RER	85 h
$\mathrm{Pe}_{\mathrm{sugar}}$	$L\bar{u}/D_s$	1408
$\mathrm{Pe}_{\mathrm{auxin}}$	$L\bar{u}/D_a$	1050
$\mathrm{Pe}_{\mathrm{cytokinin}}$	$L\bar{u}/D_a$	1135
$\mathrm{Pe}_{\mathrm{brassinosteriods}}$	$L\bar{u}/D_a$	1600
$\mathrm{Pe}_{\mathrm{giberellin}}$	$L\bar{u}/D_a$	1303

Table 3.3: Timescales of key transport processes and Peclet numbers.

transport of hormone and sugar via the phloem are given by,

$$\frac{\partial^2 \bar{U}}{\partial X^2} = \sigma_s\Big(\frac{\partial C_s}{\partial X} - \frac{\partial C_{x,s}}{\partial X}\Big) + \frac{\partial \sigma_s}{\partial X}\Big(C_s - C_{x,s}\Big) + \text{Mü}\Big(\bar{U} + \frac{1}{8}\frac{\partial P_x}{\partial X}\Big) \tag{3.36a}$$

$$\begin{aligned}\frac{\partial \bar{U} C_s}{\partial X} = (1-\sigma_s)\bar{C}_s\Big(\sigma_s(C_s(X) - C_{x,s}(X)) - \frac{\text{Mü}}{8}(P(X) - P_x(X))\Big) \\ + 2\beta_s(C_{ext,s}(X) - C_s(X)) + 2\gamma_s C_{ext,s}(X) - 2\lambda_s C_s(X),\end{aligned} \tag{3.36b}$$

$$\begin{aligned}\frac{\partial \bar{U} C_a}{\partial X} = (1-\sigma_a)\bar{C}_a\Big(\sigma_s(C_s(X) - C_{x,s}(X)) - \frac{\text{Mü}}{8}(P(X) - P_x(X))\Big) \\ + 2\beta_a(C_{ext,a}(X) - C_a(X)) + 2\gamma_a C_{ext,a}(X) - 2\lambda_a C_a(X),\end{aligned} \tag{3.36c}$$

$$\frac{\partial P}{\partial X} = -8\bar{U}(X), \tag{3.36d}$$

where,

$$\bar{C}_s = \frac{C_s + C_{ext,s}}{2}, \tag{3.37a}$$

$$\bar{C}_a = \frac{C_a + C_{ext,a}}{2} \tag{3.37b}$$

The boundary conditions for $\bar{U}$ are given by,

$$\bar{U}(0) = 0, \tag{3.38a}$$

$$\bar{U}(X_3) = 0. \tag{3.38b}$$

3.3.2.1 Additional boundary conditions

In order to close the system of equations, we require three additional boundary conditions, $C_s(0), C_a(0)$, and $P(0)$. Expanding the left-hand-side of equation (3.36b) and rearranging for $^{\partial C_s}/_{\partial X}$, we see that there is a singularity at $X = 0$ as $\bar{U}(0) = 0$,

$$\begin{aligned}\frac{\partial C_s}{\partial X}(0) = \Bigg[(1-\sigma_s(0))\bar{C}_s(0)\Big(\sigma_s(0)(C_s(0) - C_{x,s}(0)) - \frac{\text{Mü}}{8}(P(0) - P_x(0))\Big) \\ + 2(\beta_s + \gamma_s) - 2(\beta_s + \lambda_s) - C_s(0)\frac{\partial \bar{U}(0)}{\partial X}\Bigg] \Bigg/ \bar{U}(0)\end{aligned} \tag{3.39}$$

Hence, to avoid the rate of change of concentration diverging, we require,

$$(1-\sigma_s(0))\bar{C}_s(0)\Big(\sigma_s(0)(C_s(0)-C_{x,s}(0))-\frac{\text{Mü}}{8}(P(0)-P_x(0))\Big) \\ +2(\beta_s+\gamma_s)-2(\beta_s+\lambda_s)-C_s(0)\frac{\partial\bar{U}(0)}{\partial X}=0. \tag{3.40}$$

Upon substitution of $\bar{C}_s(0)$, this yields a quadratic equation for the concentration of sugar at $X=0$, $C_s(0)$.

Alongside this, we require a boundary condition for pressure at $X=0$. We substitute (3.36d) into (3.36a) and integrate with respect to X to obtain,

$$\frac{\partial\bar{U}}{\partial X}=\sigma_s(C_s-C_{x,s})-\frac{\text{Mü}}{8}(P-P_x). \tag{3.41}$$

Evaluating at $X=0$, we can rearrange for $P(0)$, which gives,

$$P(0)=\frac{8}{\text{Mü}}\left(\sigma_s(0)(C_s(0)-C_{x,s})-\frac{\partial\bar{U}}{\partial X}(0)\right)+P_x. \tag{3.42}$$

Substituting $P(0)$ into equation (3.40), we obtain,

$$C_s(0)=\frac{\Big(\frac{1-\sigma_s(0)}{2}\frac{\partial\bar{U}}{\partial X}(0)+2(\beta_s+\gamma_s)\Big)C_{ext,s}}{\Big(1-\frac{1-\sigma_s(0)}{2}\Big)\frac{\partial\bar{U}}{\partial X}(0)+2(\beta_s+\lambda_s)} \tag{3.43}$$

Using the same approach, we obtain $C_a(0)$,

$$C_a(0)=\frac{\Big(\frac{1-\sigma_a(0)}{2}\frac{\partial\bar{U}}{\partial X}(0)+2(\beta_a+\gamma_a)\Big)C_{ext,a}}{\Big(1-\frac{1-\sigma_a(0)}{2}\Big)\frac{\partial\bar{U}}{\partial X}(0)+2(\beta_a+\lambda_a)} \tag{3.44}$$

Thus, we have obtained the boundary conditions for $C_s(0)$, $C_a(0)$, and $P(0)$ in terms of ${}^{\partial\bar{U}}/_{\partial X}(0)$.

3.3.2.2 Representing the loading and unloading zones

We define the spatially dependent coefficients of solute transport and external solute concentrations as step functions between zones (loading=1, translocation=2, unloading=3). In the functions below X_1, X_2, X_3 represent the end points of the loading, translocation, and unloading zone respectively with $X_1=0.2, X_2=1.2$, and $X_3=1.4$

for consistency with loading and unloading zones prescribed in Jensen et al. (2012):

$$\mathscr{B}_k(X) = \begin{cases} \mathscr{B}_{k,1}, & 0 \leq X \leq X_1; \\ \mathscr{B}_{k,2}, & X_1 < X < X_2; \\ \mathscr{B}_{k,3}, & X_2 \leq X \leq X_3, \end{cases} \tag{3.45}$$

Here, $\mathscr{B}_k$ is used represent a general parameter where $\mathscr{B} \in \{\sigma, \beta, \gamma, \lambda, C_{ext}\}$ and the subscript $k \in \{s, a\}$ denotes sugar and hormone respectively.

Model solutions enable us to calculate the total flux of sugar and hormone into the loading zone and out of the unloading zone by integrating equations (3.36b) and (3.36c) with respect to X across the length of the loading and unloading zone respectively,

$$\begin{aligned} F_s(l_1, l_2) &= \int_{l_1}^{l_2} \frac{\partial U C_s}{\partial X} dX \\ &= \int_{l_1}^{l_2} \Big[(1-\sigma_s)\bar{C}_s \Big(\sigma_s (C_s(X) - C_{x,s}(X)) - \frac{\text{Mü}}{8} (P(X) - P_x(X)) \Big) \\ &\quad + 2\beta_s (C_{ext,s}(X) - C_s(X)) + 2\gamma_s C_{ext,s}(X) - 2\lambda_s C_s(X) \Big] dX, \end{aligned} \tag{3.46a}$$

$$\begin{aligned} F_a(l_1, l_2) &= \int_{l_1}^{l_2} \frac{\partial U C_a}{\partial X} dX \\ &= \int_{l_1}^{l_2} \Big[(1-\sigma_a)\bar{C}_s \Big(\sigma_s (C_s(X) - C_{x,s}(X)) - \frac{\text{Mü}}{8} (P(X) - P_x(X)) \Big) \\ &\quad + 2\beta_a (C_{ext,a}(X) - C_a(X)) + 2\gamma_a C_{ext,a}(X) - 2\lambda_a C_a(X) \Big] dX, \end{aligned} \tag{3.46b}$$

where $l_1 = 0$ and $l_2 = X_1$ defines the loading zone and $l_1 = X_2$ and $l_2 = X_3$ defines the unloading zone. Equations (3.46) are defined in terms of fluxes into the phloem and so unloading results in a negative value.

3.4 Analytical solutions to transport equations

3.4.1 Model zonation

In this section, we seek to derive a set of analytical solutions to the governing equations under the specific conditions that the membrane walls are semi-permeable

($\sigma_s = \sigma_a = 1$), and that Mü $\ll 1$. These derivations will follow closely the work of Jensen et al. (2012). Jensen et al. (2012) derive analytical solutions in the cases where Mü $\ll 1$ and Mü $\gg 1$. They find that the analytical solutions in the low Münch number scenario are almost identical to numerical simulations for Mü $= 1$ and provide a good approximation for Münch number values up to 10 (Jensen et al., 2012). Our governing equations differ from those described in (Jensen et al., 2012) as we have explicit terms for different forms of loading and unloading (active and diffusion), whereas Jensen et al. (2012) make use of a target concentration to define their loading and unloading mechanisms.

In order to derive a set of analytical solutions, we split the model into three zones to represent the loading zone ($i = 1$), the translocation zone ($i = 2$), and the unloading zone ($i = 3$). All model parameters are zone dependent and thus defined by step functions. Hence the system of equations becomes,

$$\frac{\partial^2 \bar{U}_i}{\partial X^2} = \frac{\partial C_{s,i}}{\partial x} - \frac{\partial C_{x,s,i}}{\partial x} + \text{Mü}\left(\bar{U}_i + \frac{1}{8}\frac{\partial P_{x,i}}{\partial X}\right) \tag{3.47a}$$

$$\frac{\partial \bar{U}_i c_{s,i}}{\partial X} = 2\beta_{s,i}(C_{ext,s,i}(X) - C_{s,i}(X)) + 2\gamma_{s,i}C_{ext,s,i}(X) - 2\lambda_{s,i}C_{s,i}(X), \tag{3.47b}$$

$$\frac{\partial \bar{U}_i C_{a,i}}{\partial x} = 2\beta_{a,i}(C_{ext,a,i}(X) - C_{a,i}(X)) + 2\gamma_{a,i}C_{ext,a,i}(X) - 2\lambda_{a,i}C_{a,i}(X), \tag{3.47c}$$

$$\frac{\partial P_i}{\partial X} = -8\bar{U}_i(X). \tag{3.47d}$$

Throughout this modelling, we make the assumption that the external source/sink concentrations ($C_{ext,s}$ and $C_{ext,a}$) are given by piecewise constant functions defined on each zone of the phloem tube and the xylem concentrations ($C_{x,s}$ and $C_{x,a}$) and pressure (P_x) are assumed to be constant. This means that for each zone of the phloem tube $\partial C_{ext,i}/\partial X = 0$, $\partial C_{x,i}/\partial X = 0$ and $\partial P_{x,i}/\partial X = 0$. Thus, we have the finalised system of equations,

$$\frac{\partial^2 \bar{U}_i}{\partial X^2} = \frac{\partial C_{s,i}}{\partial X} + \text{Mü}\bar{U}_i(x) \tag{3.48a}$$

$$\frac{\partial \bar{U}_i C_{s,i}}{\partial X} = 2\beta_{s,i}(C_{ext,s,i}(X) - C_{s,i}(X)) + 2\gamma_{s,i}C_{ext,s,i}(X) - 2\lambda_{s,i}C_{s,i}(X), \tag{3.48b}$$

$$\frac{\partial \bar{U}_i C_{a,i}}{\partial X} = 2\beta_{a,i}(C_{ext,a,i}(X) - C_{a,i}(X)) + 2\gamma_{a,i}C_{ext,a,i}(X) - 2\lambda_{a,i}C_{a,i}(C), \tag{3.48c}$$

$$\frac{\partial P_i}{\partial X} = -8\bar{U}_i(X). \tag{3.48d}$$

The boundary conditions become,

$$\bar{U}_1(0) = 0, \tag{3.49a}$$
$$\bar{U}_3(X_3) = 0, \tag{3.49b}$$

and the initial conditions remain the same as defined in equations (3.43), (3.44), and (3.42). Alongside these conditions, we require conditions that prescribe continuity between zones for the variables and their derivatives. These are given by,

$$\bar{U}_1(X_1) = \bar{U}_2(X_1), \tag{3.50a}$$
$$\bar{U}_2(X_2) = \bar{U}_3(X_2), \tag{3.50b}$$
$$\frac{\partial \bar{U}_1(X_1)}{\partial X} = \frac{\partial \bar{U}_2(X_1)}{\partial X}, \tag{3.50c}$$
$$\frac{\partial \bar{U}_2(X_2)}{\partial X} = \frac{\partial \bar{U}_3(X_2)}{\partial X}. \tag{3.50d}$$

These conditions ensure smoothness in $\bar{U}, C_s, C_a$, and P.

3.4.2 Solving in the limit Mü $\ll 1$

In the limits Mü $\ll 1$ or Mü $\gg 1$, previous studies have derived analytical solutions for the system of equations (3.48) for specific loading terms (Jensen et al., 2012). To establish if we can utilise the analytical solutions for our Arabidopsis model, we first need to calculate the Münch number for our problem. The parameters needed to calculate the Münch number are given in Table 3.4. For our model we have,

Parameter name	**Symbol**	**Value**
Phloem sap viscosity	η	1.7 mPas
Length of translocation zone	L	30.6 mm
Cell membrane permeability	L_p	5×10^{-14} m/s/Pa
Phloem tube radius	a	1.8m

Table 3.4: Parameter values required for calculating the Münch number. Values taken from (Ross-Elliott et al., 2017), phloem tube length from (Martin et al., 2002).

$$\text{Mü} = \frac{16\eta L_p L^2}{a^3} = 0.22 < 1. \tag{3.51}$$

Since the Münch number is not significantly less than 1, it is unclear whether a Mü $\ll 1$ solution would be representative of a solution for the full model. Therefore,

we now derive the analytical solution for Mü $\ll 1$ and compare it with numerical simulations to determine if this would be an appropriate approximation for our model. We note that this derivation follows that provided in Jensen et al. (2012) with the addition of an hormone equation.

Considering the limit Mü $\ll 1$, the system of equations can be rewritten as,

$$\frac{\partial^2 \bar{U}_i}{\partial X^2} = \frac{\partial C_{s,i}}{\partial X}, \tag{3.52a}$$

$$\frac{\partial \bar{U}_i C_{s,i}}{\partial X} = 2\beta_{s,i}(C_{ext,s,i}(X) - C_{s,i}(X)) + 2\gamma_{s,i}C_{ext,s,i}(X) - 2\lambda_{s,i}C_{s,i}(X), \tag{3.52b}$$

$$\frac{\partial \bar{U}_i C_{a,i}}{\partial X} = 2\beta_{a,i}(C_{ext,a,i}(X) - C_{a,i}(X)) + 2\gamma_{a,i}C_{ext,a,i}(X) - 2\lambda_{a,i}C_{a,i}(X). \tag{3.52c}$$

The boundary conditions stay the same as equations (3.49) and (3.50).

3.4.3 Loading zone

We begin by considering the system of equations in the loading zone, $i = 1$,

$$\frac{\partial^2 \bar{U}_1}{\partial X^2} = \frac{\partial C_{s,1}}{\partial X}, \tag{3.53a}$$

$$\frac{\partial \bar{U}_1 C_{s,1}}{\partial X} = 2\beta_{s,1}(C_{ext,s,1}(X) - C_{s,1}(X)) + 2\gamma_{s,1}C_{ext,s,1}(X) - 2\lambda_{s,1}C_{s,1}(X), \tag{3.53b}$$

$$\frac{\partial \bar{U}_1 C_{a,1}}{\partial X} = 2\beta_{a,1}(C_{ext,a,1}(X) - C_{a,1}(X)) + 2\gamma_{a,1}C_{ext,a,1}(X) - 2\lambda_{a,1}C_{a,1}(X). \tag{3.53c}$$

Integrating (3.53a) we obtain,

$$\frac{\partial \bar{U}_1}{\partial X} = C_{s,1}(X) - K_1, \tag{3.54}$$

where K_1 is a constant. Rearranging for $C_{s,1}(x)$ and substituting in to (3.53b) gives,

$$\frac{\partial \bar{U}_1 C_{s,1}}{\partial X} = 2(\beta_{s,1} + \gamma_{s,1})C_{ext,s,1} - 2(\lambda_{s,1} + \beta_{s,1})K_1 - 2(\lambda_{s,1} + \beta_{s,1})\frac{\partial \bar{U}_1}{\partial X}. \tag{3.55}$$

Integrating again, we obtain,

$$\bar{U}_1 C_{s,1} = 2(\beta_{s,1} + \gamma_{s,1})C_{ext,s,1}X - 2(\lambda_{s,1} + \beta_{s,1})K_1 X - 2(\lambda_{s,1} + \beta_{s,1})\bar{U}_1 + \bar{K}_1 \tag{3.56}$$

where $\bar{K}_1$ is a constant. Applying boundary condition (3.49a), we can show that,

$$\bar{K}_1 = \bar{U}_1(0)C_{s,1}(0) - 2(\beta_{s,1}+\gamma_{s,1})C_{ext,s,1}(0) + 2(\lambda_{s,1}+\beta_{s,1})K_1(0) + 2(\lambda_{s,1}+\beta_{s,1})\bar{U}_1(0) = 0. \quad (3.57)$$

Rearranging (3.56) for $C_{s,1}$ and substituting into (3.54), we obtain,

$$C_{s,1} = \frac{2(\beta_{s,1}+\gamma_{s,1})C_{ext,s,1}X - 2(\lambda_{s,1}+\beta_{s,1})K_1 x - 2(\lambda_{s,1}+\beta_{s,1})\bar{U}_1}{\bar{U}_1}, \quad (3.58)$$

$$\Rightarrow \frac{\partial \bar{U}_1}{\partial X} = \frac{2(\beta_{s,1}+\gamma_{s,1})C_{ext,s,1}X - 2(\lambda_{s,1}+\beta_{s,1})K_1 X - 2(\lambda_{s,1}+\beta_{s,1})\bar{U}_1 - K_1\bar{U}_1}{\bar{U}_1}. \quad (3.59)$$

Thus, we have eliminated $C_{s,1}$ from the equations. Note here that K_1 is given by,

$$K_1 = \frac{2(\beta_{s,1}+\gamma_{s,1})C_{ext,s,1} - \left(\partial\bar{U}_1(0)/\partial X\right)^2 - 2(\lambda_{s,1}+\beta_{s,1})\left(\partial\bar{U}_1(0)/\partial X\right)}{\partial\bar{U}_1(0)/\partial X + 2(\lambda_{s,1}+\beta_{s,1})}. \quad (3.60)$$

We observe that (3.59) is homogeneous and of first order. Therefore, we let $\bar{U}_1 = v_1 X$ and obtain,

$$\frac{\partial v_1 X}{\partial X} = \frac{2(\beta_{s,1}+\gamma_{s,1})C_{ext,s,1} - 2(\lambda_{s,1}+\beta_{s,1})K_1 - (2(\lambda_{s,1}+\beta_{s,1})+K_1)v_1}{v_1}. \quad (3.61)$$

Let $z = \log X$, then $\partial z/\partial X = 1/X$. Hence, the above equation becomes,

$$\begin{aligned} v_1 + X\frac{\partial v_1}{\partial X} &= \frac{2(\beta_{s,1}+\gamma_{s,1})C_{ext,s,1} - 2(\lambda_{s,1}+\beta_{s,1})K_1 - (2(\lambda_{s,1}+\beta_{s,1})+K_1)v_1}{v_1}, \\ X\frac{\partial v_1}{\partial X} &= \frac{2(\beta_{s,1}+\gamma_{s,1})C_{ext,s,1} - 2(\lambda_{s,1}+\beta_{s,1})K_1 - (2(\lambda_{s,1}+\beta_{s,1})+K_1)v_1 - {v_1}^2}{v_1}, \\ X\frac{\partial v_1}{\partial X} &= \frac{\partial X}{\partial z}\frac{\partial v_1}{\partial X} = \frac{\partial v_1}{\partial z} \\ &= \frac{2(\beta_{s,1}+\gamma_{s,1})C_{ext,s,1} - 2(\lambda_{s,1}+\beta_{s,1})K_1 - (2(\lambda_{s,1}+\beta_{s,1})+K_1)v_1 - {v_1}^2}{v_1}. \end{aligned} \quad (3.62)$$

This can be written as,

$$\frac{\partial v_1}{\partial z} = -\frac{L(v_1)}{v_1}, \quad (3.63)$$

where,

$$L(v_1) = {v_1}^2 + (2(\lambda_{s,1}+\beta_{s,1})+K_1)v_1 - 2(\beta_{s,1}+\gamma_{s,1})C_{ext,s,1} + 2(\lambda_{s,1}+\beta_{s,1})K_1.$$

The roots of $L(v_1)$ are given by,

$$v_{\pm,1} = -\frac{1}{2}\Big[2(\lambda_{s,1}+\beta_{s,1}) + K_1 \mp \sqrt{(2(\lambda_{s,1}+\beta_{s,1})-K_1)^2 + 8(\beta_{s,1}+\gamma_{s,1})C_{ext,s,1}}\Big]. \tag{3.64}$$

Substituting (3.60) into (3.64), we obtain,

$$v_{+,1} = \frac{\partial \bar{U}_1(0)}{\partial X}, \tag{3.65a}$$

$$\begin{aligned} v_{-,1} &= -\frac{4(\lambda_{s,1}+\beta_{s,1})^2 + 2(\lambda_{s,1}+\beta_{s,1})^{\partial \bar{U}_1(0)/\partial X} + 2(\beta_{s,1}+\gamma_{s,1})C_{ext,s,1}}{\partial \bar{U}_1(0)/\partial X + 2(\lambda_{s,1}+\beta_{s,1})} \\ &= -(C_{s,1}(0) + 2(\lambda_{s,1}+\beta_{s,1})). \end{aligned} \tag{3.65b}$$

We consider the case where $v_{+,1} \neq v_{-,1}$, i.e. the roots of $L(v_1)$ are distinct. We can invert (3.63) and integrate to obtain,

$$\begin{aligned} z(v_1) &= -\int \frac{v_1}{L(v_1)} dv_1, \\ &= -\int \frac{v_1}{(v_1 - v_{+,1})(v_1 - v_{-,1})} dv_1, \\ &= -\int \frac{-v_{+,1}}{(v_{-,1} - v_{+,1})(v_1 - v_{+,1})} - \frac{v_{-,1}}{(v_{-,1} - v_{+,1})(v_1 - v_{-,1})} dv_1, \\ &= \frac{1}{(v_{-,1} - v_{+,1})} \int \frac{v_{+,1}}{(v_1 - v_{+,1})} - \frac{v_{-,1}}{(v_1 - v_{-,1})} dv_1, \\ &= \frac{1}{(v_{-,1} - v_{+,1})} \Big[v_{+,1} \log(v_1 - v_{+,1}) - v_{-,1} \log(v_1 - v_{-,1}) \Big] + J_{a,1} \\ &= \log(v_1 - v_{+,1})^{-A_1} - \log(v_1 - v_{-,1})^{B_1} + J_{a,1}, \end{aligned} \tag{3.66}$$

where $J_{a,1}$ is a constant and $A_1 = -\frac{v_{+,1}}{(v_{-,1}-v_{+,1})}$ and $B_1 = \frac{v_{-,1}}{(v_{-,1}-v_{+,1})}$.

Recall that $\bar{U}_1 = v_1 X$ and that $z = \log X$, then (3.66) becomes,

$$\begin{aligned} & \log(X) = \log\Big(\frac{\bar{U}_1}{X} - v_{+,1}\Big)^{-A_1} - \log\Big(\frac{\bar{U}_1}{X} - v_{-,1}\Big)^{B_1} + J_{a,1}, \\ \Rightarrow \quad & x = \Big|\frac{\bar{U}_1}{X} - v_{+,1}\Big|^{-A_1} \Big|\frac{\bar{U}_1}{X} - v_{-,1}\Big|^{-B_1} + \tilde{K}_1, \\ \Rightarrow \quad & x\Big|\frac{\bar{U}_1}{X} - v_{+,1}\Big|^{A_1} \Big|\frac{\bar{U}_1}{X} - v_{-,1}\Big|^{B_1} = \tilde{K}_1, \end{aligned} \tag{3.67}$$

where $\tilde{K}_1$ is a constant of integration. Here we note that $A_1 = 1 - B_1$ and therefore we have,

$$X\Big|\frac{\bar{U}_1}{X} - v_{+,1}\Big|^{(1-B_1)} \Big|\frac{\bar{U}_1}{X} - v_{-,1}\Big|^{B_1} = \tilde{K}_1. \tag{3.68}$$

This gives an implicit solution for $\bar{U}_1(X)$ in terms of K_1 and $\tilde{K}_1$. Subsequently, (3.54) can be used to determine $C_{s,1}(x)$.

Having defined an analytical solution for the sugar (3.58) and velocity (3.68) profiles, which are equivalent to those in Jensen et al. (2012) upto the variation in loading parameters, it remains to derive an equation for the hormone concentration profile. Equation (3.53c) can be rewritten as,

$$\bar{U}_1 \frac{\partial C_{a,1}}{\partial X} + C_{a,1} \frac{\partial \bar{U}_1}{\partial X} = 2(\beta_{a,1} + \gamma_{a,1}) C_{ext,a,1} - 2(\lambda_{a,1} + \beta_{a,1}) C_{a,1}. \tag{3.69}$$

As equation (3.68) gives an implicit solution for $\bar{U}_1(x)$, the above equation can be written as,

$$\frac{\partial C_{a,1}}{\partial X} + C_{a,1}\Big(\frac{1}{\bar{U}_1}\frac{\partial \bar{U}_1}{\partial X} + \frac{2(\lambda_{a,1} + \beta_{a,1})}{\bar{U}_1}\Big) = \frac{2(\beta_{a,1} + \gamma_{a,1}) C_{ext,a,1}}{\bar{U}_1}, \tag{3.70}$$

which is a first order, linear, homogenous ODE.

3.4.4 Unloading zone

Due to the symmetry of the loading and unloading zone in our problem, solutions for $\bar{U}_3, C_{s,3}$, and $C_{a,3}$ can be found by performing a change of variables in the unloading zone, $X_2 < X < X_3$, to realign the origin to X_3. The change of variables applied is given by,

$$\xi = X_3 - x, \tag{3.71a}$$
$$\zeta_{s,i}(\xi) = C_{s,i}(x), \tag{3.71b}$$
$$\zeta_{a,i}(\xi) = C_{a,i}(x), \tag{3.71c}$$
$$\eta_i(\xi) = -\bar{U}_i(x), \tag{3.71d}$$
$$\zeta_{ext,s,i} = C_{ext,s,i}, \tag{3.71e}$$
$$\zeta_{ext,a,i} = C_{ext,a,i}, \tag{3.71f}$$

which yields the system of equations,

$$\frac{\partial^2 \eta_3}{\partial \xi^2} = \frac{\partial \zeta_{s,3}}{\partial \xi}, \tag{3.72a}$$
$$\frac{\partial \eta_3 \zeta_{s,3}}{\partial \xi} = 2\beta_{s,3}(\zeta_{ext,s,3}(\xi) - \zeta_{s,3}(\xi)) + 2\gamma_{s,3}\zeta_{ext,s,3}(\xi) - 2\lambda_{s,3}\zeta_{s,3}(\xi), \tag{3.72b}$$
$$\frac{\partial \eta_3 \zeta_{a,3}}{\partial \xi} = 2\beta_{a,3}(\zeta_{ext,a,3}(\xi) - \zeta_{a,3}(\xi)) + 2\gamma_{a,3}\zeta_{ext,a,3}(\xi) - 2\lambda_{a,3}\zeta_{a,3}(\xi), \tag{3.72c}$$

where boundary conditions associated with the unloading zone are now given by,

$$\eta_3(0) = 0, \tag{3.73a}$$

$$\bar{U}_2(X_2) = -\eta_3(X_3 - X_2), \tag{3.73b}$$

$$\frac{\partial \bar{U}_2(X_2)}{\partial X} = \frac{\partial \eta_3(X_3 - X_2)}{\partial \xi}. \tag{3.73c}$$

We can see that the equations for the new variables in the unloading zone are unchanged from the equations used to describe the loading zone in the original variables. As such, we can apply the methods described in Section 3.4.3 to obtain solutions for the new variables in the unloading zone,

$$\xi \left| \frac{\eta_3}{\xi} - v_{+,3} \right|^{(1-B_3)} \left| \frac{\eta_3}{\xi} - v_{-,3} \right|^{B_3} = \tilde{K}_3, \tag{3.74a}$$

$$\frac{\partial \eta_3}{\partial \xi} = \zeta_{s,3}(\xi) - K_3, \tag{3.74b}$$

$$\frac{\partial \zeta_{a,3}}{\partial \xi} + \zeta_{a,3}\left(\frac{1}{\eta_3} \frac{\partial \eta_3}{\partial \xi} + \frac{2(\lambda_{a,3} + \beta_{a,3})}{\eta_3} \right) = \frac{2(\beta_{a,3} + \gamma_{a,3})\zeta_{ext,a,3}}{\eta_3}. \tag{3.74c}$$

We can return to the original variables using the change of variables described in (3.71).

3.4.5 Translocation zone

We now need to determine the equations for the translocation zone, $i = 2$. In the translocation zone there is no loading or unloading, therefore, $\beta_{s/a,2} = \gamma_{s/a,2} = \lambda_{s/a,2} = 0$. The system of equations becomes,

$$\frac{\partial^2 \bar{U}_2}{\partial X^2} = \frac{\partial C_{s,2}}{\partial X}, \tag{3.75a}$$

$$\frac{\partial \bar{U}_2 C_{s,2}}{\partial X} = 0, \tag{3.75b}$$

$$\frac{\partial \bar{U}_2 C_{a,2}}{\partial X} = 0. \tag{3.75c}$$

Equations (3.75b) and (3.75c) imply conservation of sugar flux and hormone flux respectively. Hence,

$$\bar{U}_2(X) C_{s,2}(X) = \text{constant}, \tag{3.76a}$$

$$\bar{U}_2(X) X_{a,2}(X) = \text{constant}, \tag{3.76b}$$

which we can apply boundary condition (3.50a) to and obtain,

$$\bar{U}_2(X)C_{s,2}(X) = \bar{U}_2(X_1)Cs,2(X_1) = \bar{U}_1(X_1)C_{s,1}(X_1), \tag{3.77a}$$

$$\bar{U}_2(X)C_{a,2}(X) = \bar{U}_2(X_1)C_{a,2}(X_1) = \bar{U}_1(X_1)C_{a,1}(X_1), \tag{3.77b}$$

which holds for all X in $[X_1, X_2]$.

Now integrating (3.75a) we get,

$$\begin{aligned}\frac{\partial \bar{U}_2}{\partial X} &= C_{s,2}(X) + K_2 \\ &= \frac{\bar{U}_1(X_1)C_{s,1}(X_1)}{\bar{U}_2(X)} + K_2\end{aligned} \tag{3.78}$$

If $\frac{\partial \bar{U}_2}{\partial X} \neq 0$, we can invert the equation to obtain,

$$\frac{\partial X}{\partial \bar{U}_2} = \frac{\bar{U}_2}{\bar{U}_1(X_1)C_{s,1}(X_1) + K_2\bar{U}_2}, \tag{3.79}$$

which we can then integrate to obtain,

$$\begin{aligned}X(\bar{U}_2) &= \int \frac{\bar{U}_2}{\bar{U}_1(X_1)C_{s,1}(X_1) + K_2\bar{U}_2} d\bar{U}_2, \\ &= \int \frac{1}{K_2} - \frac{\bar{U}_1(X_1)C_{s,1}(X_1)}{K_2(\bar{U}_1(X_1)C_{s,1}(X_1) + K_2\bar{U}_2)} d\bar{U}_2, \\ &= \frac{\bar{U}_2}{K_2} - \frac{\bar{U}_1(X_1)C_{s,1}(X_1)}{K_2}\left[\frac{1}{K_2}\log(\bar{U}_1(X_1)C_{s,1}(X_1) + K_2\bar{U}_2)\right] + \hat{K}_1, \\ &= \frac{\bar{U}_2}{K_2} - \frac{\bar{U}_1(X_1)C_{s,1}(X_1)}{(K_2)^2}\log(\bar{U}_1(X_1)C_{s,1}(X_1) + K_2\bar{U}_2) + \hat{K}_1, \\ &= \frac{\bar{U}_2}{K_2} - \frac{\bar{U}_1(X_1)C_{s,1}(X_1)}{(K_2)^2}\log\left(\frac{1 + \frac{K_2\bar{U}_2}{\bar{U}_1(X_1)C_{s,1}(X_1)}}{1 + \frac{K_2}{C_{s,1}(X_1)}}\right) + \hat{K}_2,\end{aligned} \tag{3.80}$$

where $\hat{K}_2 = \hat{K}_1 - \frac{\bar{U}_1(X_1)C_{s,1}(X_1)}{(K_2)^2}\log(\bar{U}_1(X_1C_{s,1}(X_1) + \bar{U}_1(X_1)K_2))$. Applying the expression $X_1 = X(\bar{U}_2(X_1))$ we find that,

$$\hat{K}_2 = X_1 - \frac{\bar{U}_1(X_1)}{K_2}. \tag{3.81}$$

From the flux conservation equations, we have that,

$$C_{s,2} = \frac{\bar{U}_1(X_1)C_{s,1}(X_1)}{\bar{U}_2(X)} \tag{3.82a}$$

$$C_{a,2} = \frac{\bar{U}_1(X_1)C_{a,1}(X_1)}{\bar{U}_2(X)} \tag{3.82b}$$

For this analysis, we have assumed that $\frac{\partial \bar{U}_2}{\partial X} \neq 0$. In the case where $\frac{\partial \bar{U}_2}{\partial X} \to 0$, from (3.78) we can see that,

$$\bar{U}_2(X) \longrightarrow -\frac{\bar{U}_1(X_1)C_{s,1}(X_1)}{K_2}. \tag{3.83}$$

Thus, we have a set of analytical solutions for Münch flow across all zones of the phloem tube,

$$\tilde{K}_1 = X\left|\frac{\bar{U}_1}{X} - v_{+,1}\right|^{(1-B_1)}\left|\frac{\bar{U}_1}{X} - v_{-,1}\right|^{B_1} \tag{3.84a}$$

$$x(\bar{U}_2) = \frac{\bar{U}_2}{K_2} - \frac{\bar{U}_1(X_1)C_{s,1}(X_1)}{(K_2)^2}\log\left(\frac{1+\frac{K_2\bar{U}_2}{\bar{U}_1(X_1)C_{s,1}(X_1)}}{1+\frac{K_2}{C_{s,1}(X_1)}}\right) + \hat{K}_2, \tag{3.84b}$$

$$\tilde{K}_3 = \xi\left|\frac{\eta_3}{\xi} - v_{+,3}\right|^{(1-B_3)}\left|\frac{\eta_3}{\xi} - v_{-,3}\right|^{B_3}, \tag{3.84c}$$

where applying the boundary conditions (3.49) and (3.50) evaluates the constants.

3.4.6 Specific solution: $\bar{U}_1(X) = AX$

We consider the specific solution for the velocity, (3.84a), in the loading zone given by,

$$\bar{U}_1(X) = AX, \tag{3.85}$$

where $A = v_{+,1}$ by (3.65a). This satisfies the boundary condition (3.49a) and substitution into (3.84a) reveals that $\tilde{K}_1 = 0$ as long as $1 - B_1 > 0$ or $B_1 < 1$. Equations (3.54) and (3.65a) reveal that,

$$C_{s,1}(X) = \frac{2(\beta_{s,1} + \gamma_{s,1})C_{ext,s,1}}{v_{+,1} + 2(\lambda_{s,1} + \beta_{s,1})}. \tag{3.86}$$

We can substitute (3.85) into (3.70) and solve for a general solution,

$$C_{a,1}(X) = K_1^* X^{-\frac{v_{+,1}+2(\lambda_{a,1}+\beta_{a,1})}{v_{+,1}}} + \frac{2(\beta_{a,1}+\gamma_{a,1})C_{ext,a,1}}{v_{+,1}+2(\lambda_{a,1}+\beta_{a,1})}, \tag{3.87}$$

where K_1^* is a constant of integration that needs to be determined from initial auxin concentration conditions.

From equations (3.48) and boundary condition (3.49a) we can obtain the following equations for the sugar and hormone concentration at $X = 0$,

$$C_{s,1}(0) = \frac{2(\beta_{s,1}+\gamma_{s,1})C_{ext,s,1}}{\partial\bar{U}(0)/\partial X + 2(\lambda_{s,1}+\beta_{s,1})} = \frac{2(\beta_{s,1}+\gamma_{s,1})C_{ext,s,1}}{v_{+,1}+2(\lambda_{s,1}+\beta_{s,1})}, \tag{3.88a}$$

$$C_{a,1}(0) = \frac{2(\beta_{a,1}+\gamma_{a,1})C_{ext,a,1}}{\partial\bar{U}(0)/\partial X + 2(\lambda_{a,1}+\beta_{a,1})} = \frac{2(\beta_{a,1}+\gamma_{a,1})C_{ext,a,1}}{v_{+,1}+2(\lambda_{a,1}+\beta_{a,1})}, . \tag{3.88b}$$

Substituting (3.88b) into (3.87) it is clear that $K_1^* = 0$ and thus we have,

$$C_{a,1}(X) = \frac{2(\beta_{a,1}+\gamma_{a,1})C_{ext,a,1}}{v_{+,1}+2(\lambda_{a,1}+\beta_{a,1})}. \tag{3.89}$$

The equations for velocity, (3.84b), sugar concentration, (3.82a), and hormone concentration, (3.82b), in the translocation zone remain the same as those given in Section 3.4.5. The equations are solved in Python using the `root` function from the Scipy Optimize library (Virtanen et al., 2020).

Finally, we consider the equations for velocity, sugar concentration, and auxin concentration in the unloading zone (equations (3.74)). We calculate the velocity in the unloading zone by finding the root of equation (3.74a). We can then substitute this into equation (3.74b) and solve to find the sugar concentration, $\zeta_{s,3}$, using the `root` function. Due to the complexity of equation (3.74c), we are unable to solve for the hormone concentration analytically and as such show results for sugar concentration and velocity only.

In this specific case, with $\bar{U}_1(X) = v_{+,1}X$, there are a number of constants of integration required to find the full analytical solutions. Theses constants and the equations required to obtain them in this situation are given in Table 3.5. In the analytical simulations, we solve for these constants using the `fsolve` function from the Scipy Optimize library (Virtanen et al., 2020).

The results of the analytical simulations are shown in Figure 3.4 (shown for velocity $\bar{U}$ and sugar concentration C_s only) in comparison to low Münch number numerical

Equation	References
$\bar{K}_1 = 0$	(3.56) (3.49)a
$\bar{K}_3 = 0$	(3.56)* (3.49)b *
$K_1 = \dfrac{2(\beta_{s,1}+\gamma_{s,1})C_{ext,s,1} - (v_{+,1})^2 - 2(\beta_{s,1}+\lambda_{s,1})v_{+,1}}{v_{+,1}+2(\beta_{s,1}+\lambda_{s,1})}$	(3.60), (3.56), (3.54), (3.49)a
$K_3 = \dfrac{2(\beta_{s,3}+\gamma_{s,3})C_{ext,s,3} - (v_{+,3})^2 - 2(\beta_{s,3}+\lambda_{s,3})v_{+,3}}{v_{+,3}+2(\beta_{s,3}+\lambda_{s,3})}$	(3.60)*, (3.56)*, (3.54)*, (3.49)b*
$K_2 = v_{+,1} - \dfrac{2(\beta_{s,1}+\gamma_{s,1})C_{ext,s,1}}{2(\beta_{s,1}+\lambda_{s,1})+v_{+,1}} = -K_1$	(3.78), (3.86), (3.50c)
$\hat{K}_2 = X_1\left(1 - \dfrac{v_{+,1}}{K_2}\right)$	(3.84b), (3.50a)
$K_3 = -K_2 = K_1$	(3.78), (3.54)*, (3.50d)*
$\tilde{K}_1 = 0$	(3.84a), (3.49)a
$-\dfrac{2(\beta_{s,1}+\gamma_{s,1})C_{ext,s,1}v_{+,1}x_1}{2(\beta_{s,1}+\lambda_{s,1})K_2+v_{+,1}K_2} =$	(3.78), (3.85), (3.86)
$\dfrac{(2(\beta_{s,3}+\gamma_{s,3})C_{ext,s,3} - 2(\beta_{s,3}+\lambda_{s,3})K_3)(X_3-X_2)}{2(\beta_{s,3}+\lambda_{s,3})+K_3}$	(3.59)*, (3.50b)*, (3.50d)*
$\tilde{K}_3$ (cannot be expressed explicitly)	(3.84b), (3.84c), (3.50b)*

Table 3.5: * indicates equations for transformed variables in the unloading zone.

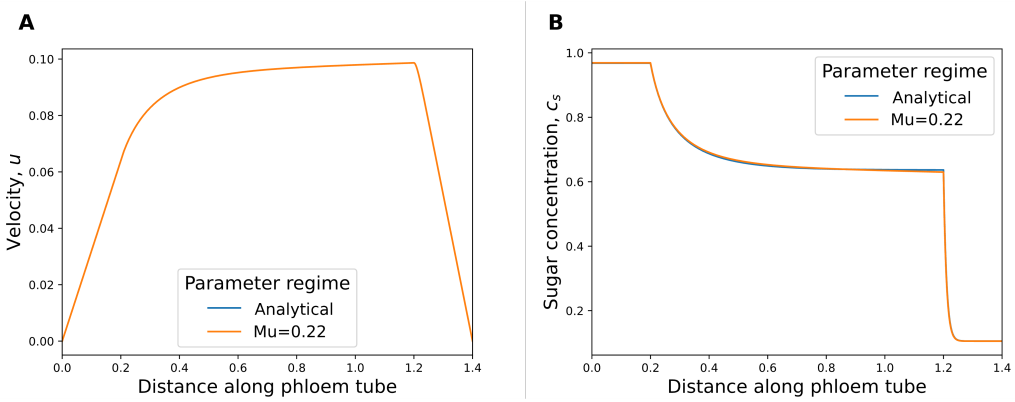


Figure 3.4: Simulations results for the analytical equations for Mü $\ll 1$ (blue), Section 3.4.6 and numerical simulations for Mü $= 0.22$ (orange), Equation (3.51). **(A)** the velocity profile; **(B)** the concentration profile for the sugar. Parameters: $\beta_s = [5,0,5]$, $\gamma_s = [0,0,0]$, $\lambda_s = [0,0,0]$, and $\sigma_s(x) = 1$.

simulations. The analytical simulations are derived in the limit Mü $\ll 1$ and replicate the results published by Jensen et al. (2012). Similarly to Jensen et al. (2012), we find that the analytical solutions in the limit Mü $\ll 1$ are an accurate approximation for numerical simulations in low Münch number conditions, with results for a typical Arabidopsis Münch number (Mü = 0.22) almost identical to the analytical solutions.

In the next section, we develop numerical simulations for the full system of equations for general Mü (3.36) so that we can solve for the hormone concentration in all zones alongside the sugar concentration and velocity. This will also allow us to consider situations where $\sigma(X) \neq 1$.

3.5 Numerical solutions to transport equations

3.5.1 Shooting method

The system of equations (3.36) along with boundary conditions (3.38), (3.42), (3.43), and (3.44) describe a boundary value problem where we have boundary conditions defined at both ends of the domain. In order to solve these equations numerically, we use a shooting method.

The shooting method requires us to convert the boundary value problem to an initial-value problem. We then solve the initial-value problem to find a solution for a given initial condition and then feed the solution into an iteration formula that allows us to correct the initial condition until we obtain a result that satisfies the second boundary-value condition. To convert equations (3.36) into an initial-value problem, we convert equation (3.38b), which is defined at the end of the phloem tube, into a condition defined at the start of the phloem tube,

$$\frac{\partial \bar{U}}{\partial X}(0) = t, \tag{3.90a}$$

where t is a constant that needs to be determined. The term $\partial \bar{U}(0)/\partial X$ is called the shooting parameter. We then solve this system to find a solution which we denote $\bar{U}(X;t)$. Our aim is to find a value for t such that $\bar{U}(X_3;t) = 0$. To do this, we first solve the initial-value problem for two initial estimates for t, t_1 and t_2, such that $\bar{U}(X_3;t_1) > 0$ and $\bar{U}(X_3;t_2) < 0$. We then use the bisection method to calculate $t_3 = (t_1 + t_2)/2$ and then solve the initial-value problem for t_3. If $\bar{U}(X_3;t_3) > 0$ we replace t_1 with t_3, and if $\bar{U}(X_3;t_3) < 0$ we replace t_2 with t_3. We repeat this process until $|\bar{U}(X_3;t)| < 10^{-6}$, at which point we consider the system solved.

3.5.2 Upwind scheme for numerical simulations

In this section, we seek numerical solutions to the full phloem model. The equations (3.36) can be rewritten for numerical simulation using an Upwind Scheme (Jensen et al., 2012). We divide the length of the phloem tube into a set of discrete points x_n, $n = 1,...,N$, and use the following substitutions for the differential terms,

$$\frac{\partial u}{\partial x} = \frac{u(x_j) - u(x_{j-1})}{\Delta x} + O(\Delta x), \tag{3.91}$$

$$\frac{\partial^2 u}{\partial x^2} = \frac{u(x_j) - 2u(x_{j-1}) + u(x_{j-2})}{\Delta x^2} + O(\Delta x), \tag{3.92}$$

$$\frac{\partial c_s}{\partial x} = \frac{c_s(x_j) - c_s(x_{j-1})}{\Delta x} + O(\Delta x), \tag{3.93}$$

$$\frac{\partial c_a}{\partial x} = \frac{c_a(x_j) - c_a(x_{j-1})}{\Delta x} + O(\Delta x), \tag{3.94}$$

$$\frac{\partial p}{\partial x} = \frac{p(x_j) - p(x_{j-1})}{\Delta x} + O(\Delta x). \tag{3.95}$$

These can be substituted into (3.36) to obtain the numerical model,

$$u_j = \frac{\left(2u_{j-1} - u_{j-2} + \sigma_{s,j}\Delta x(c_{s,j-1} - c_{s,j-2}) + \dfrac{\partial \sigma_{s,j}}{\partial x} c_{s,j-1}\Delta x^2\right)}{1 - \Delta x^2 \text{Mü}}, \tag{3.96a}$$

$$p_j = p_{j-1} - 8\Delta x u_j, \tag{3.96b}$$

$$c_{s,j} = \frac{-B_s \pm \sqrt{B_s^2 + 4A_s D_s}}{2A_s}, \tag{3.96c}$$

$$c_{a,j} = \frac{u_j c_{a,j-1} + \left[\frac{(1-\sigma_{a,j})}{2}\left(\sigma_{s,j}(c_{s,j} - c_{x,s,j}) - \frac{\text{Mü}}{8}(p_j - p_{x,j})\right) + 2(\beta_{a,j} + \gamma_{a,j})\right] c_{ext,a,j}\Delta x}{2u_j - u_{j-1} - \left[\frac{(1-\sigma_{a,j})}{2}\left(\sigma_{s,j}(c_{s,j} - c_{x,s,j}) - \frac{\text{Mü}}{8}(p_j - p_{x,j})\right) - 2(\beta_{a,j} + \lambda_{a,j})\right]\Delta x}, \tag{3.96d}$$

where,

$$\begin{aligned}
A_s &= -\frac{\sigma_{s,j}(1-\sigma_{s,j})\Delta x}{2}, \\
B_s &= 2u_j - u_{j-1} + 2\Delta x(\beta_{s,j} + \lambda_{s,j}) \\
&\quad + \frac{(1-\sigma_{s,j})\Delta x \text{Mü}}{16}(p_j - p_{x,j}) - \frac{\sigma_{s,j}(1-\sigma_{s,j})\Delta x}{2}(c_{ext,s,j} - c_{x,s,j}), \\
D_s &= c_{s,j-1}u_j + 2\Delta x(\beta_{s,j} + \gamma_{s,j})c_{ext,s,j} \\
&\quad - \left[\frac{(1-\sigma_{s,j})\Delta x \text{Mü}}{16}(p_j - p_{x,j}) + \frac{\sigma_{s,j}(1-\sigma_{s,j})\Delta x}{2} c_{x,s,j}\right] c_{ext,s,j}.
\end{aligned}$$

Note, we have used the notation $u_j = u(x_j)$, and $\Delta x = x_3/N$ for simplicity. From this point on we have ignored terms of $O(\Delta x^2)$ (or higher orders of Δx) as these are assumed negligible.

In equation (3.96c), we take the root with the plus sign as this is always greater than zero. As A_s has a maximum order of 10^{-5} (which occurs when $\sigma_s = 0.5$), we can use the binomial expansion for small A_s to obtain an approximation for the concentration equations, (3.96c), as,

$$c_{s,j} = \frac{D_s}{B_s} - A_s \frac{D_s^2}{B_s^3} + O(A_s^2). \tag{3.97}$$

Noticing that $A_s^2 = O(\Delta x^2)$ we can neglect the $O(A_s^2)$ terms in equations (3.97) as terms of $O(\Delta x^2)$ are assumed negligible.

We solve the system of governing equations numerically in `Python 3.8`.

3.5.3 Prescribing biologically motivated loading and unloading parameters

We have derived the governing equations for phloem transport under general loading and unloading mechanisms. However, the results presented will focus on parameter regimes that represent phloem loading and unloading in Arabidopsis, given experimental studies on long-distance hormone transport are predominantly in these species. Experimental studies have shown that the predominant mechanism for sugar loading in Arabidopsis is active loading (see comprehensive Table 2 in Jensen et al. (2013)). Evidence from Ross-Elliott et al. (2017) and Bret-Harte and Silk (1994) suggests that sugar unloading is passive, with bulk flow unloading being the dominant efflux component.

We consider the unloading mechanism for sugar to be passive (Oparka et al., 1994, Imlau et al., 1999), and note that evidence from Ross-Elliott et al. (2017) and Bret-Harte and Silk (1994) suggests that bulk flow unloading is the dominant efflux component. To incorporate bulk flow unloading, we set the Staverman reflection coefficient (Staverman, 1951) to be less than one in the unloading zone. This is in contrast to current models in the literature where passive sugar unloading is modelled as unloading via diffusion only (since the Staverman reflection coefficient is assumed to be 1 throughout the phloem).

Based on the above considerations, Table 3.6 gives the default sugar parameters used throughout the simulations. These parameters are defined to give equivalent sugar loading influx to parameters from (Jensen et al., 2012), but are modified as we assume active sugar loading only.

As we are modelling for a general hormone, we perform simulations for a variety

Parameter group	Default values	Parameter description
$(\sigma_{s,1}, \sigma_{s,2}, \sigma_{s,3})$	$(1,1,0 \leq \sigma_{s,3} \leq 1)$	Bulk flow
$(\beta_{s,1}, \beta_{s,2}, \beta_{s,3})$	$(0,0,5)$	Passive diffusion
$(\gamma_{s,1}, \gamma_{s,2}, \gamma_{s,3})$	$(0.16,0,0)$	Active loading
$(\lambda_{s,1}, \lambda_{s,2}, \lambda_{s,3})$	$(0,0,0)$	Active unloading
$(C_{ext,s,1}, C_{ext,s,2}, C_{ext,s,3})$	$(1,0,0.1)$	External sugar concentration

Table 3.6: Default values for sugar parameters.

of loading scenarios as the loading methods for different hormones are not well categorised. As such, for each set of sugar parameters, we model two distinct hormone cases. We consider the case where the hormone is loaded actively, and the case where the hormone is loaded passively via diffusion; although we note that it is likely that some hormones are loaded via a combination of both these mechanisms. Similarly to sugar, we assume the hormone is unloaded passively in order to investigate the impact of bulk flow unloading on hormone delivery. As such, the parameter definitions and default values for hormone parameters are given in Table 3.7.

Parameter group	Passive hormone loading	Active hormone loading
$(\sigma_{a,1}, \sigma_{a,2}, \sigma_{a,3})$	$(1,1,0 \leq \sigma_{s,3} \leq 1)$	$(1,1,0 \leq \sigma_{s,3} \leq 1)$
$(\beta_{a,1}, \beta_{a,2}, \beta_{a,3})$	$(5,0,5)$	$(0,0,5)$
$(\gamma_{a,1}, \gamma_{a,2}, \gamma_{a,3})$	$(0,0,0)$	$(0.16,0,0)$
$(\lambda_{a,1}, \lambda_{a,2}, \lambda_{a,3})$	$(0,0,0)$	$(0,0,0,)$
$(C_{ext,a,1}, C_{ext,a,2}, C_{ext,a,3})$	$(1,0,0.1)$	$(1,0,0.1)$

Table 3.7: Hormone parameters for passive and actively loaded hormone.

Given the model assumptions are predominantly based on data from Arabidopsis seedlings, we calculated the Münch number using the Arabidopsis parameters given in Table 3.4, which gives Mü$= 0.22$. This value is much lower than previously modelled species such as wheat and black locust which have values Mü$= 12$ and Mü$= 10^4$ respectively (Payvandi et al., 2014). Jensen et al. (2012) produce analytical solutions for phloem transport velocity and sugar concentration in the limit of small Münch number (repeated in Section 3.4 and extended to include hormone concentration equations). Analytical solutions have little variation from numerical solutions when Mü$= 0.22$ (Figure 3.4 – simulations with $\sigma_s = \sigma_a = 1$).

We note that the analytical solutions would be appropriate for simulations of phloem transport velocity and sugar concentration in Arabidopsis (given the low Münch number) in the case when $\sigma_{s,3} = 1$. However, we are unable to obtain full analytical solutions for the hormone concentration equations and so these must be calculated via numerical simulations. Our mathematical model has also been developed such that it can capture the phloem transport dynamics (including hormone concentration profiles) in the case where $\sigma_{s,3}, \sigma_{a,3} \neq 1$. We do not have analytical solutions for cases where $\sigma_{s,3}, \sigma_{a,3} \neq 1$, and as such, we proceed using numerical simulations for all modelling scenarios. As our model can simulate a wide range of Münch numbers, we include simulations of the impact of bulk flow unloading in both a low and high Münch number regime as an example.

3.6 Results

3.6.1 The rate of delivery to the root tip does not depend on phloem transport velocity for actively loaded sugar and hormones

Before proceeding with the simulation results, we first note that as the model is at steady state, the total flux into the phloem in the loading zone must equal the total flux out of the phloem in the unloading zone; both can be calculated using equations (3.46). For the actively loaded sugar and in cases where the hormone is actively loaded, the total flux into the phloem depends only on the prescribed external concentration and active transport rate. As a result, the total loading and unloading flux is independent of the concentrations in the phloem and the unloading parameters. Thus, for actively loaded sugar and hormones, the rate of delivery to the root tip does not depend on the phloem transport velocity.

3.6.2 Bulk flow unloading increases the phloem transport velocity

One of the key extensions of this model is the inclusion of the Staverman reflection coefficient (Staverman, 1951), which allows the model to capture the effect of unloading via bulk flow, which Ross-Elliott et al. (2017) suggest to be the dominant unloading mechanism.

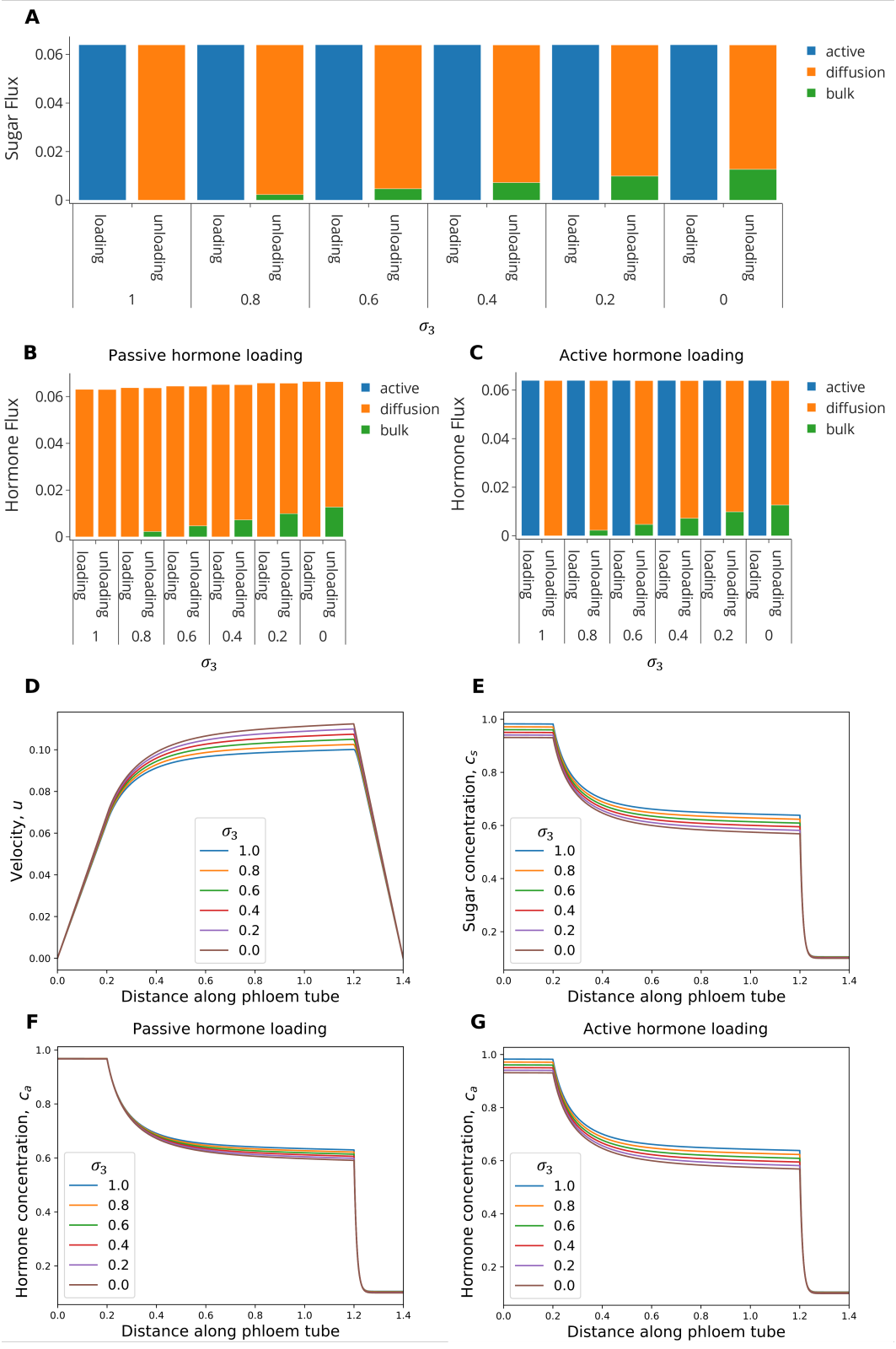


Figure 3.5: Decreasing the Staverman reflection coefficient results in an increase in bulk flow unloading for sugar and hormone. Increasing the amount of bulk flow unloading increases the phloem transport velocity and decreases the concentration of sugar in the loading zone. This results in increased hormone unloading for both passively and actively loaded hormone. ***(continues)***

Figure 3.5: **(A)** Sugar flux in the loading/unloading zones; **(B)** Hormone flux in the loading/unloading zones for passively loaded hormone; **(C)** Hormone flux in the loading/unloading zones for actively loaded hormone; **(D)** Phloem transport velocity; **(E)** Sugar concentration; **(F)** Hormone concentration for a passively loaded hormone; **(G)** Hormone concentration for an actively loaded hormone. **Sugar parameter values:** as given in Table 3.6 with additional variations to $(\sigma_{s,1}, \sigma_{s,2}, \sigma_{s,3}) = (1, 1, \text{varied})$. **Auxin parameter values:** as given in Table 3.7 with additional variations to $(\sigma_{a,1}, \sigma_{a,2}, \sigma_{a,3}) = (1, 1, \text{varied})$. **Mü** = 0.22

We first investigate the impact of bulk flow unloading by allowing the Staverman reflection coefficient for sugar, $\sigma_{s,3}$, and the general hormone, $\sigma_{a,3}$, to vary simultaneously in the unloading zone. As discussed above, the total sugar flux into and out of the phloem in the loading and unloading zones does not depend on $\sigma_{s,3}$ (Figure 3.5A). As one may expect, decreasing $\sigma_{s,3}$ allows for membrane leakage and hence there is more unloading via bulk flow. However, for the chosen model parameters (Tables 3.6 and 3.7), the model predicts that diffusive unloading of sugar always remains dominant over bulk flow unloading of sugar.

The phloem transport velocity and sugar concentration profile depend only on the Staverman reflection coefficient for sugar (equations (3.36a) and (3.36b)). Reducing the Staverman reflection coefficient for sugar increases bulk flow sugar unloading which results in a depletion of sugar in the phloem (Figure 3.5E). As the total sugar efflux in the unloading zone is fixed and prescribed by the loading parameters, the sugar depletion caused by increased bulk flow unloading implies there must also be an increase in phloem transport velocity (Figure 3.5D) to maintain the rate of efflux prescribed by the sugar loading parameters (equation (3.46a)).

For an actively loaded hormone (Figures 3.5C,G), we see that the hormone concentration profile and bulk flow contribution directly mimics the results for sugar. For a hormone loaded passively (Figure 3.5F), reducing $\sigma_{s,3}$ (which increases phloem transport velocity) also results in reduced hormone concentrations, although in this case, the change is small, and not perceptible in the loading zone. For passively loaded hormones, the model predicts that decreasing $\sigma_{s,3}$ results in a small increase in the amount of hormone loaded into the phloem, and hence delivered to the root tip, (Figure 3.5B).

These model scenarios were repeated for a high Münch number as is typical for larger plant species (Mü = 12 (Payvandi et al., 2014)). Whilst the overall shape of the phloem transport velocity profile and sugar/hormone concentration profiles change significantly from the low Münch number scenario, the over-arching impact that increasing bulk flow unloading increases phloem transport velocity remains

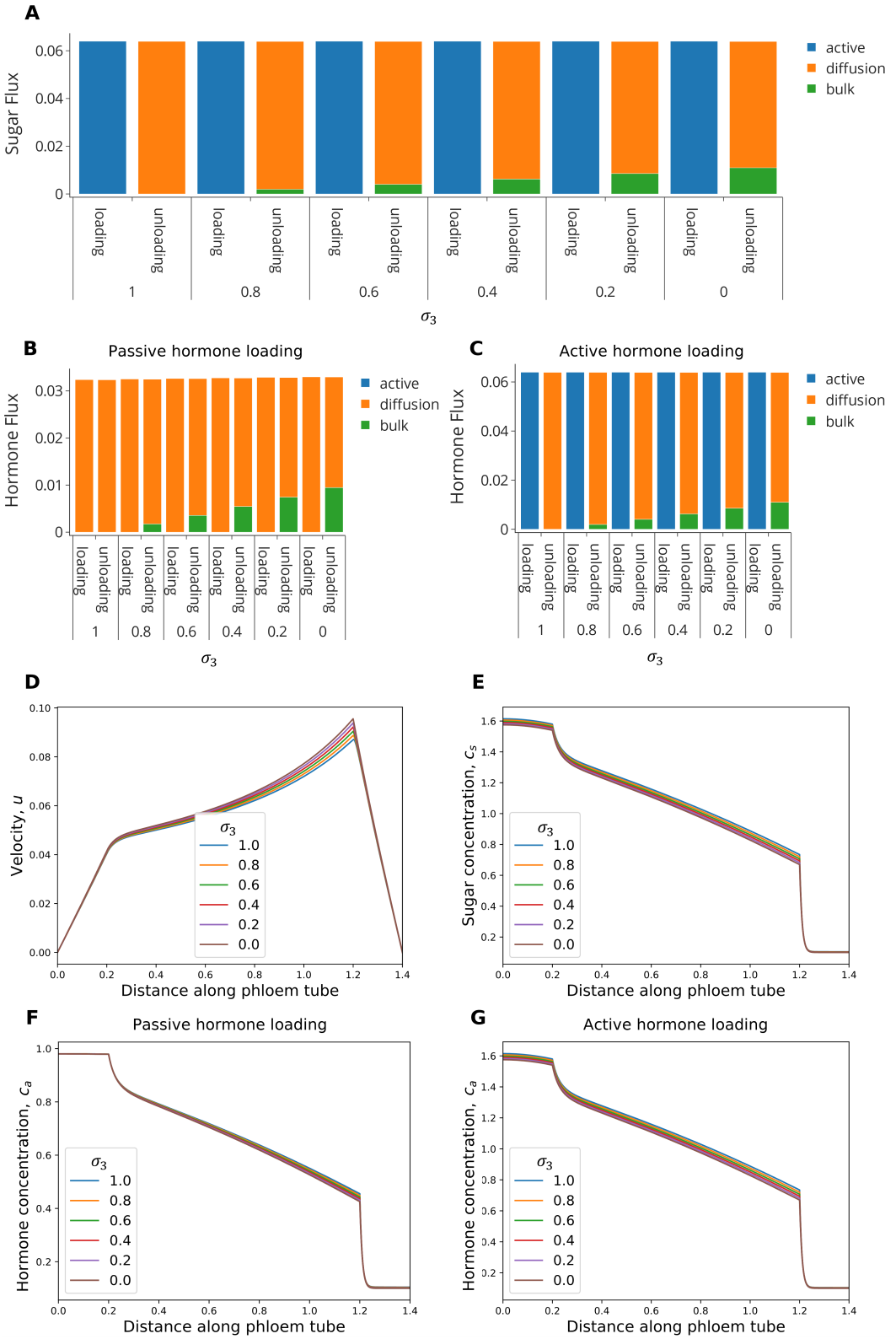


Figure 3.6: Results showing how increasing the Münch number impacts the results of varying the Staverman reflection coefficient for sugar and hormone. Velocity and concentration profiles vary in shape from Figure 3.5 but impact of varying $\sigma_{s,3}/\sigma_{a,3}$ remains consistent. ***(continues)***

Figure 3.6: **(A)** Sugar flux in the loading/unloading zones; **(B)** Hormone flux in the loading/unloading zones for passively loaded hormone; **(C)** Hormone flux in the loading/unloading zones for actively loaded hormone; **(D)** Phloem transport velocity; **(E)** Sugar concentration; **(F)** Hormone concentration for a passively loaded hormone; **(G)** Hormone concentration for an actively loaded hormone. **Sugar parameter values:** as given in Table 3.6 with additional variations to $(\sigma_{s,1}, \sigma_{s,2}, \sigma_{s,3}) = (1, 1, \text{varied})$. **Auxin parameter values:** as given in Table 3.7 with additional variations to $(\sigma_{a,1}, \sigma_{a,2}, \sigma_{a,3}) = (1, 1, \text{varied})$. **Mü** = 12

consistent with the low Münch number scenario (Figure 3.6).

3.6.3 Bulk flow unloading can dominate over diffusive unloading when the ratio between root and shoot external sugar concentrations is increased

The simulations above showed that, for the model parameters given in Tables 3.6 and 3.7, the dominant form of sugar unloading is diffusion (Figures 3.5). However, previous studies suggest that diffusive unloading of sugar alone would not be sufficient to meet the carbon demands for growth in the primary root tip of maize (Bret-Harte and Silk, 1994), and suggest that bulk flow unloading is the dominant form of sugar unloading in Arabidopsis (Ross-Elliott et al., 2017). Motivated by these studies, and the fact that the phloem loading/unloading parameters are not well characterised, we now investigate how the choice of model parameters influences the relative contributions of bulk flow and diffusive unloading.

We performed a systematic search for parameter sets that result in bulk flow unloading of sugar being dominant over diffusive unloading. Focusing on the four key sugar parameters: Staverman reflection coefficient, $\sigma_{s,3}$, rate of diffusive unloading, $\beta_{s,3}$, rate of active loading, $\gamma_{s,1}$, and the ratio between root and shoot external sugar concentrations, $C_{ext,s,3}$, we considered a range of parameters for each variable (see Table 3.8). From these parameter sets, we found multiple parameter regions that resulted in bulk flow unloading being dominant over diffusive unloading.

With a fixed rate of active sugar loading, $\gamma_{s,1}$, we found that increasing the ratio between the root and shoot external sugar concentrations, $C_{ext,s,3}$, results in a larger parameter region where bulk flow unloading is dominant over diffusive unloading (Figure 3.7). In contrast, with a fixed external sugar concentration in the unloading zone, $C_{ext,s,3}$, we see that varying the rate of active sugar loading, $\gamma_{s,1}$, has little impact on the amount of unloading occurring via bulk flow (Figure 3.8).

Parameter	Values
$\sigma_{s,3}$	$(0.0, 0.2, 0.4, 0.6, 0.8, 1.0)$
$\beta_{s,3}$	$(0.1, 0.5, 1.0, 2.5, 5.0)$
$\gamma_{s,1}$	$(0.04, 0.08, 0.16)$
$C_{ext,s,1}$	$(0.1, 0.2, 0.4)$

Table 3.8: Parameter ranges used in parameter search.

In cases where bulk flow unloading is dominant and the rate of diffusion, $\beta_{s,3}$, is small, the model can predict an accumulation of sugar in the unloading zone – a characteristic not currently described in the literature (Figures 3.7 and 3.8). This is likely due to the rate of diffusion being too low to allow the model to meet the prescribed rate of unloading flux (which is fixed for each set of simulations as we fix $\gamma_{s,1}$) without producing an extremely high concentration gradient in the unloading zone down which diffusion can occur. However, there are parameter regions where bulk flow unloading is dominant and no sugar accumulation occurs (for example, if $C_{ext,s,3}$ is sufficiently large, Figure 3.7E).

In summary, the model predicts that bulk flow unloading can be dominant over diffusive unloading. The simulations suggest that for bulk flow to dominate requires a small Staverman reflection co-efficient, $\sigma_{s,3}$, and a large ratio between the root and shoot external sugar concentrations, $C_{ext,s,3}$. Interestingly, we identified parameter regions (typically where the rate of diffusive unloading, $\beta_{s,3}$, is small) in which the model predicts accumulation of sugar in the phloem unloading zone. It is not clear whether such sugar accumulation occurs in the unloading zone of plants such as Arabidopsis that have bulk flow as their dominant form of unloading (Ross-Elliott et al., 2017). Hence, for the remaining simulation results presented, we set model parameters such that bulk flow unloading dominates over diffusive unloading, but with a sugar concentration profile that is consistent with those in the theoretical literature (Jensen et al., 2012, Payvandi et al., 2014), see Table 3.9. As hormones are smaller molecules than sugar, we assume that the hormone parameters are consistent with those specified for sugar (although with either diffusive or active loading), Table 3.10.

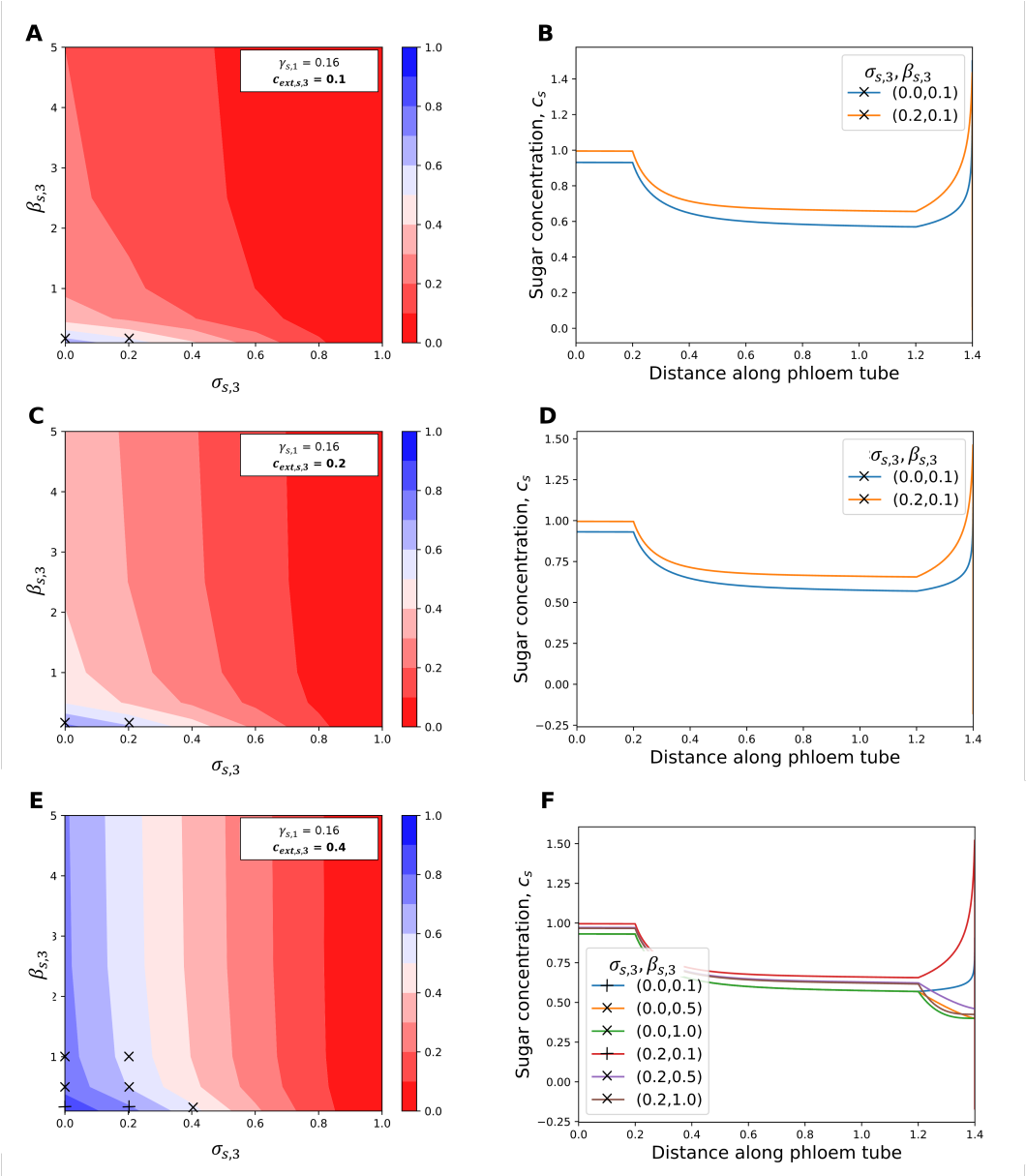


Figure 3.7: Larger external sugar concentration in the unloading zone results in more bulk flow unloading. **(A/C/E)** Contour plots show the fraction of unloading that occurs via bulk flow. Blue shades indicate bulk flow is dominant, red shades indicate diffusive unloading is dominant. Markers show parameter sets plotted in B/D/F – crosses show parameter sets where there is sugar accumulation in the unloading zone, pluses show parameter sets where sugar decreases in the unloading zone. **(B/D/F)** Parameter regimes that result in bulk flow unloading being dominant.

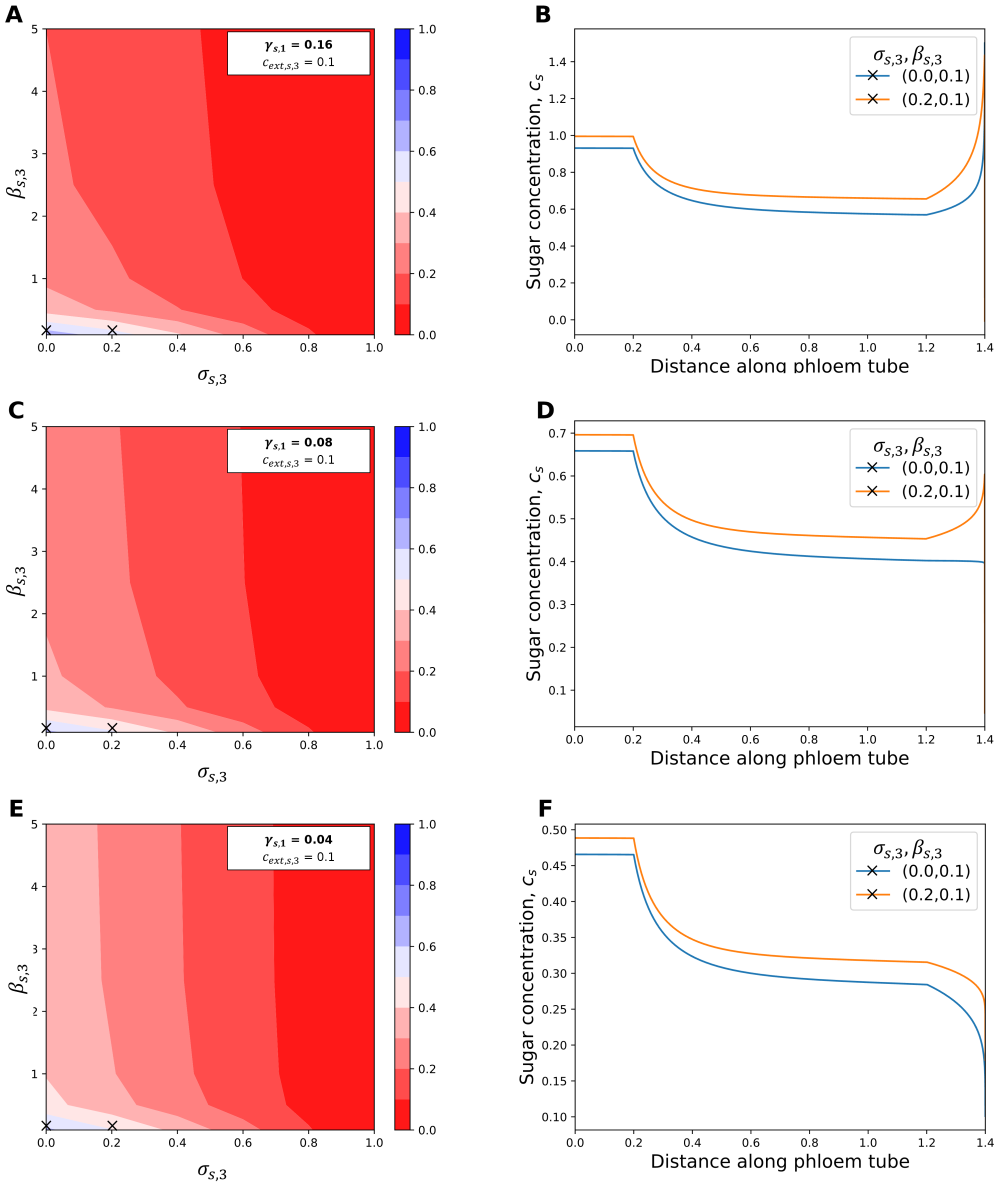


Figure 3.8: Varying active sugar loading has little impact of the dominant form of unloading (which remains diffusive). **(A/C/E)** Contour plots show the fraction of unloading that occurs via bulk flow. Blue shades indicate bulk flow is dominant, red shades indicate diffusive unloading is dominant. Markers show parameter sets plotted in B/D/F – crosses show parameter sets where there is sugar accumulation in the unloading zone, pluses show parameter sets where sugar decreases in the unloading zone. **(B/D/F)** Parameter regimes that result in bulk flow unloading being dominant.

Parameter group	Default values	Parameter description
$(\sigma_{s,1}, \sigma_{s,2}, \sigma_{s,3})$	$(1,1,0.2)$	Bulk flow
$(\beta_{s,1}, \beta_{s,2}, \beta_{s,3})$	$(0,0,1)$	Passive diffusion
$(\gamma_{s,1}, \gamma_{s,2}, \gamma_{s,3})$	$(0.16,0,0)$	Active loading
$(\lambda_{s,1}, \lambda_{s,2}, \lambda_{s,3})$	$(0,0,0)$	Active unloading
$(C_{ext,s,1}, C_{ext,s,2}, C_{ext,s,3})$	$(1,0,0.4)$	External sugar concentration

Table 3.9: Sugar parameters for simulations where bulk flow unloading dominates over diffusive unloading.

Parameter group	Passive hormone loading	Active hormone loading
$(\sigma_{a,1}, \sigma_{a,2}, \sigma_{a,3})$	$(1,1,0.2)$	$(1,1,0.2)$
$(\beta_{a,1}, \beta_{a,2}, \beta_{a,3})$	$(5^*,0,1)$	$(0,0,1)$
$(\gamma_{a,1}, \gamma_{a,2}, \gamma_{a,3})$	$(0,0,0)$	$(0.16,0,0)$
$(\lambda_{a,1}, \lambda_{a,2}, \lambda_{a,3})$	$(0,0,0)$	$(0,0,0)$
$(C_{ext,a,1}, C_{ext,a,2}, C_{ext,a,3})$	$(1,0,0.4)$	$(1,0,0.4)$

Table 3.10: Hormone parameters for model simulations where bulk flow unloading of hormone dominates over diffusive unloading.

3.6.4 Increasing active sugar loading increases phloem transport velocity and increases the rate of delivery of passively loaded hormones

Abiotic stresses, such as drought, heat stress, light intensity, and temperature have been shown to impact sucrose transporters and phloem loading in a range of plants, including Arabidopsis, maize, and wheat (Xu et al., 2018, Knox et al., 2018, Gong et al., 2015). Active sugar loading occurs via SUC transporters and varying the rate of active sugar loading, $\gamma_{s,1}$, in the model is consistent with the relative expression levels of SUC transporters changing under environmental conditions (Xu et al., 2018, Knox et al., 2018, Gong et al., 2015). We investigate how these responses to environmental cues impact hormone delivery to the root tip.

Increasing the rate of active sugar loading, $\gamma_{s,1}$, increases the total sugar loading and unloading (Figure 3.9A) (recalling that at the steady state the total loading and unloading are equal). An increase in the rate of active sugar loading is predicted to result in an increased phloem transport velocity (Figure 3.9D), consistent with experimental results from Knox et al. (2018), and an increase in sugar concentration throughout the phloem (Figure 3.9E), consistent with sucrose concentration within phloem exudate in experimental results from Xu et al. (2018). Interestingly, as the sugar loading rate is increased, the proportion of unloading that occurs via bulk flow unloading decreases (Figure 3.9A) (which is consistent with the parameter survey shown in Figure 3.8). This is due to the increase in the concentration gradient down which diffusive sugar unloading can occur as the phloem sugar concentrations are higher (Figure 3.9E).

For passively loaded hormones, increasing the rate of active sugar loading increases the amount of hormone loaded into the phloem, and hence increases hormone delivery to the root tip (Figure 3.9B). For actively loaded hormones (Figure 3.9C), the proportion of unloading that occurs via bulk flow increases as the rate of active sugar loading is increased (due to the higher phloem transport velocity). These cases suggests that environmental conditions that impact SUC-mediated active sugar transport in the shoot, such as changes in light intensity (Xu et al., 2018, Knox et al., 2018), can influence hormone delivery in the root tip via changes to the phloem transport velocity. For passively loaded hormones, the amount of hormone delivered to the root tip can be influenced by environmental conditions, whereas for actively loaded hormones, environmental conditions can influence which form of unloading dominates.

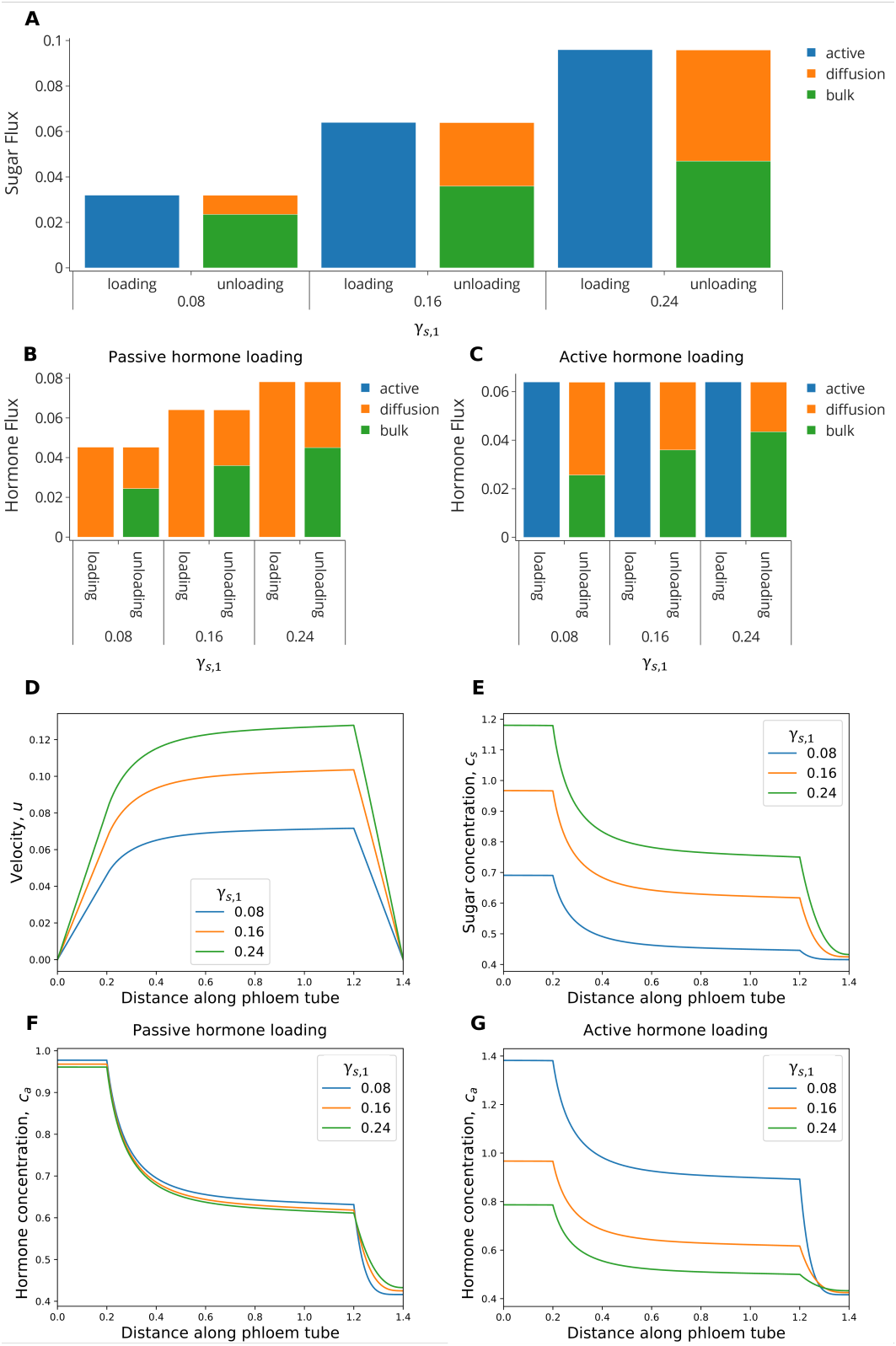


Figure 3.9: Increasing active sugar loading results in a change in the dominant form of unloading, shifting from diffusion dominant to bulk flow dominant as $\gamma_{s,1}$ increases. This occurs alongside an increase to phloem transport velocity. ***(continues)***

Figure 3.9: **(A)** Sugar flux in the loading/unloading zones; **(B)** Hormone flux in the loading/unloading zones for passively loaded hormone; **(C)** Hormone flux in the loading/unloading zones for actively loaded hormone; **(D)** Phloem transport velocity; **(E)** Sugar concentration; **(F)** Hormone concentration for a passively loaded hormone; **(G)** Hormone concentration for an actively loaded hormone. **Sugar parameter values:** as given in Table 3.9 with additional variations to $(\gamma_{s,1}, \gamma_{s,2}, \gamma_{s,3}) = (\text{varied}, 0, 0)$. **Auxin parameter values:** as given in Table 3.10. **Mü** = 0.22

In the case where the hormone is loaded via active transport (Figure 3.9G), we see a decrease in phloem hormone concentration for higher active sugar loading rates, $\gamma_{s,1}$. This is due to the fact that the rate of hormone loading is unchanged, whilst the higher phloem transport velocity transports hormone out of the loading zone more quickly, and hence there are decreased hormone concentrations in the loading zone. In the case where the hormone is loaded passively (Figure 3.9F), the impact of increasing $\gamma_{s,1}$ is the same, however, the impact is far less pronounced as the rate of hormone loading depends on the hormone concentration in the phloem and so the loading rate reduces as the internal hormone concentration approaches the external concentration.

In summary, increasing active sugar loading results in increased phloem transport velocities which influences hormone delivery to the root tip. In the case of actively loaded hormones, the model predicts a shift in the dominant unloading mechanism, whereas for passively loaded hormones, the model predicts an increase in hormone delivery to the root tip.

3.6.5 Increasing the ratio between root and shoot external sugar concentrations has little impact on the unloading of hormones

Modifications to the ratio between root and shoot external sugar concentrations, $C_{ext,s,3}$, can occur either by changes at the shoot or changes at the root. For example, application of exogenous sucrose to the root tip increases the root:shoot external sugar concentration ratio and has been shown to affect phloem transport velocity (Knox et al., 2018). Understanding how application of exogenous sucrose impacts phloem transport is important because some experiments are conducted where sucrose is incorporated into the growth medium, which potentially could influence the hormone delivery to the root tip. Another method of modifying the root:shoot external sugar concentration ratio is via changes in environmental conditions that lead to sugar accumulation in leaves (Xu et al., 2018) which increases the sugar concentration in

the source tissues and would decrease the root:shoot external sugar concentration ratio.

The model predicts a reduction in phloem transport velocity for higher $C_{ext,s,3}$ (Figure 3.10D), as observed in previous experimental studies by Knox et al. (2018). An increase in $C_{ext,s,3}$ is predicted to lead to a higher sugar concentration in the phloem, seen most notably in the unloading zone (Figure 3.10E). The model predicts that increasing $C_{ext,s,3}$ decreases the amount of diffusive sugar unloading and increases the relative contribution of the bulk flow sugar unloading (Figure 3.10A). Increasing $C_{ext,s,3}$ reduces diffusive unloading due to the reduction in the concentration gradient between the phloem sugar concentration and the external sugar concentration.

For both hormone loading scenarios, we see an increase in the phloem hormone concentration as phloem transport velocity is decreased by an increase in $C_{ext,s,3}$ (Figures 3.10F and G – this is consistent with results in Figures 3.9 D, F and G). This is more pronounced in the case where the hormone is loaded actively (Figure 3.10G) as the flux of hormone loaded into the phloem is fixed and, as such, with lower phloem transport velocities, hormone accumulates in the loading zone. For passively loaded hormone, changing $C_{ext,s,3}$ has such a small effect on the phloem hormone concentrations that there is little difference in either the total hormone efflux or the relative contribution of bulk flow unloading (Figure 3.10B).

In summary, increasing the ratio between root and shoot external sugar concentrations, $C_{ext,s,3}$, reduces the phloem transport velocity which is consistent with experimental results from Knox et al. (2018). Whilst changes to $C_{ext,s,3}$ do modify phloem transport velocity, the impact is less pronounced than changes seen when changing $\gamma_{s,1}$, and as such the impact on the unloading of hormone is less pronounced. In the case of passively loaded hormones, the model predicts that changing $C_{ext,s,3}$ has minimal impact on hormone delivery to the root tip.

3.6.6 Varying plasmodesmata density modifies phloem transport velocity though the exact relationship remains unclear

Unloading via diffusion and bulk flow occurs through plasmodesmata. As such, environmental conditions that impact plasmodesmata transport rates or plasmodesmata density will have an effect on the unloading dynamics in the model. Transport via plasmodesmata has been shown to be effected by light levels and the circadian clock (Brunkard and Zambryski, 2019), as well as osmotic stress and cold stress (Sager and Lee (2014) and references therein).

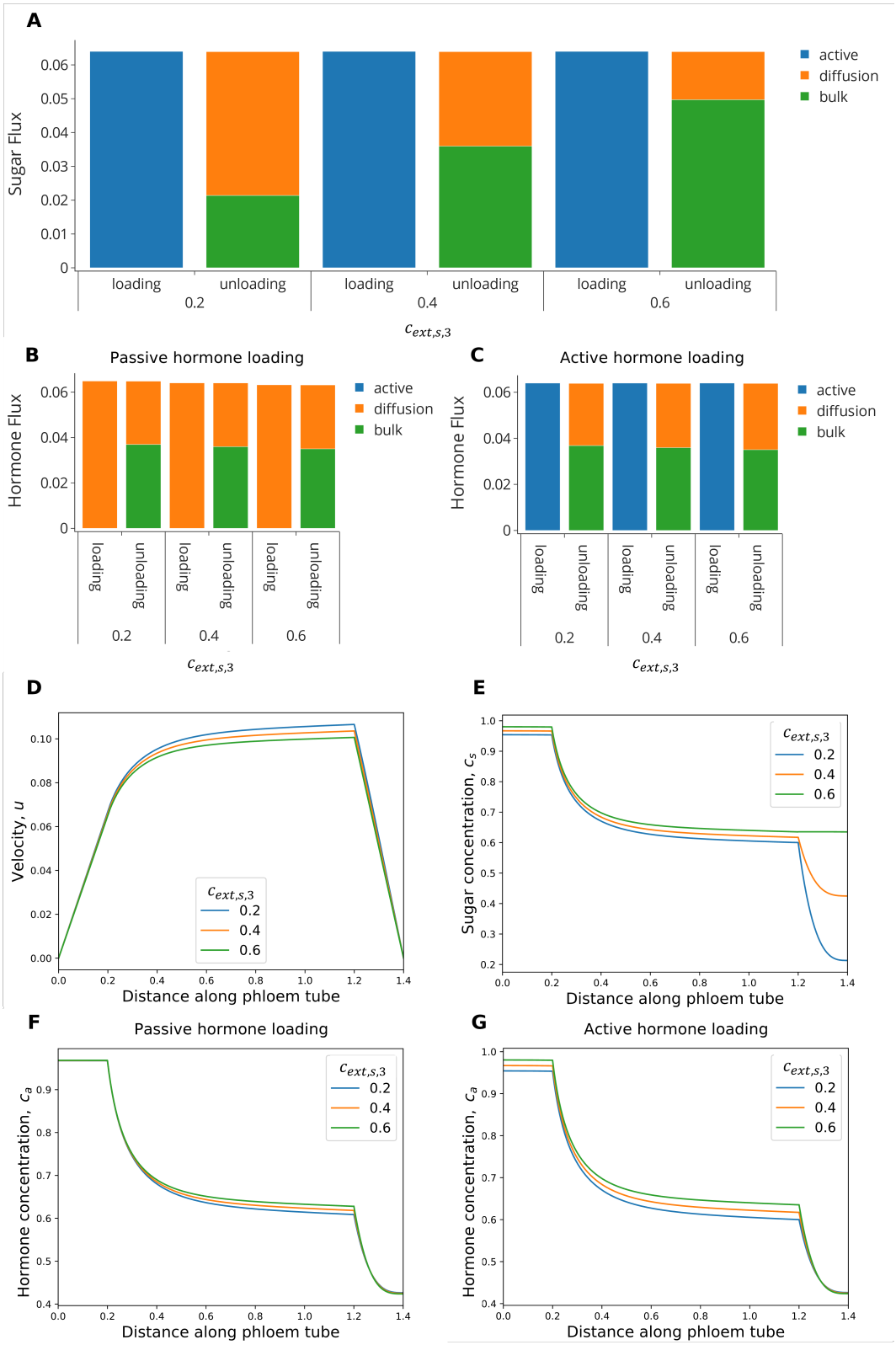


Figure 3.10: Reducing sugar sink strength by increasing $C_{ext,s,3}$, has little impact on the unloading dynamics of hormones. ***(continues)***

Figure 3.10: **(A)** Sugar flux in the loading/unloading zones; **(B)** Hormone flux in the loading/unloading zones for passively loaded hormone; **(C)** Hormone flux in the loading/unloading zones for actively loaded hormone; **(D)** Phloem transport velocity; **(E)** Sugar concentration; **(F)** Hormone concentration for a passively loaded hormone; **(G)** Hormone concentration for an actively loaded hormone. **Sugar parameter values:** as given in Table 3.9 with additional variations to $(C_{ext,s,1}, C_{ext,s,2}, C_{ext,s,3}) = (1, 0, \text{varied})$. **Auxin parameter values:** as given in Table 3.10. **Mü** = 0.22

Changes in plasmodesmata transport rates or plasmodesmata density will affect unloading via both diffusion and bulk flow. As such, to model environmental changes that impact plasmodesmata, we need to vary the diffusion coefficients for sugar and hormone, $\beta_{s,3}, \beta_{a,3}$, as well as the Staverman reflection coefficients for sugar and hormone, $\sigma_{s,3}, \sigma_{a,3}$. Increasing $\beta_{s,3}, \beta_{a,3}$ and decreasing $\sigma_{s,3}, \sigma_{a,3}$ can be considered to represent an increase in plasmodesmata transport rate or an increase in plasmodesmata density. In the following simulations, as we are varying multiple parameters simultaneously, we label the simulations as low, mid, and high to represent a scale from decreased to increased plasmodesmatal transport. Parameter values used in each scenario are given in Table 3.11 and correspond to the region shown in Figure 3.11A.

Plasmodesmata density	$\sigma_{s,3}, \sigma_{a,3}$	$\beta_{s,3}, \beta_{a,3}$
low	0.3	0.5
mid	0.2	1.0
high	0.1	1.5

Table 3.11: Parameter variations used for model scenarios of low, mid, and high plasmodesmata density.

Increasing plasmodesmatal unloading results in an increase in the contribution of bulk flow unloading (Figures 3.11B,C,D). However, it is important to note that this relationship is not well-defined and that alternative definitions of low, mid, and high plasmodesmata density could alter the proportion of unloading that occurs via bulk flow. This is seen most clearly in the curved nature of the contours in Figure 3.11A. For example, an alternative high plasmodesmata density scenario could be $\sigma_{s,3} = 0.175$, $\beta_{s,3} = 1.2$ which would give bulk flow as a fraction of unloading comparable to our current low and mid density scenarios. As such, further investigation is needed to accurately define the relationship between plasmodesmata density and model parameters $\sigma_{s,3}$ and $\beta_{s,3}$.

Increasing transport via plasmodesmata results in an increase in phloem transport

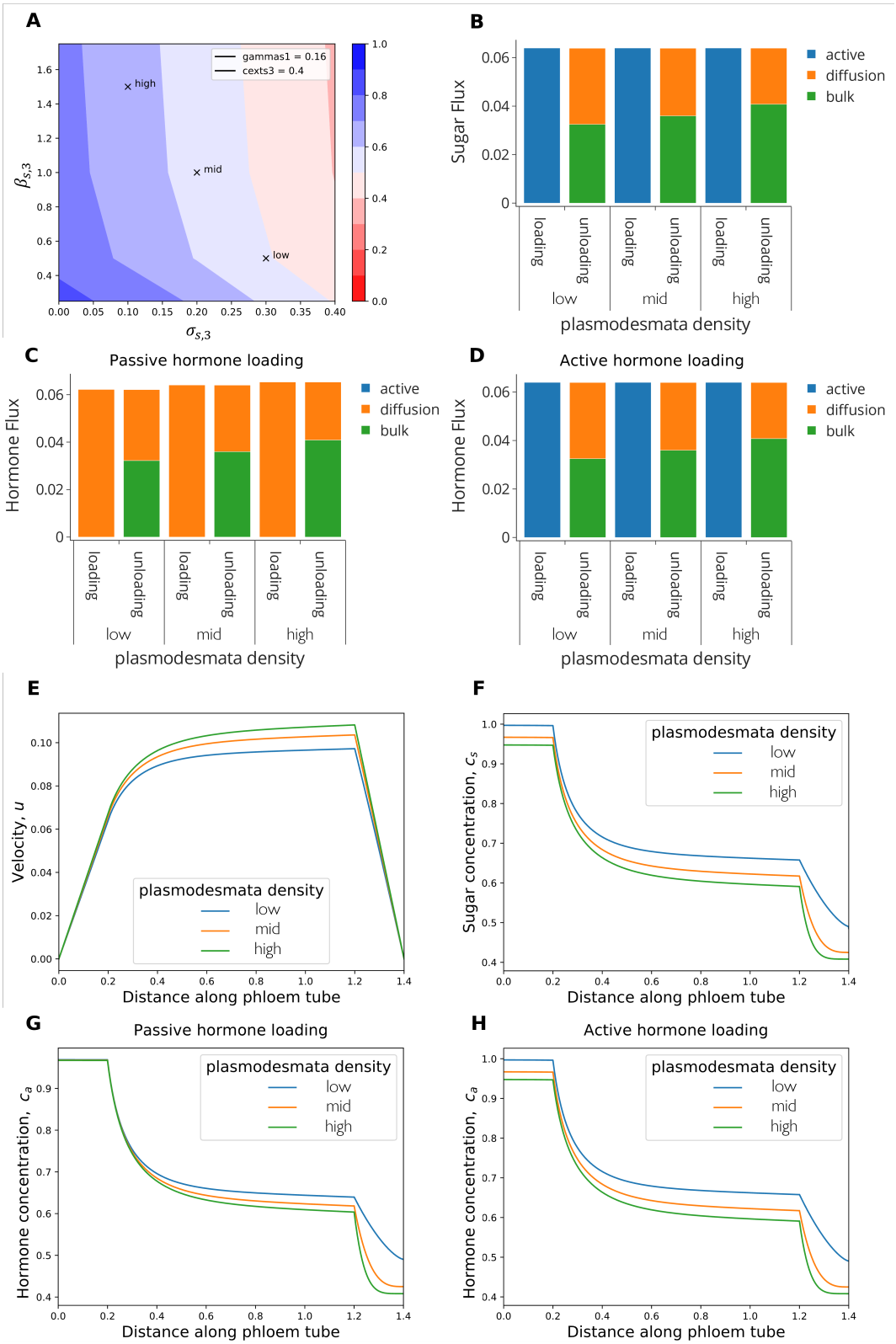


Figure 3.11: **(A)** Contour plot showing parameter region in which low, mid, and high plasmodesmata density scenarios are located. (Contour plots show the fraction of unloading that occurs via bulk flow. Blue shades indicate bulk flow is dominant, red shades indicate diffusive unloading is dominant.); ***(continues)***

Figure 3.11: **(B)** Sugar flux in the loading/unloading zones; **(C)** Hormone flux in the loading/unloading zones for passively loaded hormone; **(D)** Hormone flux in the loading/unloading zones for actively loaded hormone; **(E)** Phloem transport velocity; **(F)** Sugar concentration; **(G)** Hormone concentration for a passively loaded hormone; **(H)** Hormone concentration for an actively loaded hormone. **Sugar parameter values:** as given in Table 3.9 with additional variations to $(\beta_{s,1}, \beta_{s,2}, \beta_{s,3}) = (1, 0, \text{varied})$ and $(\sigma_{s,1}, \sigma_{s,2}, \sigma_{s,3}) = (1, 0, \text{varied})$. **Auxin parameter values:** as given in Table 3.10 with additional variations to $(\beta_{a,1}, \beta_{a,2}, \beta_{a,3}) = (1, 0, \text{varied})$ and $(\sigma_{a,1}, \sigma_{a,2}, \sigma_{a,3}) = (1, 0, \text{varied})$. **Mü** = 0.22

velocity (Figure 3.11E) and a corresponding decrease in phloem sugar concentration (Figure 3.11F). Consistently with the previous results, this results in an increase of hormone efflux in the unloading zone for passively loaded hormones (Figure 3.11C).

Increased phloem transport velocity also leads to a decrease in phloem hormone concentration in both loading scenarios (Figures 3.11G,H – consistent with previous analysis). Whilst changes in phloem transport velocity might lead to small changes in the dominant form of hormone unloading, the changes seen in the contribution to bulk flow unloading seen in Figures 3.11 C and D are most likely caused by the changes in hormone parameters associated with plasmodesmata density.

In summary, the model suggests that increasing plasmodesmata density results in an increase in phloem transport velocity which in turns leads to increased hormone delivery to the root tip for passively loaded hormones.

3.7 Conclusions

In this chapter, we have developed a mathematical model for hormone transport via the phloem that couples hormone and sugar dynamics. This model builds upon the work of (Jensen et al., 2012, 2016, Payvandi et al., 2014), extending existing models in the literature to incorporate hormone transport, bulk flow unloading, and more physical loading/unloading mechanisms.

Focusing on actively loaded sugar, the model predicts that increasing bulk flow sugar unloading or increasing the rate of active sugar loading both increase the phloem transport velocity. For passively loaded hormones, increases in phloem transport velocity are predicted to increase the amount of hormone delivered to the root tip. In contrast, for actively loaded hormone, the model shows that the total hormone delivery is independent of the sugar dynamics and phloem velocity.

Surveying parameter space, we identified regions where bulk flow unloading of

sugar dominates over diffusive unloading as suggested by Ross-Elliott et al. (2017), finding this is predominantly influenced by the choice of a small Staverman reflection co-efficient and a large ratio between shoot and root external sugar concentrations. Although the root to shoot external sugar concentration ratio has a substantial influence on the proportion of bulk flow unloading, the model predicts that increasing this ratio leads to only a small reduction in the phloem transport velocity and limited impact on hormone delivery to the root tip.

The model provides key insights into how environmental conditions that affect the sugar dynamics lead to changes in hormone delivery to the root tip. Active sugar loading is influenced by numerous environmental conditions. The model predictions align with experimental data that showed how increasing the rate of active sugar loading increases phloem transport velocity and phloem sugar concentration. Furthermore, the model predicts that the increase in active sugar loading will increase hormone delivery to the root tip for passively loaded hormones. In contrast, environmental changes that increase the ratio between root and shoot external sugar concentration are predicted to lead to only a small decrease in the phloem transport velocity and have little influence on hormone delivery.

Environmental conditions also influence plasmodesmatal densities and permeabilities and thus, the rates of passive unloading (both diffusive and bulk flow unloading). The model predicts that a higher plasmodesmatal density results in a larger phloem transport velocity, and thus increases the hormone delivery to the root tip for passively loaded hormones.

Overall, our model highlights the important role that sugar dynamics can have on hormone delivery to the root tip. Future modelling work could focus on extending the model described here to capture dynamic changes in the source/sink concentration levels. Furthermore, by deriving the model for general x-dependent external concentration levels our work can be easily extended to scenarios where there are multiple loading/unloading zones, such as unloading of sugar and hormones within growing leaves as well as at root tissues.

Chapter 4

Hybrid model of auxin dynamics in the *Arabidopsis* seedling

4.1 Introduction

To understand in detail how environmental conditions impact auxin patterning, we must consider influences across the seedling (not just in individual organs such as the root tip). In previous chapters, we developed auxin-transport models that focus on specific aspects of auxin transport within a plant. In Chapter 2, we focused on auxin transport within the root tip, presenting a model that captures carrier-mediated auxin transport via influx and efflux carriers, passive diffusion via plasmodesmata, diffusion within cell walls, and auxin synthesis and degradation. This model captures auxin transport in detail at the cell-scale, however, it relies on a constant flux boundary condition to represent transport to the root from the shoot. In Chapter 3, we focused on long-distance transport of auxin via the phloem, creating a continuum model that described how hormone transport is coupled to the transport of sugar and water. This model focuses on long-distance auxin transport; however, the root and shoot environments are not considered and concentrations external to the phloem are assumed constant within the loading and unloading zones.

4.2 Hybrid model development

To develop a virtual Arabidopsis seedling model, in this chapter we seek to couple the models formulated in Chapters 2 and 3. To achieve this, we must first establish

what each model takes as an input and produces as an output, what adjustments to model equations must be made to allow for the coupling of existing models, and what aspects of a virtual seedling are still missing from the new combined model.

Cell-based auxin transport

The cell-based auxin transport model from Chapter 2 produces the following outputs:

- Auxin concentration in each cell and cell-wall compartment;
- DII-VENUS concentrations in each cell and cell-wall compartment.

These outputs are all produced within realistic root-tip geometries. The cell-based model takes as an input a constant flux boundary condition at the shootward boundary. In the hybrid model, this will be changed so that the auxin concentration in phloem cells is fixed by the phloem auxin concentration profile from the phloem model (Figure 4.1, pale blue circles).

Long-distance continuum phloem transport model

The phloem transport model from Chapter 3 produces the following outputs:

- Phloem transport velocity profile;
- Sugar concentration profile;
- Auxin concentration profile.

These are all one-dimensional outputs that vary along the length of the phloem. An important input for the phloem model is the external auxin concentration in the root. In the phloem model, this is a fixed concentration. In the hybrid model, the external auxin concentration will be specified by the root model (Figure 4.1, green step function).

Recognising that the irregular cell shapes found in the realistic root-tip geometries used in the cell-based model would make the process of coupling the models more complicated, we first simplify the cell-based model so that it uses an idealised root-tip geometry (Figure 4.2). This template is based on that used in Mellor et al. (2022) (see Mellor et al. (2022) Supplemental Figure 2), although we include increasing cell lengths in the elongation zone (based on experimental measurements from Band et al. (2012a)). This ensures that each cell file is a straight line which allows for alignment with the phloem transport model. Data in (Ross-Elliott et al., 2017) suggests that the

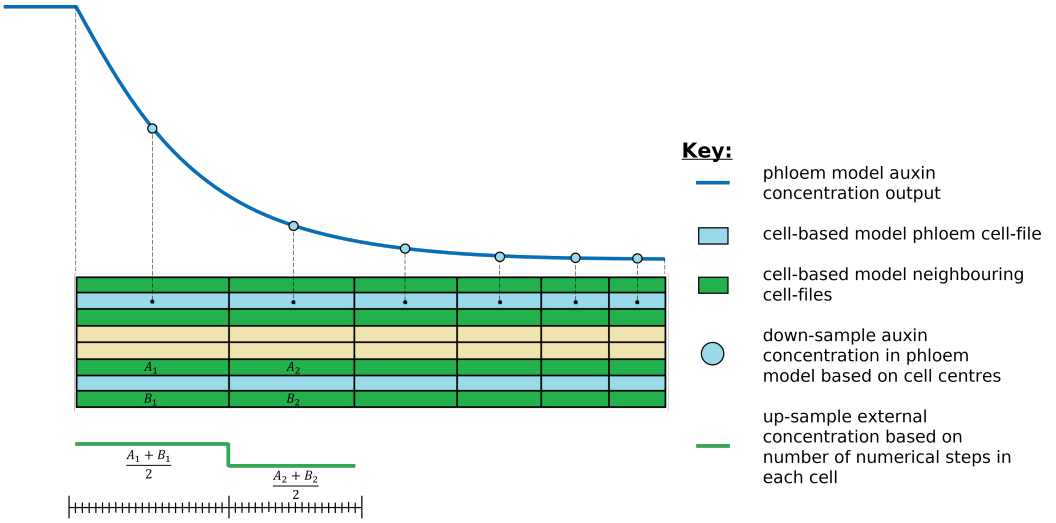


Figure 4.1: Schematic showing how the cell-based auxin transport model provides a piecewise constant external auxin concentration when solving for the phloem auxin concentration $c_a(x)$. When solving the cell-based model, the flux from the phloem into neighbouring cells is approximated based on the phloem concentration $c_a(x)$ at the x-value corresponding to the cell centre.

phloem unloading zone starts at the rootward end of the elongation zone, and has a length of 350µm (which is approximately half the length of the elongation zone). We set the shootward end of the phloem unloading zone to be the boundary of our cell-based model template. To align as closely as possible with the geometry of our phloem model, we take the width (and depth) of the phloem cell files to be $2a$, where a is the radius of the phloem tube in our continuum model.

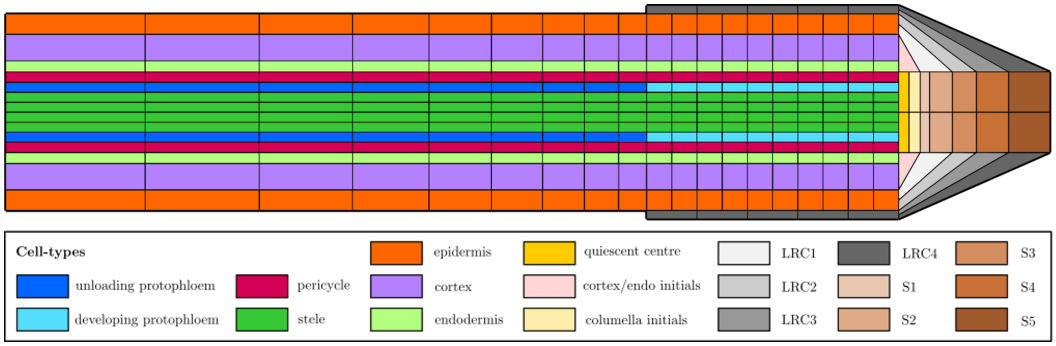


Figure 4.2: Idealised root tip geometry of an Arabidopsis seedling.

Within the idealised root-tip geometry, we have two cell files that represent the phloem. In the hybrid model, these phloem cells are not included in the cell-based root tip submodel. Instead, the auxin concentration in these phloem cells is the solution of the continuum phloem transport model. To obtain a single value for each cell, we sample the auxin concentration from the phloem modelling in the unloading zone at x-values that correspond to cell centres within the cell-based model (Figure 4.1, pale blue circles).

As the cell-based model predicts auxin concentration within each cell, the auxin concentration external to the phloem unloading zone varies spatially, which replaces the fixed external auxin concentration used in the phloem model. Each phloem cell has two neighbouring cells. As the phloem transport model is one-dimensional, we average the concentration in the two neighbouring cells to obtain one external concentration value per phloem cell. Thus, the external hormone concentration in the phloem unloading zone is a piecewise constant function that depends on the average hormone concentration in the cells adjacent to the phloem (Figure 4.1, green step function).

Finally, in the next section, we ensure the fluxes out of the phloem are consistent with the fluxes into the cell-based model (we also introduce bulk flow unloading into the cell-based transport model).

4.2.1 Auxin root dynamics

Recall the ODE for the auxin concentration within a given cell in the cell-based auxin transport model (equation (2.4a), Chapter 2),

$$\frac{d[Auxin]_i}{dt} = \alpha_i - \mu_i[Auxin]_i + \frac{1}{A_i}\sum_{j\in C_i}\sum_{k=1}^{N_{i,j}} S_{i,j,k}(J_{i,j,k} + J^p_{i,j} + B^*_{i,j}), \tag{4.1}$$

where we have introduced the term $B^*_{i,j}$ to represent auxin transport via bulk flow from cell i to cell j, noting that $B^*_{i,j} \neq 0$ only if cell i is a phloem cell. As we are using an idealised root tip geometry, we can make the following simplifications,

- $|C_i| = 4$, the number of neighbours of cell i for non-border cells;
- $N_{i,j} = 1$, the number of cell-wall segments that make up the total shared wall between cell i and cell j;
- $S_{i,j,k} = S_{i,j}$, the length of a segment of cell wall is dependent only on the cells it joins as there is only one cell-wall segment between cells ($S_{i,j} = S_{j,i}$).

For transport into cells that neighbour a phloem cell, we note that $J_{i,j,k} = 0$, if cell i is a phloem cell, given there is no carrier-mediated cell to cell transport (no transport via PINs, ABCBs, AUX1, and LAX) of auxin from phloem cells.

Hence, the combined flux into cells m and n (where cells m and n are adjacent to the

phloem) from neighbouring phloem cell i is given by,

$$J^*_{i,m,n} = J^p_{i,m} + J^p_{i,n} + B^*_{i,m} + B^*_{i,n}. \tag{4.2}$$

The plasmodesmatal flux terms $J^p_{i,m}$ and $J^p_{i,n}$ depend on the concentration gradients between cell i and cells m and n respectively. The concentration in phloem cell i is given by the phloem model concentration $c_{a,3}(x_i)$ where x_i is the centre of cell i (Figure 4.1, pale blue circles). Hence,

$$J^p_{i,j} = J_{pla}([Auxin]_j - c_{a,3}(x_i)). \tag{4.3}$$

The bulk flow fluxes $B^*_{i,m}$ and $B^*_{i,n}$ are only non-zero when cell i is a phloem cell. They are given by,

$$B^*_{i,j} = \hat{v}_i(1-\sigma_{a,3})\left(\frac{[Auxin]_j + c_{a,3}(x_i)}{2}\right), \tag{4.4}$$

where $\hat{v}_i$ is the velocity across the membrane walls of cell i in the cell-based model, and is a value we need to determine from coupling with the phloem model. Hence, the total flux via plasmodesmata into cells m and n from neighbouring phloem cell i is given by,

$$\begin{aligned} J^*_{i,m,n} = {} & J_{pla}([Auxin]_m + [Auxin]_n - 2c_{a,3}(x_i)) \\ & + \hat{v}_i(1-\sigma_{a,3})\left(\frac{[Auxin]_m + c_{a,3}(x_i)}{2} + \frac{[Auxin]_n + c_{a,3}(x_i)}{2}\right). \end{aligned} \tag{4.5}$$

In the phloem model, the flux leaving the phloem takes the form,

$$J^*_{ph} = \beta^*_{a,3}(c_{ext,a,3} - c_{a,3}) + v_{mem}(1-\sigma_{a,3})\bar{c}_{a,3}, \tag{4.6}$$

where $\bar{c}_{a,3} = \frac{c_{a,3}+c_{ext,a,3}}{2}$ and v_{mem} is the velocity across the membrane in the phloem model (defined in equation (3.9), Chapter 4). The number of particles per unit time leaving the cylindrical phloem tube is given by

$$2\pi a \int_{L_1}^{L_1+S_i} J^*_{ph} dx, \tag{4.7}$$

where $x = L_1$ is the shootward end position of cell i and S_i is the length of the walls shared by cell i and cells m and n. We simplify (4.7) by approximating J^*_{ph} to be

uniform across the length of cell i,

$$2\pi a \int_{L_1}^{L_1+S_i} J^*_{ph} dx \approx 2\pi a S_i \left[\beta^*_{a,3} \left(\frac{[Auxin]_m + [Auxin]_n}{2} - c_{a,3}(x_i) \right) + v_{mem}(x_i)(1-\sigma_{a,3}) \left(\frac{c_{a,3}(x_i) + \frac{[Auxin]_m + [Auxin]_n}{2}}{2} \right) \right]. \quad (4.8)$$

where, using model approximations, we have taken $c_{ext,a,3} = \frac{[Auxin]_m + [Auxin]_n}{2}$ and $c_{a,3} = c_{a,3}(x_i)$ to be constant across a cell length. We have also approximated the velocity across the membrane of the phloem by the velocity across the membrane at x_i (the centre of cell i).

We set (4.8) to be equal to the number of particles per unit time through the side wall of the adjacent cuboidal cells m and n, given by

$$\begin{aligned} &2\pi a S_i \left[\beta^*_{a,3} \left(\frac{[Auxin]_m + [Auxin]_n}{2} - c_{a,3}(x_i) \right) + v_{mem}(x_i)(1-\sigma_{a,3}) \left(\frac{c_{a,3}(x_i) + \frac{[Auxin]_m + [Auxin]_n}{2}}{2} \right) \right] \\ &= 2S_i a \left[(J_{pla}([Auxin]_m + [Auxin]_n - 2c_{a,3}(x_i)) + \hat{v}_i(1-\sigma_{a,3}) \left(\frac{[Auxin]_m + c_{a,3}(x_i)}{2} + \frac{[Auxin]_n + c_{a,3}(x_i)}{2} \right) \right], \end{aligned} \quad (4.9)$$

recalling that we have taken the depth of the phloem cell i to be $2a$.

We can now equate and simplify terms in (4.9) to obtain,

$$J_{pla} = \frac{\pi}{2} \beta^*_{a,3}, \quad (4.10a)$$

$$\hat{v}_i = \frac{\pi}{2} v_{mem}(x_i). \quad (4.10b)$$

This has allowed us to obtain the model parameters J_{pla} and $\hat{v}_i$ in terms of the phloem transport model parameters $\beta^*_{a,3}$ and $v_{mem}(x_i)$.

The phloem transport model in Chapter 3 is nondimensionalised meaning simulation outputs are in terms of dimensionless parameters $\beta_{a,3}$ and dimensionless velocity $\mathscr{V}_0$.

Hence, we rewrite equations (4.10) in terms of the dimensionless parameters,

$$J_{pla} = \frac{\pi a U}{2L}\beta_{a,3}, \tag{4.11a}$$

$$\hat{v}_i = \frac{\pi a U}{2L}\mathscr{V}_0(X_i), \tag{4.11b}$$

where X_i is the nondimensionalised centre of cell i, $U = 23\mu s^{-1}$ is the phloem sap viscosity, $a = 1.8\mu m$ is the phloem tube radius, and $L = 30.6mm$ is the characteristic length of the phloem translocation zone.

We have now combined the auxin transport models from Chapter 2 and 3 to create a hybrid model of auxin transport where delivery of auxin to the root tip is governed by the long-distance transport of auxin from shoot to root. Note that the derivation above is for one of the phloem cell files within the model. Derivations for the second phloem cell file are identical. Table 4.1 lists key model parameters and variables for the coupled hybrid model.

4.2.2 Incorporating a shoot compartment

In the previous section, we coupled the long-distance phloem transport of auxin to cell-to-cell based auxin transport in the root tip. To complete the seedling model, we require the addition of a shoot compartment (in which we have equations governing sugar and auxin concentration) and a root compartment to capture the consumption of sugar at the root tip.

Generally, the rate of change of the number of molecules of a solute in a compartment equals the flux per unit area into the compartment multiplied by the appropriate membrane area plus production and degradation of the solute within the compartment. Thus, with J denoting the flux into the phloem (and recalling there are two phloem cell files in a root tip), we have the following equations that describe the sugar concentration (subscript s) and auxin concentration (subscript a) in the shoot compartment (subscript 1),

$$V_{leaf}\frac{dc_{ext,s,1}}{dt^*} = V_{leaf}\alpha_{ext,s,1} - V_{leaf}\mu_{ext,s,1}c_{ext,s,1} - 4\pi a\int_0^{X_1^*} J_{s,1}dx, \tag{4.12a}$$

$$V_{leaf}\frac{dc_{ext,a,1}}{dt^*} = V_{leaf}\alpha_{ext,a,1} - V_{leaf}\mu_{ext,a,1}c_{ext,a,1} - 4\pi a\int_0^{X_1^*} J_{a,1}dx, \tag{4.12b}$$

Parameter	Dimensions	Description
$[Auxin]_i$	mol/μm^3	concentration of auxin in cell i (cell-based model)
$c_{p,q}$	mol/μm^3	concentration of solute in the phloem (phloem model)
$c_{ext,p,q}$	mol/μm^3	concentration of solute in the external tissue (phloem model)
$\bar{c}_{p,q}$	mol/μm^3	average concentration of solute in the membrane ; $\frac{c_{p,q}+c_{ext,p,q}}{2}$
$\alpha_{ext,p,q}$	mol/μm^3/s	production of solute (in shoot and root compartments)
$\mu_{ext,p,q}$	s^{-1}	solute degradation rate (in shoot and root compartments)
$\gamma_{p,1}$	μm/s	active solute loading rate
$\beta_{p,3}$	μm/s	rate of solute diffusive unloading
$\sigma_{p,3}$	-	Staverman reflection coefficient
V_{leaf}	117μm^3	volume of leaf pool (Vanhaeren et al., 2010)
V_{root}	μm^3	volume of root pool (dependent on root-tip geometry)
a	1.8μm	radius of phloem tube (Ross-Elliott et al., 2017)
L	30.6mm	length of phloem tube (Martin et al., 2002)
ε	5.9×10^{-5}	a/L
U	23μm/s	typical phloem sap velocity (Ross-Elliott et al., 2017)
V_0	μm/s	velocity of water across membrane (phloem model)
S_i	μm	length of cell i (dependent on root-tip geometry)
d_i	μm	depth of cell i (dependent on root-tip geometry)

Table 4.1: Description of model parameters in dynamic shoot and root compartments. Subscripts: $p \in \{s,a\}$; $q \in \{1,3\}$ where s is sugar and a is auxin, with 1 and 3 representing the loading and unloading zones respectively.

where,

$$J_{s,1} = \gamma^*_{s,1} c_{ext,s,1}, \tag{4.13a}$$

$$J_{a,1} = \gamma^*_{a,1} c_{ext,a,1}, \tag{4.13b}$$

represent the flux into the phloem, which we assume to be active loading for both sugar and auxin. Table 4.1 includes a list of descriptions for the parameters and terms used in the compartment models.

We nondimensionalise the system using the following relationships,

$$\begin{aligned}
(c_{s,1}, c_{ext,s,1}) &= \frac{\hat{\alpha}_{ext,s}}{\hat{\mu}_{ext,s}}(C_{s,1}, C_{ext,s,1}),\\
\gamma^*_{s,1} &= \varepsilon U \gamma_{s,1},\\
t^* &= \frac{1}{\hat{\mu}^*} t,\\
X_1^* &= L X_1\\
(c_{a,1}, c_{ext,a,1}) &= \frac{\hat{\alpha}_{ext,a}}{\hat{\mu}_{ext,a}}(C_{a,1}, C_{ext,a,1}),\\
\gamma^*_{a,1} &= \varepsilon U \gamma_{a,1},
\end{aligned}$$

where $\hat{\alpha}_{ext,s}, \hat{\mu}_{ext,s}, \hat{\alpha}_{ext,a}$, and $\hat{\mu}_{ext,a}$ represent typical production and degradation rates of sugar and auxin respectively, $\hat{\mu}^*$ represents a typical time-scale for our system, ε is the phloem aspect ratio, U is a typical phloem velocity, and L is the length of the phloem.

Thus, the non-dimensionalised shoot compartment equations for sugar and auxin are given by,

$$\frac{dC_{ext,s,1}}{dt} = \left[\frac{\alpha_{ext,s,1}}{\hat{\alpha}_{ext,s}} - \frac{\mu_{ext,s,1}}{\hat{\mu}_{ext,s}} C_{ext,s,1} - \frac{4\pi a^2 X_1 U}{V_{leaf}\hat{\mu}_{ext,s}} \gamma_{s,1} C_{ext,s,1}\right] \frac{\hat{\mu}_{ext,s}}{\hat{\mu}^*} \tag{4.14a}$$

$$\frac{dC_{ext,a,1}}{dt} = \left[\frac{\alpha_{ext,a,1}}{\hat{\alpha}_{ext,a}} - \frac{\mu_{ext,a,1}}{\hat{\mu}_{ext,a}} C_{ext,a,1} - \frac{4\pi a^2 X_1 U}{V_{leaf}\hat{\mu}_{ext,a}} \gamma_{a,1} C_{ext,a,1}\right] \frac{\hat{\mu}_{ext,a}}{\hat{\mu}^*} \tag{4.14b}$$

Since we focus on steady-state solutions of the hybrid model, we use equations (4.14) to obtain formula for the steady-state concentrations for the external concentration of solutes in the shoot. Hence, the steady-state external solute concentrations in the

shoot are given by,

$$C_{ext,s,1} = \frac{\dfrac{\alpha_{ext,s,1}}{\hat{\alpha}_{ext,s}}}{\dfrac{\mu_{ext,s,1}}{\hat{\mu}_{ext,s}} + \dfrac{4\pi a^2 X_1 U}{V_{leaf}\hat{\mu}_{ext,s}}\gamma_{s,1}}, \tag{4.15a}$$

$$C_{ext,a,1} = \frac{\dfrac{\alpha_{ext,a,1}}{\hat{\alpha}_{ext,a}}}{\dfrac{\mu_{ext,a,1}}{\hat{\mu}_{ext,a}} + \dfrac{4\pi a^2 X_1 U}{V_{leaf}\hat{\mu}_{ext,a}}\gamma_{a,1}}. \tag{4.15b}$$

4.2.3 Sugar root dynamics

To complete the virtual seedling model, we incorporate a root compartment for sugar. We capture the root dynamics with an organ-scale compartment representing a simplified root. The root compartment includes production and degradation as well as influx from the phloem. This root pool is established in a similar method to that described for the shoot sugar pool in Section 4.2.2. We have the following equation describing sugar concentration in the root compartment,

$$V_{root}\frac{dc_{ext,s,3}}{dt^*} = V_{root}\alpha_{ext,s,3} - V_{root}\mu_{ext,s,3}c_{ext,s,3} - 4\pi a\int_{X_2^*}^{X_3^*} J_{s,3}dx, \tag{4.16}$$

where the flux term, $J_{s,3}$, is given by,

$$J_{s,3} = \beta^*_{s,3}(c_{ext,s,3} - c_{s,3}) + v_0(1-\sigma_{s,3})\bar{c}_{s,3}, \tag{4.17}$$

and represents sugar unloading from the phloem via diffusion and bulk flow (here $\bar{c}_{s,3} = {}^{c_{s,3}+c_{ext,s,3}}\!/_3$ as defined in the phloem model). Table 4.1 includes the model parameters used in the root compartment model.

We nondimensionalise the system using the following relationships,

$$\begin{aligned}(c_{s,3}, c_{ext,s,3}) &= \frac{\hat{\alpha}_{ext,s}}{\hat{\mu}_{ext,s}}(C_{s,3}, C_{ext,s,3}),\\ \beta^*_{s,3} &= \varepsilon U \beta_{s,3},\\ v_0 &= \varepsilon U V_0,\\ t^* &= \frac{1}{\hat{\mu}^*} t,\\ (X_2^*, X_3^*) &= L(X_1, X_2)\end{aligned}$$

This yields the non-dimensional equation for the external sugar concentration in the root as,

$$\begin{aligned}\frac{dC_{ext,s,3}}{dt} = \Bigg[&\frac{\alpha_{ext,s,3}}{\hat{\alpha}_{ext,s}} - \frac{\mu_{ext,s,3}}{\hat{\mu}_{ext,s}} C_{ext,s,3}\\ &- \frac{4\pi a^3 U}{V_{root}\hat{\mu}_{ext,s}} \int_{X_2}^{X_3} \beta_{s,3}(C_{ext,s,3} - C_{s,3}) + V_0(1-\sigma_{s,3})\bar{C}_{s,3} dX \Bigg] \frac{\hat{\mu}_{ext,s}}{\hat{\mu}^*}.\end{aligned} \tag{4.18}$$

Resolving equation (4.18) at steady state, we yield the external sugar concentration in the root as,

$$C_{ext,s,3} = \frac{\frac{\alpha_{ext,s,3}}{\hat{\alpha}_{ext,s}} + \frac{4\pi a^2 U}{V_{root}\hat{\mu}_{ext,s,1}} \int_{X_2}^{X_3} \left(\beta_{s,3} - \frac{V_0(1-\sigma_{s,3},)}{2}\right) C_{s,3} dX}{\frac{\mu_{ext,s,3}}{\hat{\mu}_{ext,s}} + \frac{4\pi a^2 U}{V_{root}\hat{\mu}_{ext,s}} \int_{X_2}^{X_3} \left(\beta_{s,3} + \frac{V_0(1-\sigma_{s,3})}{2}\right) dX}. \tag{4.19}$$

4.2.4 Summary

In this section, we have developed a mathematical model that describes sugar and auxin dynamics across an Arabidopsis seedling. Simplified shoot dynamics for sugar and auxin are given by equations (4.15), long-distance transport of sugar and auxin is described alongside phloem water flow and pressure by equations (3.36), and sugar and auxin dynamics are captured in the root tip by equations (4.19) and (4.1). Together these equations formulate a multiscale model of auxin transport within an Arabidopsis seedling.

4.3 Numerical simulations

Numerical simulations for the cell-based submodel and continuum phloem submodel are solved using the numerical techniques described in Chapters 2 and 3 respectively. To combine these simulations into a complete simulation of the hybrid model, we use a predictor-corrector method (Figure 4.3). In this method, we run the phloem model simulations for an initial estimate of the external auxin concentration in the unloading zone. We then run the cell-based model using the phloem auxin concentration results as the fixed auxin concentration within phloem cells (using our approximations shown in Figure 4.1). We then re-run the phloem model, with updated external auxin concentration predictions from the cell-based model (using the approximations in Figure 4.1). We repeat these steps until the Euclidean distance between consecutive cell-based model outputs is less than 10^{-3}. At this point, we consider our model converged.

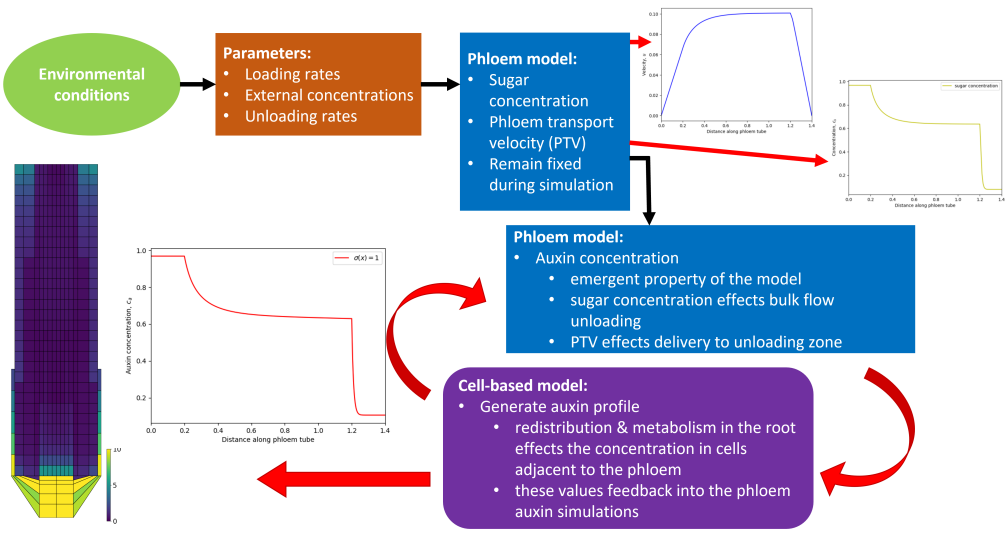


Figure 4.3: Predictor-corrector method for hybrid model simulations.

4.4 Investigating the relationship between parameters J_{pla} and $\beta_{a,3}$

The relationship between model parameters J_{pla} and $\beta_{a,3}$ is important as it ensures the diffusive flux via plasmodesmata is consistent across the two model scales. In

the cell-based auxin transport model from Chapter 2, J_{pla} is defined as,

$$J_{pla} = P_{pla} d_{i,j}, \tag{4.20}$$

where P_{pla} is the permeability per plasmodesmata (μm^3/s) and $d_{i,j}$ is the density of plasmodesmata between cells i and j (μm^{-2}). The cell-based model uses a value of $P_{pla} = 0.806$μm^3/s based on experimental measurements in (Rutschow et al., 2011) and (Zhu et al., 1998). However, this value of P_{pla} is for simple plasmodesmata (as defined by Ross-Elliott et al. (2017)) and it is reported that funnel-shaped plasmodesmata play an important role in phloem unloading in Arabidopsis (Ross-Elliott et al., 2017). Model parameter $\beta^*_{a,3}$ (μm/s) represents the rate of diffusive unloading of auxin in the phloem transport model. The simulations of the phloem model in Chapter 3 use the nondimensional parameter value $\beta_{a,3} = 1$ ($\beta^*_{a,3} = \varepsilon U \beta_{a,3}$) as initial simulations suggest this allows for bulk flow unloading to dominate over diffusive unloading as reported by Ross-Elliott et al. (2017).

Using the phloem transport model parameter value $\beta_{a,3} = 1$, we obtain a value of $J_{pla} = 3.5 \times 10^{-3}$μm^3/s (for the smallest phloem cell in the elongation zone) via equation (4.11a). This is significantly smaller than the value used in the cell-based model which is approximately 2μm^3/s. To obtain a value of J_{pla} consistent with the value used in the cell-based model, we require $\beta_{a,3} > 500$. Hence, it is unclear how best to select a value for $\beta_{a,3}$ (and hence J_{pla}) for the combined hybrid model.

Hence, we first seek to investigate the role $\beta_{a,3}$ has on model outputs. We run model simulations for the full hybrid model for a range of $\beta_{a,3}$ values ($\beta_{s,3}$ varies in the same manner as diffusion coefficients are expected to be comparable in size for the two solutes). We wish to establish which values maintain bulk flow unloading as the dominant form of phloem unloading for sugar, as well as how variations in $\beta_{a,3}$ impact the auxin concentration profile in the phloem unloading zone (Figure 4.4). Table 4.2 includes the default simulation parameter values around which all parameter value variations are based.

The most crucial result we see from these model variations is that the flux into the phloem does not always equal the flux out, which contradicts our steady-state approximation. The model approximation that the phloem concentration can be represented by the concentration at the centre of cells (Figure 4.1) when calculating fluxes is only appropriate if phloem concentrations are approximately linear over a cell length. As such, when model simulations result in steep sugar and auxin concentration profiles in the phloem unloading zone (when $\beta_{a,3}$ and $\beta_{s,3}$ values are greater than or equal to 10) the accuracy of the model approximations decreases and

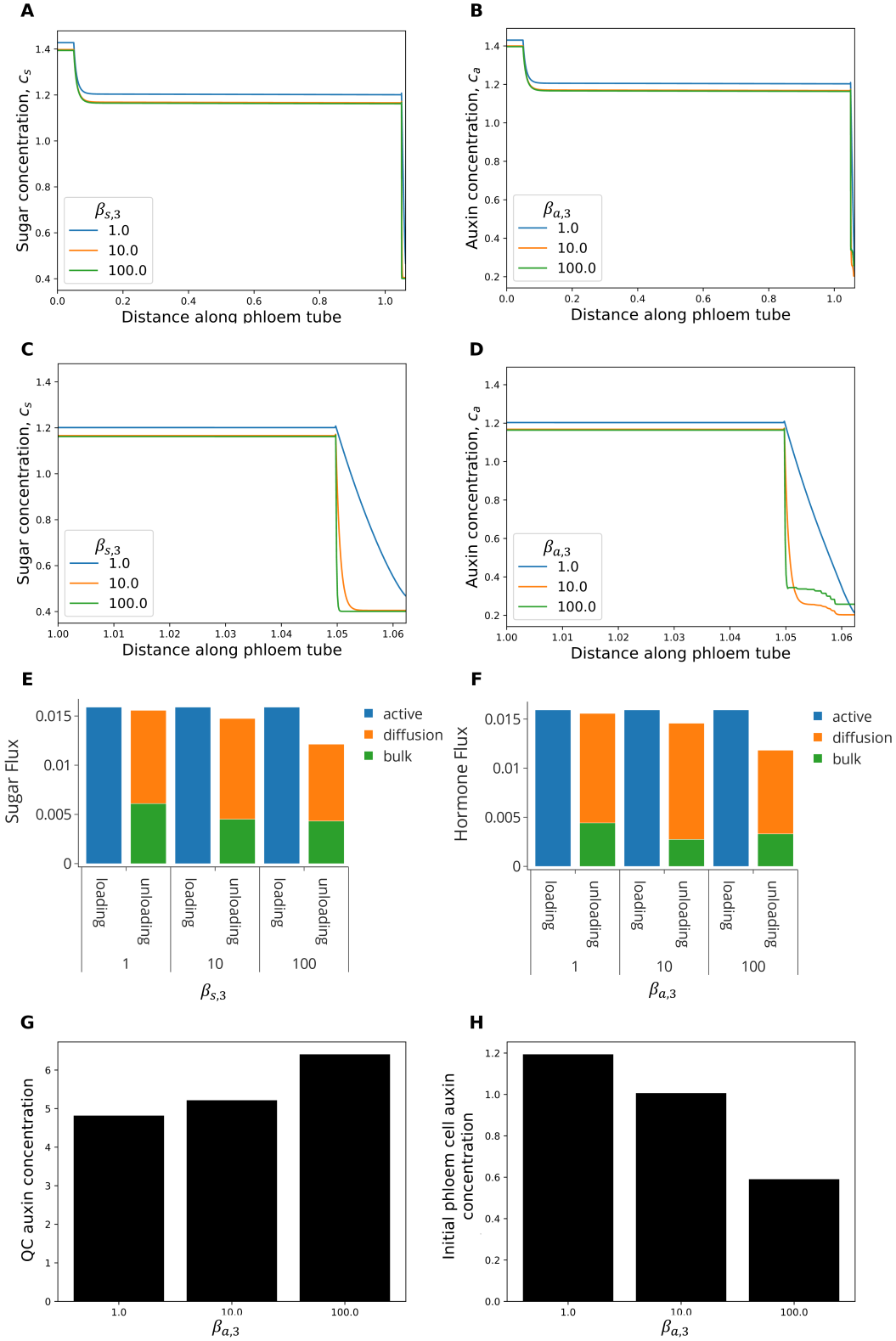


Figure 4.4: Investigating the effect of varying $\beta_{a,3}$ (and its relationship with J_{pla}) on hybrid model simulations. **(A)** Sugar concentration in the phloem; **(B)** Auxin concentration in the phloem; **(C)** Sugar concentration in the phloem unloading zone; **(D)** Auxin concentration in the phloem unloading zone; **(E)** Sugar influx and efflux; **(F)** Auxin influx and efflux; **(G)** Average auxin concentration across quiescent centre cells in the root tip; **(H)** Auxin concentration in the phloem cell at the shootward end of the root-tip template.

Parameter	Value
$\gamma_{s,1}$, $\gamma_{a,1}$	0.16
$\beta_{s,3}$, $\beta_{a,3}$	1
$\sigma_{s,3}$, $\sigma_{a,3}$	0.2
$\alpha_{s,1}$, $\alpha_{a,1}$	1 mol·μm^{-3}s^{-1}
$\mu_{s,1}$, $\mu_{a,1}$	0.1 mol·μm^{-3}s^{-1}
$\alpha_{s,3}$	0.4 mol·μm^{-3}s^{-1}
$\mu_{s,3}$	0.1 mol·μm^{-3}s^{-1}
$\hat{\alpha}_{ext,s}$, $\hat{\alpha}_{ext,a}$	1 mol·μm^{-3}s^{-1}
$\hat{\mu}_{ext,s}$, $\hat{\mu}_{ext,a}$	0.1 mol·μm^{-3}s^{-1}

Table 4.2: Default parameters used throughout model simulations.

we end up with discrepancies between flux values into and out of the phloem. In these cases, the concentration in the phloem reaches parity with the external concentration within one cell-length. Experimental data from Ross-Elliott et al. (2017) shows that unloading occurs along the whole length of the phloem unloading zone. Thus, large values of $\beta_{a,3}$ and $\beta_{s,3}$ that result in phloem concentrations reaching parity with external concentrations within one cell length are inconsistent with experimental observations. As such, for our model approximations to be valid, we require values for $\beta_{a,3}$ and $\beta_{s,3}$ that result in slowly varying sugar and auxin concentrations in the unloading zone. As such, we continue further investigations with the parameter values $\beta_{a,3} = 1 = \beta_{s,3}$.

4.5 Investigating the impact of environmental conditions on root-tip auxin patterning

In Chapter 3, we investigated how environmental conditions that impact sugar dynamics affect auxin delivery to the root tip. We modelled variations in active sugar loading, which can be affected by changes in the temperature, variations in the external sugar concentration in sink tissues, which can occur when plants are grown on medium containing sucrose, and variation in plasmodesmata density (Knox et al., 2018, Xu et al., 2018, Gong et al., 2015). However, variations in environmental conditions affect more than just the sugar signalling mechanisms. In fact, auxin production has been shown to respond to changes in environmental cues (Mroue

et al. (2018) and references therein).

In this section, we investigate the impact of varying environmental conditions on root-tip auxin patterning. We simulate variations in temperature, application of exogenous sucrose, and variation in plasmodesmata density. We incorporate changes to both sugar and auxin parameters triggered by changes in environmental cues in a step-by-step process. First, we model variations to the sugar parameters only. Secondly, we model variations to auxin parameters. Finally, we vary the sugar and auxin parameters simultaneously to understand their combined effect on root-tip auxin patterning.

4.5.1 Temperature variation

In the face of global climate change, plants are more likely to be exposed to non-seasonal temperatures. As such, it is important to understand how variations in temperature impact plant development. Knox et al. (2018) show that there are increased levels of AtSUC2 expression in Arabidopsis seedlings grown at higher temperatures. AtSUC2 is the main transporter for loading sugar into the phloem in the shoot. We can model increased AtSUC2 levels by increasing the model parameter $\gamma_{s,1}$, which represents the rate of active sugar loading (Figures 4.5 and 4.6).

Consistent with the results presented in Figure 3.9 and reported experimentally by Knox et al. (2018), the hybrid model predicts that increases in $\gamma_{s,1}$ result in increased phloem transport velocity which leads to decreased auxin concentrations in the phloem (Figure 4.5B,D,H). Decreased auxin concentrations in the phloem give rise to a small decrease in auxin concentration in the root tip (Figure 4.5G). However, the reduction in root-tip auxin concentration is minimal and does not impact the overall auxin pattern within the root tip (Figure 4.6). This is likely due to the small scale of fluxes leaving the phloem compared to the fluxes caused by carrier-mediated transport within the root tip.

Temperature has also been shown to have an effect on auxin production in the shoot. Arabidopsis seedlings grown under higher temperatures have been shown to have an increased auxin concentration in the shoot which correlates with an up-regulation of auxin biosynthesis genes in the shoot (Stavang et al., 2009, Franklin et al., 2011, Sun et al., 2012, Mroue et al., 2018). To capture these changes within the model simulations, we vary the model parameter $\alpha_{ext,a,1}$, which represents the rate of auxin production within the shoot compartment (Figures 4.7 and 4.8).

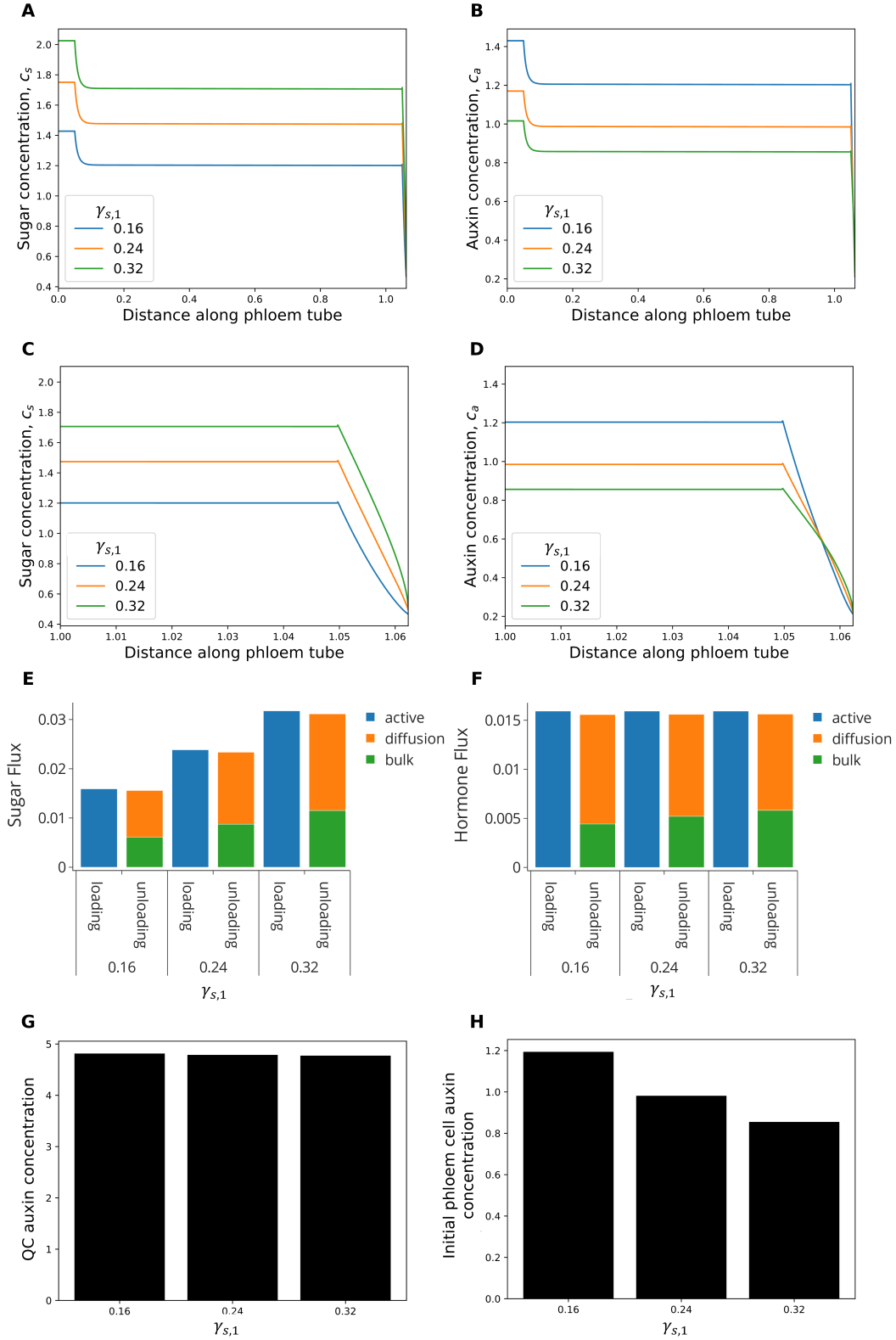


Figure 4.5: Varying the rate of active sugar loading. **(A)** Sugar concentration in the phloem; **(B)** Auxin concentration in the phloem; **(C)** Sugar concentration in the phloem unloading zone; **(D)** Auxin concentration in the phloem unloading zone; **(E)** Sugar influx and efflux; **(F)** Auxin influx and efflux; **(G)** Average auxin concentration across quiescent centre cells in the root tip; **(H)** Auxin concentration in the phloem cell at the shootward end of the root-tip template.

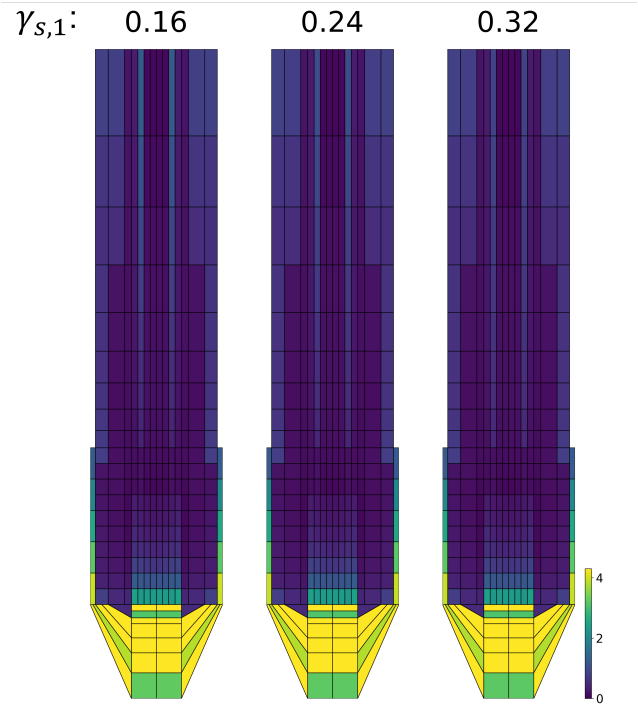


Figure 4.6: Root tip auxin distribution outputs from simulations varying the rate of active sugar loading.

Increasing the rate of auxin production in the shoot significantly increases the auxin concentration within the phloem (Figure 4.7B,D,H). It also increases the amount of auxin that is delivered to the root tip (Figure 4.7F). The increased quantities of auxin being delivered to the root tip result in an increase in auxin concentration in the quiescent centre (Figure 4.7G). The elevated levels of auxin concentration in the phloem can be seen in root-tip auxin patterning as the phloem cell files "light up" compared to neighbouring cells with lower concentrations. The increased delivery of auxin to the root tip can also be seen more broadly then in just the quiescent centre as there is an increase in the auxin maxima across the most root apical portion of the root tip (Figure 4.8).

Finally, we vary $\gamma_{s,1}$ and $\alpha_{ext,s,1}$ simultaneously to represent changes in temperature to investigate how sugar and auxin responses combine to affect auxin patterning in the root tip. Results of these simulations are shown in Figures 4.9 and 4.10. We find that the overall results of varying both sugar and auxin parameters follows closely the results from varying only auxin parameters, with increases in auxin concentration in the phloem and QC (Figure 4.9B,D,H and G).

However, the simultaneous variation of sugar parameters modifies the changes seen compared to varying only auxin parameters. Comparing the auxin concentration in the initial phloem cell for highest temperature simulations from Figure 4.9H and

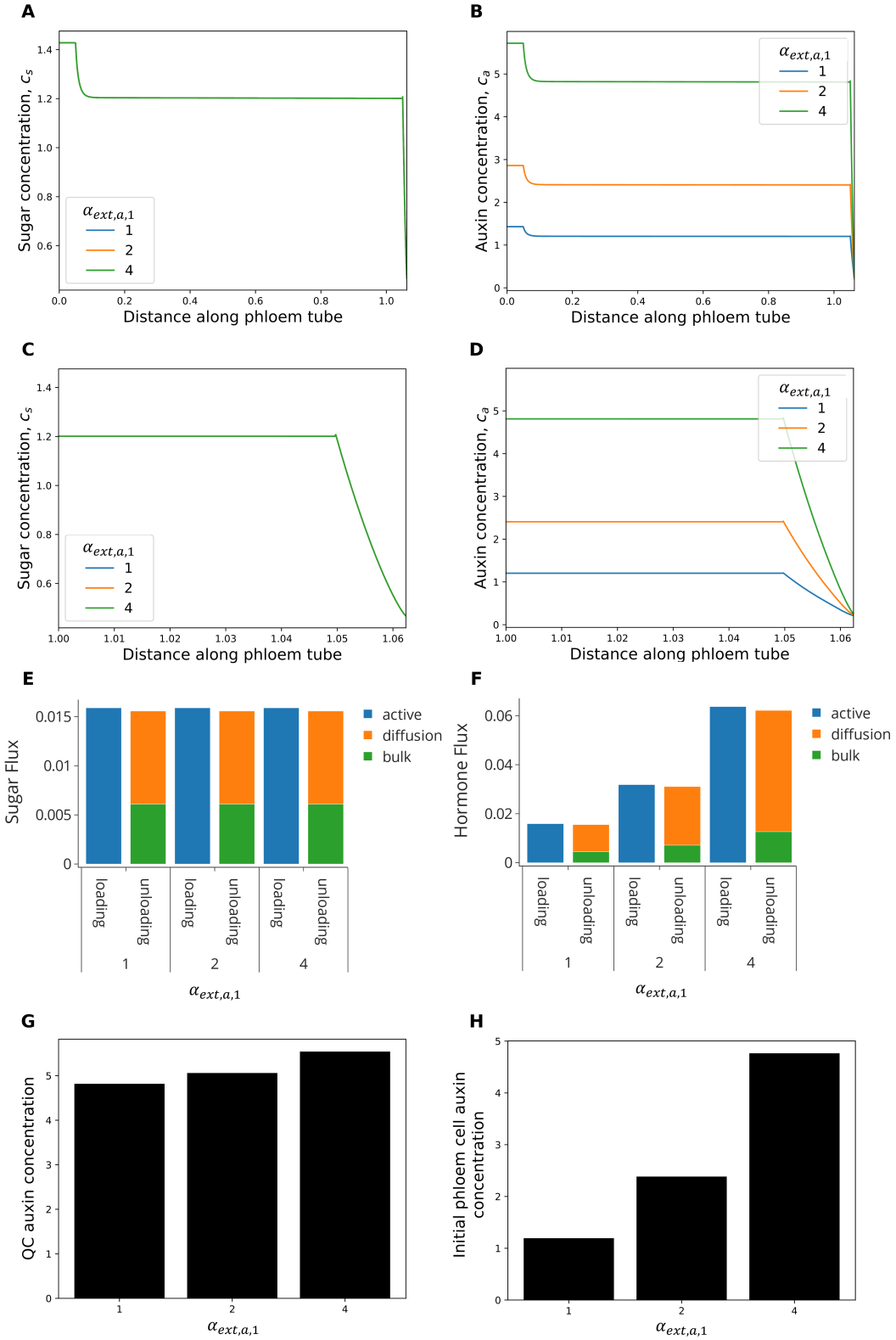


Figure 4.7: Varying the rate of auxin production in the shoot. **(A)** Sugar concentration in the phloem; **(B)** Auxin concentration in the phloem; **(C)** Sugar concentration in the phloem unloading zone; **(D)** Auxin concentration in the phloem unloading zone; **(E)** Sugar influx and efflux; **(F)** Auxin influx and efflux; **(G)** Average auxin concentration across quiescent centre cells in the root tip; **(H)** Auxin concentration in the phloem cell at the shootward end of the root-tip template.

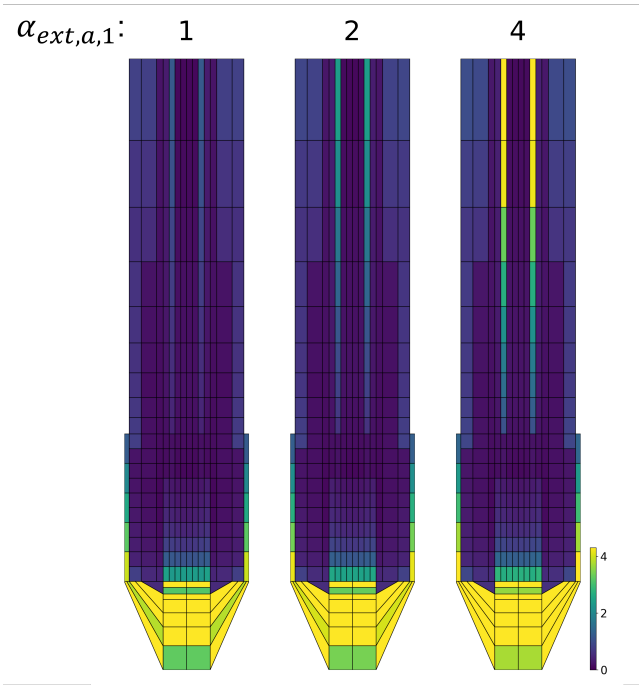


Figure 4.8: Root tip auxin distribution outputs from simulations varying the rate of auxin production in the shoot.

Figure 4.7H, we see a 28% decrease in phloem auxin concentration when sugar and auxin parameters are varied compared to simulations when only auxin parameters are varied. As such, we can see that the decrease in phloem auxin concentration seen when only varying sugar parameters acts to down-regulate the increase in phloem auxin concentration seen when varying only auxin parameters. This highlights the important role of including both sugar and auxin responses when considering changes in ambient temperature, as their responses can be antagonistic and varying their responses separately may lead to under or over estimations of impact on auxin concentration levels.

Finally, we see that varying both sugar and auxin parameters in response to an increase in temperature affects root-tip auxin patterning (Figure 4.10). For lower temperatures, the root-tip auxin patterns remain similar to those when varying only auxin parameters. However, the predicted down-regulation of phloem auxin concentration when sugar loading is reduced in response to high temperatures (Figure 4.5B,D,H) affects the auxin concentration pattern around phloem cells (Figure 4.10) when compared to the same pattern whilst only varying auxin parameters (Figure 4.8).

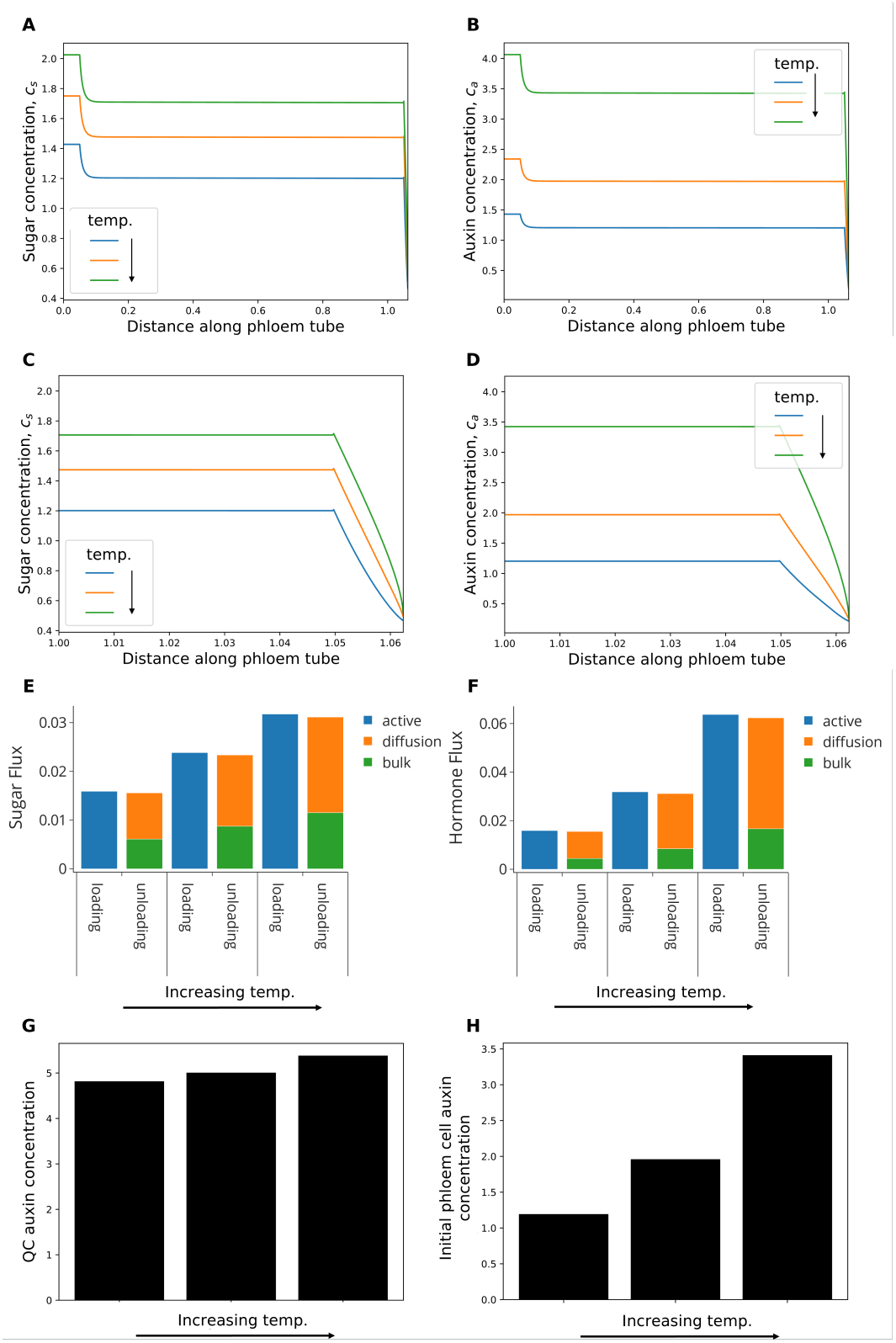


Figure 4.9: Varying sugar and auxin parameters to simulate increases in ambient temperature. **(A)** Sugar concentration in the phloem; **(B)** Auxin concentration in the phloem; **(C)** Sugar concentration in the phloem unloading zone; **(D)** Auxin concentration in the phloem unloading zone; **(E)** Sugar influx and efflux; **(F)** Auxin influx and efflux; **(G)** Average auxin concentration across quiescent centre cells in the root tip; **(H)** Auxin concentration in the phloem cell at the shootward end of the root-tip template.

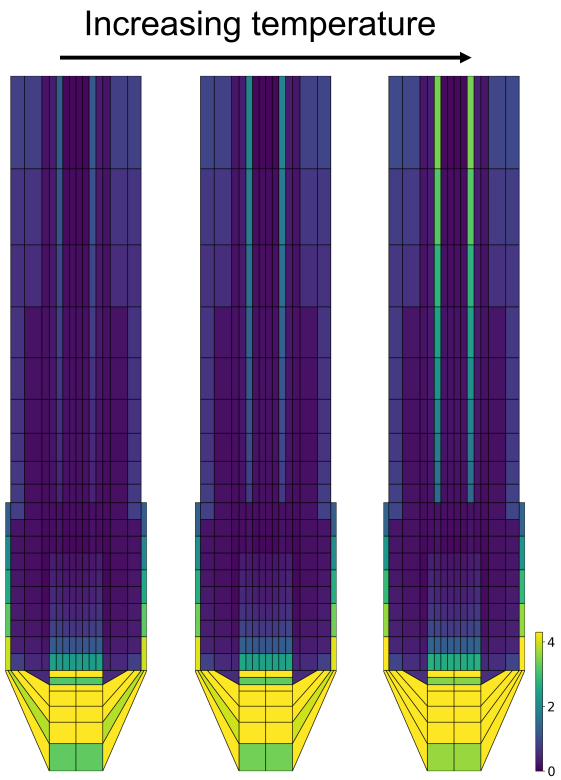


Figure 4.10: Root tip auxin distribution outputs from simulations varying sugar and auxin parameters to simulate increases in ambient temperature.

4.5.2 Exogenous sucrose application

Seedlings grown under laboratory conditions are often grown on plates containing a growth medium, which can sometimes contain sucrose. As such, it is important to understand how application of exogenous sucrose impacts the experiments being conducted. Knox et al. (2018) show that application of exogenous sucrose to the root tip of Arabidopsis seedlings (which reduces the strength of the root sink) reduces phloem transport velocity. We can capture application of exogenous sucrose by increasing the production of sugar in the root tip, $\alpha_{s,3}$ (Figures 4.11 and 4.12).

Varying the rate of sugar production in the root tip produces minimal changes in the model predictions. Increasing the rate of sugar production in the root, $\alpha_{s,3}$, reduces the strength of the root sugar sink resulting in a small increase in sugar and auxin concentration throughout the loading and translocation zone of the phloem (Figure 4.11A,C,B,D,H). However, the small increase in phloem auxin concentration does not translate to a noticeable increase in the root tip auxin maxima (Figure 4.11G) and there is no change in the root-tip auxin patterning (Figure 4.12).

Studies have shown that crosstalk between sugar signalling and auxin biosynthesis

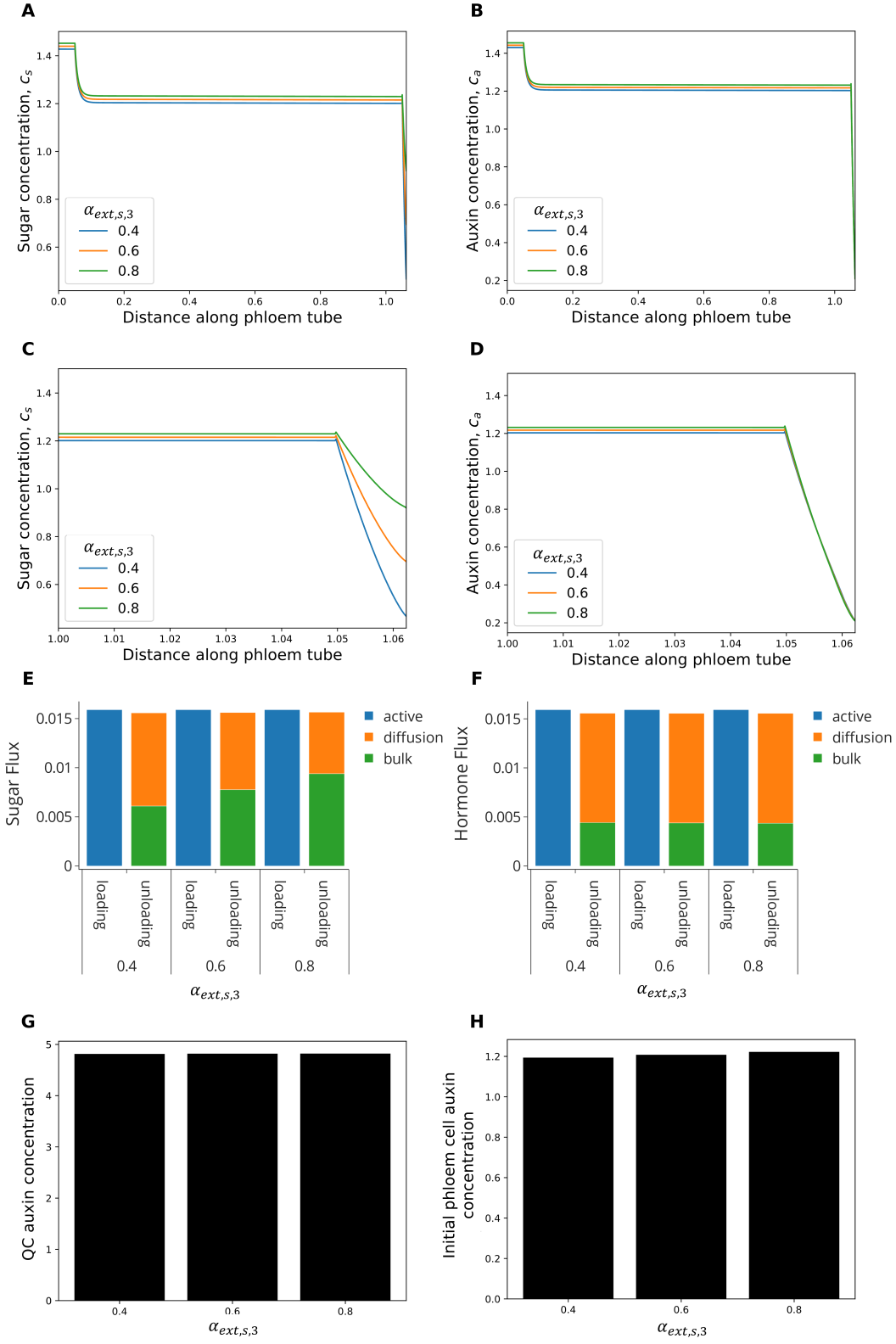


Figure 4.11: Varying the rate of sugar production in the root. **(A)** Sugar concentration in the phloem; **(B)** Auxin concentration in the phloem; **(C)** Sugar concentration in the phloem unloading zone; **(D)** Auxin concentration in the phloem unloading zone; **(E)** Sugar influx and efflux; **(F)** Auxin influx and efflux; **(G)** Average auxin concentration across quiescent centre cells in the root tip; **(H)** Auxin concentration in the phloem cell at the shootward end of the root-tip template.

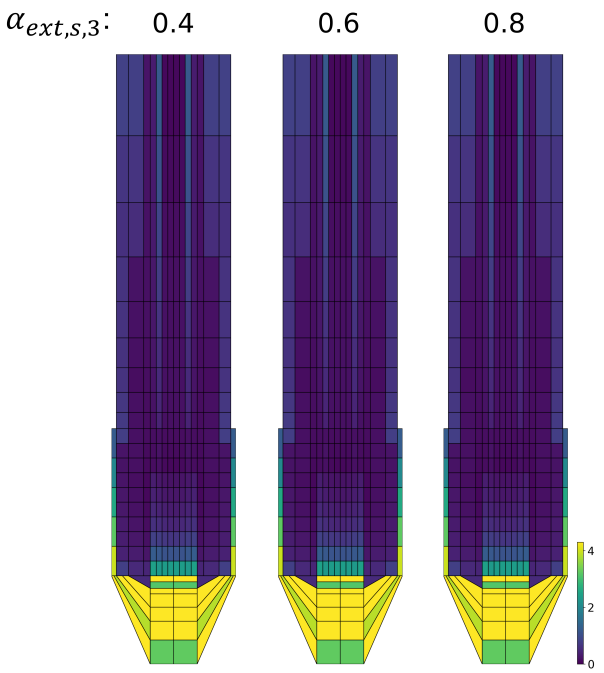


Figure 4.12: Root tip auxin distribution outputs from simulations varying the rate of sugar production in the root.

occurs in the root tip (Mroue et al. (2018) and references therein). In particular, Sairanen et al. (2012) show that there is an increase in auxin biosynthesis in the root tip of Arabidopsis seedlings grown on plates with growth medium containing glucose or sucrose. As such, to understand the impact of exposure to exogenous sucrose on root-tip auxin patterning, we need to vary the rate of auxin biosynthesis in the cell-based portion of the hybrid model. We can do this by varying the production rate for a given cell i, α_i, for all root tip cells. Recall we have two different root tip auxin production rates, α_{QC} for cells in the quiescent centre region of the root tip and α_{bk} as a rate of background synthesis in all root tip cells. When varying these production values, we multiply both α_{QC} and α_{bk} by a scalar value to increase the rate of production (Figures 4.13 and 4.14).

We see that varying root-tip auxin production has minimal influence on the concentration of auxin within the loading and translocation zone of the phloem (Figure 4.13B,D,H). However, we do see a large change in the auxin maxima within the root tip (Figure 4.13G). Figure 4.14 shows that there is a change in the root-tip auxin patterning, however, due to the small scale of the auxin fluxes leaving the phloem, we suggest that these variations in root-tip auxin patterning are driven by the change in auxin production in the root tip. To understand the true influence of increased auxin production in the root tip caused by application of exogenous sucrose, a more accurate relationship between applied sucrose concentration and root-tip auxin production would need to be determined.

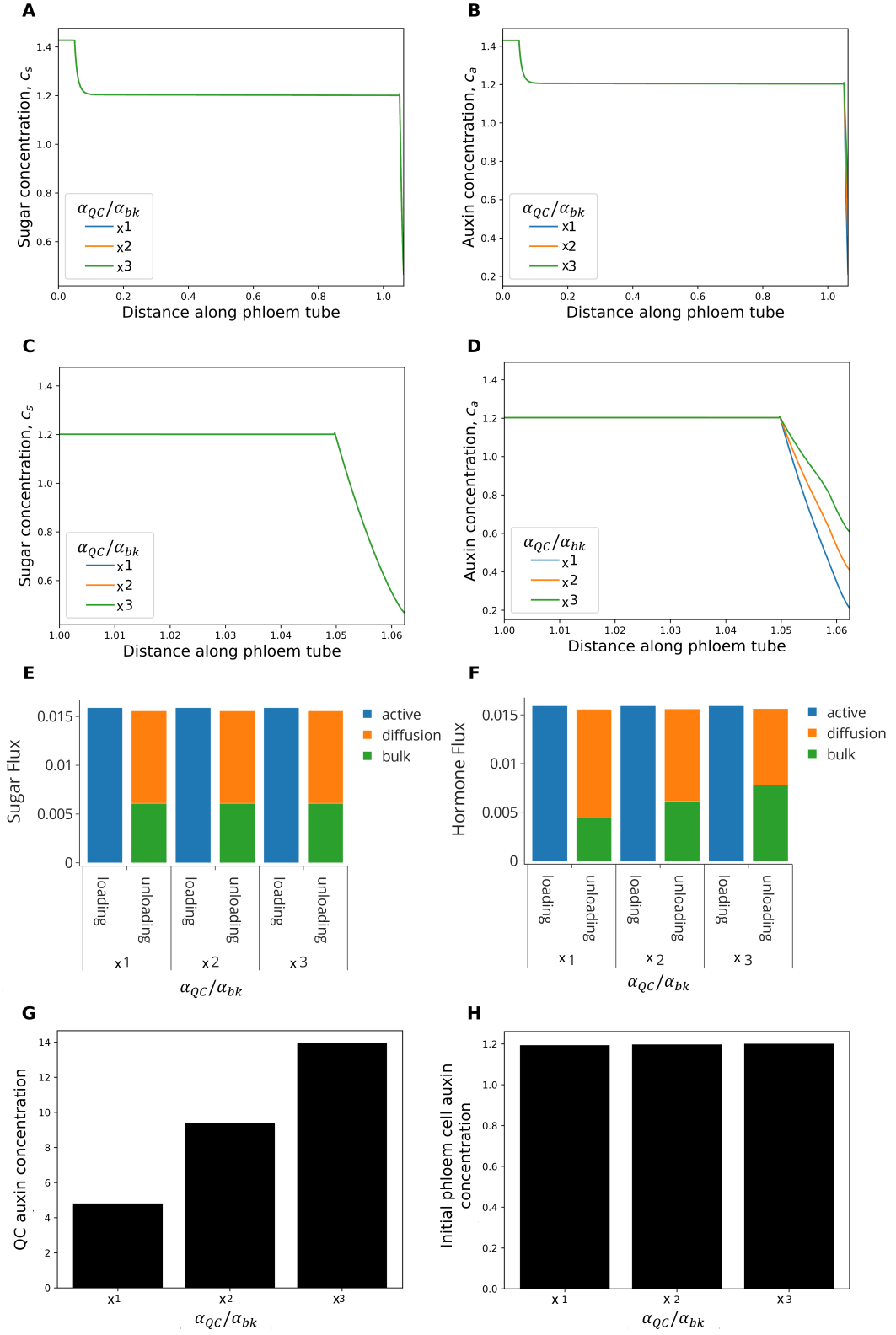


Figure 4.13: Varying the rate of auxin production in the root. **(A)** Sugar concentration in the phloem; **(B)** Auxin concentration in the phloem; **(C)** Sugar concentration in the phloem unloading zone; **(D)** Auxin concentration in the phloem unloading zone; **(E)** Sugar influx and efflux; **(F)** Auxin influx and efflux; **(G)** Average auxin concentration across quiescent centre cells in the root tip; **(H)** Auxin concentration in the phloem cell at the shootward end of the root-tip template.

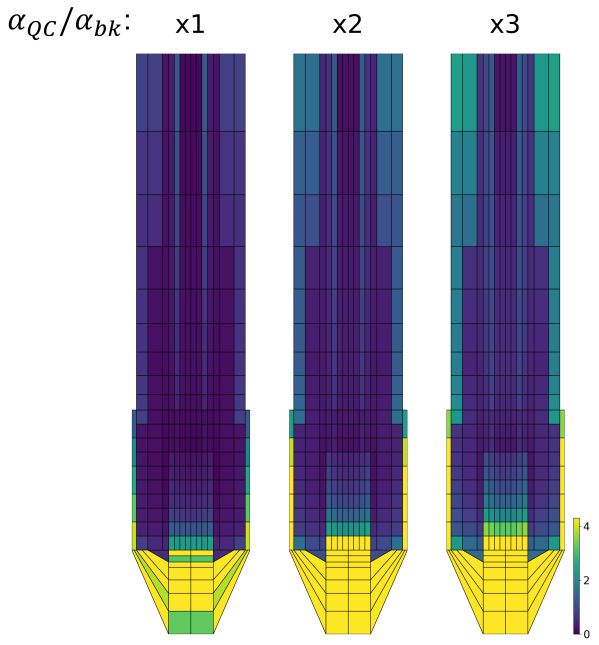


Figure 4.14: Root tip auxin distribution outputs from simulations varying the rate of auxin production in the root.

Combining the influence of sugar and auxin parameter changes under application of exogenous sucrose, we see that the results (Figure 4.15) are heavily dominated by the variation in auxin parameters. Comparing the auxin concentration in initial phloem cells for simulations representing the highest exposure to exogenous sucrose, we see that the small increase seen when varying only sugar parameters (Figure 4.11H) is increased slightly (1.1%) when auxin parameters are also varied ((Figure 4.15H)). However, this change is minimal and the root-tip auxin patterning (Figure 4.16) remains dominated by the variations caused by changes in root-tip auxin production.

4.5.3 Varying plasmodesmata density

Changes in transport via plasmodesmata (bulk flow and diffusive unloading) will be affected by environmental conditions that impact plasmodesmata density or plasmodesmata permeability. Many environmental conditions have been shown to affect transport via plasmodesmata such as light intensity (Brunkard and Zambryski, 2019) and osmotic stress (Sager and Lee, 2014). In Chapter 3, we investigated how changes in plasmodesmata density affect simulation results for the phloem transport model (Figure 3.11). These simulations changed sugar and auxin parameters related to plasmodesmatal transport simultaneously (with low, mid, and high scenarios defined in Table 3.11). In this section, we vary the parameters for sugar and auxin

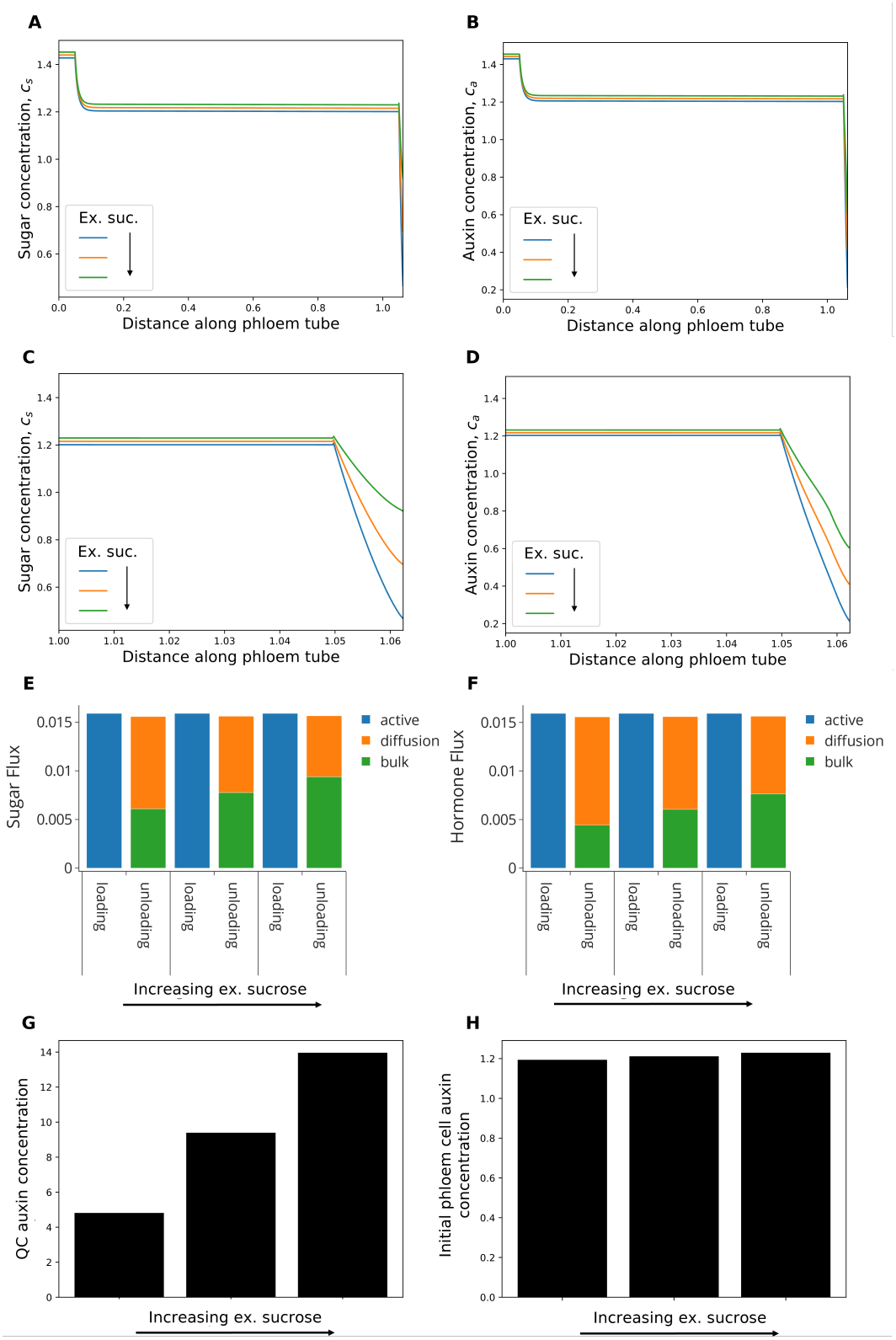


Figure 4.15: Varying sugar and auxin parameters to simulate application of exogenous sucrose to the root tip. **(A)** Sugar concentration in the phloem; **(B)** Auxin concentration in the phloem; **(C)** Sugar concentration in the phloem unloading zone; **(D)** Auxin concentration in the phloem unloading zone; **(E)** Sugar influx and efflux; **(F)** Auxin influx and efflux; **(G)** Average auxin concentration across quiescent centre cells in the root tip; **(H)** Auxin concentration in the phloem cell at the shootward end of the root-tip template.

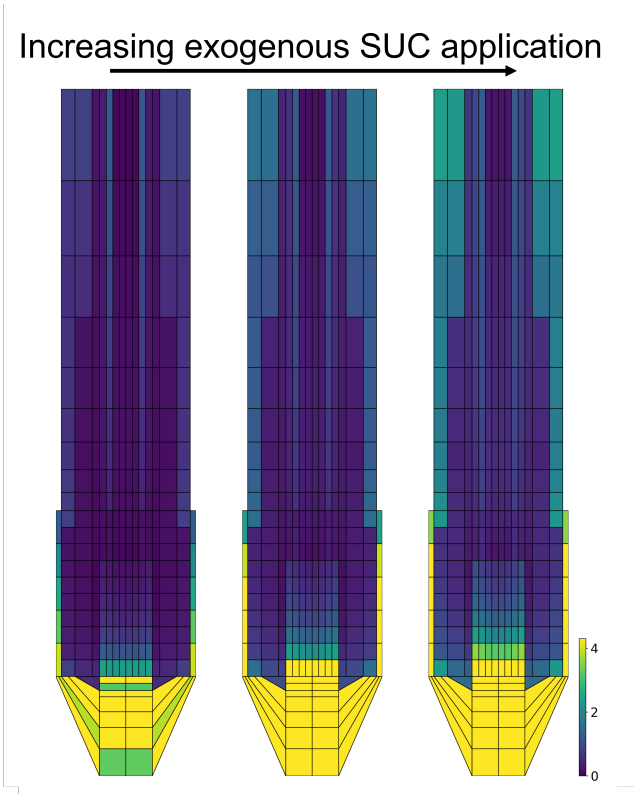


Figure 4.16: Root tip auxin distribution outputs from simulations varying sugar and auxin parameters to simulate application of exogenous sucrose to the root tip.

independently before looking at how their combined effect influences root-tip auxin patterning.

Both bulk flow unloading and diffusive unloading occur via plasmodesmata. As such, to see how varying plasmodesmatal transport rates affects root-tip auxin patterning we need to vary the parameters associated with diffusive unloading, $\beta_{s,3}$ and $\beta_{a,3}$, and the parameters associated with bulk flow unloading, $\sigma_{s,3}$ and $\sigma_{a,3}$. We begin by varying only sugar parameters related to plasmodesmatal transport.

We find that sugar unloading parameters associated with lower plasmodesmatal density have higher auxin concentration within the phloem (Figure 4.17B,D,H), however, this does not lead to an increase in root-tip auxin concentration (Figure 4.17G) and there is no change in root-tip auxin patterning (Figure 4.18).

When varying only auxin unloading parameters associated with plasmodesmatal density, we find that simulations for low plasmodesmatal density also have higher phloem auxin concentration (Figure 4.19B,D,H). However, as we have now modified the parameters associated with auxin phloem unloading (low plasmodesmatal density means less phloem unloading), we see a decrease in root-tip auxin concentration (Figure 4.19G), however, the change in QC concentration is small and we see no

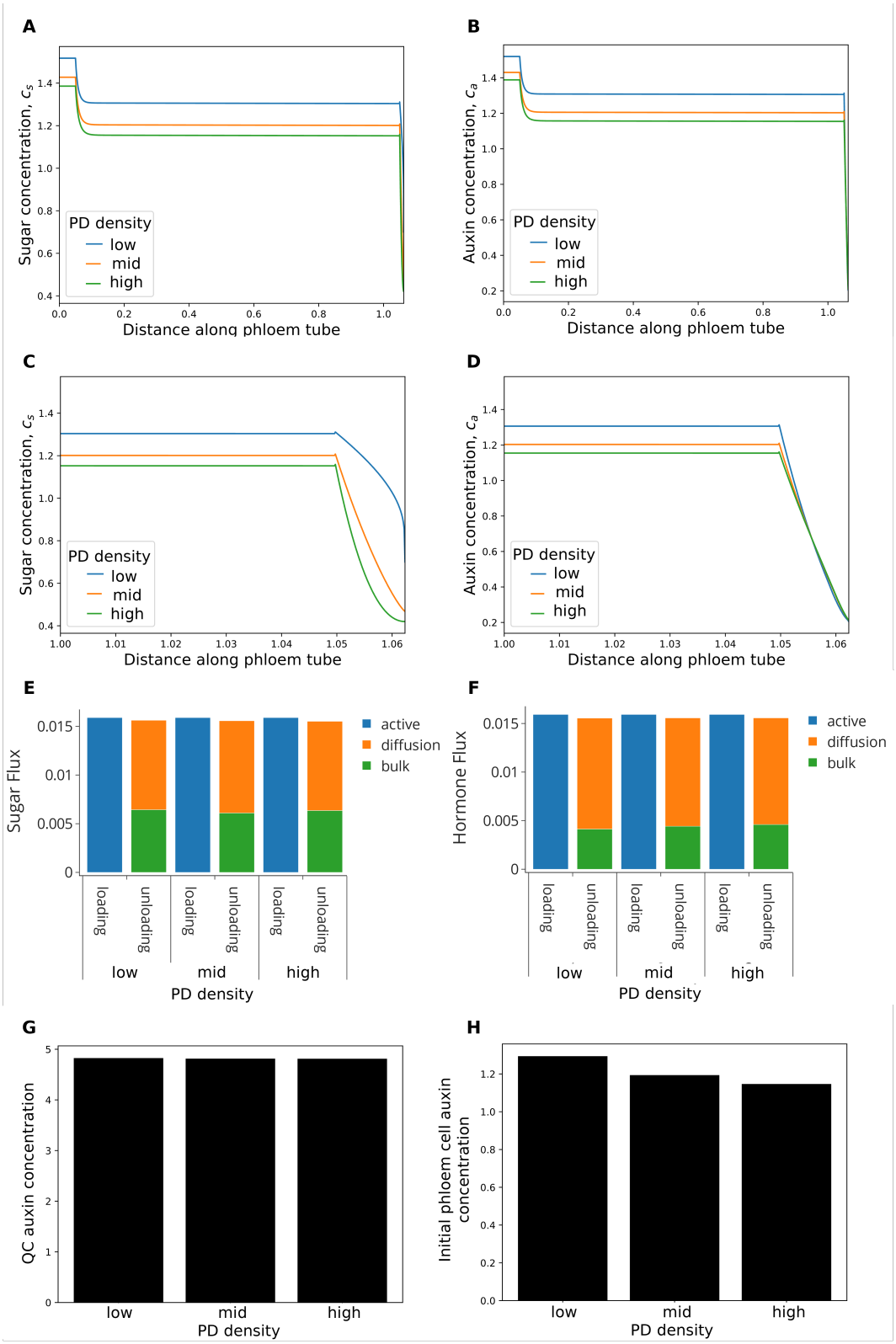


Figure 4.17: Varying plasmodesmatal density for sugar parameters only. **(A)** Sugar concentration in the phloem; **(B)** Auxin concentration in the phloem; **(C)** Sugar concentration in the phloem unloading zone; **(D)** Auxin concentration in the phloem unloading zone; **(E)** Sugar influx and efflux; **(F)** Auxin influx and efflux; **(G)** Average auxin concentration across quiescent centre cells in the root tip; **(H)** Auxin concentration in the phloem cell at the shootward end of the root-tip template.

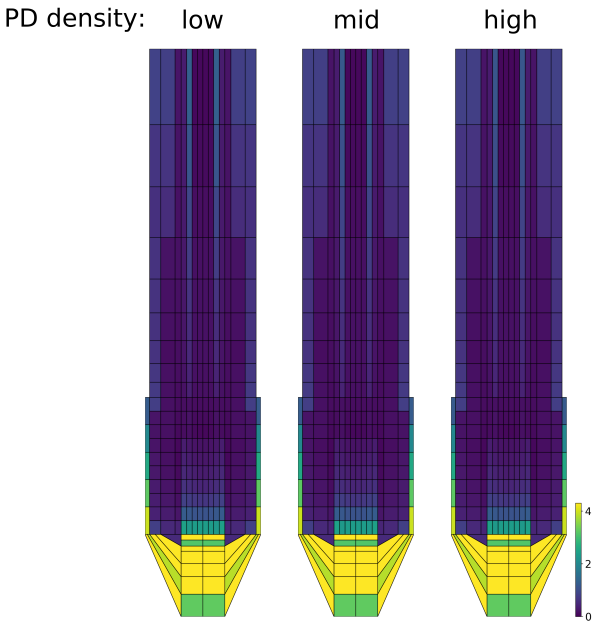


Figure 4.18: Root tip auxin distribution outputs from simulations varying plasmodesmatal density for sugar parameters only.

noticeable effect on root-tip auxin patterning (Figure 4.20).

Finally, when varying both sugar and auxin parameters associated with plasmodesmatal density, we continue to see the increase in phloem auxin concentration associated with varied sugar parameters (Figure 4.21B,D,H) but we also see the reduction in QC concentration associated with changes in auxin parameters (Figure 4.21G). These effects have no noticeable effect on root-tip auxin patterning (Figure 4.22).

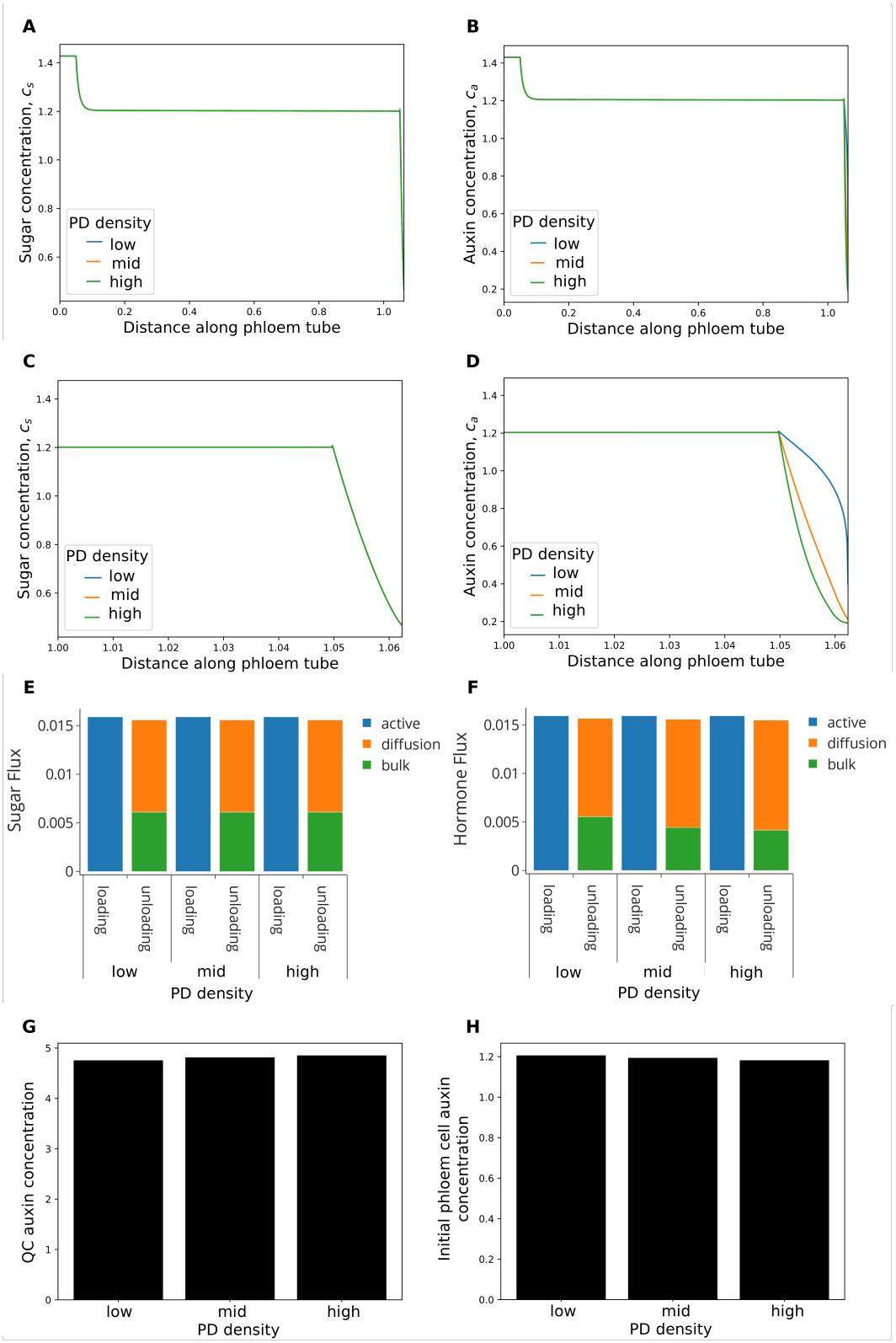


Figure 4.19: Varying plasmodesmatal density for auxin parameters only. **(A)** Sugar concentration in the phloem; **(B)** Auxin concentration in the phloem; **(C)** Sugar concentration in the phloem unloading zone; **(D)** Auxin concentration in the phloem unloading zone; **(E)** Sugar influx and efflux; **(F)** Auxin influx and efflux; **(G)** Average auxin concentration across quiescent centre cells in the root tip; **(H)** Auxin concentration in the phloem cell at the shootward end of the root-tip template.

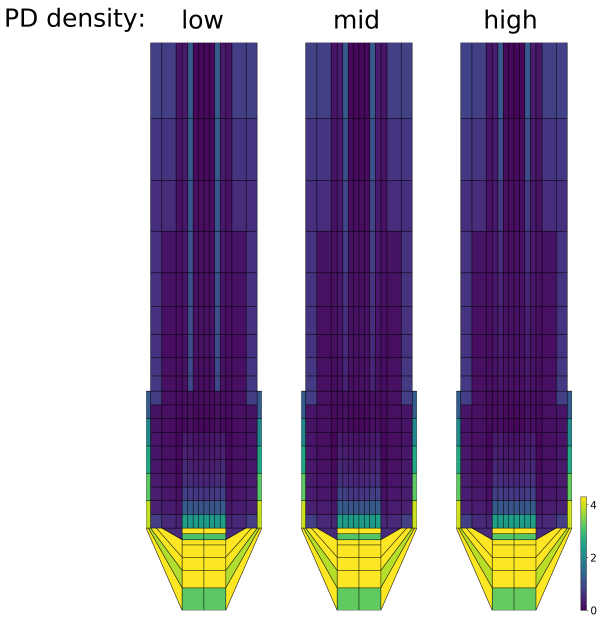


Figure 4.20: Root tip auxin distribution outputs from simulations varying plasmodesmatal density for auxin parameters only.

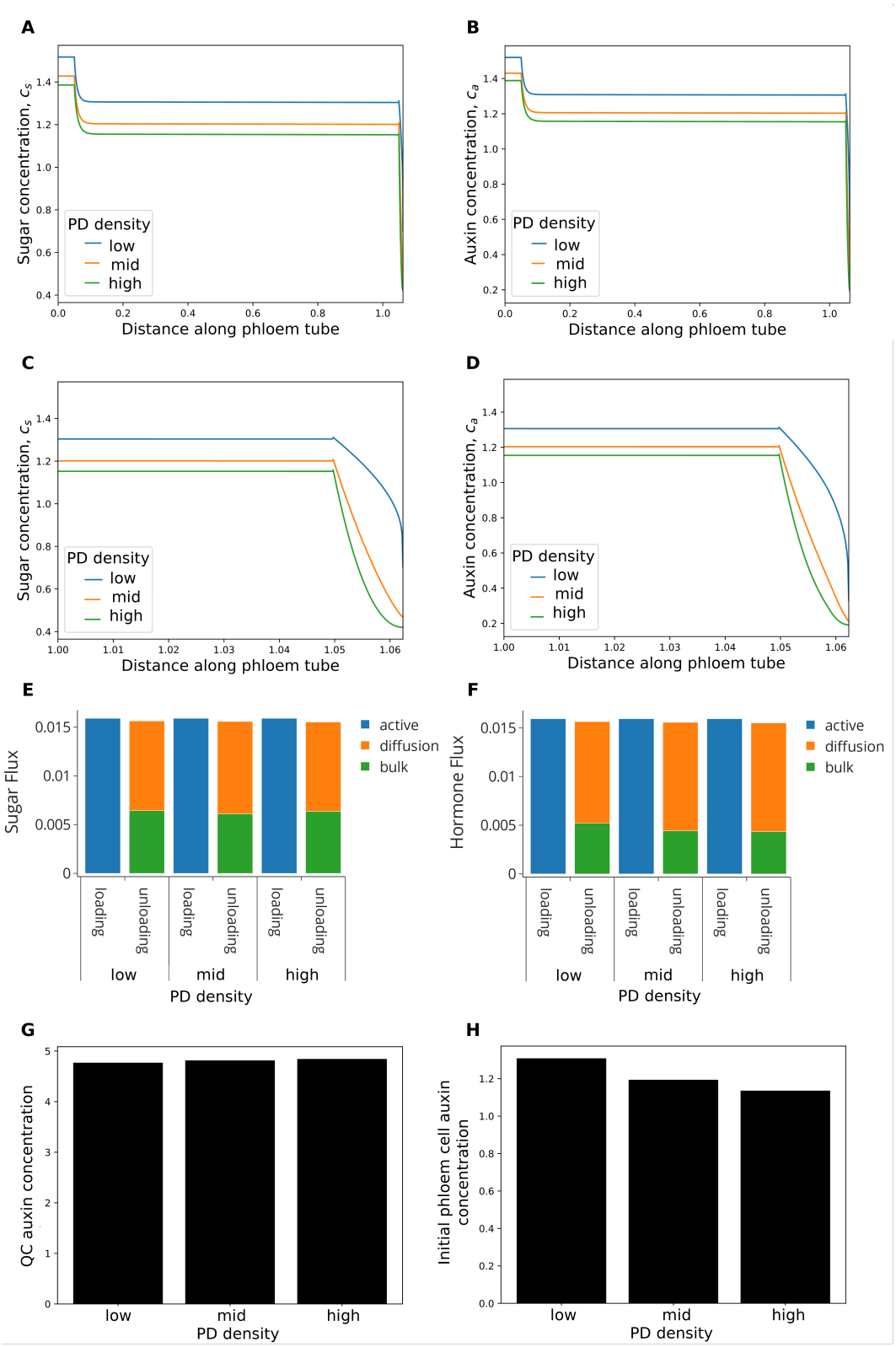


Figure 4.21: Varying plasmodesmatal density. **(A)** Sugar concentration in the phloem; **(B)** Auxin concentration in the phloem; **(C)** Sugar concentration in the phloem unloading zone; **(D)** Auxin concentration in the phloem unloading zone; **(E)** Sugar influx and efflux; **(F)** Auxin influx and efflux; **(G)** Average auxin concentration across quiescent centre cells in the root tip; **(H)** Auxin concentration in the phloem cell at the shootward end of the root-tip template.

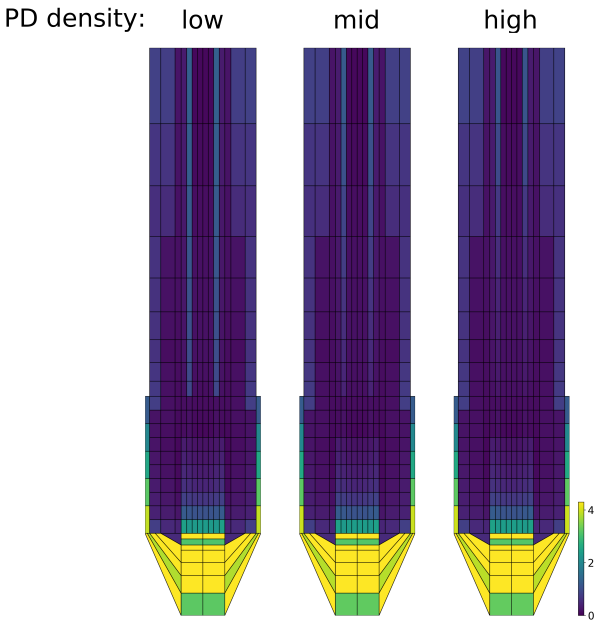


Figure 4.22: Root tip auxin distribution outputs from simulations varying plasmodesmatal density.

4.6 Conclusions

In this Chapter, we have developed a novel mathematical model of a "virtual" Arabidopsis seedling that captures production and degradation of sugar and auxin in a shoot compartment, long-distance transport of sugar and auxin in the phloem, and cell-scale transport of auxin within the root tip. This model has been used to investigate the role that environmental changes across the shoot and root have on root-tip auxin patterning. Through the combination of sugar and auxin modelling, we have been able to establish how the combined effect of environmental influences on the production and transport of sugar and auxin molecules interact to influence root-tip auxin patterning.

Our results show that, within parameter regimes studied, environmental influences on sugar transport and production alone does not influence root-tip auxin patterning significantly. Under variations in ambient temperature, varying sugar parameter $\gamma_{s,1}$ resulted in a small reduction to root tip auxin concentration, though this did not significantly alter the root-tip auxin pattern (Figure 4.6). Simulations representing exposure to exogenous sucrose and plasmodesmata density (where only sugar parameters were varied) showed similar results, with no noticeable changes in root-tip concentration or root-tip auxin patterning.

When varying auxin parameters, we saw more distinct changes in root-tip auxin patterning in model scenarios where auxin production was being modified. This occurred whether the synthesis was changing in the shoot or the root but was more pronounced when root-related synthesis parameters were changed (Figure 4.14). This emphasises the importance of getting the scale of model parameters correct and highlights that potential work may be needed to ensure model results are not being overly influence by auxin production rates. We also note that the difference in the scaling of parameters in the phloem and root tip models may be influential: radial velocities across the phloem membrane are considered of order εU where ε is the phloem aspect ratio ($\varepsilon = {}^{a}/_{L} = 5.9 \times 10^{-5}$) and U is a typical phloem velocity ($U = 23\mu\text{ms}^{-1}$). The resulting scale ($\varepsilon U = 1.35 \times 10^{-3}$) is much smaller than typical PIN-mediated membrane transport (we take $P_{PIN} = 0.5$) which may result in the carrier-mediated transport dominating the root-tip auxin patterning. Many of the model parameters used within this hybrid model are not well characterised, and future experimental work may aid in establishing biologically relevant parameter values.

In the cases where both sugar and auxin parameters were varied in response to

changes in environmental conditions, we saw that the effects of varying sugar and auxin parameters separately combined. In particular, when varying parameters under changes in ambient temperature, we saw that the influence on auxin concentration of sugar and auxin parameters opposed each other. Whilst the changes caused by sugar parameters were small, they acted to down-regulate changes in root-tip auxin concentration caused by variations in auxin parameters by 27%. This highlights the importance of considering both sugar and auxin changes when modelling variations in environmental cues. Modelling work presented in this Chapter is consistent with modelling results in Chapters 2 (Supplementary Figure A.1) and 3. Future modelling work should continue to consider the influence of environmental conditions on both sugar and auxin parameters in order to understand the influence of environmental cues on root-tip auxin patterning.

Chapter 5

Conclusions

This thesis has used mathematical modelling of auxin transport throughout the model plant *Arabidopsis thaliana* to investigate what influences auxin patterning in the root apex. In Chapter 2, motivated by experimental data that challenged the consensus that auxin in the root tip is synthesised in the shoot and delivered to the root, we formulated a root-tip auxin transport model with a boundary condition that prescribes an increased production rate in shoot boundary cells to investigate the role of local auxin synthesis on auxin patterning in the root tip. These investigations revealed that auxin synthesis across the whole root tip plays an important role in auxin patterning and that the ratio of shoot-derived auxin to root-derived auxin needs to shift away from shoot dominance in order to replicate reciprocal grafting experimental data.

Chapter 3 focused on the impact of changes in environmental conditions on hormone delivery to the root tip. We developed a phloem transport model based on the Münch pressure flow hypothesis that included the passive advection of a small molecule (taken to be auxin in this thesis) with the flow of phloem sap. Alongside the inclusion of hormone transport, we expanded existing phloem transport models to be representative of the model plant *Arabidopsis thaliana* by allowing bulk flow unloading through the inclusion of the Staverman reflection coefficient. Through the variation of model parameters that are influenced by environmental conditions, such as the rate of sugar loading, external source concentrations and external sink concentrations, we found that environmental changes that lead to an increase in phloem transport velocity result in increased delivery of passively loaded hormones to the root tip.

Finally, in Chapter 4 we developed a multiscale model of a "virtual" Arabidopsis seedling that simulates long distance sugar and auxin transport within the phloem,

cell-scale auxin transport in the root-tip, and production and degradation of sugar and auxin in a shoot compartment. This model enabled us to investigate the influence of variations in environmental conditions across the whole seedling on root-tip auxin patterning. Extending the environmental investigations in Chapter 3, we also considered the effect that environmental conditions may have on auxin parameters. We found that the response of both auxin and sugar parameters to environmental cues are important when considering the impact on root-tip auxin patterning.

5.1 Local auxin biosynthesis in the root tip is important for root tip auxin patterning

Chapter 2 addressed the role of local auxin synthesis on auxin patterning in the root tip. Experimental data from Brumos et al. (2018) showed that the auxin maxima in the root tip was maintained in grafting experiments where an auxin biosynthesis mutant shoot was grafted to a WT root. They also showed that the auxin maxima could not be maintained when a WT shoot was grafted onto an auxin biosynthesis mutant root. However, model simulations of grafting experiments using the model developed by Mellor et al. (2020) were unable to replicate grafting experimental results. These experimental data, along with the previous model's inability to replicate the results, challenged our existing understanding that auxin in the root tip is primarily synthesised in the shoot and delivered to the root tip. We hypothesised that the role of local auxin synthesis in the root tip plays an important role in auxin patterning at the root apex.

To investigate the role of local auxin synthesis on root tip auxin patterning, we extended the multicellular auxin transport model developed by Band et al. (2014) and Mellor et al. (2020) to include a boundary condition that prescribes an increased production rate in shoot boundary cells. Shifting from a fixed concentration boundary condition to the new boundary condition enabled us to more accurately compare the significance of local auxin biosynthesis in the root tip with the auxin being delivered to the root from the shoot. We investigated the model's ability to capture the root-tip auxin patterns seen in grafting experiments performed by Brumos et al. (2018) (Figure 2.2). In particular, we focused on whether the synthesis rate in the QC region of the root tip or the inclusion of a low rate of synthesis in all root-tip cells played important roles in root-tip auxin patterning.

To make the comparisons between model simulations and experimental data, we developed a combined approach based on the data available to us. Due to the COVID-

19 pandemic, we were unable to obtain experimental results that would replicate the grafting experiments in plants harbouring the DII-VENUS fluorescent reporter. Such experimental data would have enabled us to make direct comparisons between DII-VENUS experimental data and DII-VENUS simulation outputs. Instead, we quantified the fluorescent intensity of DR5:GFP signals in the grafting experiments published by Brumos et al. (2018) and compared the fold-change in fluorescent intensity between different grafting experiments with the fold-change in average auxin output from the model simulations. We then used these fold-change values to define a measure of how well the model fit the experimental data. We also used existing DII-VENUS data from WT and knockout mutants, alongside the cosine similarity coefficient, to ensure that adaptations to the model were not impacting previously published results (from Band et al. (2014) and (Mellor et al., 2020)) on auxin patterning in the root tip.

To investigate the model's ability to capture root-tip auxin patterns seen in grafting experiments, we first excluded the background synthesis rate in root cells (as was suggested by Brumos et al. (2018)); however, this did not increase the model's ability to capture the results of grafting experiments. We then hypothesised that increased auxin synthesis in the QC region would enable the model predictions to agree with grafting data. However, simulations showed that the synthesis rate in the QC region had to be increased to a non-biophysical regime in order to capture auxin patterning seen in the root tip of grafting experiments. Hence, we shifted our focus towards the ratio of shoot-derived auxin to root-derived auxin. We found that shifting this ratio away from shoot dominance, by reducing the influx from the shoot, enabled the model to capture the results of grafting experiments whilst maintaining biophysical auxin biosynthesis rates within the root tip. We conclude that local auxin biosynthesis throughout the root-tip tissues plays a critical role in determining auxin levels in the root apex.

5.2 Environmental conditions that modify phloem transport velocity affect hormone delivery to the root tip

Auxin synthesised in the shoot is advected to the root tip via the phloem. The results obtained in Chapter 2, that the ratio between shoot-derived and root-derived auxin is important for auxin patterning in the root tip, led us to question what processes affect auxin delivery to the root. In order to address this question, we developed a

mathematical model of phloem transport that incorporated the passive advection of auxin with the flow of sap. With this model, we were able to investigate how changes in environmental conditions may affect auxin delivery to the root tip. Multiple environmental conditions have been shown to affect phloem transport velocity, such as temperature, light intensity, and external sucrose application at the root-tip (Xu et al., 2018, Knox et al., 2018, Gong et al., 2015), and as auxin is advected with the flow of phloem sap, we hypothesised that these environmental conditions were also likely to affect auxin delivery to the root tip.

There are many existing phloem transport models in the literature (Minchin et al., 1993, Bidel et al., 2000, Thompson and Holbrook, 2003, Jensen et al., 2011, 2012, Payvandi et al., 2014, Jensen et al., 2016, van den Herik et al., 2021, Nakad et al., 2021). Existing phloem transport models have focused on the relationship between phloem transport velocity and sugar concentration in the phloem, and are often simulated in larger plant species or trees. In Chapter 3, we expanded upon phloem transport models in the literature (Jensen et al., 2012, Payvandi et al., 2014) to include the transport of a small molecule (in this thesis taken to be a hormone) that doesn't affect the osmotic gradient that drives phloem flow. Key model developments, alongside the inclusion of a hormone concentration, include defining loading and unloading mechanisms in a manner that allows them to be directly related to experimental conditions, and the inclusion of the Staverman reflection coefficient which allows sugar and hormone to be advected through the phloem membrane with water flow. The inclusion of the Staverman reflection coefficient enables the model to capture the effects of bulk flow phloem unloading, a mechanism that experimental results suggest is the dominant method of unloading in the Arabidopsis root tip (Ross-Elliott et al., 2017). We identified a parameter regime in which the model is able to capture unloading dynamics where bulk flow unloading is dominant over diffusive unloading, as suggested by Ross-Elliott et al. (2017).

We used the model to investigate our hypothesis that environmental conditions that alter phloem transport velocity impact hormone delivery to the root tip. The rate of active sugar loading can be influenced by numerous environmental conditions and the model predicts that increasing the rate of active sugar loading results in an increase in phloem transport velocity (inline with experimental results from Knox et al. (2018)). Environmental conditions can also influence plasmodesmatal densities and permeabilities and the model predicts that higher plasmodesmatal density also results in an increase in phloem transport velocity. The model also predicts that increasing bulk flow unloading increases the phloem transport velocity. In all simulated cases that resulted in an increase in phloem transport velocity, we saw an increase in the amount of hormone delivered to the root tip provided the

hormone is passively loaded. Overall, the model highlights the important role that sugar dynamics can have on hormone delivery to the root tip.

5.3 Varying environmental conditions influences root-tip auxin patterning via changes in both sugar and auxin parameters.

Work in this thesis has focused on the transport of auxin within different organs of an Arabidopsis seedling (Chapter 2: root tip, Chapter 3: the phloem). In Chapter 4, we developed a novel mathematical model of a "virtual" Arabidopsis seedling. This model coupled the two mathematical models from previous chapters together with models of auxin and sugar production and degradation in a shoot compartment to create a hybrid model of auxin transport across the whole Arabidopsis seedling. With this model, we were able to investigate how changes in environmental conditions across the whole seedling influence root-tip auxin patterning.

Changes in environmental conditions have been shown to affect both sugar and auxin parameters. Changes in ambient temperature have been linked to increased active sugar loading (via increased expression of *AtSUC2*) (Knox et al., 2018) and increased auxin biosynthesis in shoots (Stavang et al., 2009, Franklin et al., 2011, Sun et al., 2012, Mroue et al., 2018). Application of exogenous sucrose (that can occur when sucrose is included in experimental growth medium) has been suggested to decrease active sugar loading (via decreased *AtSUC2* expression) (Knox et al., 2018) and increase auxin biosynthesis within the root tip (Sairanen et al., 2012, Mroue et al., 2018). Finally, variation in plasmodesmata density will affect transport of both sugar and auxin. As such, when investigating the influence of environmental changes on root-tip auxin patterning, we considered the effect of variations in both sugar and auxin parameters.

We find that, for existing parameter regimes, environmental influences on sugar parameters have minimal impact on root-tip auxin patterning. We find that changes to auxin parameters have a more substantial effect on root-tip auxin patterning, particularly when auxin production is modified. However, the model predicted that changes in initial phloem cell auxin concentration caused by varying sugar and auxin parameters in response to changes in environmental cues (in particular changes in ambient temperature) are sometimes opposed. This demonstrated the important role of both sugar and auxin parameters in controlling the root-tip auxin levels when

considering changes in environmental cues.

5.4 Future directions

There are a number of ways in which the work in this thesis could be extended. Extensions could aim to gain further understanding of: auxin patterning within the root tip of a broader range of plant species; long-distance transport of a variety of small signalling molecules; and whole plant auxin dynamics in young seedlings.

5.4.1 Local auxin biosynthesis experiments

Current published results of grafting experiments, (Brumos et al., 2018), use the DR5 auxin reporter to visualise auxin distribution in the root tip. DR5 has a complex non-linear relationship with auxin, which depends on the ARFs present in different tissues. Obtaining experimental images of DII-VENUS signals in conditions mimicking grafting experiments would allow us to use the DII-VENUS model described in Section 2.2.6 to make direct comparisons between the results of the model and experimental images. Chemical blockers of auxin biosynthesis could be used to mimic the effects of the grafting experiments performed by Brumos et al. (2018) in Arabidopsis seedlings harbouring the DII-VENUS fluorescent reporter.

There are three reported auxin biosynthesis chemical blockers: aminoethoxyvinyl-glycine (AVG), L-amino-oxyphenylpropionic acid (AOPP) (Soeno et al., 2010), and L-kynurenine (Kyn) (He et al., 2011). The L-kynurenine chemical inhibitor has been shown to phenocopy (replicate characteristics found in different genotypes (Taiz and Zeiger, 2010)) the *wei8 tar2* mutant (He et al., 2011) used in the reciprocal grafting experiments by performed by Brumos et al. (2018). As such, we propose that L-kynurenine would be a suitable auxin biosynthesis inhibitor to use to mimic grafting experiments. Figure 5.1 shows the proposed experimental design that would allow L-kynurenine to mimic the grafting experiments. Performing these experiments and comparing the resulting DII-VENUS data with model predictions would provide a more accurate test of the relative roles of shoot-derived and root-derived auxin in root-tip auxin patterning.

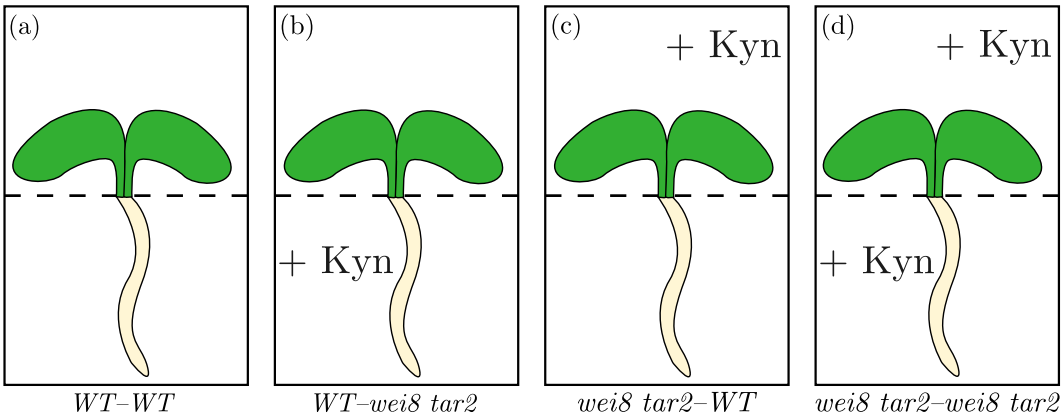


Figure 5.1: Proposed experimental set-up. Arabidopsis seedlings would be grown on split medium plates and Kyn would be applied to inhibit auxin biosynthesis in the root or shoot. The grafting experiment each set-up is mimicking is listed beneath the design.

5.4.2 Modelling auxin transport in the model crop species *Oryza sativa*

Rice is a staple crop for over half the world's population. Recent predictions indicate the population is set to rise to 8 billion by 2025. To meet the increased demand on food resources, it is predicted that rice production needs to increase by 40% by 2030 (Khush, 2005). As the demand for rice increases over the next decade, we need rice varieties that can produce higher and more stable yields under changing climate conditions. Rice will have to be grown using existing farmlands to avoid deforestation of areas of important biodiversity and with less fertiliser, to reduce the environmental impact of the chemicals used (Khush, 2005). An understanding of the processes that govern rice development is a crucial step in the development of improved crop species (Izawa and Shimamoto, 1996).

The work in this thesis has focused on simulations in the model species *Arabidopsis thaliana*. There are numerous benefits to studying Arabidopsis as it is quick to grow and has transparent roots that are easy to image. However, Arabidopsis is a dicotyledon and, as such, has many aspects of development that are different to rice and other crop species that are monocotyledons. As such, transferring the knowledge gained from Arabidopsis models into models of crop species (such as rice) is a crucial step in understanding how environmental changes will effect plant growth, and the resulting impacts this will have on yields and food resources.

Many important discoveries exist that will enable auxin-transport models in Arabidopsis to be adapted to model such processes in the crop species rice. For example, similarly to Arabidopsis, the main auxin synthesis pathway in rice is via the *TAA/YUC* mediated pathway (where *TAA* genes catalyse the conversion of tryptophan into IPyA

and then *YUC* genes catalyse the conversion of IPyA into IAA) (Stepanova et al., 2008, Ljung, 2013, Wang et al., 2017).

To investigate the role of auxin in rice developmental processes, high-resolution auxin reporters are required. Yang et al. (2017) developed two high-resolution auxin response reporters for rice, DII-VENUS and DR5-VENUS (which are well established as auxin reporters in Arabidopsis). In rice, DII-VENUS and DR5-VENUS provided complementary signals for auxin distribution. Yang et al. (2017) show that the distribution of auxin in rice is similar to that seen in Arabidopsis and suggest this highlights the important role of polar auxin transport in both monocot (rice) and dicot (Arabidopsis) plants.

There are known analogues for PIN and AUX1/LAX proteins in rice (Wang et al., 2017), however, few studies have been performed on polar auxin transport in rice. AUX1 is known to be an auxin transporter in Arabidopsis and has been shown to be important in lateral root development (Marchant et al., 2002, Swarup et al., 2008). Zhao et al. (2015) investigate the role of *OsAUX1* in lateral root development in rice. Their study of *osaux1* loss-of-function mutants resulted in a significant decrease in the number of lateral roots indicating that *OsAUX1* is required for lateral root formation in rice (similarly to Arabidopsis) (Zhao et al., 2015). Further results in this paper support the evidence that *OsAUX1* encodes an auxin influx carrier in rice.

Auxin dynamics have been shown to play a major role in responses to environmental stress (Gong et al., 2015, Knox et al., 2018, Xu et al., 2018). Rice yields can be reduced under abiotic stresses caused by climate change, such as drought and increased temperature (Gao et al., 2007). The auxin-transport models described in this thesis have contributed to our understanding of stress response mechanisms in Arabidopsis. To be able to develop rice varieties with suitable tolerance levels to abiotic stresses, we need to have an understanding of the mechanisms that govern rice's ability to tolerate abiotic stresses. Translating our existing auxin-transport models into crop species (such as rice) could provide the useful insights into stress responses needed to develop rice varieties with improved yields under stress conditions.

5.4.3 Extending the phloem transport model to incorporate Taylor dispersion

Under the assumption that the Staverman reflection coefficient is equal to 1 (i.e. the phloem membrane is semi-permeable), Nakad et al. (2021) make a significant advancement in modelling the transport of solutes in the phloem by incorporating

Taylor dispersion. When a solute is added to a flowing fluid it spreads out under molecular diffusion and variations in velocity across the cross-section of the pipe. Taylor (1953) showed that, in impermeable tubes, these effects add an apparent diffusion term to the radially averaged equations that acts to increase the effects of diffusion (Taylor, 1953).

In Chapter 3, when radially averaging equation (3.17), we make the assumption (consistent with phloem models from (Thompson and Holbrook, 2003, Jensen et al., 2011, 2012, Payvandi et al., 2014, Jensen et al., 2016)) that,

$$\frac{\partial \overline{V_{x,0} C_0}}{\partial X} = \bar{V}_{x,0} \frac{\partial \bar{C}_0}{\partial X} + \bar{C}_0 \frac{\partial \bar{V}_{x,0}}{\partial X},$$

where barred terms represent radial averaging. This assumption neglects the effects of Taylor dispersion. Nakad et al. (2021) expand on the work of Taylor (1953) to study the effects of Taylor dispersion on osmotically driven flows. As well as recovering the apparent diffusion term from (Taylor, 1953), their work yields an additional adjustment term for radially averaged advection.

In most existing phloem transport models (Thompson and Holbrook, 2003, Jensen et al., 2011, 2012, 2016), including the one in Chapter 3, the effects of diffusion are neglected due to the high value of the Péclet number. Payvandi et al. (2014) highlighted the important role of diffusion in the boundary layers under high Münch number conditions, and the work of Nakad et al. (2021), including the effects of Taylor dispersion, further highlights that the role of diffusion may be important in phloem transport models. As such, future model developments could formulate the effects of boundary layers and Taylor dispersion in a model including bulk flow unloading (i.e. variation of the Staverman reflection coefficient) in the small Münch number regime (that is relevant for Arabidopsis). Incorporating the effects of membrane leakage via the Staverman reflection coefficient and the effects of Taylor dispersion is likely to be a complex modelling task, but one that will significantly enhance our understanding of solute transport in the phloem.

5.4.4 Transport models for other small signalling molecules

The primary focus of this thesis has been on the transport of auxin within the model species Arabidopsis. However, the development of the phloem transport model in Chapter 3 is not auxin specific. The phloem transport model could be used to study any small molecule transported via the phloem that has minimal impact on the osmotic potential. Therefore, a natural use of this model would be to expand its

use to look at the influence environmental conditions have on the delivery of other important signalling molecules such as GA, cytokinins, and ABA.

Whilst the adaptation of the phloem transport model might be quite straightforward, adapting the multicellular model to capture the movement of other small molecules in the root tip would require a more detailed understanding of how these small molecules are transported. Due to the complex nature of the multicellular auxin transport model, it is likely that most aspects of transport for other small molecules could be captured with adaptations to existing transport mechanisms.

5.4.5 Whole plant modelling with a "virtual" seedling

The final model development in this thesis was the coupling of cell-scale auxin transport with long-distance auxin transport to create a hybrid model that represents the whole plant as a "virtual" seedling. This model captures sugar and auxin dynamics across the whole plant.

Our hybrid model utilises a highly simplified shoot compartment to represent the cotyledons of a young seedling. Expanding the shoot compartment to include more advanced sugar and auxin dynamics (from shoot-based models in the literature such as (Chew et al., 2014)) would enable more detailed investigations into sugar and auxin distributions across the whole plant.

The hybrid model captures the velocity of phloem sap within the phloem, however, the dynamics of water flow are not considered beyond the phloem portion of the model. We could extend the hybrid model to include detailed descriptions of water flow, particularly in and around the root-tip (Couvreur et al., 2018) or by coupling with the transport of water in the xylem (van den Herik et al., 2021). This could enable the model to be used to investigate the impact of environmental conditions in the soil (such as soil compaction and air gaps) on whole plant transport dynamics.

Extensions of the hybrid model designed to produce a "virtual" seedling provide an avenue towards mathematical models that will be able to capture transport dynamics of sugar, water, and auxin within a whole seedling. Influences from the whole plant's environment (i.e. high temperatures are likely to impact water conditions at both the shoot and root) will be able to be model simultaneously. The production of a "virtual" seedling that responds dynamically to whole-plant scale conditions whilst still producing finer scale insights for specific organs of interest (in this thesis the root tip) will improve our ability to understand the influences of climate change on

plant growth and development.

Appendix A

Supplementary Figures

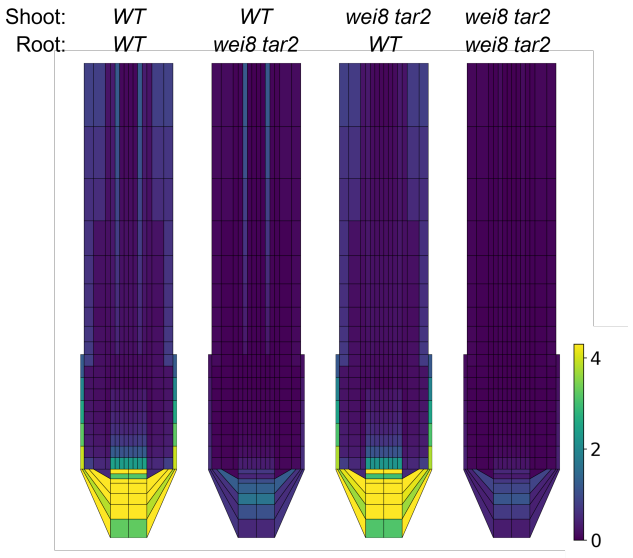


Figure A.1: Simulation of reciprocal grafting experiments (Brumos et al., 2018) using the newly developed hybrid model. Results are consistent with experimental images and simulations in Chapter 2.

Bibliography

Andjelkovic, V. (2018). Introductory chapter: Climate changes and abiotic stress in plants. In *Plant, Abiotic Stress and Responses to Climate Change*. IntechOpen.

Baker, D. (2000a). Vascular transport of auxins and cytokinins in ricinus. *Plant Growth Regulation*, 32(2-3):157–160.

Baker, D. A. (2000b). Long-distance vascular transport of endogenous hormones in plants and their role in source: sink regulation. *Israel Journal of Plant Sciences*, 48(3):199–203.

Band, L. R. and King, J. R. (2012). Multiscale modelling of auxin transport in the plant-root elongation zone. *Journal of Mathematical Biology*, 65(4):743–785.

Band, L. R., Úbeda-Tomás, S., Dyson, R. J., Middleton, A. M., Hodgman, T. C., Owen, M. R., Jensen, O. E., Bennett, M. J., and King, J. R. (2012a). Growth-induced hormone dilution can explain the dynamics of plant root cell elongation. *Proceedings of the National Academy of Sciences*, 109(19):7577–7582.

Band, L. R., Wells, D. M., Fozard, J. A., Ghetiu, T., French, A. P., Pound, M. P., Wilson, M. H., Yu, L., Li, W., Hijazi, H. I., Oh, J., Pearce, S. P., Perez-Amador, M. A., Yun, J., Kramer, E., Alonso, J. M., Godin, C., Vernoux, T., Hodgman, T. C., Pridmore, T. P., Swarup, R., King, J. R., and Bennett, M. J. (2014). Systems analysis of auxin transport in the arabidopsis root apex. *The Plant Cell*, 26(3):862–875.

Band, L. R., Wells, D. M., Larrieu, A., Sun, J., Middleton, A. M., French, A. P., Brunoud, G., Sato, E. M., Wilson, M. H., Péret, B., Oliva, M., Swarup, Ranjan andSairanen, I., Parry, G., Ljung, K., Beeckman, T., Garibaldi, J. M., Estelle, M., Owen, M. R., Vissenberg, K., Hodgman, T. C., Pridmore, T. P., King, J. R., Vernoux, T., and Bennett, M. J. (2012b). Root gravitropism is regulated by a transient lateral auxin gradient controlled by a tipping-point mechanism. *Proceedings of the National Academy of Sciences*, 109(12):4668–4673.

Bao, Y., Aggarwal, P., Robbins, N. E., Sturrock, C. J., Thompson, M. C., Tan, H. Q., Tham, C., Duan, L., Rodriguez, P. L., Vernoux, T., et al. (2014). Plant roots use a patterning mechanism to position lateral root branches toward available water. *Proceedings of the National Academy of Sciences*, 111(25):9319–9324.

Bennett, M. J., Marchant, A., Green, H. G., May, S. T., Ward, S. P., Millner, P. A., Walker, A. R., Schulz, B., and Feldmann, K. A. (1996). Arabidopsis aux1 gene: a permease-like regulator of root gravitropism. *Science*, 273(5277):948–950.

Bhalerao, R. P., Eklöf, J., Ljung, K., Marchant, A., Bennett, M., and Sandberg, G. (2002). Shoot-derived auxin is essential for early lateral root emergence in arabidopsis seedlings. *The Plant Journal*, 29(3):325–332.

Bidel, L., Pages, L., Riviere, L., Pelloux, G., and Lorendeau, J. (2000). Massflowdyn i: a carbon transport and partitioning model for root system architecture. *Annals of botany*, 85(6):869–886.

Bishopp, A., Lehesranta, S., Vatén, A., Help, H., El-Showk, S., Scheres, B., Helariutta, K., Mähönen, A. P., Sakakibara, H., and Helariutta, Y. (2011). Phloem-transported cytokinin regulates polar auxin transport and maintains vascular pattern in the root meristem. *Current Biology*, 21(11):927–932.

Blakeslee, J. J., Bandyopadhyay, A., Lee, O. R., Mravec, J., Titapiwatanakun, B., Sauer, M., Makam, S. N., Cheng, Y., Bouchard, R., Adamec, J., et al. (2007). Interactions among pin-formed and p-glycoprotein auxin transporters in arabidopsis. *The Plant Cell*, 19(1):131–147.

Blaustein, M. P., Kao, J. P., and Matteson, D. R. (2011). *Chapter 3: Osmotic pressure and water movement*, pages 17–29. Elsevier Health Sciences.

Blilou, I., Xu, J., Wildwater, M., Willemsen, V., Paponov, I., Friml, J., Heidstra, R., Aida, M., Palme, K., and Scheres, B. (2005). The pin auxin efflux facilitator network controls growth and patterning in arabidopsis roots. *Nature*, 433(7021):39–44.

Bret-Harte, M. S. and Silk, W. K. (1994). Nonvascular, symplasmic diffusion of sucrose cannot satisfy the carbon demands of growth in the primary root tip of zea mays l. *Plant Physiology*, 105(1):19–33.

Brumos, J., Robles, L. M., Yun, J., Vu, T. C., Jackson, S., Alonso, J. M., and Stepanova, A. N. (2018). Local auxin biosynthesis is a key regulator of plant development. *Developmental Cell*, 47(3):306–318.

Brunkard, J. O. and Zambryski, P. (2019). Plant cell-cell transport via plasmodesmata is regulated by light and the circadian clock. *Plant physiology*, 181(4):1459–1467.

Brunoud, G., Wells, D. M., Oliva, M., Larrieu, A., Mirabet, V., Burrow, A. H., Beeckman, T., Kepinski, S., Traas, J., Bennett, M. J., et al. (2012). A novel sensor to map auxin response and distribution at high spatio-temporal resolution. *Nature*, 482(7383):103.

Casimiro, I., Marchant, A., Bhalerao, R. P., Beeckman, T., Dhooge, S., Swarup, R., Graham, N., Inzé, D., Sandberg, G., Casero, P. J., et al. (2001). Auxin transport promotes arabidopsis lateral root initiation. *The Plant Cell*, 13(4):843–852.

ChemSpider, Royal Society of Chemistry (2021a). CSID:391354 – brassinolide. `http://www.chemspider.com/Chemical-Structure.391354.html`. Accessed: 2021-09-17.

ChemSpider, Royal Society of Chemistry (2021b). CSID:395716 – trans-zeatin. `http://www.chemspider.com/Chemical-Structure.395716.html`. Accessed: 2021-09-17.

ChemSpider, Royal Society of Chemistry (2021c). CSID:6223 – giberellic acid. `http://www.chemspider.com/Chemical-Structure.6223.html`. Accessed: 2021-09-17.

Chen, Q., Dai, X., De-Paoli, H., Cheng, Y., Takebayashi, Y., Kasahara, H., Kamiya, Y., and Zhao, Y. (2014). Auxin overproduction in shoots cannot rescue auxin deficiencies in arabidopsis roots. *Plant and Cell Physiology*, 55(6):1072–1079.

Chew, Y. H., Wenden, B., Flis, A., Mengin, V., Taylor, J., Davey, C. L., Tindal, C., Thomas, H., Ougham, H. J., De Reffye, P., et al. (2014). Multiscale digital arabidopsis predicts individual organ and whole-organism growth. *Proceedings of the National Academy of Sciences*, 111(39):E4127–E4136.

Chhun, T., Uno, Y., Taketa, S., Azuma, T., Ichii, M., Okamoto, T., and Tsurumi, S. (2007). Saturated humidity accelerates lateral root development in rice (oryza sativa l.) seedlings by increasing phloem-based auxin transport. *Journal of experimental botany*, 58(7):1695–1704.

Couvreur, V., Faget, M., Lobet, G., Javaux, M., Chaumont, F., and Draye, X. (2018). Going with the flow: multiscale insights into the composite nature of water transport in roots. *Plant physiology*, 178(4):1689–1703.

Cramer, G. R., Urano, K., Delrot, S., Pezzotti, M., and Shinozaki, K. (2011). Effects of abiotic stress on plants: a systems biology perspective. *BMC plant biology*, 11(1):163.

de Dorlodot, S., Forster, B., Pagès, L., Price, A., Tuberosa, R., and Draye, X. (2007). Root system architecture: opportunities and constraints for genetic improvement of crops. *Trends in plant science*, 12(10):474–481.

Di Mambro, R., De Ruvo, M., Pacifici, E., Salvi, E., Sozzani, R., Benfey, P. N., Busch, W., Novak, O., Ljung, K., Di Paola, L., Marée, A. F. M., Costantino, P., Grieneisen, V. A., and Sabrina, S. (2017). Auxin minimum triggers the developmental switch from cell division to cell differentiation in the arabidopsis root. *Proceedings of the National Academy of Sciences*, 114(36):E7641–E7649.

Du, H., Liu, H., and Xiong, L. (2013). Endogenous auxin and jasmonic acid levels are differentially modulated by abiotic stresses in rice. *Frontiers in plant science*, 4:397.

el Showk, S., Blomster, T., Siligato, R., Marée, A. F., Mähönen, A. P., Grieneisen, V. A., et al. (2015). Parsimonious model of vascular patterning links transverse hormone fluxes to lateral root initiation: auxin leads the way, while cytokinin levels out. *PLoS Comput Biol*, 11(10):e1004450.

Food and Agriculture Organization of the United Nations (2018). The state of food security and nutrition in the world 2018. `www.fao.org/publications/sofi/en/`. Date accessed: 16.05.2019.

Food Security Information Network (2019). Global report on food crises. `www.fsinplatform.org/global-report-food-crises-2019`. Date accessed: 16.05.2019.

Franklin, K. A., Lee, S. H., Patel, D., Kumar, S. V., Spartz, A. K., Gu, C., Ye, S., Yu, P., Breen, G., Cohen, J. D., et al. (2011). Phytochrome-interacting factor 4 (pif4) regulates auxin biosynthesis at high temperature. *Proceedings of the National Academy of Sciences*, 108(50):20231–20235.

Gao, J.-P., Chao, D.-Y., and Lin, H.-X. (2007). Understanding abiotic stress tolerance mechanisms: recent studies on stress response in rice. *Journal of Integrative Plant Biology*, 49(6):742–750.

Geisler, M., Aryal, B., Di Donato, M., and Hao, P. (2017). A critical view on abc transporters and their interacting partners in auxin transport. *Plant and Cell Physiology*, 58(10):1601–1614.

Gong, X., Liu, M., Zhang, L., Ruan, Y., Ding, R., Ji, Y., Zhang, N., Zhang, S., Farmer, J., and Wang, C. (2015). Arabidopsis atsuc2 and atsuc4, encoding sucrose transporters, are required for abiotic stress tolerance in an aba-dependent pathway. *Physiologia Plantarum*, 153(1):119–136.

Gosting, L. J. and Morris, M. S. (1949). Diffusion studies on dilute aqueous sucrose solutions at 1 and 25 with the gouy interference method. *Journal of the American Chemical Society*, 71(6):1998–2006.

Grieneisen, V. A., Xu, J., Marée, A. F., Hogeweg, P., and Scheres, B. (2007). Auxin transport is sufficient to generate a maximum and gradient guiding root growth. *Nature*, 449:1008–1013.

Hayashi, K.-i., Arai, K., Aoi, Y., Tanaka, Y., Hira, H., Guo, R., Hu, Y., Ge, C., Zhao, Y., Kasahara, H., et al. (2021). The main oxidative inactivation pathway of the plant hormone auxin. *Nature communications*, 12(1):1–11.

He, W., Brumos, J., Li, H., Ji, Y., Ke, M., Gong, X., Zeng, Q., Li, W., Zhang, X., An, F., Wen, X., Li, P., Chu, J., Sun, X., Yan, C., Yan, N., Xie, D., Yang, Z., Stepanova, A., Alonso, J., and Guo, H. (2011). A smale-molecule screen identifies L-kynurenine as a competitive inhibitor of taa1/tar activity in ethylene-directed auxin biosynthesis and root growth in arabidopsis. *The Plant Cell*, 23:3944–3960.

Imlau, A., Truernit, E., and Sauer, N. (1999). Cell-to-cell and long-distance trafficking of the green fluorescent protein in the phloem and symplastic unloading of the protein into sink tissues. *The Plant Cell*, 11(3):309–322.

Izawa, T. and Shimamoto, K. (1996). Becoming a model plant: the importance of rice to plant science. *Trends in Plant Science*, 1(3):95–99.

Jensen, K., Lee, J., Bohr, T., Bruus, H., Holbrook, N., and Zwieniecki, M. (2011). Optimality of the münch mechanism for translocation of sugars in plants. *J R Soc Interface*, 8(61):1155–1165.

Jensen, K. H., Berg-Sørensen, K., Bruus, H., Holbrook, N. M., Liesche, J., Schulz, A., Zwieniecki, M. A., and Bohr, T. (2016). Sap flow and sugar transport in plants. *Reviews of Modern Physics*, 88(3):035007.

Jensen, K. H., Berg-Sørensen, K., Friis, S. M., and Bohr, T. (2012). Analytic solutions and universal properties of sugar loading models in münch phloem flow. *Journal of theoretical biology*, 304:286–296.

Jensen, K. H., Savage, J. A., and Holbrook, N. M. (2013). Optimal concentration for sugar transport in plants. *Journal of the Royal Society Interface*, 10(83):20130055.

Kedem, O. and Katchalsky, A. (1958). Thermodynamic analysis of the permeability of biological membranes to non-electrolytes. *Biochimica et biophysica Acta*, 27:229–246.

Khush, G. S. (2005). What it will take to feed 5.0 billion rice consumers in 2030. *Plant molecular biology*, 59(1):1–6.

Kiba, T., Kudo, T., Kojima, M., and Sakakibara, H. (2011). Hormonal control of nitrogen acquisition: roles of auxin, abscisic acid, and cytokinin. *Journal of experimental botany*, 62(4):1399–1409.

Kleine-Vehn, J., Dhonukshe, P., Swarup, R., Bennett, M., and Friml, J. (2006). Subcellular trafficking of the arabidopsis auxin influx carrier aux1 uses a novel pathway distinct from pin1. *The Plant Cell*, 18(11):3171–3181.

Knoblauch, M., Vendrell, M., De Leau, E., Paterlini, A., Knox, K., Ross-Elliot, T., Reinders, A., Brockman, S. A., Ward, J., and Oparka, K. (2015). Multi-spectral phloem-mobile probes: properties and applications. *Plant physiology*, 167(4):1211–1220.

Knox, K. and Oparka, K. (2018). Illuminating the translocation stream. *Current opinion in plant biology*, 43:113–118.

Knox, K., Paterlini, A., Thomson, S., and Oparka, K. (2018). The coumarin glucoside, esculin, reveals rapid changes in phloem-transport velocity in response to environmental cues. *Plant physiology*, 178(2):795–807.

Korson, L., Drost-Hansen, W., and Millero, F. J. (1969). Viscosity of water at various temperatures. *The Journal of Physical Chemistry*, 73(1):34–39.

Kramer, M. and Went, F. (1949). The nature of the auxin in tomato stem tips. *Plant physiology*, 24(2):207.

Lacombe, B. and Achard, P. (2016). Long-distance transport of phytohormones through the plant vascular system. *Current opinion in plant biology*, 34:1–8.

Lee, M., Jung, J.-H., Han, D.-Y., Seo, P. J., Park, W. J., and Park, C.-M. (2012). Activation of a flavin monooxygenase gene yucca7 enhances drought resistance in arabidopsis. *Planta*, 235(5):923–938.

Liu, W., Li, R.-J., Han, T.-T., Cai, W., Fu, Z.-W., and Lu, Y.-T. (2015). Salt stress reduces root meristem size by nitric oxide-mediated modulation of auxin accumulation and signaling in arabidopsis. *Plant physiology*, 168(1):343–356.

Ljung, K. (2013). Auxin metabolism and homeostasis during plant development. *Development*, 140(5):943–950.

Ljung, K., Hull, A. K., Celenza, J., Yamada, M., Estelle, M., Normanly, J., and Sandberg, G. (2005). Sites and regulation of auxin biosynthesis in arabidopsis roots. *The Plant Cell*, 17(4):1090–1104.

Lynch, J. P. (2007). Roots of the second green revolution. *Australian Journal of Botany*, 55(5):493–512.

Malekpoor Mansoorkhani, F., Seymour, G., Swarup, R., Moeiniyan Bagheri, H., Ramsey, R., and Thompson, A. J. (2014). Environmental, developmental, and genetic factors controlling root system architecture. *Biotechnology and Genetic Engineering Reviews*, 30(2):95–112.

Marchant, A., Bhalerao, R., Casimiro, I., Eklöf, J., Casero, P. J., Bennett, M., and Sandberg, G. (2002). Aux1 promotes lateral root formation by facilitating indole-3-acetic acid distribution between sink and source tissues in the arabidopsis seedling. *The Plant Cell*, 14(3):589–597.

Martin, T., Oswald, O., and Graham, I. A. (2002). Arabidopsis seedling growth, storage lipid mobilization, and photosynthetic gene expression are regulated by carbon: nitrogen availability. *Plant physiology*, 128(2):472–481.

Mashiguchi, K., Tanaka, K., Sakai, T., Sugawara, S., Kawaide, H., Natsume, M., Hanada, A., Yaeno, T., Shirasu, K., Yao, H., et al. (2011). The main auxin biosynthesis pathway in arabidopsis. *Proceedings of the National Academy of Sciences*, 108(45):18512–18517.

Mellor, N., Band, L. R., Pěnčík, A., Novák, O., Rashed, A., Holman, T., Wilson, M. H., Voß, U., Bishopp, A., King, J. R., Ljung, K., Bennett, M. J., and Owen, M. (2016). Dynamic regulation of auxin oxidase and conjugating enzymes *AtDAO1* and *GH3* modulates auxin homeostasis. *Proceedings of the National Academy of Sciences*, 113(39):11022–11027.

Mellor, N. L., Voß, U., Janes, G., Bennett, M. J., Wells, D. M., and Band, L. R. (2020). Auxin fluxes through plasmodesmata modify root-tip auxin distribution. *Development*, 147(6).

Mellor, N. L., Voß, U., Ware, A., Janes, G., Barrack, D., Bishopp, A., Bennett, M. J., Geisler, M., Wells, D. M., and Band, L. R. (2022). Systems approaches reveal that abcb and pin proteins mediate co-dependent auxin efflux. *The Plant Cell*, 34(6):2309–2327.

Minchin, P., Thorpe, M., and Farrar, J. (1993). A simple mechanistic model of phloem transport which explains sink priority. *Journal of experimental botany*, 44(5):947–955.

Moore, S., Zhang, X., Mudge, A., Rowe, J. H., Topping, J. F., Liu, J., and Lindsey, K. (2015). Spatiotemporal modelling of hormonal crosstalk explains the level and patterning of hormones and gene expression in arabidopsis thaliana wild-type and mutant roots. *New Phytologist*, 207(4):1110–1122.

Mroue, S., Simeunovic, A., and Robert, H. S. (2018). Auxin production as an integrator of environmental cues for developmental growth regulation. *Journal of experimental botany*, 69(2):201–212.

Münch, E. (1926). Dynamik der saftstromungen. *Ber. Deut. Bot. Ges.*, 44:68–71.

Nakad, M., Witelski, T., Domec, J.-C., Sevanto, S., and Katul, G. (2021). Taylor dispersion in osmotically driven laminar flows in phloem. *Journal of Fluid Mechanics*, 913.

Naser, V. and Shani, E. (2016). Auxin response under osmotic stress. *Plant molecular biology*, 91(6):661–672.

Nobel, P. S. (2020). *Physicochemical and environmental plant physiology*. Elsevier, fifth edition.

Noh, B., Murphy, A. S., and Spalding, E. P. (2001). Multidrug resistance–like genes of arabidopsis required for auxin transport and auxin-mediated development. *The Plant Cell*, 13(11):2441–2454.

Oparka, K., Duckett, C., Prior, D., and Fisher, D. (1994). Real-time imaging of phloem unloading in the root tip of arabidopsis. *The Plant Journal*, 6(5):759–766.

Oparka, K. J. and Turgeon, R. (1999). Sieve elements and companion cells—traffic control centers of the phloem. *The Plant Cell*, 11(4):739–750.

Paterlini, A. (2020). Uncharted routes: exploring the relevance of auxin movement via plasmodesmata. *Biology Open*, 9(11).

Payvandi, S., Daly, K. R., Zygalakis, K., and Roose, T. (2014). Mathematical modelling of the phloem: The importance of diffusion on sugar transport at osmotic equilibrium. *Bulletin of mathematical biology*, 76(11):2834–2865.

Petersson, S. V., Johansson, A. I., Kowalczyk, M., Makoveychuk, A., Wang, J. Y., Moritz, T., Grebe, M., Benfey, P. N., Sandberg, G., and Ljung, K. (2009). An auxin gradient and maximum in the arabidopsis root apex shown by high-resolution

cell-specific analysis of iaa distribution and synthesis. *The Plant Cell*, 21(6):1659–1668.

Porco, S., Pěnčík, A., Rashed, A., Voß, U., Casanova-Sáez, R., Bishopp, A., Golebiowska, A., Bhosale, R., Swarup, R., Swarup, K., Peňáková, Novák, O., Staswick, P., Hedden, P., Phillips, A. L., Vissenberg, K., Bennett, M. J., and Ljung, K. (2016). Dioxygenase-encoding atdao1 gene controls iaa oxidation and homeostasis in arabidopsis. *Proceedings of the National Academy of Sciences*, 113(39):11016–11021.

Pound, M. P., French, A. P., Wells, D. M., Bennett, M. J., and Pridmore, T. P. (2012). Cellset: novel software to extract and analyze structured networks of plant cells from confocal images. *The Plant Cell*, 24(4):1353–1361.

Pradal, C., Dufour-Kowalski, S., Boudon, F., Fournier, C., and Godin, C. (2008). Openalea: a visual programming and component-based software platform for plant modelling. *Functional Plant Biology*, 35(10):751–760.

Rahman, A., Bannigan, A., Sulaman, W., Pechter, P., Blancaflor, E. B., and Baskin, T. I. (2007). Auxin, actin and growth of the arabidopsis thaliana primary root. *The Plant Journal*, 50(3):514–528.

Regnault, T., Davière, J.-M., Wild, M., Sakvarelidze-Achard, L., Heintz, D., Bergua, E. C., Diaz, I. L., Gong, F., Hedden, P., and Achard, P. (2015). The gibberellin precursor ga 12 acts as a long-distance growth signal in arabidopsis. *Nature Plants*, 1(6):15073.

Ross-Elliott, T. J., Jensen, K. H., Haaning, K. S., Wager, B. M., Knoblauch, J., Howell, A. H., Mullendore, D. L., Monteith, A. G., Paultre, D., Yan, D., Otero, S., Bourdon, M., Sager, R., Lee, J.-Y., Helariutta, Y., Knoblauch, M., and Oparka, K. (2017). Phloem unloading in arabidopsis roots is convective and regulated by the phloem-pole pericycle. *Elife*, 6:e24125.

Rutschow, H. L., Baskin, T. I., and Kramer, E. M. (2011). Regulation of solute flux through plasmodesmata in the root meristem. *Plant physiology*, 155(4):1817–1826.

Sager, R. and Lee, J.-Y. (2014). Plasmodesmata in integrated cell signalling: insights from development and environmental signals and stresses. *Journal of experimental botany*, 65(22):6337–6358.

Sairanen, I., Novák, O., Pěnčík, A., Ikeda, Y., Jones, B., Sandberg, G., and Ljung, K. (2012). Soluble carbohydrates regulate auxin biosynthesis via pif proteins in arabidopsis. *The Plant Cell*, 24(12):4907–4916.

Sasaki, T., Suzaki, T., Soyano, T., Kojima, M., Sakakibara, H., and Kawaguchi, M. (2014). Shoot-derived cytokinins systemically regulate root nodulation. *Nature communications*, 5(1):1–9.

Soeno, K., Goda, H., Ishii, T., Ogura, T., Tachikawa, T., Sasaki, E., Yoshida, S., Fujioka, S., Asami, T., and Shimada, Y. (2010). Auxin biosynthesis inhibitors, identified by a genomics-based approach, provide insights into auxin biosynthesis. *Plant and Cell Physiology*, 51(4):524–536.

Spalding, E. P. (2013). Diverting the downhill flow of auxin to steer growth during tropisms. *American Journal of Botany*, 100(1):203–214.

Starling, E. H. (1896). On the absorption of fluids from the connective tissue spaces. *Classic Papers in Critical Care*, 19:303.

Stavang, J. A., Gallego-Bartolomé, J., Gómez, M. D., Yoshida, S., Asami, T., Olsen, J. E., García-Martínez, J. L., Alabadí, D., and Blázquez, M. A. (2009). Hormonal regulation of temperature-induced growth in arabidopsis. *The Plant Journal*, 60(4):589–601.

Staverman, A. (1951). The theory of measurement of osmotic pressure. *Recueil des Travaux Chimiques des Pays-Bas*, 70(4):344–352.

Stepanova, A. N., Robertson-Hoyt, J., Yun, J., Benavente, L. M., Xie, D.-Y., Doležal, K., Schlereth, A., Jürgens, G., and Alonso, J. M. (2008). Taa1-mediated auxin biosynthesis is essential for hormone crosstalk and plant development. *Cell*, 133(1):177–191.

Stepanova, A. N., Yun, J., Robles, L. M., Novak, O., He, W., Guo, H., Ljung, K., and Alonso, J. M. (2011). The arabidopsis yucca1 flavin monooxygenase functions in the indole-3-pyruvic acid branch of auxin biosynthesis. *The Plant Cell*, 23(11):3961–3973.

Sun, J., Qi, L., Li, Y., Chu, J., and Li, C. (2012). Pif4–mediated activation of yucca8 expression integrates temperature into the auxin pathway in regulating arabidopsis hypocotyl growth. *PLoS genetics*, 8(3):e1002594.

Swarup, K., Benková, E., Swarup, R., Casimiro, I., Péret, B., Yang, Y., Parry, G., Nielsen, E., De Smet, I., Vanneste, S., et al. (2008). The auxin influx carrier lax3 promotes lateral root emergence. *Nature cell biology*, 10(8):946.

Swarup, R., Friml, J., Marchant, A., Ljung, K., Sandberg, G., Palme, K., and Bennett, M. (2001). Localization of the auxin permease aux1 suggests two functionally

distinct hormone transport pathways operate in the arabidopsis root apex. *Genes & development*, 15(20):2648–2653.

Swarup, R., Kramer, E. M., Perry, P., Knox, K., Leyser, H. O., Haseloff, J., Beemster, G. T., Bhalerao, R., and Bennett, M. J. (2005). Root gravitropism requires lateral root cap and epidermal cells for transport and response to a mobile auxin signal. *Nature cell biology*, 7(11):1057–1065.

Taiz, L. and Zeiger, E. (2010). *Plant Physiology*. Sinauer Associates, Inc, fifth edition.

Taylor, G. I. (1953). Dispersion of soluble matter in solvent flowing slowly through a tube. *Proceedings of the Royal Society of London. Series A. Mathematical and Physical Sciences*, 219(1137):186–203.

Thompson, M. V. and Holbrook, N. M. (2003). Application of a single-solute non-steady-state phloem model to the study of long-distance assimilate transport. *Journal of Theoretical Biology*, 220(4):419–455.

Titapiwatanakun, B. and Murphy, A. S. (2009). Post-transcriptional regulation of auxin transport proteins: cellular trafficking, protein phosphorylation, protein maturation, ubiquitination, and membrane composition. *Journal of Experimental Botany*, 60(4):1093–1107.

Truskey, G. A., Yuan, F., and Katz, D. F. (2004). *Chapter 9: Transvascular Transport*, pages 465–485. Pearson.

Ulmasov, T., Murfett, J., Hagen, G., and Guilfoyle, T. J. (1997). Aux/iaa proteins repress expression of reporter genes containing natural and highly active synthetic auxin response elements. *The Plant Cell*, 9(11):1963–1971.

van den Berg, T., Korver, R. A., Testerink, C., and ten Tusscher, K. H. (2016). Modeling halotropism: a key role for root tip architecture and reflux loop remodeling in redistributing auxin. *Development*, 143(18):3350–3362.

van den Berg, T., Yalamanchili, K., De Gernier, H., Teixeira, J. S., Beeckman, T., Scheres, B., Willemsen, V., and Ten Tusscher, K. (2021). A reflux-and-growth mechanism explains oscillatory patterning of lateral root branching sites. *Developmental Cell*, 56(15):2176–2191.

van den Herik, B., Bergonzi, S., Bachem, C. W., and Ten Tusscher, K. (2021). Modelling the physiological relevance of sucrose export repression by an flowering time homolog in the long-distance phloem of potato. *Plant, cell & environment*, 44(3):792–806.

Vanhaeren, H., Gonzalez, N., and Inzé, D. (2010). Hide and seek: uncloaking the vegetative shoot apex of arabidopsis thaliana. *The Plant Journal*, 63(3):541–548.

Virtanen, P., Gommers, R., Oliphant, T. E., Haberland, M., Reddy, T., Cournapeau, D., Burovski, E., Peterson, P., Weckesser, W., Bright, J., van der Walt, S. J., Brett, M., Wilson, J., Jarrod Millman, K., Mayorov, N., Nelson, A. R. J., Jones, E., Kern, R., Larson, E., Carey, C., Polat, İ., Feng, Y., Moore, E. W., Vand erPlas, J., Laxalde, D., Perktold, J., Cimrman, R., Henriksen, I., Quintero, E. A., Harris, C. R., Archibald, A. M., Ribeiro, A. H., Pedregosa, F., van Mulbregt, P., and Contributors, S. . . (2020). SciPy 1.0: Fundamental Algorithms for Scientific Computing in Python. *Nature Methods*, 17:261–272.

Wang, Y., Zhang, T., Wang, R., and Zhao, Y. (2017). Recent advances in auxin research in rice and their implications for crop improvement. *Journal of Experimental Botany*, 69(2):255–263.

Xu, Q., Chen, S., Yunjuan, R., Chen, S., and Liesche, J. (2018). Regulation of sucrose transporters and phloem loading in response to environmental cues. *Plant Physiology*, 176(1):930–945.

Yang, J., Yuan, Z., Meng, Q., Huang, G., Périn, C., Bureau, C., Meunier, A.-C., Ingouff, M., Bennett, M. J., Liang, W., and Zhang, D. (2017). Dynamic regulation of auxin response during rice development revealed by newly established hormone biosensor markers. *Frontiers in plant science*, 8:256.

Zhang, Y., Kilambi, H. V., Liu, J., Bar, H., Lazary, S., Egbaria, A., Ripper, D., Charrier, L., Belew, Z. M., Wulff, N., et al. (2021). Aba homeostasis and long-distance translocation are redundantly regulated by abcg aba importers. *Science advances*, 7(43):eabf6069.

Zhao, H., Ma, T., Wang, X., Deng, Y., Ma, H., Zhang, R., and Zhao, J. (2015). Osaux 1 controls lateral root initiation in rice (o ryza sativa l.). *Plant, cell & environment*, 38(11):2208–2222.

Zhao, Y. (2018). Essential roles of local auxin biosynthesis in plant development and in adaptation to environmental changes. *Annual review of plant biology*, 69:417–435.

Zhu, T., Lucas, W., and Rost, T. (1998). Directional cell-to-cell communication in the arabidopsis root apical meristem i. an ultrastructural and functional analysis. *Protoplasma*, 203(1):35–47.